Universitat Politecnica de Catalunya

Phase Synchronization Scheme for Very Long Baseline Coherent Arrays

Ph.D. Dissertation

Juan Carlos Merlano Duncan

Advisors:

Prof. Jordi J. Mallorquí Franquet

Prof. Francisco López Dekker

Barcelona, July 2012

UPC 2012

Phase Synchronization Scheme for Very Long Baseline Coherent Arrays

J.C. Merlano Duncan

Department of Signal
Theory and Communications

UNIVERSITAT POLITÈCNICA DE CATALUNYA
BARCELONATECH

Phase Synchronization Scheme for Very Long Baseline Coherent Arrays

Ph.D. Thesis Dissertation

by

Juan Carlos Merlano Duncan

UPC Campus Nord, Building D3-114, tel +34934017426

juan.merlano@tsc.upc.edu

Thesis Advisors:

Jordi J. Mallorquí, Ph.D.

UPC Campus Nord, Building D3-211, tel +34934017229,

mallorqui@tsc.upc.edu

Paco López Dekker, Ph.D.

UPC Campus Nord, Building D3-113, tel +34934017199

paco.dekker@tsc.upc.edu

June 25, 2012

Acknowledgements

This research work has been supported by the Spanish National Research MICINN and EU FEDER under projects TEC2008-06764-C02-01 and TEC2011-28201-C02-01. Additionally, this research has also been founded by a collaboration agreement with Altamira Information.

First of all I would like to express my gratitude to my Advisor, Prof. Jordi Mallorquí, for giving me the possibility to do my thesis in the Remote Sensing Group as well as for his guidance, patience, dedication, advices and funding during these years.

I would like express my gratitude in special manner to my Co-Director, Prof. Paco López Dekker, for his guidance, motivation, and suggestions that were fundamental for the development of this thesis.

I would like to express my gratitude to Albert Marton, Ruben Tardio, and Joquim Giner, for their continuous assistance in the laboratory during all these years.

I would like to thank my office mates for their collaboration, in special to Isaac Ramos, Ricardo Barrios, Juan Carlos Rodriguez, Sergio Duque, Mariví Tello, and Santiago Capdevila.

Finally I would like to thank to all the people of the department of Signal Theory and Communications (TSC) for their support during these years.

Preface

Precise phase synchronization of clock or local oscillator signals over distributed systems is a recurring requirement in the design of a wide range of systems, with applications in telecommunications and, for example, in phased arrays. Addressing this requirement is a challenging task when the distance between the subsystems is large in terms of the wavelength and, in particular, when this electrical distance is time-varying.

Carrier phase synchronization is the most important challenge in order to implement distributed beamforming systems and to optimize their power efficiency. At the same time, phase synchronization is crucial for the implementation of distributed (bistatic / multistatic) radar systems.

In the last decades different techniques for remote phase synchronization have been proposed. In 1968 Thompson discussed, compared and classified the available techniques for reducing propagation induced phase fluctuations in frequency distribution systems and presented the principle of round trip stabilization systems. These phase synchronization schemes are Phase Locked Loops (PLL) in which the phase offset is measured directly for the signal which travels along the two-way path, and a direct feedback action closes the loop.

The most important challenge for the design of these systems is the implementation of a method for the discrimination between the waves that travel in opposite directions in the transmission channel. One approach that has been proposed in previous works to fulfill this requirement is the use of different frequencies.

This Ph.D. thesis dissertation presents a new scheme for remote carrier phase synchronization in which a set of tones with similar frequencies are simultaneously used to synchronize two separated stations. In the proposed scheme, the bandwidth required by

the set of tones traveling along the loop can be reduced wherewith the phase fluctuations generated by the dispersive effects of the medium can be drastically reduced.

The proposed scheme was prototyped and tested in the laboratory, with satisfactory results, and a possible application of the phase synchronization prototype has been evaluated.

In order to show the excellent behavior of the phase synchronization prototype a simple distance measurement experiment has been carried out. In that experiment the variations of a distance are obtained from the variations of a measured phase using the synchronization prototype.

Contents

List of Figures

List of Tables

Chapter 1

Introduction

Microwave Active Remote Sensing and specifically Synthetic Aperture Radar (SAR) systems are widely used in spaceborne and airborne platforms. In Active Remote Sensing Systems, a signal is transmitted towards the target using a transmission subsystem, and the information is obtained from the scattered signal through a reception subsystem. In this way, the images are generated using the amplitude and the phase of the received signal. Some spaceborne platforms such as ERS-1, ERS-2, RADARSAT, RADARSAT-2, ENVISAT, and TerraSAR-X have shown the usefulness of monostatic SAR systems as a global tool for Earth monitoring and observation over the last decades.

Moreover, in the last years new lines of research have appeared in the study of new configurations and geometries. In particular, the feasibility of innovative bistatic and multistatic configurations in SAR imaging is now being investigated. Within this framework, the Remote Sensing Laboratory of the Universitat Politècnica de Catalunya (UPC) has developed a C and X-band receiver for a ground-based bistatic-SAR system using the European Space Agency's (ESA) ERS-2 and ENVISAT, and the German Aerospace Agency's (DLR) TerraSAR-X as opportunity transmitters. This SAR Bistatic Receiver for INterferometric Applications has been named SABRINA.

The first SABRINA prototype has been tested experimentally, and the first bistatic images have been obtained with a fixed receiver in a ground based configuration. This study allowed to recognize the two most important restrictions and challenges of the configuration. First, there is a lack of explicit synchronization with the SAR transmitter, in both carrier phase and time synchronization. The second restriction comes for the ground based configuration itself, in which the receiver generally looks at the scene with

a grazing incidence thereby limiting the study of the scattering phenomena with other angles and in some extent the quality of the reconstructed bistatic image.

The next step in the evolution of SABRINA is the development of SABRINA-UAV, a receiver capable to be hold by an unmanned airborne platform in order to implement bistatic geometries with different receiver incidence angles.

The implementation of the bistatic receiver in a mobile platform would lead to unexpected variations in its position. These variations are generated by vibrations and small displacements of the platform which are equivalent to phase changes of the received signal. In addition, the precise geographic location and position tracking of the platform is required in the post-processing of the received data for the generation of the bistatic image. These effects make even more complicated the synchronization issues, where the carrier phase synchronization is required to focus the bistatic data and time synchronization is required for its calibration in order to perform correctly the SAR post-processing.

On the other hand, the use of an airborne receiver working jointly with a ground based receiver, and in general the use of coherent multistatic configurations will allow the development of new applications such as microwave tomography, real 3D imaging, and advanced processing for enhanced resolution using spatial diversity.

For the design of a coherent distributed system, it is required to implement a set of elements (transmitters and/or receivers) whose microwave carrier phases are locked to a common reference, and the phase shift between the elements can be controlled and adjusted regardless of the physical delay of the transmission medium used to distribute the reference. This becomes a difficult task if the elements are widely separated.

A stable local reference can be generated at a central point, which can be distributed directly towards remote locations via cables or radiation links. In this case the phase observed at the remote locations will not be stable due to changes in the electrical path of the transmission medium. The electrical path strongly depends on parameters such as temperature and pressure. These parameters affect the physical dimension of the transmission lines due to thermal expansion and also vary its dielectric constant. These effects cannot be neither easily analytically modeled nor be parameterized.

Therefore, the main objective of this Doctoral Thesis is to propose a Remote Carrier

Phase Synchronization System suitable for the implementation of very large baseline locally distributed microwave coherent transmitters and receivers. The proposed scheme is based on a distributed Phase Locked Loop (PLL), which finds the round trip phase delay of the transmission medium and compensates it at a central point.

The first application of the proposed scheme is for the operation of the airborne based bistatic SAR receiver, SABRINA-UAV. Notwithstanding, the proposed synchronization system is also considered for the implementation of a short range interferometric radio positioning system based in a ground based array of coherent transmitters. This radio location system will be designed to localize the position of the airborne bistatic receiver (or receivers) during the acquisition, therefore the phase variations induced by the platform movement can be compensated. Furthermore, the bistatic receiver can implement an independent phase synchronization link between one of the units of the array. Thus the receiver would obtain an absolute phase reference complementary to the positioning information obtained from the complete array.

This thesis is organized as follows: first this document studies the state of the art of systems for distributed carrier phase synchronization. The proposed scheme is evaluated, analyzed, and modeled, explaining its advantages and differences over the previous works. Then the design and construction process of the synchronization scheme prototype is explained , and the obtained experimental results are documented. Finally, the use of the proposed carrier synchronization scheme in an interferometric radio location system is analyzed and studied in concordance with the requirements of SABRINA-UAV.

1.1 Objectives

The main objective of this Doctoral Thesis is to propose a Remote Carrier Phase Synchronization System suitable for the implementation of very large baseline locally distributed microwave coherent transmitters and receivers.

Thus, the proposed system will be used for the distribution of a local oscillator signal, from a central unit to remote units. Each remote unit will be connected to the central unit through a phase synchronization loop which will ensure a constant phase offset among the two units regardless of the actual variations in the delay of the transmission line used

to interconnect them.

In general, the synchronization system is designed to be applied in the carrier synchronization of bistatic or multistatic SAR receivers. In order to accomplish the main objective the following specific objectives must be fulfilled:

- Study of the state of the art of similar systems implemented in different engineering fields. Some examples must be studied in depth, reviewing its similarities and differences, in addition to the capabilities and features achieved by each of them.

- Complete analysis of the requirements prior to the design of the Carrier Synchronization System. These requirements will be determined by the final application of the synchronization loop: the unmanned airborne based bistatic receiver SABRINA-UAV, designed by the Remote Sensing Laboratory at the Universitat Politècnica de Catalunya.

- Functional design of the Phase Synchronization System. In this step the requirements and characteristics of the subsystems must be specified. Among these subsystems there are the transmission media and the blocks of a Central Unit and a Remote Unit which perform a peer-to-peer phase synchronization link. Special care is given to this step, where the design must be restricted in cost and complexity, to prove the feasibility of such a system. The complete system must be modeled by means of computer simulations and also parametrized analytically.

- Design and simulation of the complete carrier phase synchronization system at hardware level. In this step all the sub-blocks of the systems must be specified.

- Construction and prototyping of the constitutive blocks of the system. Here, a prototype with one central unit and one remote unit must be constructed separately. The hardware prototypes must be tested and the results must be documented.

- Testing over the complete carrier phase synchronization system. The performance of one complete Phase Synchronization Loop must be tested and the results must be documented, providing an experimental validation to the proposed scheme.

- Study of feasibility of implementation of a short range interferometric radio positioning system using the proposed carrier phase synchronization scheme. The positioning system will be used in location and position tracking of the bistatic SAR receiver. Therefore, the design parameters will be studied and defined in concordance with the design of the airborne based Bistatic SAR receiver.

Chapter 2

Applications of Remote Carrier Phase Synchronization

2.1 Synthetic Aperture Radar

After the deployment of conventional radar systems in the second half of the 20th century, the use of moving platforms, such as orbital satellites and airplanes was the key for further developments. This approach was the origin of the Synthetic Aperture Radar (SAR), which has become a mature field and have been proved to be a useful tool for Earth observation and monitoring. Many missions (SEASAT, SIR-C, SRTM, ERS-1, ERS-2, RADARSAT, RADARSAT-2, ENVISAT and TerraSAR-X, among others) have demonstrated the usefulness of this concept. In the last years the systems have highly improved, increasing resolution and/or coverage by using sophisticated antenna pointing methods and advanced transmission and reception subsystems [18, 95].

Unlike conventional radars, the resolution in SAR systems is not determined directly by the beamwidth of the radiation pattern obtained by the single antenna or the antenna array used. These systems use a short physical antenna, but by means of the platform movement they synthesize the effect of a very long antenna. Therefore it is improved the azimuth resolution, which is the resolution in the direction of the displacement of the platform, also called along-track direction [18].

This improvement is achieved making use of the Doppler history generated by the movement of the platform with respect to the fixed target. An example of the orbital SAR geometry is shown in Figure 2.1.

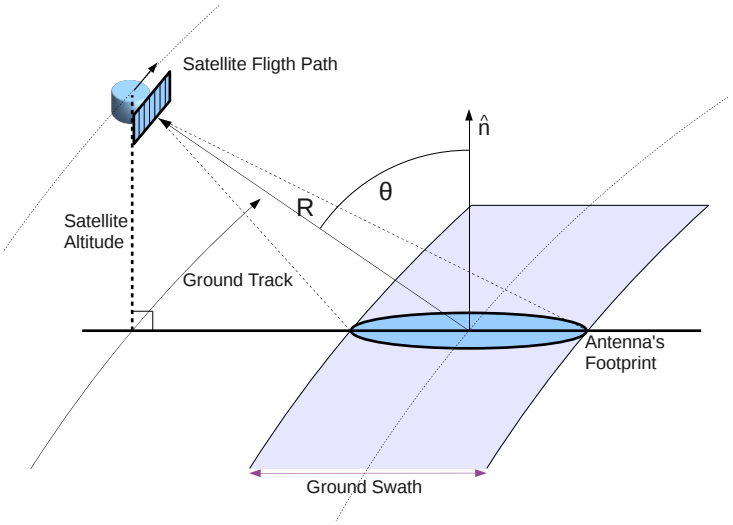

Figure 2.1: Geometry of a monostatic spaceborne SAR system.

The incidence angle θ is taken from the line normal to the target surface to line of incidence of the radar signal [95, 100].

The slant range resolution, Δr, of a monostatic SAR system is the conventional radar range resolution and is given by

$$\Delta r = \frac{c}{2B} \tag{2.1}$$

Where B is the system frequency bandwidth, and c is the speed of light. Accordingly, the ground range resolutions is equal to

$$\Delta r_{\mathrm{g}} = \frac{c}{2B \cdot \sin\,\theta} = \frac{\Delta r}{\sin\,\theta} \tag{2.2}$$

Regarding the azimuth resolution, it is given by the relation between the velocity of the moving platform v_{sar}, and the Doppler bandwidth Δf_{d}, by

$$\Delta r_{\mathrm{a}} = \frac{v_{\mathrm{sar}}}{\Delta f_{\mathrm{d}}} = \frac{L_{\mathrm{a}}}{2} \tag{2.3}$$

which is a function of the azimuth gain of the transmit-receive antenna, which depends on the antenna length, L_a. The smaller the antenna is in azimuth, the less directive it would be. However, a higher resolution is obtained, because the synthetic aperture is larger and therefore a more directive antenna is synthesized.

In summary, SAR systems in monostatic configurations is a mature field and new lines of research have appeared in the study of new configurations and geometries. Following this direction, the feasibility of innovative bistatic and multistatic configurations in SAR imaging is now being studied. One of these bistatic systems is the TanDEM-X Mission, which has the goal of generating a global Digital Elevation Model (DEM) with an unprecedented accuracy. It will be achieved by means of a second SAR satellite flying in a tandem orbit configuration with TerraSAR-X. Furthermore, other configurations including orbital transmitters combined with airborne or land based fixed receivers have been studied, opening the the possibility to explore alternative geometries and different scattering mechanisms [95, 100].

2.2 SABRINA: A SAR Bistatic Receiver for Interferometric Applications

The Remote Sensing Laboratory at the Universitat Politècnica de Catalunya (UPC) has developed a C-band and X-band receiver for a ground-based bistatic-SAR system using conventional SAR satellites as transmitters of opportunity. This SAR Bistatic Receiver for INterferometric Applications has been named SABRINA, and it has been successfully tested with ESAs' ERS-2 and ENVISAT, CSA's Radarsat-2 and DLR's TerraSAR-X satellites.

This system provided an experimental platform to study most aspects of the bistatic SAR systems, such as scattering phenomena, data processing, interferometric applications [21, 24, 64], and hardware related aspects. Particular emphasis was made on those aspects linked to synchronization, such as time or Pulse-Repetition-Frequency (PRF) synchronization and carrier phase synchronization [66, 93].

For example, it has been observed that the use of a local oscillator in a receiver which is not synchronized with the transmitter, drastically increases the impact of oscillator phase noise, which cause significant errors in both the SAR focusing and the interferometric phase. This is analyzed and quantified in [59].

Figure 2.2 shows the Bistatic SAR geometry. Here θ_{t} and θ_{r} are the incidence angles,

with respect to the transmitter and the receiver, both relative the vector normal to the target area.

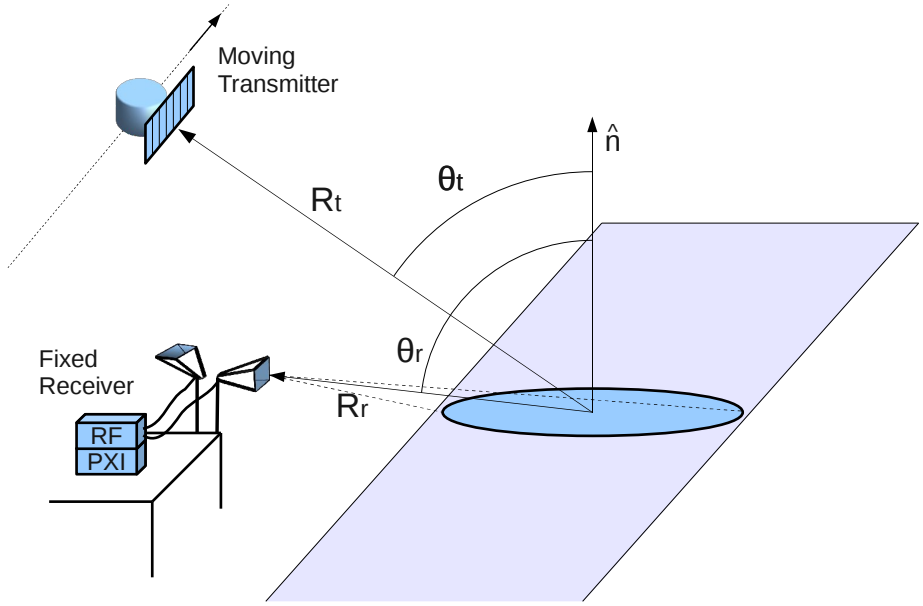

Figure 2.2: Bistatic geometry. The figure shows the moving transmitter, the fixed receiver, and the beam pattern of the receive antenna covering a portion of the strip illuminated by the transmitter.

2.2.1 Bistatic SAR Geometry

Bistatic ground range resolution

In the monostatic SAR, the ground range resolution is obtained by the intersection of the ground surface with the range spheres, centered at the transmitter. Therefore, in a bistatic geometry the ground range resolution is obtained by the intersection of ellipsoid surfaces, with foci at the positions of the transmitter and the receiver, with the ground surface. For a given azimuth angle these ellipsoids reduce to 2-D ellipses. Wherewith the ground resolution can be approximated by

$$\Delta r_{\mathrm{g}} = \frac{c}{B \cdot (\sin \theta_{\mathrm{t}} + \sin \theta_{\mathrm{r}})} \tag{2.4}$$

From this expression, it can be seen that the bistatic ground range resolution is equal

to the monostatic one when both incidence angles, θ_{t} and θ_{r}, are equal.

There are two possible configurations for a bistatic geometry. In the first configuration, which is called *back scattering*, θ_{t} and θ_{r} have the same sign. In the second, θ_{r} has the opposite sign of θ_{t}, and this configuration is called *forward scattering*.

In a typical *back scattering* scenario, the receiver is at ground level, which represents an incidence angle of around 90°, and the transmitter has an incidence angle ranging from 15° to 40° depending on the sensor and acquisition mode, for instance for ERS-2 and ENVISAT in mode IS2 it is around 21°. Whereupon, the obtained resolution with this configuration is around 13 m, much better than the 24 m resolution of the corresponding monostatic case.

In a *forward scattering* configuration example, using also ENVISAT as transmitter and a ground based receiver ($\theta_{\mathrm{t}} = -21°$ and $\theta_{\mathrm{r}} = 90°$), the obtained resolution is around 31 m, which is not very different than the corresponding monostatic case.

There is a special case of forward scattering, in which θ_r is equal to $-\theta_{\mathrm{t}}$, consequently, denominator in Equation (2.4) becomes zero [80, 93, 103], and thus, the resolution is completely lost. This particular case is known as specular scattering.

Bistatic azimuth resolution

The azimuth resolution in a bistatic geometry depends on the bistatic Doppler bandwidth, $\Delta f_{\mathrm{d,bist}}$, and the transmitter velocity with a similar relation that for a conventional SAR system, by

$$\Delta r_{\mathrm{a,bist}} = \frac{v_{\mathrm{sar}}}{\Delta f_{\mathrm{d,bist}}} \tag{2.5}$$

In the bistatic case, the azimuth beam pattern of the transmitting antenna affects the azimuth resolution in one direction, unlike the monostatic case in which the azimuth antenna gain is applied in two ways, one for transmission and another one for reception. Thus, the Doppler bandwidth for a bistatic system is determined by the 1-way antenna azimuth gain. If the transmission beam pattern is approximated by a Gaussian function, the ratio between the 1-way and 2-way beam patterns is $\sqrt{2}$. Hence, the bistatic azimuth

resolution becomes

$$\Delta r_{\mathrm{a,bist}} = \frac{v_{\mathrm{sar}}}{\Delta f_{\mathrm{d}}/\sqrt{2}} = \sqrt{2} \cdot \Delta r_{\mathrm{a,mono}} \tag{2.6}$$

Bistatic radar range equation

The signal to noise ratio for a given resolution cell in a bistatic geometry can be obtained following the steps of the monostatic case [18, 93]. After SAR processing and for a given normalized radar cross section σ^0, this can be expressed as

$$\mathrm{SNR}_{\mathrm{bist}} = \frac{B_{\text{2-way}}}{B_{\text{1-way}}} \frac{P_{\mathrm{av}} G_{\mathrm{t}} G_{\mathrm{r}} \lambda^3 \sigma^0 \Delta r_{\mathrm{g}}}{(4\pi)^3 R_{\mathrm{t}} R_{\mathrm{r}}^2 k T_0 F_{\mathrm{r}} v_{\mathrm{sar}}} \tag{2.7}$$

where $B_{\text{2-way}}$ is the two-way antenna azimuthal beamwidth of the transmit–receive antenna; $B_{\text{1-way}}$ is the one-way transmit azimuthal beamwidth, G_{t} and G_{r} are the transmit and receive gains, respectively, R_{t} and R_{r} are the distances from the target to the transmitter and the receiver, T_0 is the input noise temperature, F_{r} is the receiver noise figure, and P_{av} is the average radiated power. This expression is only valid for the fixed receiver scenario, while further considerations must be taken for configurations in which the receiver is moving.

Another result that can be extracted from the bistatic radar range equation is the improvement in SNR of the bistatic case compared to the monostatic one. The ratio of the SNR improvement, under the assumption that both receivers (the bistatic and monostatic) have the same noise figure, is given by

$$\frac{\mathrm{SNR}_{\mathrm{bist}}}{\mathrm{SNR}_{\mathrm{mono}}} \sim \frac{G_{\mathrm{r}} R_{\mathrm{t}}^2}{G_{\mathrm{t}} R_{\mathrm{r}}^2} \tag{2.8}$$

In a urban scenario, with the receiver at a distance around 10 km, and using ENVISAT as transmitter, the improvement ratio will be in the order of 40 dB, if similar values of the transmitter and receiver gain, G_{t} and G_{r}, are considered. Thus, in a practical implementation, the gain and noise figure requirements for a bistatic receiver can be relaxed in a few dB without a considerable loss in the signal quality.

Carrier and time synchronization

Synchronization is a key challenge for any bistatic system. Thus, there are systems that can work in a cooperative mode, in which the transmitter and the receiver explicitly exchange synchronization information. This is the case of TanDEM-X, launched in 2010 by the German Aerospace Agency, that is based on two TerraSAR-X radar satellites flying in close formation [58]. In this system, a dedicated synchronization link is used to quantify and compensate oscillator's phase noise. [10, 113]. (Explained in Section 3.1.2) On the other hand, opportunistic systems such as SABRINA, in which different opportunity transmitters can be used, do not have explicit carrier phase and timing synchronization schemes. For this reason, the synchronization information must be extracted from sampling of a direct signal obtained through an antenna pointed at the transmitter satellite.

The data from the direct channel and the scattered channels are sampled continuously along a temporal acquisition window for a satellite overpass. This temporal window is centered at the estimated zero Doppler time, which is the instant when the transmitter is closest to the target area. This time is calculated using the simplified general perturbations version 4 (SGP4) orbit propagation algorithm, which is used as an input two-line Keplerian-element (TLE) sets which can be downloaded from a number of sources (for example, from the space-track portal available at http://space-track.org). The acquisition window must be large enough to contain all the useful data, even with some error in the calculation of the zero Doppler time (generated by the errors in orbit prediction) and some offset in the clock of the acquisition system. The PRF synchronization, which is in some extent the time synchronization required to process the SAR image, is obtained from the acquired data in the post-processing.

Implementation of the fixed receiver

The bistatic receiver is divided into two functional blocks, the Radio Frequency block (RF) and the digital acquisition subsystem. The RF block in the first version of the receiver has two down-conversion channels, a channel for the direct path and another for the scattered one. Figure 2.3 shows a general diagram of the dual channel receiver.

Each channel down-converts the received signal centered at C or X-bands, to the

intermediate frequency IF. The value of the IF is adjusted to allocate the average frequency of the chirp at one quarter of the sampling frequency window, and hence is equal to

$$IF = \left(n + \frac{1}{4}\right) \cdot F_s, \text{ for } n = \{0, 1\} \tag{2.9}$$

In the first version of the receiver, the direct and the scattered channels were adjusted to have different gains, considering that the direct path has higher input power than the scattered one.

The input power in the scattered channel was estimated using the the radar equation, while the input power in the direct one was estimated using the Friis power transmission equation, which is

$$P_{\mathrm{r}} = P_{\mathrm{t}} G_{\mathrm{t}} G_{\mathrm{r}} \left(\frac{\lambda}{4\pi R_{\mathrm{t}}}\right)^2 \tag{2.10}$$

Where λ is the wavelength associated to the carrier frequency. For ENVISAT, and

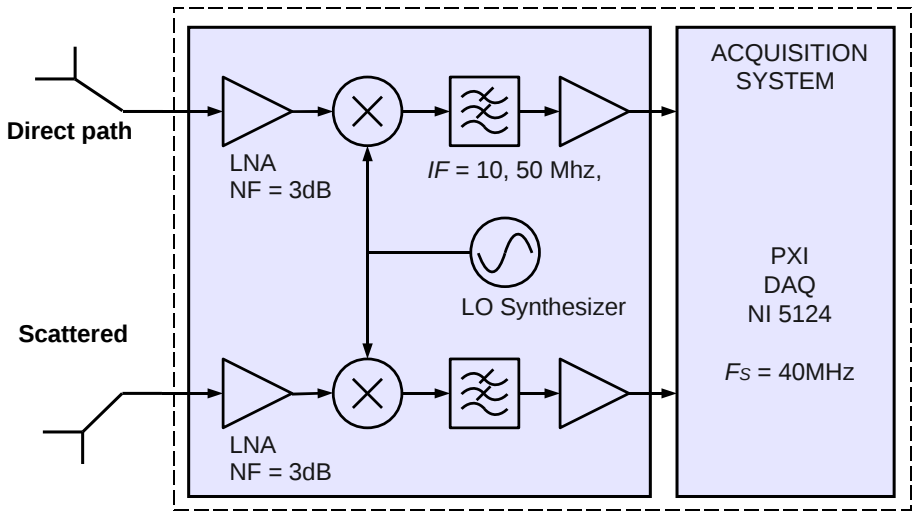

Figure 2.3: Receiver diagram of the dual channel receiver. The first channel is connected to an antenna pointed directly at the satellite to obtain a clean reference signal. The second channel receives the scattered signal. Both signals are sampled continuously and down-converted to an $IF = (n + 1/4)F_s$, with $n = \{0, 1\}$. Taken from [93].

a receive-antenna gain of 18 dBi, the expected average power in the direct channel is around of -45 dBm. With this input power the SNR of the receiver is 56 dB, where the noise power was calculated with a 16 MHz chirp bandwidth, a noise figure of 3

dB, and assuming that the antenna temperature is significantly lower than the system's temperature since it is pointing almost to the zenith. The bistatic radar equation suggest a lower power in the scattered channel, however, in practice strong signals from the direct path and local reflections slip in to the scattered channel. For this reason, in the current version of the receiver all channels have the same conversion gain of 40 dB, and the same noise figure of 3 dB. Additionally, in the current version two more down-conversion channels were added, for a total of four, to collect more scattered paths in order to use them in interferometric and/or polarimetric applications. The local oscillator used for the down-conversion is generated with a custom synthesizer based in a PLL, which uses a very low phase noise frequency reference. The acquisition subsystem is based on a PXI system featuring an off-the-shelve National Instruments PXI-5124 card, providing a 12-bit resolution and a sampling rate up to 200 MHz. By continuous sampling at 40 MS/s, the on board memory, of 512 MB for each channel, provides a continuous-sampling window of 6.3 s, which is enough for the observation times required for the use of ENVISAT and ERS-2 transmitters, which is roughly 0.9 s, and long enough to accommodate prediction errors, which in practice, have been found to be of less than half a second [93].

Experimental results

SABRINA has been tested locally from the roof of a building at the UPC Campus in Barcelona. Figure 2.4 shows the SABRINA prototype setup for a bistatic acquisition. The test area is northwest of the campus and includes the Sant Pere Martir Hill, which can be seen in the background of the picture. The system has been tested routinely using the track 151 of the ENVISAT's orbit, for which Barcelona is centered in the swath, in a backscattering-like geometry. Figure 2.5 shows an example of bistatic-SAR image produced by SABRINA next to an aerial photograph of the area. The image shows the intensity of the scattered signal relative to its maximum, and it has been geocoded and projected on a DEM of the area. Topographic contour lines have been overlaid to help the interpretation of the image. After signal processing, it has been found that the obtained range and azimuth resolution are very similar to the theoretical values.

Figure 2.4: SABRINA prototype deployed on the roof of a building at the UPC Campus during an acquisition. One antenna points at the ENVISAT, while the second antenna points west toward the region of interest, which is the Sant Pere Martir Hill (in the background). Taken from [93].

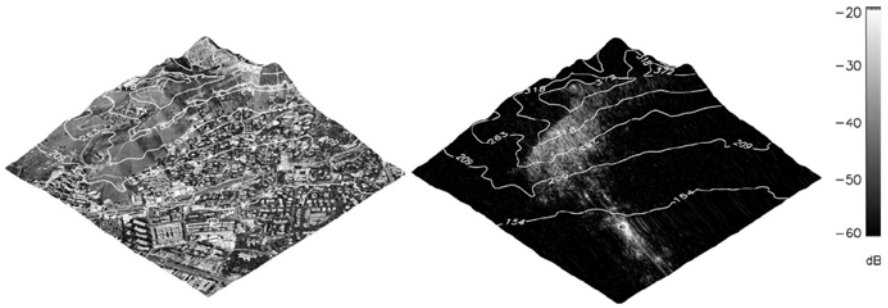

Figure 2.5: Aerial ortophoto (left) and bistatic-SAR image (right) of the test area. Both images are geographically referenced and projected on the DEM of the area, with topographic contour lines overlaid. The bistatic-SAR image represents the received power referenced to the maximum received power (in decibel scale). Taken from [93].

2.2.2 SABRINA-UAV

SABRINA has been an useful tool to experimentally validate bistatic SAR configurations. However, this receiver presents some geometric limitations associated to a fixed receiver ground based system. The most important of these limitations is the inability to vary the receiver incidence angle, which is attached to a ground incidence angle of $\sim 90°$.

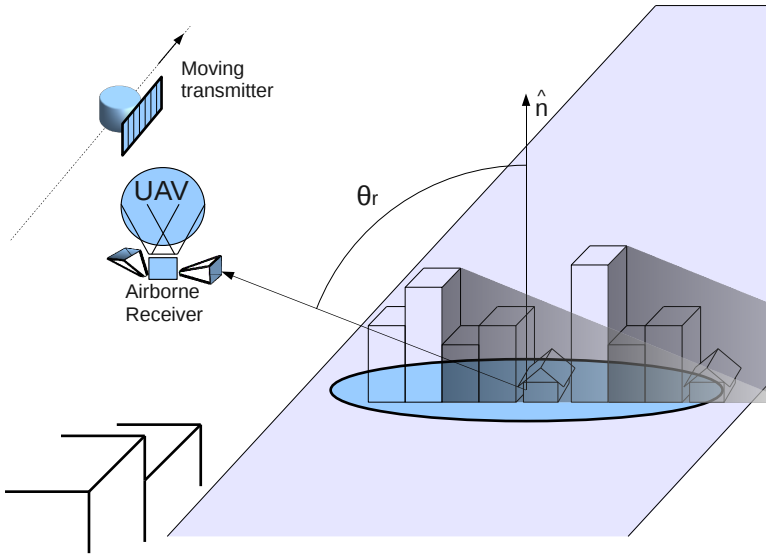

(a) Geometry with high incidence angle presents higher shadowing effect.

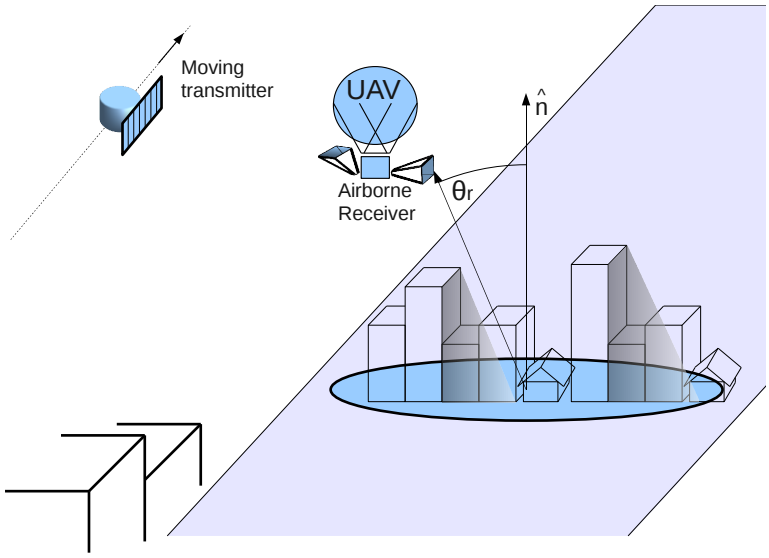

(b) Geometry with low incidence angle presents lower shadowing effect.

Figure 2.6: Geometry of the airborne receiver based bistatic system.

With grazing incidence angles the configuration is largely affected by what is known

as the shadowing effect, which means that some target surfaces are hidden to the receiver by other elements in the target scenario. On the other hand, a bistatic receiver can be a valuable tool for an experimental study of the scattering phenomena and the radar cross section of different surfaces with their polarimetric responses if the study can be performed for many scattering angles distinct than those of the monostatic case. Therefore, the next step in the evolution of SABRINA, is SABRINA-UAV, which is a compact and low-weight receiver, working at C and X bands, that can be carried by an Unmanned Airborne Vehicle (UAV). The use of this UAV platform eliminates the angle limitation associated to the fixed ground based system, and makes possible the study of bistatic configurations with different incidence angles [73, 111]. The airborne-receiver bistatic configuration is depicted in Figure 2.6. Here, it can be observed that the shadowing effect can be avoided with lower receiver incidence angles [73].

Challenges in the implementation of the receiver suitable for an UAV platform

There are some considerations that must be taken into account in the design of the UAV bistatic receiver. First, the ideal platform for this application should be capable of changing its position within a volume, and should be fixed at a desired point during the bistatic acquisition. The movement of the platform during the acquisition, even with a known constant velocity, will make the signal processing substantially more difficult, with no additional benefits. Hence, the receiver platform can be a helicopter or an aerostat balloon, being the second option more feasible in terms of simplicity and costs. In fact, the chosen platform for the implementation of SABRINA-UAV is a commercial product sell as *Helikite*. This product is a combination of an aerostat balloon and a kite, it can rise to heights up to 1000 m, and has a load capacity of 9 kg. Photographies of this flying platform is shown in Figure 2.7

Figure 2.7: Photographies of Helikite, the Aerostat-Kite UAV platform. Regular balloons are pushed down by wind, whereas Helikite aerostats are actually pushed up by it. Helikite has the capacity of flying to a thousand feet in high winds.

The most evident requirement for the receiver is to have a low weight, as low as possible in order to meet the 9 kg maximum payload of the *Helikite* platform. Also, the receiver must include all the control circuitry, the radio frequency front-end and the acquisition system. The second requirement, and the most important one, is the synchronization and localization of the receiver. This requirement is more strict than that of the fixed receiver case. These requirements can be summarized as follows:

- Motion compensation: In the same way as in the fixed receiver configuration, the use of a local oscillator in the receiver which is not synchronized to the transmitter is an issue for the focusing of the bistatic image. Moreover, in an UAV platform the vibrations and variations in the position during the acquisition are directly equivalent to phase noise in the local oscillator, then its effects are considerably worse. For this reason it is necessary to implement a subsystem that performs a continuous recording over time of the variations in the position of the platform around a fixed point. This information will be used in post-processing to compensate the effects of these variations.

- Localization of the receiver: The absolute 3D position of the receiver must be determined in order to perform correctly the signal processing of the received data.

- PRF synchronization: It is advisable to implement a PRF synchronization mechanism in order to decrease the total throughput required to store the received data. So that the receiver stores only the segments of time which contains the reflections of the SAR pulse on the target area.

Implementation of the receiver

The SABRINA-UAV receiver has the same functionalities than the fixed ground based receiver. However, in this case the design is optimized in weight, size and energy consumption. A general block diagram of the bistatic receiver is shown in Figure 2.8. This diagram describes the SAR receiver that is designed to be carried by an UAV. In this version the receiver has three RF down-conversion chains, one of these channels is used for the direct path, while the other two receive the scattered signal in a polarimetric or interferometric configuration.

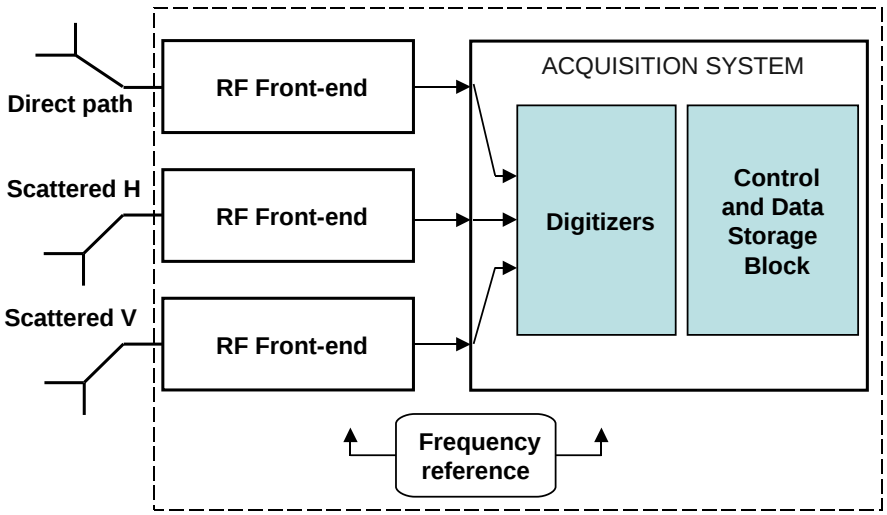

Figure 2.8: Simplified diagram of SABRINA-UAV. Functionally, each channel has the same characteristics that the ground based receiver, with a chain gain of 40 dB, and a noise figure of 3 dB.

The RF Front-ends were integrated using PCB design, integrating each channel into a single board to reduce size and weight.

In addition to the reception of the signals at C and X-bands from the SAR system, the receiver can also be used to obtain signals from a set of ground based auxiliary

transmitters used for radio localization.

Implementation of the acquisition system in the receiver

The acquisition system performs the analog to digital conversion of the IF signals, and then selects and stores the data used to obtain the bistatic SAR image. This is done using a set of analog to digital converters and a Control and Data Storage Block.

The Control and Data Storage Block has an internal clock used to determine the start of the data acquisition window, which is centered at the zero Doppler time (the time instant when the transmitter is closest to the target area). Additionally, this block automatically detects the presence of the SAR signals and synchronizes the receiver to the satellite Pulse Repetition Frequency (PRF). This block selects and stores only the segments of the acquired data that contain relevant information for a given range of interest. Hence, the requirements for average data throughput and total amount of memory are reduced in comparison with a system recording in a continuous time basis.

The throughput required to store continuously the three channels is given by

$$\text{Throughput} = F_s \times N\text{bits} \times 3. \tag{2.11}$$

For example, the required throughput to store ENVISAT signals sampling at 40 MSPS will be 1.44 Gbits/s. This required value can be lowered if the PRF synchronization mechanism is implemented, storing only short segments of the digitized data. Thus, using the maximum ground range of interest, $r_{\mathrm{g,max}}$, the length of the segment required to be stored, t_{acq}, is calculated as follows:

$$t_{\mathrm{acq}} = \tau + \frac{\sin\theta_{\mathrm{t}} + \sin\theta_{\mathrm{r}}}{c} \times r_{\mathrm{g,max}} \tag{2.12}$$

Where τ is the duration of the chirp pulse. Therefore, the duty cycle of the acquisition, that is the percentage of throughput lowering, is given by $t_{\mathrm{acq}} \times \mathrm{PRF}$.

In this case, the duty cycle for storing ENVISAT data (ASAR mode IS2) for a maximum ground range of 10 km will be 0.12, and the required throughput lowered to 173 Mbits/s.

The PRF synchronism recovery is implemented by means of pulse compression of the direct path signal. This functionality is performed in hardware and real time with the FFT algorithm. Consequently, the filter output is introduced to the Peak Detector and Synchronization block, which regenerates the PRF pulses. A functional diagram of this is shown in Figure 2.9

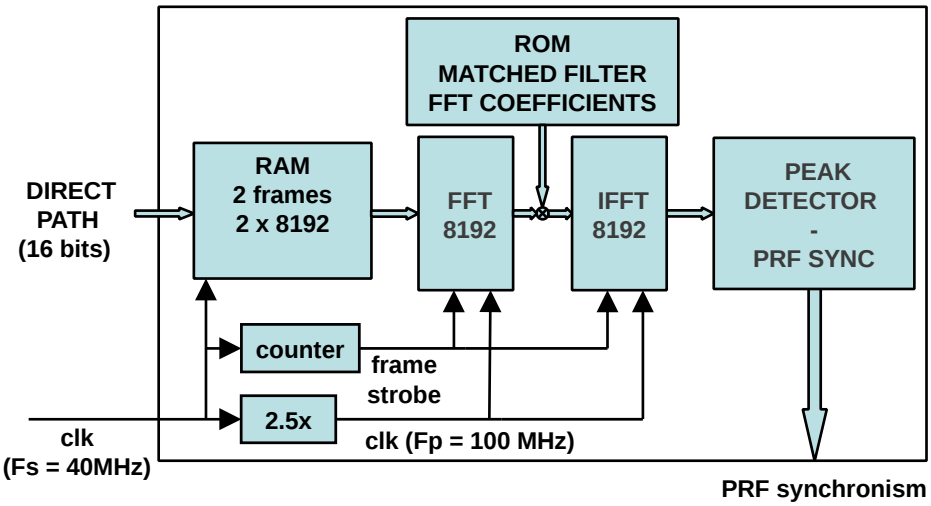

Figure 2.9: Simplified diagram of the PRF recovery block. In this particular example (ENVISAT ASAR mode IS2) the frame length is 8192 samples.

The peak detection is done by frames, where the frame length is given by the length of the FFT transformations used in compression. A peak is detected if the maximum output of the filter in a frame surpasses a threshold level. This threshold varies adaptively depending on the power average of the filter output. The PRF synchronism information is used to determine which of the data stored in buffers is relevant and need to be recorded in a massive storage device.

The logic functions of the acquisition system are implemented in a high density Programmable Logic Device (PLD) taking advantage of its velocity, logic density and size of its internal memory blocks, that are used to buffer the input data.

In particular, the acquisition system is implemented in a compact and low weight prototyping tool, based on a PLD. This tool has a set of four high speed 16 bits ADCs at 225 MSPS; a high density PLD, in fact the Xilinx Virtex-5 SX95 FPGA (Field Programmable Gate Array), in combination with 2 GB of DDR2 SRAM memory and an

external massive non-volatile storage device.

The PLD has internal ROM modules to store the coefficients of the chirp-matched filter. Moreover, the PLD computes concurrently the FFT and IFFT with a clock rate that is 2.5 times the sampling rate, allowing a continuous processing of all the input data [73, 85]. For ENVISAT IS2 mode chirp, the length of the transform blocks is 8192; and the length of the filter in samples is 1040 samples. Both transforms are implemented with a fixed integer input representation of 16 bits.

In future implementations, SABRINA-UAV will be able to receive signals from an auxiliary array and use it to obtain its localization. These localization signals can be received using the same RF chains used to down-convert the bistatic SAR signals. Similarly, the localization information can be processed by the Control and Data Storage Block. This process is also based on matched filtering and peak detection, and can be executed concurrently in the PLD reusing some blocks of the PRF synchronism recovery. The memory buffers and the first direct FFT block are some examples of blocks which can be reused.

Carrier Phase Synchronization

One of the most promising applications of an airborne based bistatic receiver is its use in combination with the fixed ground based receiver, for which, both receivers must operate coherently in order to implement a very long baseline tomographic configuration.

Thereupon, the synchronization of two or more bistatic receivers is a possible application of the Carrier Phase Synchronization Scheme proposed in this thesis.

2.3 High precision interferometric distance measurement

One of the most important applications of remote carrier phase synchronization is the measurement of distances. In this case the obtained resolution will be a fraction of the wavelength of the used carrier. The implementation of a remote carrier phase synchronization system is based in the measurement of the phase offset associated to a transmission

medium which is used to transmit a local oscillator signal from a central point to a remote location. It is possible to obtain the distance from the central point to the remote location using this phase offset if two parameters are well known: the exact frequency of the carrier and the speed of propagation of that wave in the medium. The measured phase offset depends on the speed of propagation of the electromagnetic wave and has an ambiguity given by the carrier wavelength. Thereby, if the distance d, to be measured, is longer than one wavelength, λ, then the phase measure will contain a 2π ambiguity. The measured phase ϕ_{measured} is

$$\phi_{\text{measured}} = \phi_{\text{medium}} \pmod{2\pi} \tag{2.13}$$

where ϕ_{medium} is the total phase offset introduced by the transmission medium. This ambiguity cannot be resolved with a single value of the carrier wavelength. Then the distance will be equal to

$$d = \left(\frac{\phi_{\text{measured}}}{2\pi} + N \right) \cdot \lambda \tag{2.14}$$

being N an unknown positive integer. The measurement may be profitable if a previous approximated value of the distance is known. Therefore it will be possible to measure the differential changes over a known value with a resolution much more precise than one wavelength. In the synchronization system the phase offset of the medium is measured and compensated at the central point in order to maintain a constant phase (for changes in the distance) in the remote location. Thus, the resolution of the differential measurement is given by the phase error of the compensated loop. Hence, the standard deviation of the phase error of the compensated system, $\sigma_{\phi\text{error}}$, will determine the standard deviation of the differential longitude measurement σ_d, with

$$\sigma_d = \left(\frac{\sigma_{\phi\text{error}}}{2\pi} \right) \cdot \lambda. \tag{2.15}$$

On the other hand, the ambiguity problem can be resolved with some methods proposed in recent publications. These methods are based on the repetition of the phase offset measurements using two or more carriers carriers with slightly different wavelengths [6, 7, 112]. One of these methods is explained in Section 3.1.1.

There are other possible applications for phase synchronization in distance measurement in addition to the one-dimensional case. For example, it is possible to transmit microwave signals from two (or more) synchronized units to an additional common receiver in order to measure displacements in other axes. The transmitted signals can be modulated, for example, with complex frequency sweep patterns in order to improve the characteristics of the signal acquired by the common receiver. Therefore the units can transmit similar waveforms to the ones used by the SAR system explained in Section 2.1. The common receiver will monitor the displacements of the remote unit if the central unit is attached to a fixed reference position. One example of this configuration is shown in Figure 2.10. Here it can be seen that the common receiver can monitor the displacements of the remote unit in the vertical axis, Y, making use of the reference signal sent from the central unit.

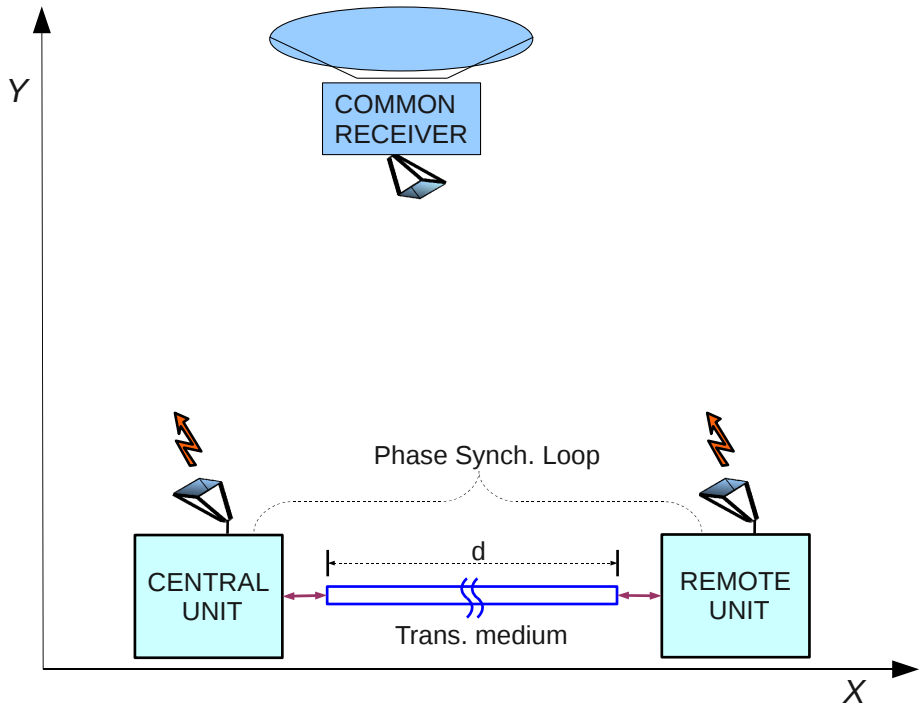

Figure 2.10: Simplified diagram of the high precision displacement measurement using a common receiver and two synchronized transmitters. The small displacements in the Y axis in the remote unit can be detected with high precision in the common receiver.

This configuration can be extended to a set of remote units synchronized in phase, using the central unit as a reference in a star topology. The proposed configuration may

be used in subsidence monitoring of terrains. Additionally, if all the synchronized units of the star topology are attached to a fixed position then this set can be used to provide a precise location of the common receiver, and even to many receivers. Thereupon a radio localization system can be implemented.

2.4 Additional applications of the carrier phase synchronization scheme

2.4.1 Radio Positioning Systems

Radio positioning or radio location is understood as the unambiguous placement of a certain individual or object with respect to a known reference point, using the radio electric spectrum. This reference point is often assumed to be the center of the Earth coordinate system. In general, the reference point can be any point on the Earth that is known to the system and which coordinates can be related to.

In some radio positioning systems it is not only important to obtain the position of a object in the space, but also obtain temporal evolution of the position of this object.

In particular, a tracking system is a special case of radio positioning working under a precise time reference and on several occasions in real time. In those applications, it is important to know the time information in order to obtain the position of a certain object in an specific instant, and also to infer high orders derivatives of the position, i.e. speed and acceleration. Thus, future positions of the device, as a function of time, can be predicted [34].

A radio navigation system is a special case of radio positioning which performs tracking functions in order to help users to move to a desired destination. Modern radio positioning came with the advent of wireless communications by the end of 19th century. The first radio location system to be invented was the Radio Direction Finder, a device that was able to detect the angle in which a transmitter was located. It is performed rotating a directional antenna, and finding the angle of maximum received power. This device was the forebear of VOR (VHF Omni-range Radial Systems) and DVOR (Doppler VOR) systems [28, 82, 109].

The firsts operative radar systems were developed in the first half of the 20th century, and were used in navigation applications. Subsequently great developments in the field of radio positioning were done, arriving to the wide variety of systems currently available.

In last years terrestrial radio navigation has been providing highly reliable and accurate navigation service for both civil and military users. The most popular terrestrial radio navigation systems have been: Radio Beacons, Loran, Omega, VOR/DME, TACAN, and ILS/MLS. In addition, the TRANSIT satellite radio navigation system was widely used for both civil and military applications latter in the 60s [13, 46].

One of the most popular systems was Loran (Long Range Navigation System), which was proposed in 1940 and was based in a set of synchronized beacons radiating signals that were received by the target receivers. Consequently, the receivers calculate their position using the time arrival difference of the signals of the different beacons.

Later, with the beginning of the space exploration between 1960 and 1970, the satellite positioning system were started to be deployed. Today GPS is the most used satellite positioning system. Furthermore, in the last decade, other kinds of positioning system were developed. In particular, there have been significant developments in positioning systems that works using the architecture of digital wireless communications, such as mobile personal communications, Third Generation Partnership Project (3GPP), Ultra Wide Band (UWB) [116], Wireless LAN and Bluetooth [9, 20, 43, 104].

Distributed localization systems based on carrier phase measurements

Recently, there have been proposed some examples of radio localization systems which are based in sets of coherent transmitters. Among these are the references [69,101,104]. They make use of the carrier synchronization between the set of transmitters and implement techniques based in the distance measurements similar to the explained in Section 2.3. They obtain higher resolution that conventional positioning systems but they have to face the challenge of the possible ambiguity in the measurements [101].

2.4.2 Phased Arrays

Arrays systems are widely used in radar, radio navigation, radiometry, and communications. These systems work under the same theory of operation, which is based in the use of sets of geometrically distributed antennas that operate coherently. Where coherency means that the phase of the transmitted or received signals are controlled in order to generate constructive or destructive interferences at desired geometrical points [36]. The first use of a phased array was in a communication link between the United States and the United Kingdom in 1930. Later, the array technology was the key point in the developments in radar and radiometry.

The arrays are shaped in many geometrical forms, and their collecting area is made up of several antenna elements. These elements can be separated by distances that can range from a few millimeters to hundreds of kilometers. In general, the collecting aperture of an antenna array will increase when the area occupied by the array increases. However, for a given area, the gain is directly proportional to the number of radiating elements. In radioastronomy, the typically used arrays are very wide, with diameters in the order of the diameter of the earth, and sparsely populated. In contrast, radars systems use densely populated arrays, with areas in a range of tens of meters, in order to obtain beams with very low sidelobes [11, 36, 49, 54, 87].

Arrays can be classified in active and passive arrays. In an active array, each radiating element is connected directly to an active transceiver. In a passive array the number of active transceivers is lower than the number of radiating elements. Thus, in passive arrays one or more radiating elements are connected to one transceiver by means of a transmission medium, and the phase change of this connection must be characterized.

On the other hand, in active arrays the coherency is controlled by the phase synchronization between transceivers. In some cases, when the antennas are widely separated, the connections between transceivers are not implemented with transmission lines. The antennas of these arrays can be dispersed in one or more continents, forming a Very Long Base Line Interferometer (VLBI), or VLBI networks. The signals are recorded separately in each location using extremely precise time references, usually obtained from atomic clocks. Then these data are collected and processed coherently at a central point.

Challenges and Recent Progress in Distributed Beamforming

The impulse observed in developments of phased arrays application in radars and radiometry has also occurred in the communications in the last decades, specially in personal mobile communications, with the advent of the MIMO (Multiple Input Multiple Output) systems [1, 27, 44, 45]. In these applications, distributed transmit beamforming is a form of cooperative communication in which multiple active transmitters simultaneously send a common message and control the phase of their transmissions so that the signals constructively combine at the intended destinations [77].

With the use of distributed beamforming the power gain of the system is increased, which can be translated to higher ranges, rates, or energy efficiency. Other advantages of these approaches result from the reduction of the power scattered in unintended directions, thereby reducing interferences and security risks.

Among the requirements for the implementation of these systems are the signal distribution and timing synchronization. Alhough, the most important and difficult challenge still is the phase synchronization, which is required to combine constructively the signals at the destination. In free space propagation, the power gain obtained by an array of N antennas is N^2, from the power transmitted by a single antenna. In this way, a gain of N is obtained from the total transmitted power. Other advantage of distributed beamforming is the capability to generate very high gains with longer wavelengths, providing much better performance in lossy mediums and in clutter environments, since radio waves diffract around obstacles better. A typical example, taken from [77], is a terrestrial deployed sensor network of low power single-antennas, transmitting measurements to an overflying Unmanned Aerial Vehicle (UAV), as can be seen in Figure 2.11. This example can be extended to other applications, for example a land-based radio navigation systems used by the UAV, and other kind of communications with the UAV (as the systems explained in Section 2.2). In this scenario, each single antenna transmits a power of -10 dBm, with a carrier centered at 3 GHz, and a bandwidth of 10 MHz. The UAV is at a height of 3000 meters (typical for an intermediate range UAV).

Thus, the received power, assuming a transmit antenna gain of 2 dBi and a receive antenna gain of 10 dBi will be -110 dBm. With a noise figure in the receiver of 6 dB the

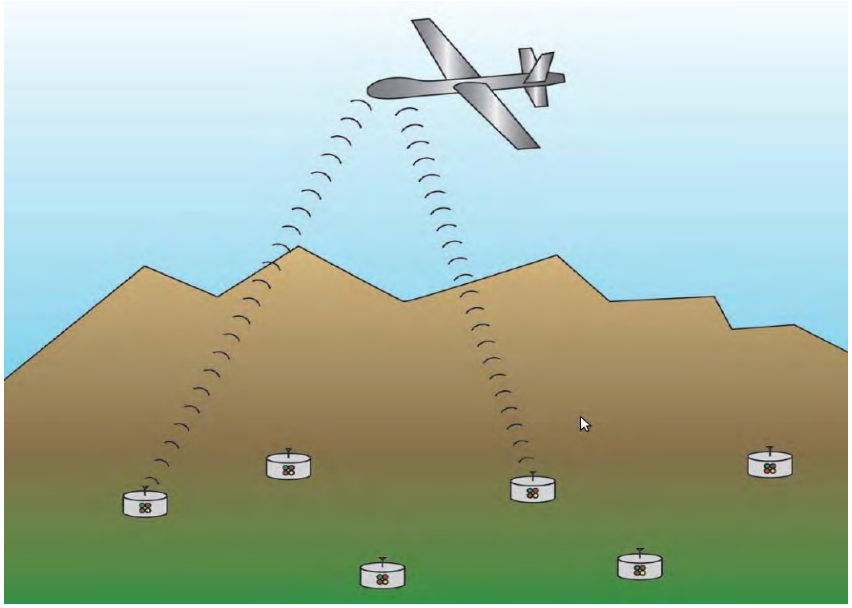

Figure 2.11: Sensor network transmitting measurements to an overflying aircraft. (Taken from [77])

noise power is -97 dBm (thermal noise 300 Kelvin). Therefore, the SNR at the receiver for a single transmitter is -13 dB, which makes infeasible a communication with an acceptable spectral efficiency. However, if 20 distributed antennas coherently synchronized transmit the same power of -10 dBm, the total power in the receiver will be increased by N^2, which is in this case 400 times, or equivalently a gain of 26 dB, which increases the SNR in the receiver to +13 dB. This could enable, according to [77], for example, upload of image/video data or summaries of sensor data collected over long periods of time (days or even months). But also, can be used to extend the range of reception of the control and navigation signals for the UAV.

In [77] it is stated that distributed carrier synchronization is the most difficult and important challenge in the implementation of distributed beamforming, and cites some schemes used to solve this problem, which were proposed recently by different research groups [14, 15, 76, 98]. These schemes are explained in Section 3.1.

Chapter 3

Theoretical Background and State of the Art

3.1 Remote carrier phase synchronization

In some applications in telecommunications and other engineering fields, such as phased antenna arrays, precise control of the phase in oscillator signals over distributed subsystems is required.

In the most common scenario, the stable local oscillator reference is generated at a central point and it is distributed directly towards remote locations via cables or radiation links. In these cases, the phase observed at the remote locations will not be stable due to changes in the electrical path of the transmission medium. The electrical paths strongly depend on parameters such as temperature and pressure. These parameters affect the physical dimensions of the transmission medium due to thermal expansion and also vary its dielectric constant. These behaviors cannot be easily modeled nor parameterized analytically in order to implement methods to correct and compensate their effects.

In the last decades, the phase stability and coherency of oscillating signals in remote locations within a system has been studied. More precisely, in Radio Astronomy, some schemes have been devised in order to solve this problem, that is present in Radio Telescopes which are based in arrays of antennas. One of the early works which uses a round trip stabilization system was "A constant phase local oscillator system for a cross type radio telescope" published in 1966 by A.G. Little and others [63]. This work proposes a round trip phase compensation system for phase stabilization. In this case, the medium was a one mile wave guide which had one germanium diode in the middle of the line. A

square signal voltage was applied to the diode to generate a square wave that traveled in the line. Using the round trip delay measurement the instantaneous frequency of the master oscillator was adjusted to keep the overall phase length constant with an operation frequency of 397 MHz. This publication stated that this system was "very cheap". That was stated as cheap compared to an implementation of active temperature and pressure control over the complete line, which was the only available solution at that moment for phase stabilization.

However, the work that shows the principle of the round trip stabilization circuits was published in 1968 with the title "Phase Stabilization of Widely Separated Oscillators" [97]. In this paper, the available techniques for reducing propagation-induced phase fluctuations in frequency distribution systems were discussed and compared. The transmission lines of the systems studied here are cables or radiation links, including optical beam links. Furthermore, this article divides the stabilization systems in two main approaches: open loop systems and closed loop systems.

In open loop systems one or more parameters are monitored, under the assumption that the behavior of these parameters are significantly correlated with the phase change of the transmission line. If the relationship between the monitored parameters and the associated propagation phase error can be obtained, either theoretically or empirically, hence the parameters can be used to compensate the error. In this case, the system proposed in [63] can be classified as an open loop system.

In contrast, in closed loop systems the delay is measured directly over the signal which travels along the path and a direct feedback action closes the loop. An example of closed system was previously demonstrated by the same research group in 1965 and is explained in [97]. The operation was based in the transmission of two CW signals at slightly different frequencies in opposite directions over a wireless radio link. At each extreme of the link the strong local signal and the remote signal are mixed, generating in this way an IF signal. These two IF signals are taken to a common point (can be in any of the two stations) and are introduced into a phase comparator. Then, the output of the phase comparator is used to control a mechanical waveguide phase shifter to compensate the phase effects of the complete path. In general, this is the concept that was used by

the following works, and also the base for the present Thesis.

Other examples of phase controlled loops are shown in [61], and [7], where two similar systems are implemented. In [61, A Phase-Stabilized Local-Oscillator System for a Synthesis Radio Telescope., T. L. Landecker and J.F. Vaneldik, 1982] a cable distribution system is described. Here a 1.4 GHz oscillator signal is distributed over multiple remote units within a Synthesis Radio Telescope. Then, as in [97], two CW signals at slightly different frequencies are transmitted in opposite directions, and additionally an IF signal is transmitted from the central unit to the remote unit. This signal is equivalent to the IF signal in [97] and is called reference frequency. It can be noticed that this signal has a frequency significantly lower than the CW signals, being 10 MHz in this case. [90, 91].

In [7, A Technique for Microwave Ranging and Remote Phase Synchronization, Leonid Belostotski, T. L. Landecker, and D. Routledge, 2002] a similar system was implemented, but for a 22 GHz L.O. in a Large Adaptive Reflector (LAR), a Wideband Radio Telescope, which uses a radiation link. The round trip phase measurement system was used to perform an accurate distance measurement between the central unit and an airborne remote unit. The obtained phase accuracy was 5°.

Recently in the last years, the problem of remote carrier phase synchronization has also been studied in the communications field. This interest is generated by the popularization of techniques which use cooperative spatial diversity and the Multiple Input Multiple Outputs MIMO systems [1]. Some examples of techniques for carrier phase synchronization for distributed transmit beam forming are summarized in [77, Distributed Transmit Beam forming: Challenges and Recent Progress, 2009]. Among others, in this article are referenced two other documents in which two techniques for remote carrier phase synchronization are described.

The first is [15, A Method for Carrier Frequency and Phase Synchronization of Two Autonomous Cooperative Transmitters, 2005]. This work proposes a method to synchronize the carrier phase of two separate transmitters in order to send a common message to a destination node. The method is based in the transmission of a sinusoidal continuous wave reference beacon from the destination node to the transmitters using the wireless medium. The transmitters are phase locked to this reference and they use it to gen-

erate secondary beacons with different frequencies. The phase coherency between the transmitters is obtained by interchanging their secondary beacons using also the wireless medium.

The second publication is [14, Time-Slotted Round-Trip Carrier Synchronization for Distributed Beamforming, 2008]. This publication proposes a similar scheme used to enable distributed beamforming in multiuser wireless communication systems. This technique is also based in the "round-trip" approach as in [15], however in this case a single frequency is used for all beacons and carriers. Thus, the signals from different transmitters are separated using time division duplexing applied in a ring topology. The benefit of using a single frequency for the carrier and all beacons is that channel reciprocity is maintained in dispersive and multipath propagation scenarios. The lack of continuous synchronization implies that periodic resynchronization is necessary to avoid unacceptable levels of phase drift during operation. This method was based on a previous work, [76, On the Feasibility of Distributed Beamforming in Wireless Networks, 2007], which implements a similar scheme but with a hierarchical topology. In that scheme the transmitters receive a beacon from the destination node and bounce back to the destination with another beacon in order to estimate and quantify the phase delay in each channel. These quantized phase delays are then codified and sent to the appropriate transmitters for local phase pre-compensation.

These synchronization schemes were devised to perform beamforming from a set of distributed transmitters, which pretend to send a common message to a remote destination node. However, it is also possible to point the main beam to other desired directions adjusting the phase offset in each one of the transmitters.

Finally, other examples of carrier phase synchronization methods were proposed recently in the remote sensing community. This method was implemented for the synchronization between the two satellites in the TanDEM-X bistatic system [30, 33, 113, 114], and is based in the patent [10, Method for drift compensation with radar measurements with the aid of reference radar signals, 2005]. The proposed scheme is based in the interchange of modulated pulses between the two stations, following a similar approach than the method proposed in [76].

The following subsections describe previous systems proposed for carrier phase synchronization. In particular, Subsection 3.1.1 describes the scheme used in [6, 7, 61] which is the base for the present Thesis.

3.1.1 A technique for microwave ranging and remote phase synchronization

A scheme for remote carrier phase synchronization based in a bidirectional link is explained in references [6, 7, 61]. In that system the phase change produced by the round trip delay over an operation frequency, f_{op}, is calculated and compensated in a closed loop.

This bidirectional link was implemented using a coaxial cable in [61] and using the wireless medium in [6, 7]. However, in a general scheme, as presented here, the medium can be wired or wireless. Figure 3.1 depicts this scheme, showing the central unit, the remote unit and the generic transmission medium, which is represented by the block in the middle of the central unit and the remote unit, labeled as "Trans. medium". The operation of this scheme will be explained in the following.

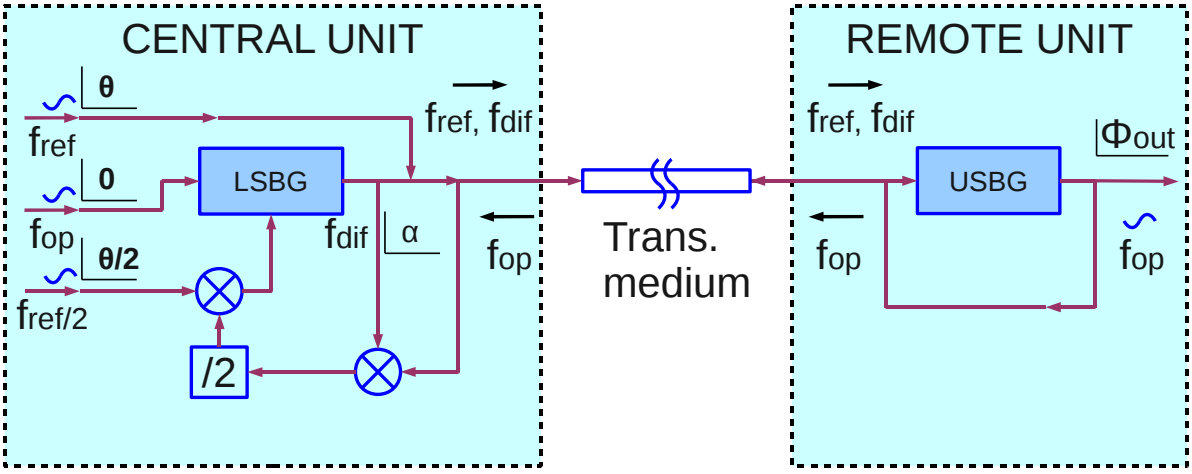

Figure 3.1: Simplified general system scheme. Here is implemented a bidirectional link using three frequencies, f_{op}, f_{ref}, and f_{dif}, with $f_{op} = f_{ref} + f_{dif}$. (Adapted from [61]).

Absolute phase reference

In the design of some systems it is necessary to calculate the absolute phase of signals with different frequencies. In order to calculate this absolute phase, it is assumed an ideal time reference, or zero time, for which the phases are referred. Hence, the phase of a sinusoidal tone at a given frequency is relative to the cosine function of that frequency starting at zero time, $t = 0$.

Phase behavior in the remote phase synchronization system

The central unit transmits to the remote unit two tones with two different frequencies, f_{ref}, and f_{dif}, which added are equal to the operation frequency ($f_{\text{ref}} + f_{\text{dif}} = f_{\text{op}}$).

One of these two tones has a fixed frequency f_{ref} and phase θ taken from an external reference. The other one is adjusted in phase using the round trip offset. This tone is generated in a Lower Side Band Generator (LSBG) with f_{dif} frequency and phase α.

At the remote unit, these signals are received, each one with a phase offset given by the transmission media, ϕ_{ref} and ϕ_{dif}. The two received signals are mixed in an Upper Side Band Generator (USBG), adding the received phases. The phase of the output signal (with f_{op} frequency) at the remote unit is

$$\phi_{\text{out}} = \theta + \alpha + \phi_{\text{ref}} + \phi_{\text{dif}}. \tag{3.1}$$

Then, this signal, which has a frequency of f_{op}, is retransmitted to the Central Unit. Hence, a phase offset of ϕ_{op} is added, to obtain a phase of $\theta + \alpha + \phi_{\text{ref}} + \phi_{\text{dif}} + \phi_{\text{op}}$. In the central unit, it is mixed down with the original signal of frequency f_{dif} which was transmitted, in order to subtract the transmitted phase α.

In this way, it is obtained a tone with frequency f_{ref} and a phase of $\theta + \phi_{\text{ref}} + \phi_{\text{dif}} + \phi_{\text{op}}$, which contains the round trip phase offset introduced by the transmission line. This signal is passed through a frequency divider and then mixed up with a tone with frequency $f_{\text{ref/2}}$ and phase $\theta/2$ (the reference divided by 2), to obtain one input of the Lower Side Band Generator (LSBG). The frequency of this input is f_{ref} and its phase is $-\alpha$. Then, the

output phase of the LSBG, α, will be

$$\alpha = -\theta - \frac{\phi_{\text{ref}} + \phi_{\text{dif}} + \phi_{\text{op}}}{2}. \tag{3.2}$$

The absolute phase output at the remote unit, ϕ_{out}, is obtained replacing the value of α in 3.1,

$$\phi_{\text{out}} = \frac{\phi_{\text{ref}} + \phi_{\text{dif}} - \phi_{\text{op}}}{2}. \tag{3.3}$$

If the transmission line is not dispersive then the phase delay ϕ_{op} will be exactly equal to $\phi_{\text{ref}} + \phi_{\text{dif}}$, because $f_{\text{op}} = f_{\text{ref}} + f_{\text{dif}}$. Therefore, the absolute phase ϕ_{out} will be exactly zero, for any time delay in the transmission line and regardless of the reference phase θ.

The phase offset introduced by the transmission medium, in modulo 180° because of the halving process, can be measured through the values of θ and α, by $\phi_{\text{line}} = \theta + \alpha \pmod{\pi}$.

Chinese remainder theorem.

The Chinese Remainder Theorem has been widely used for range-ambiguity resolution in multiple-PRF radar systems [7, 95]. It can be stated as follows. Let L be a large integer to be determined, and let the "rulers", m_1, m_2, m_3 be positive pairwise coprime integers, with $m_1 m_2 m_3 = m$. More than three rulers are also valid, but in this specific case three rulers are used [6, 112].

A set of remainders can be obtained using a set of rulers, where counting and determination of the remainders β_1, β_2, β_3 is equivalent to

$$\beta_j = L \pmod{m_j} \qquad \text{for} \quad j = 1, 2, 3. \tag{3.4}$$

A set of positive integer coefficients C_1, C_2, and C_3, can be found for a given set of rulers, which fulfill the condition

$$C_j \pmod{m_j} = (m/m_j) b_j \pmod{m_j} = 1 \qquad \text{for} \quad j = 1, 2, 3. \tag{3.5}$$

Where each each b_j is found as the smallest positive number which fulfills Equation 3.5,

which in other words means that multiplied by (m/m_j) produces as remainder the unity modulo m_j. Then, the value of L can be obtained with

$$\sum_{j=1}^{j=3} C_j \beta_j = L \pmod{m} \tag{3.6}$$

Hence, this theorem shows that the unknown number L can be found through the measured remainders, obtaining the result with an indetermination proportional to m.

As an example, an unknown integer L equal to 610 must be determined. The rulers $m_1 = 7, m_2 = 8, m_3 = 9$ are used obtaining the remainders $\beta_1 = 1, \beta_2 = 7, \beta_3 = 2$. The coefficients associated to the rulers are $C_1 = 288, C_2 = 441, C_3 = 280$. Then the obtained value of $L(\text{mod } m)$ becomes $1 \times 288 + 2 \times 441 + 7 \times 280 = 3130(\text{mod } 504)$. Thus, the possible values of L are $106, 610, 1114, ..., 3130, ...$ and the right value can easily be chosen using *a priori information* about the distance.

This Theorem has been applied in [6, 7] for the resolution of the distance ambiguities caused by inability to count integral numbers of wavelengths obtained with the phase synchronization system. Thus, the ambiguities are solved introducing two more phase synchronization loops working at different frequencies. While the phase in each synchronization loop is measured with an ambiguity of 180 degrees due to the frequency halving process.

A continuous length, L', can be measured using resolution elements with length r, determining also the wavelengths $\lambda_j = 2 \cdot r \cdot m_j$, associated with the operation frequency of each synchronization loop. Thus, the measured phases become

$$\phi_j = 2\pi \frac{L'}{\lambda_j} \pmod{\pi} \qquad \text{for} \quad j = 1, 2, 3. \tag{3.7}$$

From this phase the values of β_j can be found through

$$\beta_j = \lfloor \frac{\phi_j}{\pi} m_j \rfloor \qquad \text{for} \quad j = 1, 2, 3. \tag{3.8}$$

In the example presented in [6] the length of the resolution element is set to 0.05 mm, the set of rulers m_1, m_2, m_3 is set to 119, 124, 129, (relative primes). They found

$b_1, b_2, b_3 = 50, 119, 42$, and $m = m_1, m_2, m_3 = 1903524$. Then $C_1, C_2, C_3 = 799800, 1826769, 1180480$, and consequently the distance ambiguity occurs every 95.17 m.

3.1.2 Phase synchronization link for a bistatic SAR

The documents [33,113,114] present the schemes for remote carrier phase synchronization which are used to synchronize the phase of the two TanDEM-X satellites. The used scheme is in the patent [10, Method for drift compensation with radar measurements with the aid of reference radar signals. U.S. Patent 2005/0 083 225 A1, 2005], and it is based in the interchange of modulated pulses between the two stations, following a similar approach than the method proposed in [76] (explained in Section 3.1.3), however in this case using radar pulses.

In the context of this application, two satellites follow an orbit in a close formation, with a variable distance between them of few hundreds of meters. The instruments on both satellites are advanced high resolution X-band synthetic aperture radars, which are used to operate a SAR imaging system in both monostatic and bistatic configurations. In the bistatic configurations, one of the two satellites works as transmitter and the other one as receiver.

The carrier frequency, of 9.65 GHz, is generated separately at each of the satellites multiplying the frequency of a precise frequency reference using a phase locked loop.

However, the implementation of a bistatic system requires phase coherency between the local oscillators of the two satellites [30], and would impose enormous requirements on the USO (Ultra Stable Oscillators) stability, since the demodulation of the microwave signal is performed by separate clock references. It has been shown that state of the art USOs present frequency drifts at microwaves frequencies in the order of thousands of Hertz [70], which can degrade significantly the performance of the bistatic system.

In addition to drifts in the references, the distance between the satellites and their relative velocities are variables that must be controlled. A change in distance is equivalent to a phase shift and a change in the relative velocities is equivalent to a Doppler shift.

Thus, to solve this problem, the phases of the two carrier oscillators are synchronized by means of a dedicated bidirectional radio link. The system operates measuring the

round trip phase offset including the phase changes introduced by the bidirectional link. Then a compensation phase is computed and applied in one of the satellites. Figure 3.2 shows the general synchronization schemes proposed in [113] to be used in TanDEM-X system.

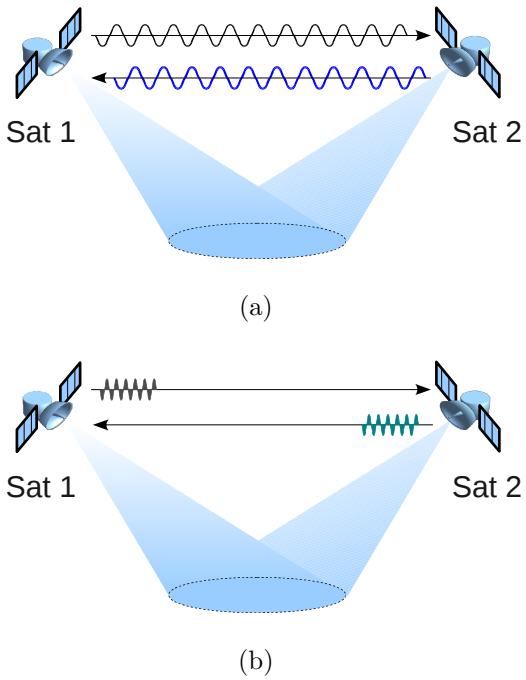

Figure 3.2: TanDEM-X Synchronization schemes. (a) Continuous duplex. (b) Pulsed (duplex/alternate). Taken from [113]

In general, satellites 1 and 2 demodulate the phases of the received synchronization signals, using its local oscillator, to obtain $\phi_{21}(t)$ and $\phi_{12}(t)$ respectively. As a consequence, the compensation phase $\phi_c(t)$ is obtained by computing the difference

$$\phi_c(t) = \frac{\phi_{21}(t) - \phi_{12}(t)}{2} \tag{3.9}$$

There are two main synchronization schemes used in the TanDEM-X system: the continuous duplex synchronization and the pulsed duplex/alternate. The continuous duplex synchronization scheme, which has been first suggested in [30], is shown in Figure 3.2a. In this scheme, that was further investigated in [108], both satellites 1 and 2 transmit and receive their local oscillator signals continuously. In this scheme, the performance strongly depends on the isolation between the transmission and reception subsystems in

each of the satellites, in order to decouple the transmitted and received oscillator signals, which may cause problems when using the same carrier frequency.

Additionally, there is the pulsed synchronization scheme, shown in Figure 3.2b. Here, each satellite repeatedly transmits its synchronization pulse. For pulsed duplex synchronization, both satellites transmit synchronization pulses at the same time instants. In the case of pulsed alternate synchronization, there is a time delay between the transmit instants of satellites 1 and 2. The concept is somehow similar to microwave ranging used to determine the separation between platforms [56, 68]; however, phase synchronization requires a different processing and hardware approach. The phase detection is carried out in practice, e.g., through digital pulse compression of the recorded radar data. Figure 3.3 shows a timing diagram for the exchange of synchronization pulses.

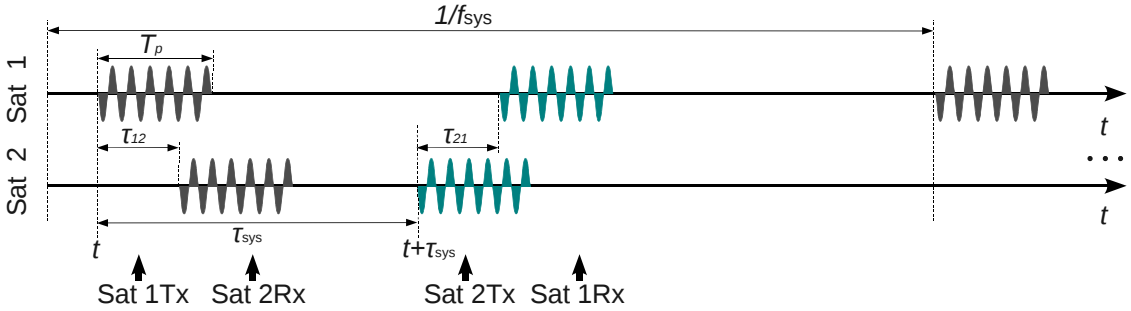

Figure 3.3: Timing diagram for the exchange of synchronization pulses in TanDEM-X system. Taken from [113]

As shown in Figure 3.3, satellite 1 transmits one pulse of duration T_p starting at time $= t$, which is received by satellite 2 after the propagation time τ_{12}. Meanwhile, satellite 2 transmits its synchronization pulse to the satellite 1 at $t + \tau_{\text{sys}}$, which is received by satellite 1 after the propagation time τ_{12}. This procedure may be repeated periodically at a synchronization rate f_{sys}, and is repeated during the data acquisition.

The pulse compression is carried out by the correlation of the measured signal with the (known) transmission signal. The position of the correlation maximum describes the rough time position between the start of the measurement and the arriving signal. In addition to the pulse compression gain, there is a gain associated to the averaging over multiple pulses, which is a procedure described in [113] as azimuth compression, taking the terminology from the used in SAR processing.

In both schemes, continuous duplex and pulsed/alternate, the phase of the local reference signal is already subtracted during the data acquisition by mixing the received signal down to I/Q baseband branches.

In these schemes the phase variations or unbalances in the I/Q demodulation will generate phase errors in the compensated system. If the down-conversion of the received signal, with an average frequency f_i, were pretended to be implemented using a hypothetical intermediate frequency f_{IF} approach, then one additional local oscillator signal with frequency $f_i + f_{\mathrm{IF}}$, would be needed in each reception subsystem. Thereby, each local oscillator would add a phase indetermination to the system.

Demodulated phase ϕ_{ji} obtained from the received pulse

Following the same terms used in [113], satellite i transmits a synchronization signal which is received by satellite j, where $i, j \in 1, 2$. The instantaneous frequency of oscillator i at the time of the start of the data acquisition t_0 is $f_i = f_0 + \Delta f_i$, where f_0 is the nominal frequency and Δf_i is a constant frequency offset. The phase $\phi_i(t)$ at time t is the integration over frequency,

$$\phi_i(t) = 2\pi \int_{t_0}^{t} f_i(t)dt + \phi_{\mathrm{ini}\ i} + n_{\phi i}(t) \tag{3.10}$$

where $\phi_{\mathrm{ini}\ i}$ is the initial time-independent phase and $n_{\phi i}(t)$ is the oscillator phase noise. In the other hand, $\phi_j(t)$, the phase of the j oscillator behaves in the same way, and is evaluated at $t + \tau_{ij}$ the moment in which it starts to receive the synchronization pulse from satellite i, with

$$\phi_j(t + \tau_{ij}) = 2\pi \int_{t_0}^{t+\tau_{ij}} f_j(t)dt + \phi_{\mathrm{ini}\ j} + n_{\phi j}(t + \tau_{ij}) \tag{3.11}$$

Thus, the demodulated phase $\phi_{ji}(t)$, available at satellite j is the difference between 3.11 and 3.10.

Continuous duplex synchronization

In the continuous duplex synchronization both satellites transmit the unmodulated local oscillator continuously during the data acquisition [108, 113]. The propagation delays in both directions are assumed equal, $\tau_{12} = \tau_{21} = \tau = r/c_0$, where r is the distance between the two satellites. Combining equations 3.9, 3.10 and 3.11, the compensation phase is obtained

$$\begin{aligned}\phi_c(t) =& 2\pi(\Delta f_2 - \Delta f_1)t + n_{\phi 2}(t+\tau) - n_{\phi 1}(t+\tau) \\ &+ \pi(\Delta f_2 - \Delta f_1)\tau + \phi_{\text{ini 1}} - \phi_{\text{ini 2}} \\ &+ \frac{1}{2}(\phi_{\text{SNR1}}(t+\tau) - \phi_{\text{SNR2}}\,(t+\tau)).\end{aligned} \tag{3.12}$$

The frequency offset term $2\pi(\Delta f_2 - \Delta f_1)t$, in first line of 3.12, is a linear phase ramp, which can be extracted to correct the frequency offset error of the SAR signal, being to some extent deterministic. However, also in the first line, are the most important random variables that contain the information required to compensate the link, and they are the phase noise in the oscillators, $n_{\phi 2}(t+\tau)$ and $n_{\phi 1}(t+\tau)$. For this study it is assumed that both oscillators have the same spectral density, equal to $\gamma^2 S_\phi(f)$, where $S_\phi(f)$ is the spectral density of the low frequency reference (10 MHz in that case) and γ is the scaling factor used to obtain the frequency of the microwave oscillator.

For the analysis in [113], τ is considered constant, thus the second line in 3.12 will be constant. Thereby, the main error of the synchronization link comes from the noise in the set of receiver subsystems, and is grouped in a single variable for the complete link ϕ_{SNR} (Can also be called ϕ_{link}).

The spectral density function of the variable ϕ_{SNR} becomes

$$S_{\phi\text{SNR}}(f) = \frac{1}{2B_w\ \text{SNR}} \tag{3.13}$$

Finally, the SNR is improved using azimuth compression, which is equivalent to a low pass filter, $H_{\text{az}}(f)$, averaging the signal in a period T_a, obtaining a total phase variance

of

$$\sigma^2_{\text{link}} = \frac{\sigma^2_{\text{SNR}}}{2} = \frac{1}{4B_w \text{ SNR}} \int_{-B_w/2}^{+B_w/2} |H_{\text{az}}(f)|^2 df \tag{3.14}$$

Pulsed duplex synchronization

In the pulsed duplex scheme the compensation phase is sampled in discrete time instances, $t_k = k/f_{\text{syn}}$, with k positive integer, obtaining

$$\begin{aligned} \phi_c(t_k) =& \pi(\Delta f_2 - \Delta f_1)(2t_k + \tau) + n_{\phi 2}(t_k + \tau) - n_{\phi 1}(t_k + \tau) \\ &+ \frac{1}{2}(\phi_{\text{SNR1}}(t_k + \tau) - \phi_{\text{SNR2}}\,(t_k + \tau)) \end{aligned} \tag{3.15}$$

There are others sources of error in the compensation phase, implicit to the sampling process. If the quantification error is not taken into account there can be listed two main errors. The first error is generated by the aliasing effect over the spectrum of the sampled signal, the second one derives from the interpolation effect, which is the lost of the phase information contained by the portion of the spectrum which is outside of the Nyquist bandwidth [113].

The total link phase variance can be computed by the sum of the variances of each of the noise contributors by

$$\sigma^2_{\text{link}} = \sigma^2_{\text{i}} + \sigma^2_{\text{a}} + \frac{1}{2}\sigma^2_{\text{SNR}} \tag{3.16}$$

Where, σ^2_{i}, σ^2_{a} and $\frac{1}{2}\sigma^2_{\text{SNR}}$ are the variances of the errors generated by the aliasing effect, the interpolation error and the system noise, respectively. Their quantities are obtained as follows

$$\begin{aligned} \sigma^2_{\text{i}} &= 2\gamma^2 \int_{f_{\text{syn}}/2}^{\infty} S_\phi(f)|H_{\text{az}}(f)|^2 df \\ \sigma^2_{\text{a}} &= 2\gamma^2 \sum_{i=1}^{\infty} \int_{-f_{\text{syn}}/2}^{+f_{\text{syn}}/2} S_\phi(f + if_{\text{syn}})|H_{\text{syn}}(f)H_{\text{az}}(f)|^2 df \\ \frac{1}{2}\sigma^2_{\text{SNR}} &= \frac{1}{4f_{\text{syn}}\ SNR} \int_{-f_{\text{syn}}/2}^{+f_{\text{syn}}/2} |H_{\text{syn}}(f)H_{\text{az}}(f)|^2 df \end{aligned} \tag{3.17}$$

Discussion

The system studied in [113] is also capable of determining the variation of the time delay $\tau = \tau_{ji} = r/c_0$. Although it is not mentioned in [113], this capability makes possible the estimation of the phase and Doppler variations used by the synchronization link. An estimate of this phase, ϕ_τ, is obtained from the demodulated phases in each satellite, and is given by

$$\phi_\tau = \frac{\phi_{21}(t) + \phi_{12}(t)}{2} \tag{3.18}$$

Thus, the variation in the separation between satellites can be monitored for changes lower than the wavelength of the carrier frequency. In [113] is not specified that the system can be used to determine the total separation between the satellites, nor defined a method for timing synchronization.

3.1.3 Pulsed phase synchronization scheme used for distributed beam forming in a wireless communication link

A pulsed phase synchronization scheme used for distributed beamforming in a wireless communication link is proposed in: "On the Feasibility of Distributed Beamforming in Wireless Networks" [76]. The scheme is based in the transmission of pulses of the oscillator signal, between a master unit and a slave unit, obtaining in this way an estimate of the phase offset introduced by the transmission medium.

In the master unit a stable carrier tone is generated to be the zero phase reference. This oscillator is modulated by a small square pulse of duration T_1, and is transmitted to the slave unit. At the other end, the slave unit receives this pulse and generates another tone locked in phase to the received signal. To perform this, the slave unit uses a voltage controlled oscillator which is locked to the incoming signal. The phase of the received signal will be the phase of the locked VCO, and will be equal to $0 + \phi_{\text{line}}$, where ϕ_{line} is the phase offset introduced by the propagation delay.

As a response, the slave unit bounces back to the master unit another pulse with duration T_2, using the signal generated with the locked VCO. This bounced pulse is received by the master unit, and its phase that would be $2\phi_{\text{line}}$ is compared with the zero

phase local reference, to obtain the phase $\Delta\phi$. Assuming that the channel is symmetric, thus the propagation delay is the same in both directions, an estimate of the line phase offset can be computed from the measured phase $\Delta\phi$. This estimate, $\hat{\phi}_{\text{line}}$ is given by

$$\hat{\phi}_{\text{line}} = \frac{\Delta\phi}{2} \tag{3.19}$$

This estimated value is used to compensate the phase in the slave unit, and can be subtracted as an offset to the synchronization pulse sent in the master unit, or it can be applied as an offset to the VCO in the slave unit.

The operation of this scheme relies on the assumption that the phase offsets introduced by the components (amplifiers, switches, etc.) used in the master and slave units are constant, and therefore are not taken into account for the phase computation.

Therefore, in absence of noise the measured phase will be

$$\Delta\phi = (2\phi_{\text{line}} \bmod 2\pi) \tag{3.20}$$

This scheme cannot determine the number of cycles wrapped in the measured phase, which would be useful to determine the actual time delay in order to perform time synchronization. In addition the operation of dividing by two the measured phase will introduce a phase indetermination of 180°. This indetermination can be tolerated depending on the application; and in the case of [76] does not affect the distributed beam forming process.

The beam forming process is performed using this pulsed synchronization scheme with multiple slave units, which use the compensated carrier in the transmission for beam forming directly. Then, the system performs the synchronization process periodically. The master unit at the beginning of a synchronization period sends the master synchronization pulse, which is received by all slave units. The slaves send their synchronism pulses at different time slots, using a Time Division Duplex (TDD) approach. In this way, the synchronization procedure adds overhead to the communication protocol.

Each slave unit, after receiving the master synchronization pulse, holds the voltage applied to the VCO, running in open loop, until the next synchronization period. During

this time the phase varies according to the phase noise characteristics of the VCO. The phase noise in the VCO will determine the performance of the system, and will also determine the trade-off with the other parameters such as overhead, pulse duration, number of units, and allowed phase error. It is required for the pulse time T_1 to be long enough to allow the phase acquisition in the phase locked loop.

In [76] one simulation is presented; in there the VCO open loop noise is modeled as a wide band (white) Gaussian noise process with normalized spectral density N_p. For a value of -120 dB in N_p, and synchronization period of 1 ms the phase drift remained below 40°.

3.2 Phase Locked Loops

A Phase Locked Loop (PLL) is a control system in which the variable that is controlled is the phase of a periodic signal. In principle a PLL consists of three basic components: a phase detector, a loop filter and a Voltage Controlled Oscillator (VCO).

When the loop is locked, the control voltage is such that the phase of the VCO is equal to the phase of the input signal to the phase detector [39, 40]. The signal generated by the phase detector is introduced in the loop filter to generate the control voltage which is applied to the VCO. The loop filter has a low pass transfer function, and its order determines the order of the loop. First and second order loops are widely used. According to [40], the phase locked loops are also divided by its type, where the type depends on the number of ideal integrators present in the loop. Thus a type-1 PLL has only the integrator given by the phase accumulation generated by the VCO transfer function, and a type-2 PLL will have an additional integrator in the loop filter. Reference [41] is a recent publication, by the same author of [40], which states that at the end all the analog PLL are type-1 because an ideal integrator is not physically realizable, thus, higher orders simulations are recommended [19, 29, 32, 52, 62].

Chapter 4

Carrier Phase Synchronization System Analysis, Requirements and Design

4.1 Introduction

In the framework of the Remote Sensing Lab at Universitat Politècnica de Catalunya, there are two applications which motivated this thesis and the design of a remote carrier phase synchronization system. Both applications are in some extent related to the implementation of the airborne based bistatic SAR receiver, SABRINA-UAV.

The first application comes from the need of high precision location and tracking of SABRINA-UAV. The tracking precision must be considerably lower than one carrier wavelength which is in the order of tens of millimeters for carriers at C and X bands. Thus, the scheme would be used in the phase synchronization of a set of distributed transmitters used for radio location of the mobile receiver.

In general, a phase synchronization system can be used to implement a high precision distance measurement in one dimension. This distance estimation can be obtained from a phase measurement with a given carrier wavelength and its use can be extended to the 2-D and 3-D cases.

The second application which may be implemented in a near future is the phase synchronization for two or more bistatic radar receivers. Wherewith, two bistatic receivers, for example SABRINA-UAV and SABRINA (ground based) can be synchronized to work together. This arrangement may be be used in tomographic applications of long baseline exploiting the difference in height between the airborne and the ground based receiver.

In addition to this, it is known that the techniques to synchronize multiple separate oscillators may be used in other applications in telecommunications and remote sensing. Among these applications there are the distributed beamforming, MIMO systems, and active or passive very long baseline interferometric arrays. Each application requires specific functionalities and specific behaviors of the synchronization system.

In the next sections of this Chapter the design parameters of a phase synchronization system will be analyzed and the design requirements for a experimental implementation will be determined.

4.2 Phase Synchronization in Coherent Arrays

In recent years, various techniques for phase synchronization have been developed in order to implement coherent antenna arrays. These systems can be classified in two main approaches, the synchronization schemes and the peer-to-peer synchronization schemes.

In the phase arrays that implement joint synchronization techniques more than two stations are simultaneously and jointly synchronized [5, 14, 78, 98]. These systems, which were described in Section 3.1.3, work with the transmission of a reference signal, from a common source to the multiple units, in a similar procedure to the implemented in the passive calibration of phased arrays.

On the other hand, there are coherent arrays based on the implementation of peer-to-peer synchronization links between its units. The operation of these arrays are typically based in a centralized topology, despite other topologies are also possible.

In any case, this thesis proposes a phase synchronization link between two stations. Therefore the arrays that will use this synchronization link can be implemented with a centralized topology. In this topology the phase and frequency reference of the complete array is generated at a central point and is distributed to the remote units using the phase synchronization link.

4.2.1 Array implementation using a remote carrier phase synchronization link between two stations

The proposed synchronization method is applied to construct synchronized arrays in which multiple stations are synchronized to a common central reference in a centralized topology. Figure 4.1 shows a simplified diagram of a synchronized array. Here the central phase reference is named the central unit.

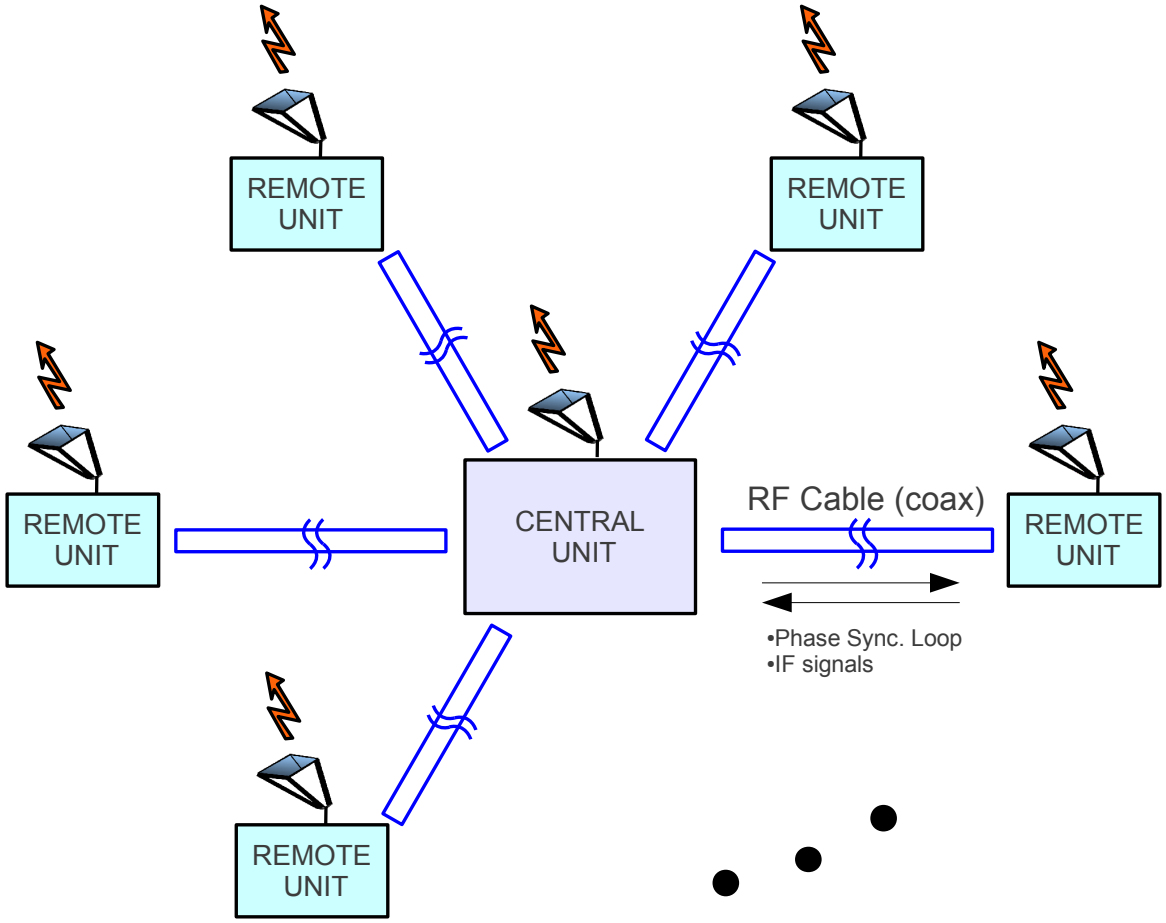

Figure 4.1: Conceptual diagram of the centralized array of synchronized units. RF cables are used for the interconnection between the remote units and the central unit. The units in the array may be used as transmitters or receivers.

As it can be seen in Figure 4.1, each remote unit is synchronized using an independent phase synchronization loop. Also, for simplicity it is assumed that each phase synchro-

nization loop is implemented in an independent guided transmission medium. So the problem of multiplexing multiple phase synchronization links is relaxed by doing that in physically separated channels. Notwithstanding, the theory developed in the design of one synchronization loop may yield the foundations for the future design of a synchronization system with many units sharing a single transmission medium.

In particular, the designed single synchronization loop is implemented with a microwave cable. The cable connection can also be used for the transmission of other signals additional to the used for the synchronization, such as control signals or data communications, depending on the final application of the array. One of these applications is the distance measurement from each of the synchronized stations working as transmitters to a common external mobile receiver. If the position of the receiver is well known or parametrized thus the signals collected in the receiver can be used to determine the relative changes in position of the synchronized transmitters. This configuration can be used to monitor the subsidences of an unstable terrain over a wide area.

Otherwise, if the position of the elements of the array are well known, but the position of the mobile receiver is unknown, then the system can be used to obtain the position of the receiver. Then this system can be called a "Very long baseline interferometric radio location system". It is said that the system has a "large baseline" because the interferometric baseline, which depends on the distance among the units, is considerably larger than one carrier wavelength.

The use of long baseline arrays has some advantages over conventional arrays. Among these advantages are the reduction of signal coupling between the elements and the possibility to obtain large apertures.

4.2.2 Remote carrier phase synchronization between two stations

The reference carrier signal can be generated at a central point as a sinusoidal function of time t with a given frequency ω_0 and phase θ_0, modeled by

$$c(t) = e^{-j(\omega_0 t + \theta_0)}. \tag{4.1}$$

This signal is propagated in the space with a constant speed to a remote location which is at a distance d to the central point. So, the signal observed at the remote location will be

$$c(t) = e^{-j(\omega_0 t + \theta_0 - \phi_d)}, \tag{4.2}$$

with $\phi_d = 2\pi d/\lambda$. Therefore the objective of a carrier synchronization system is to measure the phase difference ϕ_d and compensate it at the remote location, having the two tones perfectly phase synchronized.

In some cases this phase offset can be parametrized, as in the case of arrays of antennas interconnected with short transmission lines. Nevertheless, the problem becomes more complex when the distance among the two points become longer and cannot be determined directly. The phase offset will be still unknown even if there was a way to precisely measure the distance. In guided media the speed of propagation, which is required to estimate the phase offset, cannot be directly obtained because it varies with the parameters of the transmission medium such as temperature and pressure, and a direct relationship cannot be easily obtained. In addition, others mechanical parameters can also affect the propagation phase offset, for example, a slight bending in most of the commercial RF coaxial cables will change locally its propagation constants. This mechanical problem is not present in rigid wave guides. For this reason, some arrays used for radio astronomy in the middle of the twentieth century used rigid waveguides controlled in temperature and pressure along the complete line in order to stabilize the phase of the carrier at remote locations.

The use of unguided media is neither a solution to the problem, and it may become even more complex due to multipath effects and the random variations over time of the channel properties.

Therefore, some methods have been proposed to solve this problem. These systems, working in a closed loop, measure and compensate the propagation induced phase variations of the carrier signal.

On the other hand, other configurations also exist in which two local oscillator signals are generated at two separate locations. As is explained in previous sections, it is not possible that two oscillators generated independently operate exactly at the same frequency.

Even using state-of-the-art Ultra Stable Oscillators (USO) the frequency differences in C and X bands carriers will be in the order of hundreds of Hertz. Moreover, each oscillator will have an independent random phase drift determined by the spectral properties of its phase noise. These effects make the synchronization even more complicated.

The requirement for these systems is to synchronize both distant oscillators. In one of the possible configurations one oscillator can be locked in frequency to the other. This operation can be combined with a compensation to the phase offset introduced by the channel. In previous works it has been shown that it is possible to implement systems that compensate both, phase errors, the ones generated by the drift differences among the two oscillators and the ones generated by the channel offset.

Figure 4.2 outlines the carrier phase synchronization between two stations. This process works under the assumption that the channel is symmetric. That means that the channel properties are equal for both directions of propagation. Thereby, the propagation delay and the phase offset (ϕ_d) for a given carrier frequency will be the same in both directions. Under this assumption, if the channel round trip phase offset can be measured it will be possible to find the one way offset dividing this measurement by two.

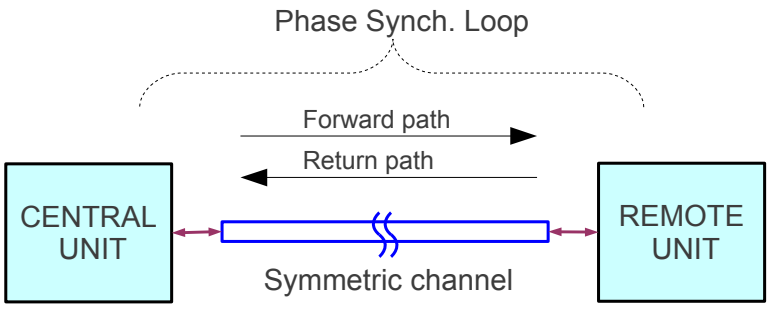

Figure 4.2: Simplified carrier phase synchronization scheme between two stations.

A closed loop phase synchronization system will be based in the transmission of signals traveling in both directions between two separate stations. The performance of the synchronization loop must be quantified by a closed loop phase transfer function. This closed loop transfer function will depend on the open loop transfer function of the transmission channel.

4.2.3 Technological alternatives for remote carrier phase synchronization between two stations

The most important technological requirement for a closed loop system is the implementation of the channel duplexing in order to discriminate the signals flow in the two different directions.

Among the possible solutions for channel duplexing are:

- Time division duplexing
- CW transmission with frequency division duplexing
- Code/Orthogonal division duplexing

Time division duplexing

In the Time Division Duplexing schemes the units transmit signals modulated by pulses of finite duration at different time instants. In these cases the duration of the transmitted pulses determines the signal duty cycle. There are some examples of these schemes. Some of them are described in Section 3.1.

The SNR of the demodulated pulse is proportional to the total energy transmitted during a integration time. Then if the duty cycle of the signal is reduced then the SNR of the demodulated phase will be reduced. If the transmitted tone is modulated by a square wave of duty cycle lower than 100 % hence the peak transmitted power must be increased in order to maintain the same SNR of the demodulated phase.

Time division duplexing is also commonly used when a single channel is shared for many phase synchronization links. An example of this is the use of the air as the transmission medium used to synchronize one central unit to multiple remote units, using a TDMA (Time Division Multiple Access) approach. Nevertheless, a system of this type relies on the assumption that there is a previous time synchronization among the units. In this context, the efficiency of the synchronization protocol will depend on the precision of the previous time synchronization. It will be necessary to allocate guard times between consecutive pulses which duration will be proportional to the jitter of the time synchronization performed in the multiple units. Moreover, it would be required to implement

pulse shaping using techniques used in communication protocols in order to improve the spectral characteristics of the transmitted signals. In addition to the pulse shaping it also is possible to apply a modulation to the carrier tone wherewith the bandwidth of transmitted signal is widened.

CW transmission with frequency division duplexing

There also exists the possibility that the two separate stations transmit continuous wave (CW) signals (or equivalently a 100% duty cycle). If it is given that the stations transmit unmodulated tones with the same frequency then the performance of the synchronization loop will depend on the directivity of the transmission and reception subsystems in each of the stations. If the carriers are frequency-modulated in order to duplex the signals traveling in opposite directions, then the modulated signal will introduce another unknown phase offset to the system. Besides that, the propagation constants of the medium are evaluated at different frequencies, obtaining different values for each transmitted carrier frequency.

For this reason, a solution to implement CW systems, is that each station transmits a tone with a slightly different frequency. That is the method proposed in [6, 7, 61]. In these systems the duplexing is performed using frequency multiplexing. In this way, it is required to transmit, from one of the stations to the other, the frequency difference between the transmitted tone and the received tone. This frequency difference signal is in some extent similar to an IF demodulated tone, and generally has a frequency substantially lower than the frequency of the carriers.

One disadvantage of the frequency duplex schemes is the possible dispersion effects generated by the use of multiple carrier frequencies. Whereas these dispersive effects are not present in the schemes that use a single carrier frequency.

Code/Orthogonal division duplexing

There are also other schemes suitable for the transmission of modulated CW signals in phase synchronization links. These schemes use orthogonal signaling in order to discriminate the signal that travel in opposite directions of the transmission channel. As

examples of that is the use of orthogonal chirps to modulate the carrier, and the use of spread spectrum codification techniques. The system complexity of these methods is greater than the complexity of the other ones [35].

4.2.4 Performance requirements for the Remote Carrier Phase Synchronization Schemes depending on the final application

There are different requirements for the different types of synchronization systems depending on the final application. In general two types of phase stability are required, the long term phase stability and the short term phase stability. The long term phase stability is equivalent to an absolute phase offset stability and the short term phase stability is equivalent to a frequency stability. Some applications will require one of them, while other both.

One example of application that requires a short term phase stability is the scheme implemented for the TanDEM-X satellites. This pair of satellites require a very stable frequency offset during one radar acquisition interval. That is equivalent to maintain the phase evolution exactly the same in two oscillators and therefore the same phase offset during the period of time in which is done a radar acquisition.

In that implementation the absolute phase offset can change from one acquisition to another. This is not a problem for this bistatic radar system. The total phase offset between the transmitter and the receiver can be estimated in the post processing of the data.

On the other hand, in the implementation of a high precision distance measurement, or in a interferometric radio location system, the absolute phase offset must be well parameterized and well known, and must be constant for hours, days and maybe years.

The absolute phase offset requirement is also present in the implementation of distributed beamforming, as explained in Section 2.4.2. However, in this system the short term phase stability requirement is relaxed if the absolute phase offset is maintained within a given range of values. As explained in Section 2.4.2, the achievable beamforming gains are not very sensitive to short term phase errors. To quantify this, in the

simplest beamforming scenario, consider the example of two equal amplitude signals from two transmitters combining at a receiver with relative phase error of $\Delta\phi$. The amplitude of the combined signal will be given by

$$|1 + e^{j\Delta\phi}| = 2\cos\left(\frac{\Delta\phi}{2}\right) \tag{4.3}$$

A relative large error of 40° gives a signal amplitude of 1.87 which is 93 % of the maximum possible amplitude of 2. The short term phase variations or equivalently the high frequency phase variations can be tolerated in these kind of systems. Nevertheless, for a following instant (after days, months or years) the absolute phase offset must remain within that range of 40° .

4.2.5 Time synchronization as a complement to Carrier Phase Synchronization Systems

In some phase synchronization links the channel delay is much greater than one complete period of the carrier frequency. If the scheme is performed between two widely separate units, then there will be a long time delay introduced by the channel that will not be characterized by the phase synchronization loop. In these cases the overall phase offset is determined by the time delay associated to the channel and may contain many complete cycles.

The phase synchronization systems cannot discriminate the phase offsets in more than one cycle, wherewith a phase ambiguity of complete cycles cannot be avoided.

For this reason it is commonly required to design a complementary time synchronization subsystem when a carrier phase synchronization scheme is implemented.

Some applications require to determine the complete delay introduced by the channel. One application that has this requirement is an interferometric system for distance measurement. In this system the distance estimation is obtained from the ambiguous phase if the integer number of hidden cycles is determined.

The measurement of the total delay is also required in phased array applications in communications and remote sensing. For example, if the array is used in an interfero-

metric radio positioning system the time synchronization will be strictly necessary.

In general, the time delay information is required for the digital synthesis (DACs), digital data acquisition (ADCs) or symbol timing in communications. Also if the array is used for communication purposes, the time synchronization is crucial to synchronize the baseband symbols in order to obtain higher (power, bandwidth) efficiency and operate at higher data rates.

When a carrier phase synchronization is implemented then the time synchronization process becomes an integer counting problem. If the electrical path of the channel is given by ϕ, then the phase synchronization systems are able to measure $\phi \pmod{\pi}$. Then the total length is obtained if the integer number or wrapped cycles are determined.

One of the options to measure the total delay of the channel using a phase synchronization scheme is to deploy in parallel a number of phase synchronization links with similar carrier frequencies over the same channel. This option is explained in the Section 3.1, where the integer counting problem was solved using the Chinese Remainder Theorem. This approach has the disadvantage given by the complexity and cost associated to the implementation of many independent synchronization loops. Also, the propagation constants may vary if the the operation frequency of the synchronization loop is changed, wherewith the resolution of the total measurement is affected.

Other alternatives for time synchronization using only one phase synchronization loop instead of the implementation of multiple synchronization loops in parallel are also possible. It is possible to implement the carrier synchronization loop using envelope-modulated carriers with lower frequency signals working as a time reference.

The implementation of the time synchronization system complementary to the phase synchronization scheme is not the objective of this Ph.D. thesis. However, the phase synchronization system implemented in this work is designed under the premise that it would be used to implement a complementary time synchronization system in the future.

4.3 Specific design requirements for the proposed Phase Synchronization Scheme

This Ph.D. thesis studies and proposes an alternative Carrier Phase Synchronization System. In addition to the practical application of the designed scheme at our Laboratory, this work is performed as a theoretical study for this type of systems.

The proposed scheme is based on a CW transmission with frequency multiplexing. This option was chosen among the possible technological alternatives for the system implementation listed on previous section.

A performance analysis is done for the proposed system. This analysis studies the system phase stability, in terms of short and long term phase stability.

In summary, the carrier phase synchronization system proposed in this thesis must synchronize two separated units under two design goals:

- Short term phase stability: Maintains the same frequency in the two separate units, which is equivalent to decrease the frequency error (and maintain the same phase difference history between the two units). This requirement is quantified by the phase stability of the loop, and is given by the phase noise and frequency drift between the carrier signals in both units.

- Long term phase stability: Controls and monitors the absolute phase offset among the carrier signals for long periods of time. This requirement is determined by the phase offset of the synchronization loop in the carrier signals in both units.

In addition to these requirements it is also desired to maintain the quality of the carrier signals in both units. Thus, it is required to decrease the signal distortion, the presence of spurs and harmonics, and the presence of additive and noise.

This signal quality will be mainly determined by the quality of the reference signal in the central unit. Notwithstanding, the quality of the signal loop will be affected by the characteristics of the transmission medium and by the quality of the components of the subsystems used to construct the synchronization link. Thus, the system performance must be modeled in function of the channel and subsystem properties.

4.4 Conceptual Design and Analysis of an ideal Single Carrier CW Remote Phase Synchronization Scheme

The advantages of the Continuous Wave (CW) Phase Synchronization Schemes have been explained in the previous chapter, so this Section studies the possible implementations of this technique. The most simple possible implementation is based in the round trip transmission of a single carrier frequency between two distant stations: one central unit and one remote unit. This conceptual design is important to demonstrate the theory of CW synchronization loops, though it is not designed to be used in a practical implementation.

In this system the central unit introduces a sinusoidal tone with a fixed frequency in a transmission channel. This tone is received by the the remote unit which synchronizes its own oscillator to this frequency and retransmits the regenerated tone back to the central unit. The Central Unit recovers this feedback tone and computes the phase offset induced by the transmission channel. With this information the Central Unit adjusts the phase of its transmitted tone using half of the channel phase offset estimation.

For the design of this loop it is assumed that the transmission and reception subsystems in both units are completely directional. Where "directional" refers to the capacity to separate and distinguish two different waves depending on its propagation direction (forward or reverse). That means that there will not be any interference between the two tones which travel in opposite directions in the channel.

In addition, it is also assumed that the channel is perfectly matched and adapted to the central unit and the remote unit. This means that there will be no reflections on the line, and thereby all the incident energy in each reception subsystem is absorbed.

This behavior could be obtained using ideal circulators, perfectly matched to the transmission line at each front-end of the Remote and Central Units. This scheme is reproduced in Figure 4.3.

The carrier, with a frequency of f_c, is injected at the Central Unit, and gives the input reference phase θ_{in}. The central unit transmits one tone with the frequency f_c and a phase α which is equal to the input phase θ_{in} plus an offset, θ_s, which is introduced to

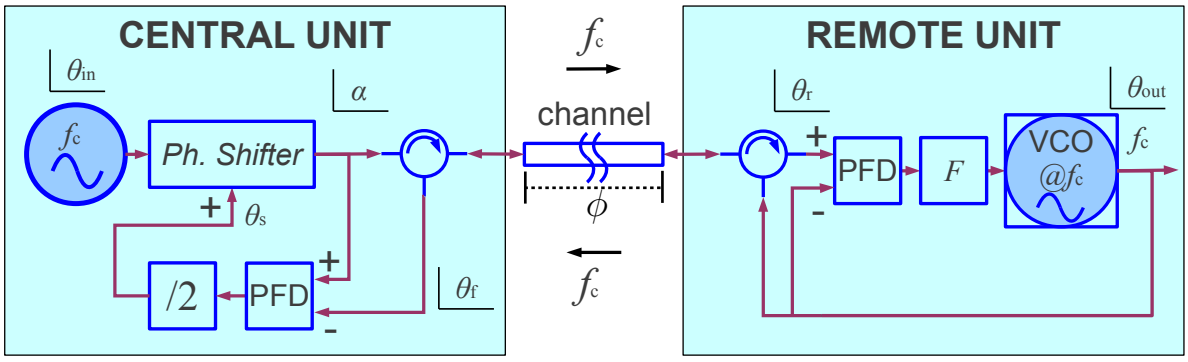

Figure 4.3: Conceptual Single Carrier CW Remote Phase Synchronization Scheme. For the design it has been assumed perfect signal directionality in the subsystems.

a controlled variable phase shifter.

The transmission channel, which is a symmetric channel, introduces a time delay equivalent to a phase delay of $-\phi$ for the transmitted signal at the frequency f_c, thereby, the remote unit receives a tone with a phase of θ_r. In addition, this received signal is attenuated and corrupted by additive noise, which makes harder the detection of the incoming phase, which in some cases can be masked by noise.

The remote unit regenerates the received phase, θ_r, in its own Voltage Controlled Oscillator (VCO). The output phase of the VCO, θ_{out}, is compared to the input phase θ_r in a Phase-Frequency Detector (PFD) whose error output indicates the instantaneous phase difference. When the loop inside the remote unit is *locked*, the control voltage is such that the phase of the output signal, θ_{out}, is exactly equal to the phase of the input signal θ_r.

In order to reduce the effects of noise, the error signal is averaged over some period of time, using the filter F whose output is used to establish the frequency of the VCO. In addition to the external noise, the closed loop inside the remote unit also controls the phase noise generated internally by the VCO, which is not an ideal oscillator.

The regenerated phase, which is introduced in the negative branch of the PFD, is transmitted back to the central unit through the front-end circulator. The central unit receives this feedback signal trough its circulator. The PFD present in the central unit compares θ_f, the phase of the feedback signal, with α, the phase of the transmitted signal. The output of the PFD is divided by 2 and filtered using the transfer function H, whose

output, θ_s, is the phase offset introduced to the variable phase shifter.

There are some characteristics of this scheme, that make it unfeasible for a practical implementation in addition to the requirement of perfect directionality of the subsystems. One of these conditions is that the PFD in the central unit and the PFD at the remote unit must operate at the carrier frequency f_c. This frequency for a common microwave system is in the order of GHz, whereas typical PFD perform well at frequencies of the order of few MHz. On the other hand, the PFDs are designed to work linearly when the phase error is zero or very small. However in the design of this conceptual scheme the PFD at the central unit must work with a phase error different to zero and equivalent to the round trip phase offset introduced by the transmission channel (2 ϕ).

Although, this scheme is not practically feasible it gives an approximation to the performance that can be obtained with a lossy transmission channel and a non ideal VCO. This performance can be quantified by a loop transfer function for each of the inputs to the loop, and is derived as follows.

4.4.1 Performance of the Single Carrier CW Phase Synchronization Scheme

As it has been mentioned previously, the proposed single Carrier synchronization scheme is merely conceptual. However, it is the starting point for quantifying the performance of a general CW synchronization synchronization system. The most important factors that must be characterized are, the effects of the transmission channel and the quality of the oscillators in the remote unit.

The performance of the system is quantified by means of phase transfer functions which are used to interconnect the signal nodes along the complete loop. This transfer functions are used to quantify the effects of the phase inputs in the loop. These inputs (including the noise) are described using conventional Laplace transforms.

The analysis is performed in the same way as is performed in the PLL literature [8, 39, 40] where the analyzed variable is the phase, instead of the signal amplitude or power.

Channel characterization

The channel is described by means of a transfer function, a phase offset and a phase noise input.

As the system state variable is a phase then the transfer function of the channel must be a frequency dependent delay. For this reason the transfer function is an unitary-magnitude transfer function, this means that the magnitude of the transfer function will be one for all the frequencies. For instance, if the channel has a non-dispersive response then its behavior will be a constant delay of all frequencies with a linear phase. In the following, this phase transfer function is labeled as G_{ch}, which correspond to a one-way transfer function. For a given time delay τ_d, G_{ch} can be written in the Laplace transform domain as

$$G_{\text{ch}}(s) = e^{-\tau_d s} \tag{4.4}$$

The channel introduces a phase offset $-\phi$. This phase offset is computed from the wave propagation equation for the carrier on the channel. For a constant time delay this phase offset is equal to $-\tau_d f_{\text{c}}$.

The phase offset ϕ and the noise ϕ_n are introduced at the additive node at the end of the channel, as seen in Figure 4.4, which shows the block model for the transmission channel.

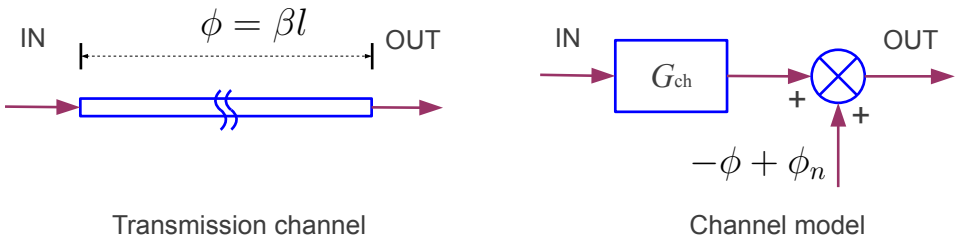

Figure 4.4: Block modeling of the transmission channel.

The phase noise input is relative to the carrier amplitude which is attenuated by the channel. Therefore, if only the thermal noise is considered then the phase noise introduced by the channel can be computed from the transmitted carrier power and the channel attenuation.

The phase noise input is equivalent to the phase noise generated by an additive amplitude noise that is added to a clean sinusoidal signal [40]. For this analysis it is assumed that the additive amplitude noise $n(t)$ is stationary, Gaussian, passband, real and zero mean. This noise is added to the ideal sinusoidal signal to obtain:

$$v_i(t) = V_s \sin(\omega_i t + \theta_i) + n(t) \tag{4.5}$$

The equivalent phase deviation is obtained in an idealized scenario introducing this corrupted signal to an ideal phase detector, whose reference is the clean sinusoidal. The bandpass noise can be decomposed in the two projections over the reference phase

$$n(t) = n_c(t)\cos(\omega_i t + \theta_i) - n_s(t)\sin(\omega_i t + \theta_i) \tag{4.6}$$

where $\sigma^2_{n_c} = \sigma^2_{n_s} = \sigma^2_n$. The phase output of the phase detector for a given time is

$$\phi_n(t) = \arctan\left(\frac{n_c(t)}{V_s + n_s(t)}\right) \tag{4.7}$$

For high values of V_s under conditions of large signal-to-noise ratio it becomes

$$\phi_n(t) = \frac{n_c(t)}{V_s} \tag{4.8}$$

Thus the variance of the output phase ϕ_n is equal to

$$\sigma^2_{\phi_n} = \frac{\sigma^2_{n_c}}{V_s^2} = \frac{\sigma^2_n}{V_s^2} \tag{4.9}$$

The signal-to-noise ratio of the input corrupted signal is $\mathrm{SNR}_i = V_s^2/2\sigma_n^2$. Thus the variance of the detected phase can be rewritten as $\sigma^2_{\phi_n} = 1/2\mathrm{SNR}_i$.

The additive phase noise introduced by the thermal noise at both receiver ends (central and remote) of the transmission channel can be analyzed with this model. It is assumed that the equivalent system temperature is equal at both channel ends.

For the special case of white noise and a received carrier power of P_r, the power spectrum density of the phase noise becomes $S_{\phi n}(f) = N_0/2P_\mathrm{r}$. The received carrier

amplitude is equal to the transmitted amplitude divided by L, which is the loss of the channel. Then the power spectrum density of the input phase noise is equal to $S_{\phi n}(f) = N_0 L^2/2P_\mathrm{t}$.

Transfer functions in the central unit

The central unit is analyzed as a block with two inputs and one output. As it can be seen in Figure 4.3, the output variable of this block is α, the phase of the transmitted tone. The inputs are the phase reference θ_in and the phase of the received feedback tone θ_f.

The phase shifter in the central unit (see Figure 4.3) is modeled by the transfer function $H(s)$. This block is a phase follower, with two inputs, one for the reference θ_in phase and other for the the phase shift input θ_s. Here $H(s)$ is dimensionless (radians/radians) and has unitary steady state response. Figure 4.5 shows an equivalent block diagram of the complete loop with the block transfer functions.

The Central Unit transfer function in closed loop for the input reference phase becomes

$$G_{\text{C-in}}(s) = \frac{\alpha(\theta_\mathrm{in}(s))}{\theta_\mathrm{in}(s)} = \frac{H(s)}{1 - H(s)/2} = \frac{2H(s)}{2 - H(s)} = 2G_\mathrm{C}(s) \tag{4.10}$$

Similarly, the transfer function for the input feedback phase becomes

$$G_{\text{C-fb}}(s) = \frac{\alpha(\theta_\mathrm{f}(s))}{\theta_\mathrm{f}(s)} = \frac{-H(s)/2}{1 - H(s)/2} = \frac{-H(s)}{2 - H(s)} = -G_\mathrm{C}(s) \tag{4.11}$$

Transfer functions in the remote unit

The main transfer function in the remote unit is the one which relates the phase received by the remote unit θ_r with the output phase θ_out.

This closed loop transfer function is obtained from the open loop transfer function of the remote unit. The open loop consists of the PFD, the loop filter and the VCO.

The open loop transfer function is

$$G_\mathrm{o}(s) = K_\mathrm{d} \cdot F(s) \cdot K_\mathrm{v}/s \tag{4.12}$$

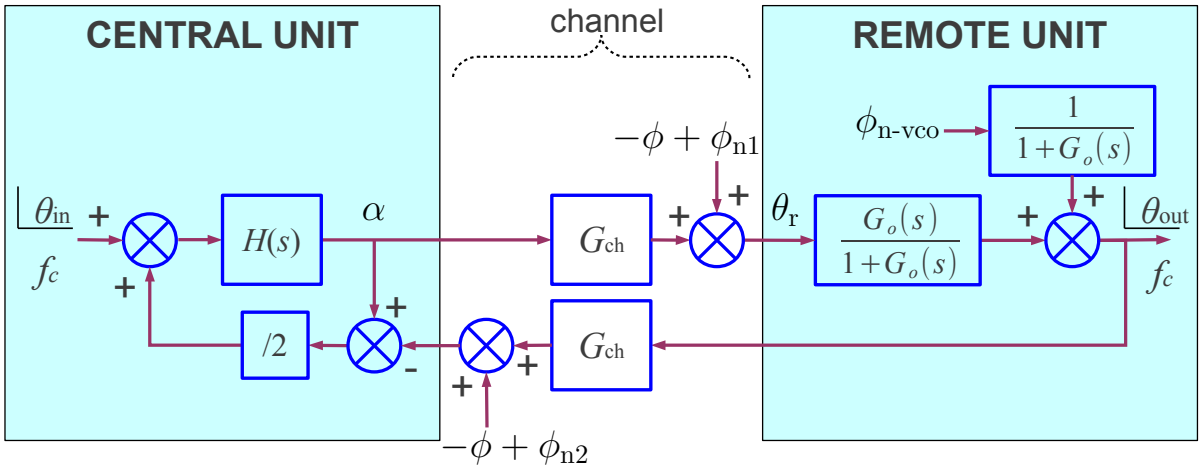

Figure 4.5: Block diagram of the Single Carrier CW Remote Phase Synchronization Scheme. The inputs for this block diagram are: the input phase reference θ_{in}, the phase noise and phase delay added in two points of the channel $-\phi + \phi_{\text{n1}}, -\phi + \phi_{\text{n2}}$, and the phase noise added by the VCO, $\phi_{\text{n-vco}}$.

where K_{d} is the constant of the phase detector, $F(s)$ is the transfer function of the loop filter and K_{v}/s is the transfer function of the VCO (The phase is the integral of the frequency which is proportional to the input amplitude).

The forward closed loop transfer function for the remote unit becomes

$$G_{\text{R}}(s) = \frac{\theta_{\text{out}}(\theta_{\text{r}}(s))}{\theta_{\text{r}}(s)} = \frac{G_{\text{o}}(s)}{1 + G_{\text{o}}(s)} \tag{4.13}$$

Other important relationship for the loop in the remote unit is the transfer function for the phase noise introduced by the VCO. This relationship is given by

$$G_{\text{R-vco}}(s) = \frac{\theta_{\text{out}}\left(\phi_{\text{n-vco}}(s)\right)}{\phi_{\text{n-vco}}(s)} = \frac{1}{1 + G_{\text{o}}(s)} \tag{4.14}$$

Transfer functions for the complete loop

An equivalent simplified block diagram is plotted in order to obtain the transfer functions of the complete phase synchronization loop. This diagram in shown in Figure 4.5.

The complete loop transfer function can be written using the functions of central and

remote units, which are respectively

$$G_{\mathrm{C}}(s) = \frac{H(s)}{2 - H(s)} \quad \text{and} \quad G_{\mathrm{R}}(s) = \frac{G_{\mathrm{o}}(s)}{1 + G_{\mathrm{o}}(s)}, \tag{4.15}$$

The complete loop transfer function for the input reference phase can be expressed as

$$G_{\mathrm{in}}(s) = \frac{\theta_{\mathrm{out}}(\theta_{\mathrm{in}}(s))}{\theta_{\mathrm{in}}(s)} = \frac{2G_{\mathrm{C}}G_{\mathrm{ch}}G_{\mathrm{R}}(s)}{1 + G_{\mathrm{C}}G_{\mathrm{ch}}^2G_{\mathrm{R}}(s)} \tag{4.16}$$

It can be observed from Equation 4.16 that the complete loop has a unitary steady state gain. Therefore, the output phase will follow the input phase with a delay given by the complete loop. This delay depends on the delays of the loop filters and the transmission channel.

The output phase will be affected by the phase offset and phase noise introduced by the channel and the phase noise generated within the VCO. These are disturbance inputs for the complete phase loop and its effects are quantified subsequently. In general, the denominator of Equation 4.16 will be the general denominator for the other transfer functions of complete loop.

The effect of the phase noise generated by the VCO over the output phase is

$$G_{\mathrm{vco}}(s) = \frac{\theta_{\mathrm{out}}(\phi_{\text{n-vco}}(s))}{\phi_{\text{n-vco}}(s)} = \frac{\dfrac{1}{1 + G_{\mathrm{o}}(s)}}{1 + G_{\mathrm{C}}G_{\mathrm{ch}}^2G_{\mathrm{R}}(s)} \tag{4.17}$$

This function tends to be zero as the magnitude of the loop filter, $G_{\mathrm{o}}(s)$, becomes higher. In addition, the steady state gain of the main denominator of Equation 4.17 is two, which means that the phase noise generated by the VCO is divided by two by the complete loop.

Equivalently, the impact of the phase changes generated by the channel is determined by its transfer function. These functions are obtained with the direct path which affects the numerator and the general denominator of the loop. Thus, the transfer function for the input node which is in the receiver of the remote unit is

$$G_{\phi 1}(s) = \frac{G_{\mathrm{R}}(s)}{1 + G_{\mathrm{C}}G_{\mathrm{ch}}^2G_{\mathrm{R}}(s)} \tag{4.18}$$

And the function for the input phase offset of the received feedback signal in the central unit is

$$G_{\phi 2}(s) = \frac{-G_{\mathrm{C}} G_{\mathrm{ch}} G_{\mathrm{R}}(s)}{1 + G_{\mathrm{C}} G_{\mathrm{ch}}^2 G_{\mathrm{R}}(s)} \tag{4.19}$$

Phase offset of the complete compensated loop in steady state

The phase error of the complete phase synchronization loop in steady state are found found with the loop transfer functions. Thus the phase offset in the output θ_{out} is obtained for an input channel phase offset ϕ.

Commonly, the dynamic behavior and the transient response of the complete loop is mostly determined by the loop filters. In a typical implementation the loop filters have a bandwidth of a few kilohertz that is equivalent to a delay in the order of milliseconds, whereas the delay of a one kilometer transmission channel is in the order of microseconds.

The phase offset ϕ is introduced at both channel ends, wherewith the phase output as a function of ϕ is

$$\begin{aligned} \theta_{\mathrm{out}}(\phi) &= -\phi(s) G_{\phi 1}(s) - \phi(s) G_{\phi 2}(s) \\ &= -2\phi(s)(G_{\phi 1}(s) + G_{\phi 2}(s)) \end{aligned} \tag{4.20}$$

It might be said that the changes in ϕ would affect the channel transfer function G_{ch}, however if the variations in the time delay associated to ϕ are small compared to the total channel delay then these effects can be neglected.

The phase mismatch generated by the channel offset $\phi(s)$ becomes

$$\begin{aligned} \theta_{\mathrm{out}}(\phi(s)) &= -2\phi(s) \left(\frac{G_{\mathrm{R}}(s) - G_{\mathrm{C}} G_{\mathrm{ch}} G_{\mathrm{R}}(s)}{1 + G_{\mathrm{C}} G_{\mathrm{ch}}^2 G_{\mathrm{R}}(s)} \right) \\ &= -2\phi(s) G_{\mathrm{R}}(s) \left(\frac{1 - G_{\mathrm{C}} G_{\mathrm{ch}}(s)}{1 + G_{\mathrm{C}} G_{\mathrm{ch}}^2 G_{\mathrm{R}}(s)} \right) \end{aligned} \tag{4.21}$$

The steady state value of this function are readily evaluated by means of the final value theorem of Laplace transforms, which can be written as

$$\lim_{t \to \infty} \theta_{\mathrm{out}}(\phi(t)) = \lim_{s \to 0} = s \cdot \theta_{\mathrm{out}}(\phi(s)) \tag{4.22}$$

The output phase offset is first evaluated for an unitary phase step input, $\phi(s) = 1/s$. With the intermediate results:

$$\lim_{s\to 0} G_{\mathrm{R}}(s) = 1, \qquad \lim_{s\to 0} G_{\mathrm{C}}(s) = 1, \tag{4.23}$$

the steady state output value becomes

$$\begin{aligned}\lim_{t\to\infty} \theta_{\mathrm{out}}(\phi(t)) &= \lim_{s\to 0} -2s \cdot \left(\frac{1}{s}\right) \cdot G_{\mathrm{R}}(s) \left(\frac{1 - G_{\mathrm{C}}G_{\mathrm{ch}}(s)}{1 + G_{\mathrm{C}}G_{\mathrm{ch}}^2 G_{\mathrm{R}}(s)}\right) \\ &= -2 \cdot \frac{1-1}{1+1} = 0.\end{aligned} \tag{4.24}$$

This Equation shows that an step change in the channel phase offset will have no effect over the complete compensated loop in steady state. This result can also be extended to the cases of pulse inputs, which may be square or not square pulses.

Next, suppose that the channel phase is linearly changing with time at constant rate. This effect can be generated by the Doppler effect if the electrical length of the channel is changed by a movement between the remote and central unit with constant velocity. In this case the input with a rate of $2\Delta f_d$ is $\phi(s) = \Delta f_d / s^2$, and the output phase becomes

$$\begin{aligned}\lim_{t\to\infty} \theta_{\mathrm{out}}(\phi(t)) &= \lim_{s\to 0} -2s \cdot \left(\frac{\Delta f_d}{s^2}\right) \cdot G_{\mathrm{R}}(s) \left(\frac{1 - G_{\mathrm{C}}G_{\mathrm{ch}}(s)}{1 + G_{\mathrm{C}}G_{\mathrm{ch}}^2 G_{\mathrm{R}}(s)}\right) \\ &= \lim_{s\to 0} \Delta f_d \, \frac{1 - G_{\mathrm{ch}}(s)}{s} = \Delta f_d \lim_{s\to 0} \frac{1 - e^{s\tau_d}}{s} \\ &= \Delta f_d \, \tau_d\end{aligned} \tag{4.25}$$

Therefore, for a channel phase offset increasing at constant rate Δf_d the phase offset output of the compensated system will be a constant, and the frequency error between the two units will be zero.

A change in the ramp rate will change this phase offset, but can only be generated by an acceleration between the two units. This behavior meets the requirements, for

example, for a bistatic transmitter/receiver pair because it is not strictly needed to know the absolute phase offset between the two units.

The absolute phase offset between the two units for different relative velocities (phase ramp rates) can be obtained if the total temporal channel delay, τ_d is known, which in this model has been assumed constant for the small changes in the channel phase ϕ.

The total channel delay can be obtained by means of a temporal synchronization. This temporal synchronization cannot be obtained using only the phase synchronization system, because there is an ambiguity in the number of wrapped phase cycles included in the total temporal delay. For this reason, in some applications it may be necessary to complement the phase synchronization systems with time synchronization systems .

System response to the additive channel phase noise

In addition to the absolute phase offset, both units receive a signal corrupted by additive noise. This effects are modeled by the phase noise inputs ϕ_{n1}, and ϕ_{n2}, which are two uncorrelated white noise phase inputs.

The variance of the output phase θ_{out} associated to a ϕ_{n1} with a power spectral density of $S_{\phi \mathrm{n1}}(s)$ is

$$\begin{aligned}\sigma^2_{\theta\mathrm{out}}(\phi_{\mathrm{n1}}) &= \int_{-\infty}^{\infty} S_{\phi\mathrm{n1}}(s)\ \left|G_{\phi 1}(s)\right|^2\ ds = 2\int_{0}^{\infty} S_{\phi\mathrm{n1}}(s)\ \left|G_{\phi 1}(s)\right|^2\ ds \\ &= \frac{N_0 L^2}{P_{\mathrm{T1}}}\int_{0}^{\infty}\left|G_{\phi 1}(s)\right|^2\ ds = \frac{N_0 L^2}{P_{\mathrm{T1}}}\int_{0}^{\infty}\left|\frac{G_{\mathrm{R}}(s)}{1+G_{\mathrm{C}}G^2_{\mathrm{ch}}G_{\mathrm{R}}(s)}\right|^2\ ds\end{aligned} \tag{4.26}$$

where N_0 is the power spectrum density of the amplitude noise, L is the 1-way channel attenuation and P_{T1} is the carrier power transmitted by the central unit.

Equivalently, the variance output generated by ϕ_{n2} (which is at the other end of the channel) is

$$\sigma^2_{\theta\mathrm{out}}(\phi_{\mathrm{n2}}) = \frac{N_0 L^2}{P_{\mathrm{T2}}}\int_{0}^{\infty}\left|G_{\phi 2}(s)\right|^2\ ds = \frac{N_0 L^2}{P_{\mathrm{T2}}}\int_{0}^{\infty}\left|\frac{G_{\mathrm{C}}G_{\mathrm{ch}}G_{\mathrm{R}}(s)}{1+G_{\mathrm{C}}G^2_{\mathrm{ch}}G_{\mathrm{R}}(s)}\right|^2\ ds \tag{4.27}$$

Now it is defined the bandwidth

$$\mathrm{BW} = \int_0^\infty |G_\mathrm{R}(s)|^2 \; ds \tag{4.28}$$

The Equations 4.26 and 4.27 can be simplified in terms of the BW. First $G_\mathrm{C}G_\mathrm{ch}G_\mathrm{R}(s)$ in the numerator of Equation 4.27 can be approximated by $G_\mathrm{R}(s)$ if the bandwidth of $G_\mathrm{R}(s)$ is lower than the bandwidth of $G_\mathrm{C}G_\mathrm{ch}(s)$. Then the common denominator for Equations 4.26 and 4.27 can be simplified evaluating $G_\mathrm{C}G_\mathrm{ch}^2G_\mathrm{R}(s)$ as one within the loop bandwidth and zero outside the loop bandwidth, wherewith the denominator in both equations is equal to 2 within the loop bandwidth. Thus the variances are

$$\sigma^2_{\theta\mathrm{out}}(\phi_\mathrm{n1}) = \frac{N_0L^2\mathrm{BW}}{4\ P_\mathrm{T1}}, \qquad \sigma^2_{\theta\mathrm{out}}(\phi_\mathrm{n2}) = \frac{N_0L^2\mathrm{BW}}{4\ P_\mathrm{T2}}, \tag{4.29}$$

Finally, the total phase noise variance is

$$\begin{aligned}\sigma^2_{\theta\mathrm{out}}(\phi_\mathrm{n1},\phi_\mathrm{n2}) =&\ \sigma^2_{\theta\mathrm{out}}(\phi_\mathrm{n1}) + \sigma^2_{\theta\mathrm{out}}(\phi_\mathrm{n2}) \\ =&\frac{N_0L^2\mathrm{BW}}{4\ P_\mathrm{T1}} + \frac{N_0L^2\mathrm{BW}}{4\ P_\mathrm{T2}} \\ =&\frac{N_0L^2\mathrm{BW}}{4}\left(\frac{1}{P_\mathrm{T1}} + \frac{1}{P_\mathrm{T2}}\right)\end{aligned} \tag{4.30}$$

For a total transmitted power P_TT equally distributed in both carriers, ($P_\mathrm{T1} = P_\mathrm{T2}$, and $P_\mathrm{TT} = P_\mathrm{T1} + P_\mathrm{T2}$), the total phase variance is

$$\sigma^2_{\theta\mathrm{out}}(\phi_\mathrm{n1},\phi_\mathrm{n2}) = \frac{N_0L^2\mathrm{BW}}{P_\mathrm{TT}} \tag{4.31}$$

Phase noise of the complete synchronization loop and bandwidth optimization

The total phase noise at the output is the superposition of the outputs generated by the channel phase noise, the VCO noise, and also for the phase noise of the input phase

reference. The total phase noise variance is

$$\sigma^2_{\theta\text{out}} = \sigma^2_{\theta\text{out}}(\phi_{\text{n1}}, \phi_{\text{n2}}) + \sigma^2_{\theta\text{out}}(\phi_{\text{n-vco}}) + \sigma^2_{\theta\text{out}}(\theta_{\text{in}}) \tag{4.32}$$

where each of the terms of the last Equation are the variances of the phase outputs produced by the inputs ϕ_{n1}, ϕ_{n2}, $\phi_{\text{n-vco}}$, and θ_{in}.

Therefore the loop bandwidth must be optimized in order to reduce the total output phase noise. The first term of the Equation 4.32 is the channel phase noise and was found in previous paragraph. The Equations for the other contributors are

$$\begin{aligned} \sigma^2_{\theta\text{out}}(\phi_{\text{n-vco}}) &= \int_0^\infty |\phi_{\text{n-vco}}(s) \cdot G_{\text{vco}}(s)|^2 \, ds, \\ \sigma^2_{\theta\text{out}}(\theta_{\text{in}}) &= \int_0^\infty |\theta_{\text{in}}(s) \cdot G_{\text{in}}(s)|^2 \, ds \end{aligned} \tag{4.33}$$

The most simple bandwidth optimization can be performed if the filters are modeled as ideal filters with a rectangular response in frequency. As stated previously, the loop bandwidth is determined by the bandwidth of $G_{\text{R}}(s)$, if its bandwidth is smaller than $G_{\text{C}}(s)$ the bandwidth.

It can be observed that the transfer functions $G_{\phi 1}(s), G_{\phi 2}(s), G_{\text{vco}}(s)$ and $G_{\text{vco}}(s)$ have a common factor which comes from the characteristic denominator,

$$\frac{1}{1 + G_{\text{C}} G^2_{\text{ch}} G_{\text{R}}(s)} \tag{4.34}$$

Then, this common factor will be equal to 1/2 within the loop bandwidth and 1 outside the bandwidth.

The response of the numerators of the channel noise inputs has unitary magnitude within the loop bandwidth, whereas the numerator for the VCO noise is the complement to the loop bandwidth, with an unitary response outside the loop bandwidth and a zero response inside the bandwidth. Summarizing, the transfer functions for a loop bandwidth

of BW can be simplified to

$$G_{\phi 1}(s) = -G_{\phi 2}(s) = \begin{cases} 1/2 & \text{if } |s| \leq \text{BW} \\ 0 & \text{if } |s| > \text{BW} \end{cases}$$

$$G_{\text{vco}}(s) = \begin{cases} 0 & \text{if } |s| \leq \text{BW} \\ 1/2 & \text{if } |s| > \text{BW} \end{cases} \tag{4.35}$$

$$G_{\text{in}}(s) = \begin{cases} 1 & \text{if } |s| \leq \text{BW} \\ 0 & \text{if } |s| > \text{BW} \end{cases}$$

The phase noise contributors are divided in two. First the channel phase noise and the reference phase noise contribute to the phase noise within the loop bandwidth. Second the VCO phase noise, which contributes to the total phase noise for frequencies outside the bandwidth.

In a conventional PLL the optimum bandwidth the frequency of the crossover between the phase noise spectrum of the in-band contributors and the VCO phase noise spectrum [8, 39, 40].

The in-band phase noise spectrum is

$$\begin{aligned} S_{\text{BW}}(s) = \; & S_{\phi \text{n1}}(s) \left|\frac{1}{2}\right|^2 + S_{\phi \text{n2}}(s) \left|\frac{1}{2}\right|^2 + S_{\theta \text{in}}(s) \left|1\right|^2 \\ = \; & \frac{1}{2}\frac{N_0 L^2}{P_{\text{TT}}} + S_{\theta \text{in}}(s) \end{aligned} \tag{4.36}$$

where

$$S_{\phi \text{n1}}(s) = S_{\phi \text{n2}}(s) = \frac{1}{2}\frac{N_0 L^2}{P_{\text{T1}}} = \frac{N_0 L^2}{P_{\text{TT}}} \tag{4.37}$$

and $S_{\theta \text{in}}(s)$ is the phase noise spectrum of the reference.

The value of $S_{\mathrm{BW}}(s)$ is compared with the VCO phase noise spectrum

$$S_{\mathrm{OBW}}(s) = S_{\phi\mathrm{nvco}}(s)\left|\frac{1}{2}\right|^2 \tag{4.38}$$

If both functions (4.36 and 4.38) decrease monotonically with frequency then the optimum bandwidth is located at the interception point where $S_{\mathrm{BW}}(s)$ is equal to $S_{\mathrm{OBW}}(s)$.

Figure 4.6 shows an illustrative example with the interception of these two curves. Here $S_{\mathrm{OBW}}(f)$ presents a typical power spectral density of a VCO with a spectrum mainly dominated by the $1/s$ term. The curve of the power spectral density for the phase noise contributors inside the loop bands, $S_{\mathrm{BW}}(f)$, consist of line segments with different slopes in the logarithmic scale, and is dominated in the high frequencies by white noise floor.

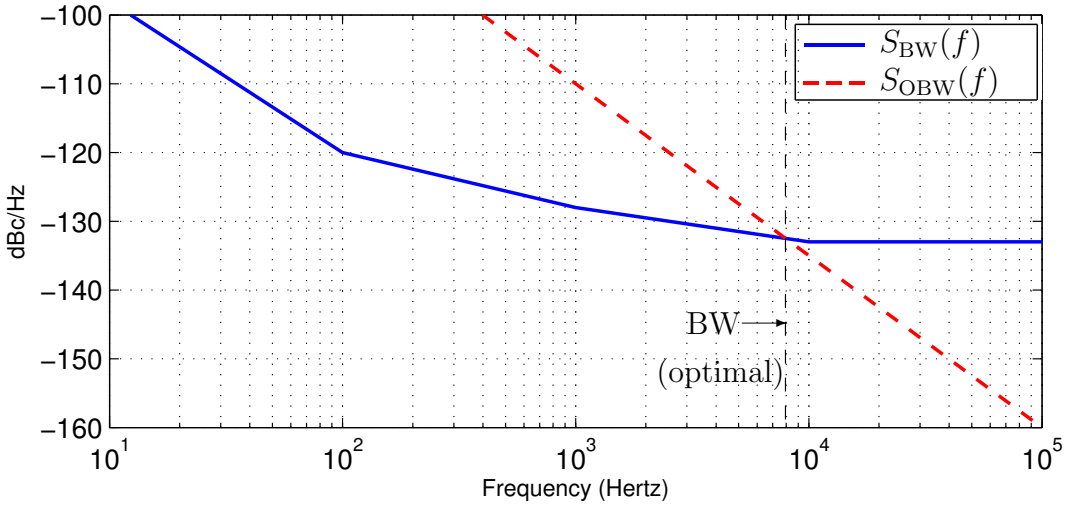

Figure 4.6: Illustrative plot of the power spectral densities of the phase noise contributors in the single carrier phase synchronization loop. The optimal loop bandwidth is determined by the interception of the two power spectral density curves.

This analysis gives the first step in the design of the synchronization loop, however, in the actual implementation the loop components must be designed using non ideal components. For example, the loop filters may be implemented with low order transfer functions which have lower delay and better transient responses. In the PLL literature the second order loop is the most widely applied because of its simplicity, good performance, and dynamic response [39, 40]. Therefore, the second order loop is the first candidate to implement the transfer functions in the central and remote unit, $G_{\mathrm{C}}(s)$ and $G_{\mathrm{R}}(s)$.

Stability of the complete synchronization loop

The stability of the synchronization loop, seen as the dynamic equilibrium of the system, as studied in the control theory, is determined by the characteristic denominator of the transfer function of the complete loop.

The dynamic stability of a system is defined as follows: A system is said to be stable if the output is bounded for every input to the system that is bounded.

Thus, the system will be stable if all poles of the closed loop transfer function remain in the left half of the s-plane. From the loop characteristic Equation (4.34), stability is ensured if the magnitude of the transfer function

$$\left|G_{\mathrm{C}}G_{\mathrm{ch}}^{2}G_{\mathrm{R}}(s)\right| \leq 1 \tag{4.39}$$

for all s.

The channel transfer function $G_{\mathrm{ch}}(s)$, which is stable, is modeled by a constant delay $e^{-s\tau_d}$, wherewith the factor $G_{\mathrm{ch}}^{2}(s) = e^{-2s\tau_d}$, has an unitary magnitude response for all frequencies. $G_{\mathrm{R}}(s)$ and $G_{\mathrm{C}}(s)$, which are also unconditionally stable, are designed to have a flat unitary response within the bandwidth.

Then the complete loop will be stable depending on the gain of $G_{\mathrm{C}}(s)$ and $G_{\mathrm{R}}(s)$. In a practical implementation its frequency response is not completely flat and may have some overshoot gain near to the bandwidth frequency corner.

If in a practical design $G_{\mathrm{C}}(s)$ or $G_{\mathrm{R}}(s)$ have a overshoot gain, then a stability analysis for the complete loop must be done.

The root locus analysis cannot be performed since the delay transfer function for the channel cannot be decomposed in a set of discrete zeros and poles. However, the Bode gain-phase analysis may be used to determine the system stability.

To conclude, in addition to the loop stability and the physical feasibility of the loop filters, the practical situation departs from the idealized model in a number of ways. The most challenging problem that must be accomplished is the directivity required by the components in the loop. Is by this reason that this thesis proposes a variation over the single carrier scheme which uses different CW frequency modulations in order to

circumvent this difficulty.

4.5 Proposed Carrier Phase Synchronization Scheme: Dual Frequency CW Loop

In this Ph.D. thesis a new CW remote carrier phase synchronization scheme has been proposed and designed. The proposed system was designed to fulfill the requirements given in Section 4.3. The ideal single carrier CW remote phase synchronization scheme proposed in the previous section can ideally meet these requirements, however a practical scheme must be developed from this conceptual scheme. The new design must fulfill other two practical challenges:

The first challenge is to implement a method for duplexing the two signals that travel in opposite directions along the transmission channel. This requirement was solved in the conceptual scheme assuming that all the subsystems along the loop are perfectly directional.

The second challenge is the implementation of a practical phase compensation subsystem in the Central Unit different to the proposed in the conceptual scheme. In a feasible compensation subsystem, the phase must be measured with a non-ideal phase detector. The practical detectors are designed to be used only at the operation point of zero phase error.

The directivity requirement is circumvented in other phase synchronization loops with frequency multiplexing [7, 61]. The scheme proposed by Landecker [61] is an example of these type of systems. In these cases the frequencies of the direct and feedback tones are different, hence the phase difference obtained in the Central Unit is not a constant but a phase ramp similar in some extent to an IF demodulated signal. This signal, which has a frequency substantially lower than the frequency of the two carriers, must be retransmitted in order to close the loop.

This scheme will work properly as far as the propagation velocity in the medium is the same for all the used frequencies, or in other words, the channel is not dispersive. The differences in the propagation velocities for the different tones would introduce phase

errors to the overall compensated loop. As the channel distance increases, the error would become greater. Additionally, in practical implementations the channel and the loop subsystems have a bandpass behavior and are matched only to a limited bandwidth.

4.5.1 First alternative: Amplitude Modulated phase synchronization scheme

One alternative to implement the duplexing using frequency discrimination is to multiply the amplitude of the first transmitted carrier with an external low frequency modulating signal, obtaining a suppressed-carrier double sideband modulation. This envelope modulation is observed previous works. In [63] a diode in the middle of a waveguide is modulated in order to obtain an estimation of the channel offset of the complete waveguide. In [107] an amplitude-modulated signal emitting from a transmitter is received by a passive receiver in order to implement an unidirectional synchronization link. In the receiver this signal is passed through a coherent envelope detector which regenerates the carrier and demodulates the envelope. The carrier becomes the phase-frequency reference of the receiver and the low frequency envelope is used to trigger a sampling clock.

Thus, a hypothetical variation over the single carrier synchronization scheme can be analyzed. For example, the forward carrier can modulated in amplitude with an external low frequency modulating tone. Hence, if the input carrier is $c(t) = \cos(\omega_c t + \theta_{\text{in}})$ and the modulating signal is $m(t) = \cos(\omega_m t + \theta_m)$ then the transmitted modulated signal becomes

$$\begin{aligned} x(t) &= \cos(\omega_c t + \theta_{\text{in}}) \cos(\omega_m t + \theta_m) \\ &= \frac{1}{2}\left[\cos((\omega_c + \omega_m)t + \theta_{\text{in}} + \theta_m)\right] + \frac{1}{2}\left[\cos((\omega_c - \omega_m)t + \theta_{\text{in}} - \theta_m)\right] \end{aligned} \tag{4.40}$$

After the propagation time, τ_{d}, the remote unit receives $x(t - \tau_{\text{d}})$, which is a delayed version of $x(t)$ equivalent to

$$x(t - \tau_{\text{d}}) = \frac{1}{2}\left[\cos((\omega_c + \omega_m)(t - \tau_{\text{d}}) + \theta_{\text{in}} + \theta_m) + \cos((\omega_c - \omega_m)(t - \tau_{\text{d}}) + \theta_{\text{in}} - \theta_m)\right] \tag{4.41}$$

The Remote Unit receives this signal and uses it to regenerate the carrier obtaining the average frequency of the two incoming tones. This operation cannot be performed with an ordinary PLL since ordinary PLLs are not able to lock to a suppressed carrier modulated signal [40]. However, the frequency averaging operation is equivalent to add the two incoming frequencies and divide the result by two. This behavior can be obtained with an Upper Side Band Generator (USBG) in combination with a frequency divider. The normalized output of an USBG would be

$$\begin{aligned} u(t) &= \cos\left(2\omega_c(t-\tau_\mathrm{d}) + 2\theta_\mathrm{in}\right) \\ &= \cos\left(2\omega_c t - 2\omega_c\tau_\mathrm{d} + 2\theta_\mathrm{in}\right) \end{aligned} \tag{4.42}$$

Whereupon, the frequency divider output becomes

$$\begin{aligned} y(t) &= \cos\left(\omega_c t - \omega_c\tau_\mathrm{d} + \theta_\mathrm{in}\right) \\ &= \cos\left(\omega_c t - \phi + \theta_\mathrm{in}\right) \end{aligned} \tag{4.43}$$

Hence the carrier is regenerated at the Remote Unit with the phase offset, $\phi = \omega_c\tau_\mathrm{d}$ (radians), associated to the carrier frequency ($f_c = \omega_c/2\pi$). This tone is transmitted back to the Central Unit in order to close the loop. With this arrangement, the received tones in the Remote Unit can be isolated from the strong regenerated tone using a stop band filter centered at f_c. In the Central Unit the feedback carrier is received and its phase is processed exactly as was done in the single carrier scheme. The hypothetical AM synchronization scheme is shown in Figure 4.7.

In this arrangement the directivity requirement is alleviated, and the direction of the signals are discriminated using frequency filtering. Nevertheless, this scheme does not provide a solution for a practical implementation of the phase compensation in the Central Unit. The Phase Frequency Detectors (PFD) used in conventional PLLs are designed to work linearly for small phase differences near to zero. Although, in the synchronization scheme the obtained phase difference, which is given by the channel delay, will have a non-zero value in steady state. In addition, the implementation of a DC-controlled phase shifter (the actuator of the control loop) can be a difficult task.

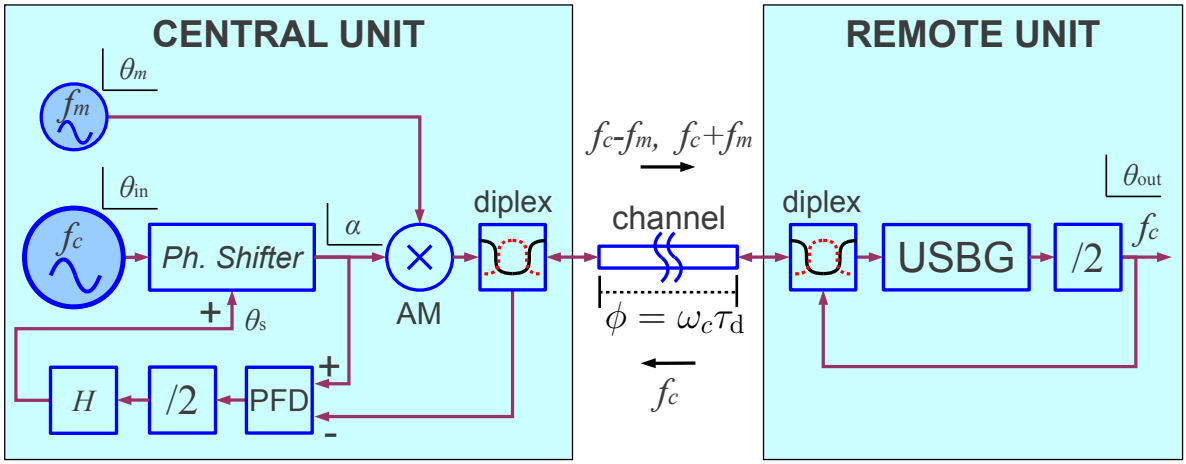

Figure 4.7: Hypothetical Amplitude Modulated Carrier Phase Synchronization Scheme. The block labeled as "diplex" is a frequency diplexer in which two ports are multiplexed onto a third port with a stop-band response response centered at f_c for the first port and the complementary pass-band response for the second port.

These issues can be resolved with a modification over the AM phase synchronization scheme in which the phase compensation is not performed at zero frequency. The carrier phase synchronization scheme proposed in this thesis fulfills these characteristics and is exposed as follows.

4.5.2 Proposed alternative: dual frequency synchronization scheme

The proposed scheme is based on the use of two sub-carriers for the forward direction signal, as performed in the AM synchronization scheme, in which the frequency average of the two sub-carriers is exactly the nominal carrier frequency f_c. In the proposed loop, in contrast to the AM scheme, the two tones are generated independently. The first tone, x_1 has an external fixed phase and the other one, x_2, has a phase which is adjusted in order to compensate the complete loop offset.

Following the nomenclature of the AM synchronization scheme, the first tone has a frequency $f_1 = f_c - f_m$, and an unknown arbitrary phase θ. The frequency of the second tone is $f_1 = f_c + f_m$, and its phase α is adjusted in order to compensate the channel phase offset and the effects of the unknown phase θ. In steady-state, if the loop is compensated correctly then the value of α must be equal to $2\phi - \theta$. Wherewith the output phase at

the remote unit will be zero (in relation to the carrier input phase θ_{in} which is assumed to the zero reference).

The remote unit in this scheme is identical to the remote unit of the AM synchronization scheme. Thus, the remote unit regenerates a carrier with frequency f_{c} and sends it back to the Central Unit. The phase of the feedback signal observed in the central unit is given by

$$\theta_{\text{f}} = \frac{\theta}{2} + \frac{\alpha}{2} - 2\phi. \tag{4.44}$$

This phase can be used to obtain α, the desired phase in the controlled tone. The terms $\alpha/2$ and $\theta/2$ may be compensated from the received feedback signal using a frequency-divided version of the two transmitted tones. If it is assumed that the carrier input phase, θ_{in} is zero, then it is possible to obtain a tone suitable for the down-conversion of the received feedback signal. This down-conversion tone is obtained by mixing the phase of the carrier and the frequency-divided the tones. The phase of the down-conversion carrier is

$$\theta_{\text{down-conversion}} = 0 + \frac{\alpha}{2} - \frac{\theta}{2} \tag{4.45}$$

and its frequency

$$f_{\text{down-conversion}} = f_2 = f_c + \frac{f_1}{2} - \frac{f_2}{2} \tag{4.46}$$

Whereupon, the decoded phase becomes

$$\theta_{\text{decoded}} = \theta_{\text{down-conversion}} - \theta_{\text{f}} = 2\phi - \theta \tag{4.47}$$

and its frequency

$$f_{\text{decoded}} = f_m = f_2 - f_c \tag{4.48}$$

Finally, the controlled tone, whose frequency is $f_2 = f_c + f_m$, is obtained through an up-conversion of the carrier and the decoded low frequency signal. Then its phase, α, becomes

$$\alpha = 0 + \theta_{\text{decoded}} = 2\phi - \theta \tag{4.49}$$

A flow diagram of the generation of x_2, the controlled tone, is shown in Figure 4.8. This diagram shows how it is possible to obtain the compensation tone without the

implementation of a direct zero-frequency phase detection.

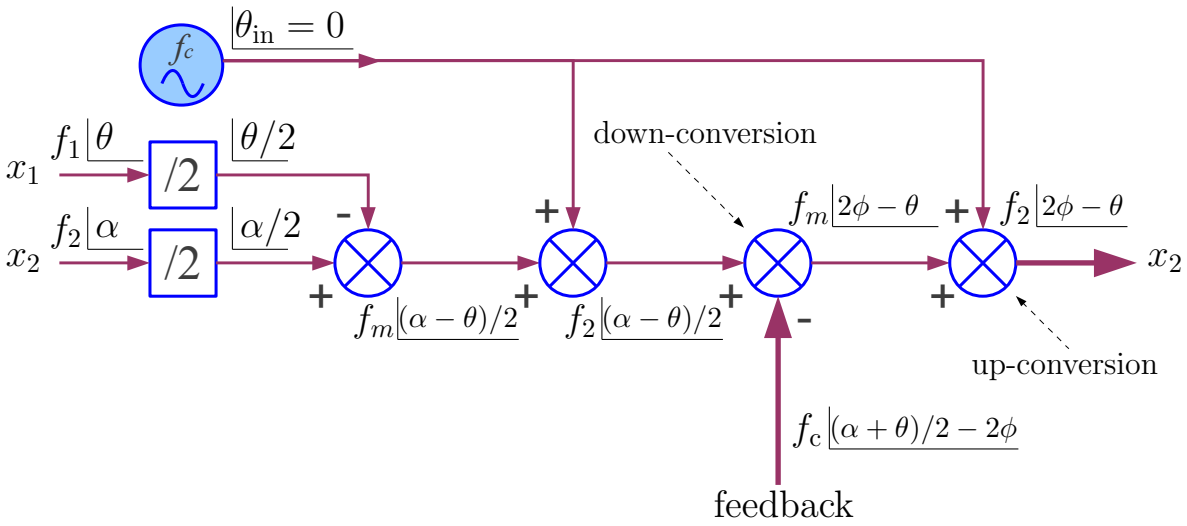

Figure 4.8: Flow diagram of the generation of the compensation tone x_2 in the Central Unit with a non-zero phase detection. The phases/frequencies are added or subtracted with ideals interception nodes. The feedback signal is the tone received by the central unit with a f_c frequency. In steady state the phase of x_2 (the output) becomes $\alpha = 2\phi - \theta$.

The diagram shown in Figure 4.8 also shows that the carrier reference is introduced two times in the flow diagram, both with positive sign. Hence, the diagram can be simplified replacing the two interception nodes of the carrier reference input with one only interception node for an input signal with a frequency of two times the carrier reference f_c. In addition, a tone with a frequency of $2f_c$ is also generated on the remote unit in the USBG block. Then it is also possible to use the loop to synchronize a carrier with two times the frequency f_c. This loop configuration has the advantage on characterizing the channel using tones which are one half the frequency of the synchronized carrier. Thus, the synchronization loop will be affected by lower attenuation for a given carrier frequency value.

Figure 4.9 shows the flow diagram of the generation of the compensation tone using a carrier with a frequency of $2f_c$ equal to f_{op}.

The diagrams shown in Figures 4.8 and 4.9 are based in the use of additive interception nodes that resemble upper sideband or lower sideband mixers depending on the sign on input of the interception node. Notwithstanding, in a practical implementation the output tone must be obtained using regenerative phase locking. A practical phase following

circuit in which the output signal is also one of its inputs is only possible with regenerative phase locking [40].

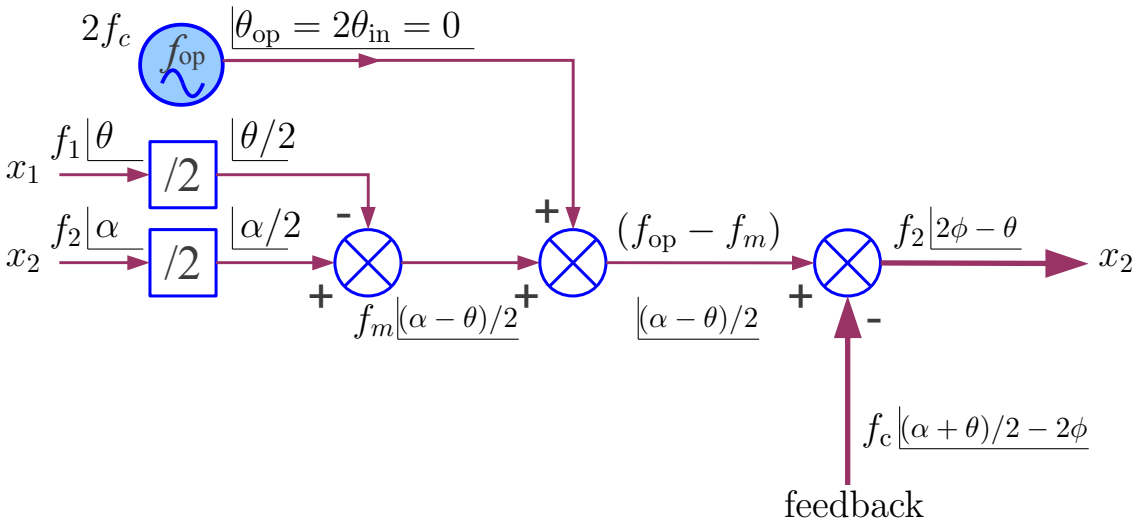

Figure 4.9: Flow diagram of the controlled tone generation with a reference carrier with twice the frequency f_c in the Central Unit.

The proposed dual frequency synchronization scheme is based on the phase tracking diagram of Figure 4.9. A general diagram of the complete phase synchronization loop is shown in Figure 4.10. In this diagram the order of the interception points in the loop is changed, though the overall result is maintained.

Both units are connected to the transmission channel through a three-port frequency multiplexer device. This device filters three different bands around the frequencies of the three transmitted tones, f_1, f_2, and f_c.

The Lower Side Band Generator Block in the Central Unit generates the phase-controlled tone x_2 with a frequency-offset regenerative phase locked loop. For this implementation in particular, the positive phase input of the LSBG is the carrier tone with the operation frequency, $f_{op} = 2f_c$ and the negative phase input is a tone with f_1 frequency and a phase equal to $\theta - 2\phi$ equivalent to $-\alpha$. Additionally, the phase difference between this tone and x_1 can be used to measure the channel phase offset externally.

One advantage of the proposed scheme is that the channel characterization can be performed with a set of frequencies, f_1, f_2, and f_c, with a very small separation among them without any compromise to the system accuracy. At the cost of the selectivity requirement given to the frequency multiplexers in both units. If high selective filters are

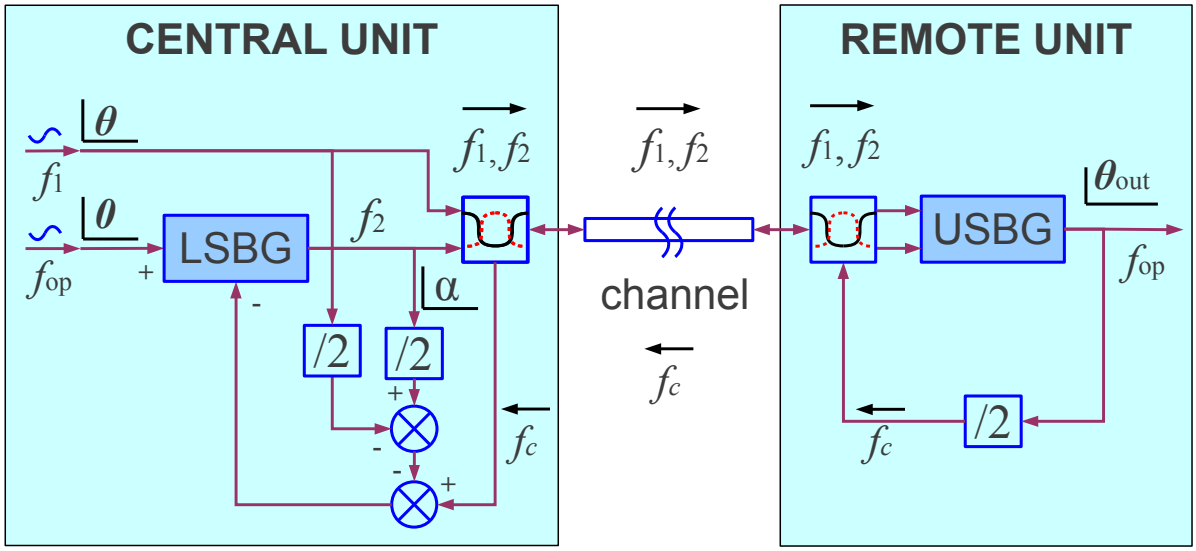

Figure 4.10: Flow diagram of the controlled tone generation with a reference carrier frequency of $f_{\text{op}} = 2f_c$ in the Central Unit.

used to implement the multiplexer then high time delay is introduced into the loop. If the filter delays are not taken into account, the synchronization scheme become the single carrier round loop of Section 4.4 as the loop bandwidth (given by f_m) tends to zero.

A practical complete synchronization loop was designed using the proposed conceptual scheme shown in Figure 4.10. For the implementation of the actual loop other factors must be analyzed. The first factor is determined by the time and phase delay induced by the components along the loop, and the stability of its behavior as a function of time. For some components this behavior is critical, must be well characterized and parameterized, and determines the performance of the complete loop. However, for other components this behavior is compensated in the closed loop inside each of the units.

The second factor to be analyzed is the phase acquisition behavior of the loop, understood as the loop ability to go from an initial state in which the phase condition of the closed loop are not fulfilled to a state in which the stable phase conditions are fulfilled. Stability and phase acquisition are issues widely studied in PLL literature for loops in which only one controlled oscillator is involved. Notwithstanding, the proposed synchronization loop has two different oscillators. Therefore, an extra analysis for the phase acquisition of the complete system must be done, and other subsystems must be

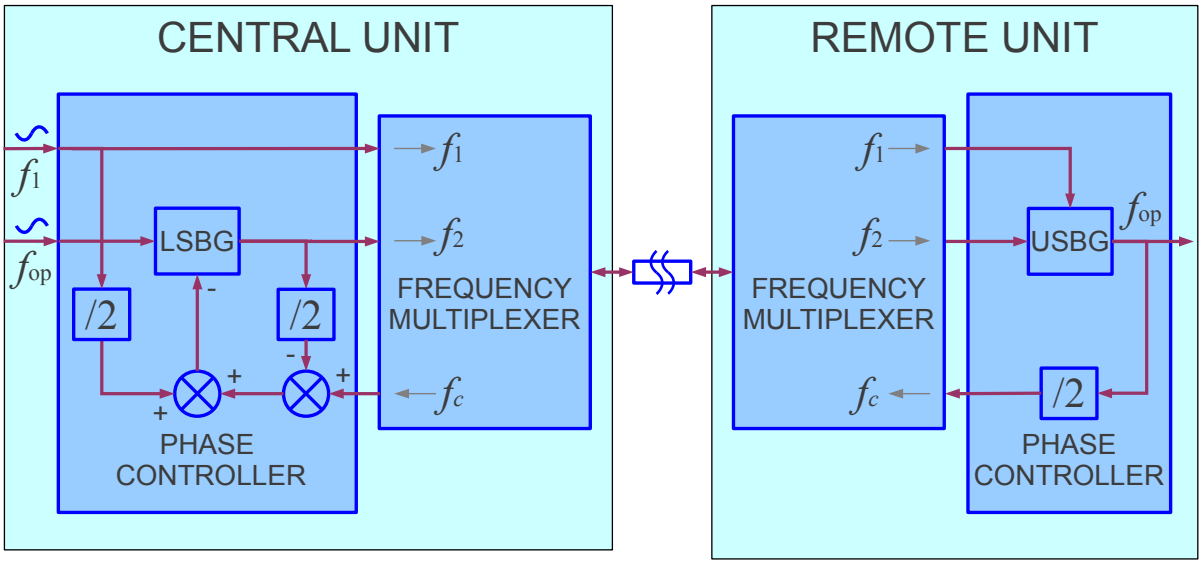

Figure 4.11: Simplified system scheme

designed to facilitate the acquisition process.

The proposed phase synchronization scheme can be simplified in a general scheme departing from the scheme presented in Figure 4.10. This simplified scheme is shown in Figure 4.11

4.5.3 Sideband generators implementation for the Dual Frequency Phase Synchronization Scheme

The proposed carrier phase synchronization scheme is based on two sideband active generators, the LSBG (Lower Side Band Generator) in the Central Unit and the USBG (Upper Side Band Generator) in the Remote Unit. Within the proposed design these block can be implemented with frequency-offset PLLs [39, 40]. In these circuits an input phase reference is followed and the output is shifted in frequency by another external input.

LSBG block in the Central Unit

A LSBG is a device used to obtain the phase difference between two inputs signals. In particular, The LSBG block used in the Central Unit, as shown in Figure 4.12, is implemented with a frequency offset PLL (OPLL, also called Frequency-Translation PLLs).

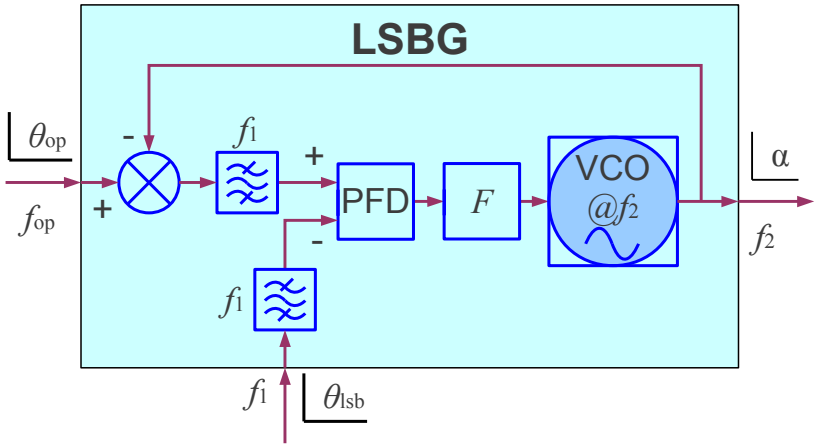

Figure 4.12: LSBG block implemented with an OPLL topology. (Used in Central Unit)

The block diagram within the Central Unit must be rearranged in such a way that the negative input to the LSBG is a tone with f_1 frequency and $-\alpha$ phase. The open loop transfer function in the LSBG is given by $G_o = K_d F(s) K_v / s$, where K_d is the constant of the phase detector, $F(s)$ is the loop filter transfer function and K_v is the constant associated to the VCO. In steady state, α, the output phase of the LSBG will be the phase difference $(\theta_{op} - \theta_{lsb})$. The characteristic equation of the output phase becomes

$$\alpha = (\theta_{op} - \theta_{lsb})\, G_L(s). \tag{4.50}$$

The transfer function $G_L(s)$ which is the closed loop transfer function for the LSBG, has an unitary magnitude response and is given by

$$G_L(s) = \frac{K_d F(s) K_v}{s + K_d F(s) K_v} = \frac{G_o(s)}{1 + G_o(s)} \tag{4.51}$$

where $G_o(s) = K_d F(s) K_v / s$ is the open loop transfer function of the LSBG.

USBG block in the Remote Unit

An USBG is used in the Remote Unit to add the phases of the two received tones. The output of the USBG will be used to generate another tone whose frequency is the average of the two first tones. This average is obtained dividing by two the frequency of the USBG output. This process is equivalent to recover the carrier of a AM double sideband

suppressed-carrier signal.

Similarly than the LSBG in the Central Unit, the USBG can be implemented by means of a OPLL. An USBG with a OPLL topology is shown in Figure 4.13. The transfer function of the USBG has also unitary response, and is given by

$$G_{\mathrm{U}}(s) = \frac{K_{\mathrm{d}} F'(s) K_{\mathrm{v}}}{s + K_{\mathrm{d}} F'(s) K_{\mathrm{v}}} = \frac{G'_{\mathrm{o}}(s)}{1 + G'_{\mathrm{o}}(s)} \tag{4.52}$$

where $F'(s)$ is the transfer function of the loop filter, and K_{d} and K_{v} are the constants associated to the PFD and the VCO, and $G'_{\mathrm{o}}(s) = K_{\mathrm{d}} F'(s) K_{\mathrm{v}}/s$ is the open loop transfer function in the USBG.

The values of K_{d} and K_{v} are not necessarily the same in the USBG than in the LSBG, thought they have the same symbols for simplicity of notation. In the Laplace transform domain, given that the two received phases are θ_{u1} and θ_{u2}, the output phase will be

$$\theta_{\mathrm{out}} = (\theta_{\mathrm{u1}} + \theta_{\mathrm{u2}})\, G_{\mathrm{U}}(s) \tag{4.53}$$

The USBG with the OPLL topology has some disadvantages that make its physical im-

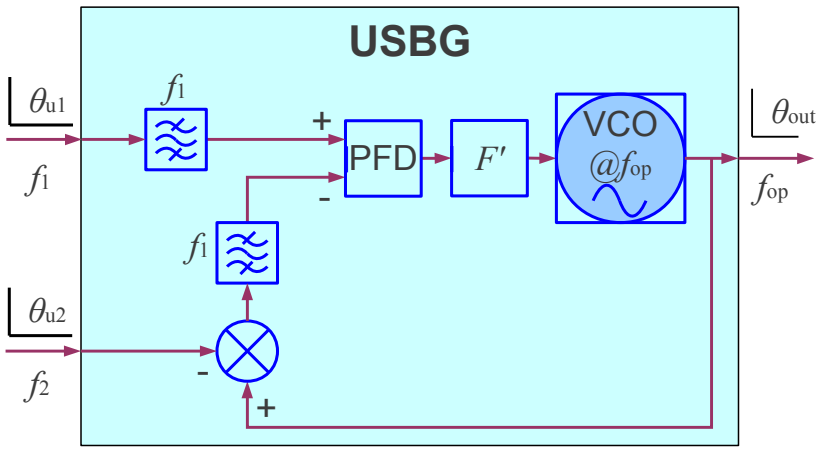

Figure 4.13: USBG block implemented with an OPLL topology. (Used in Remote Unit)

plementation impractical for this specific application. The most remarkable disadvantage is its lack of symmetry in the two received signal paths. The first received signal is taken directly to the PFD and the other signal is down-converted using a product-mixer. The mixer generates an attenuation that is not present in the first signal path, thereby the

power budget must be different for each transmitted tones. This requirement becomes more strict when the PFD has small power range of operation. Moreover, in practice the product-mixer is not a perfectly linear device and as a consequence its phase behavior depends on the amplitude of the received signal.

Other disadvantage of the OPLL topology for the USBG is that the PFD must work at the frequency of the first tone (f_1), which is similar to the carrier frequency, f_c which is typically higher than the maximum input frequency allowed by most of the PFDs, which are designed to work at relative low frequencies.

Therefore, a variation over the original topology is proposed to avoid the disadvantages of the direct OPLL topology. The modified receiver topology is based on Figure 4.14, which is a new topology different to the conventional OPLL, which down-converts separately both tones that arrive to the RU. Figure 4.14 shows the inputs θ_{u1} and θ_{u2},

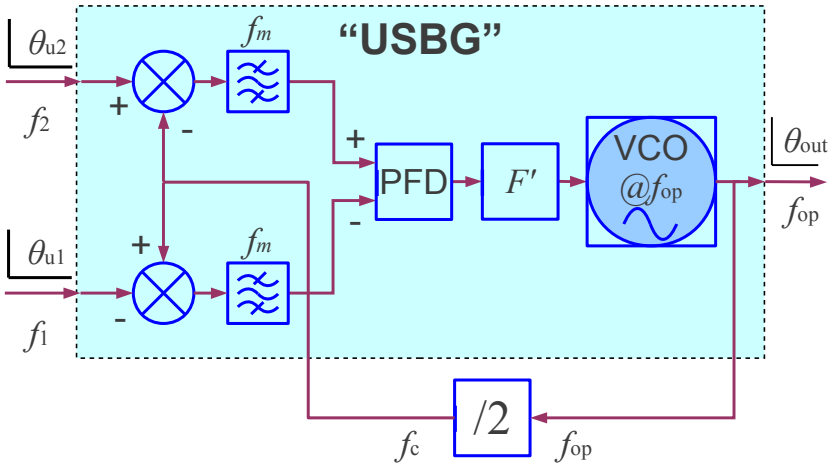

Figure 4.14: USBG functionality implemented with a symmetric down-conversion topology. (Used in Remote Unit. Note that $f_m = (f_2 - f_1)/2$)

which are the phases of the tones received by the Remote Unit, with frequencies f_1 and f_2, respectively. The phase of the low frequency down-converted signals will be $\theta_{out}/2 - \theta_{u1}$, and $\theta_{u2} - \theta_{out}/2$. If these phases are compared in the PFD, and the loop is closed then they will be equal, and θ_{out} will be $\theta_{u1} + \theta_{u2}$, which is equivalent to the output phase of an USBG.

The PLL equation for the symmetric down-conversion topology is

$$\theta_{\text{out}} = [(\theta_{\text{u2}} - \theta_{\text{out}}/2) - (\theta_{\text{out}}/2 - \theta_{\text{u1}})] \cdot K_{\text{d}} F'(s) K_{\text{v}} \tag{4.54}$$

Which is equivalent to

$$\theta_{\text{out}} = (\theta_{\text{u2}} + \theta_{\text{u1}}) \cdot \frac{K_{\text{d}} F'(s) K_{\text{v}}}{1 + K_{\text{d}} F'(s) K_{\text{v}}} = (\theta_{\text{u2}} + \theta_{\text{u1}}) \cdot G_{\text{U}}(s) \tag{4.55}$$

The phase transfer function for the VCO noise, $\theta_{\text{n-vco}}(s)$, is

$$\frac{\theta_{\text{out}}(\phi_{\text{n-vco}}(s))}{\phi_{\text{n-vco}}(s)} = \frac{s}{s + K_{\text{d}} F'(s) K_{\text{v}}} = \frac{1}{1 + G'_{\text{o}}(s)} \tag{4.56}$$

The Separated Down-Conversion presents strong advantages over the conventional OPLL, the most important one is that phase and amplitude fluctuations generated by the the frequency divider are inside the closed loop within the Remote Unit. So, the phase noise introduced in the $f_{\frac{\text{op}}{2}}$ path (frequency divider and $f_{\frac{\text{op}}{2}}$ amplification paths) is filtered by the low-pass transfer function G_{U}. The same will apply to the noise and phase variations generated in the f_{op} and within the Remote Unit. As a consequence, the high frequency phase noise components that are present in digital frequency dividers (typically digital) can be removed.

Another advantage is that the phase detection in the Separated Down-Conversion topology is performed at a significantly lower frequency. This frequency is half of the separation between the two tones which arrive to the Remote Unit ($(f_2 - f_1)/2$). The standard PFDs will have better noise performance working at these lower frequencies. Moreover, the phase variations generated by imbalances in the two input paths to the PFD are drastically reduced.

One step further in the implementation of a Separated Down-Conversion scheme may be the use of a VCO with double of the f_{op} frequency, and a frequency divider by four. Thus, there will be no need of an external frequency doubler in the final application in order the remove the π phase ambiguity that is proper to the phase synchronization systems (see Section 3.1).

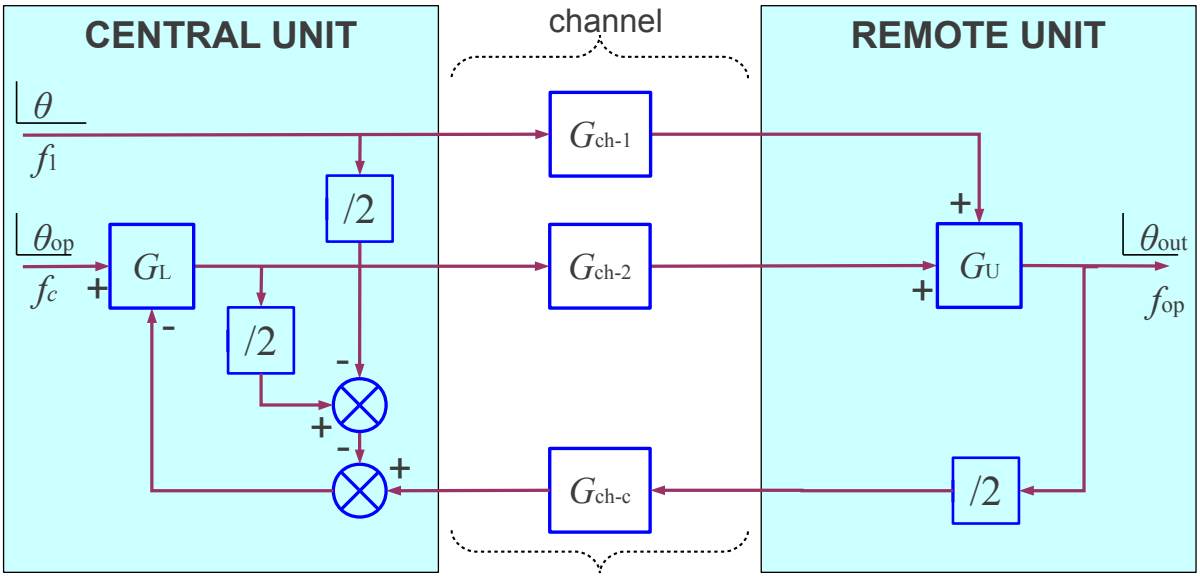

Figure 4.15: Simplified block diagram of the Dual Frequency CW Remote Phase Synchronization Scheme. The inputs for this block diagram are: the input phase reference θ_{op}, the modulating phase θ.

4.5.4 Phase Transfer Functions for the Dual Frequency Phase Synchronization Loop.

The phase transfer functions for the complete Dual Frequency Phase Synchronization Loop are obtained from the transfer function of the blocks in the Remote and Central Units and the blocks for the channel transfer functions. Figure 4.15 shows an equivalent block diagram for the complete loop. Here the transfer functions for the sideband generators are in the blocks labeled with G_{U} and G_{L}. A channel transfer function is given for each one of the single frequencies transmitted in the channel, f_1, f_2, and f_{c}, and are labeled consecutively $G_{\text{ch-1}}$, $G_{\text{ch-2}}$ and $G_{\text{ch-c}}$. These blocks are modeled by a constant time delay exactly as was done in Section 4.4.

Phase transfer functions of the complete loop for the input phases (θ_{op} and θ)

The inputs for this block diagram are the phases θ and θ_{op}. Here the phase noise inputs are not included and the frequency multiplexers are obviated.

The closed loop transfer function of the Central Unit includes the LSBG transfer function $G_{\mathrm{L}}(s)$ and the frequency divider, and is equal to

$$\frac{\alpha(\theta_{\mathrm{op}}(s))}{\theta_{\mathrm{op}}(s)} = \frac{2G_{\mathrm{L}}(s)}{2-G_{\mathrm{L}}(s)} = 2G_{\mathrm{C}}(s) \tag{4.57}$$

with

$$G_{\mathrm{C}}(s) = \frac{G_{\mathrm{L}}(s)}{2-G_{\mathrm{L}}(s)} \tag{4.58}$$

The complete phase transfer function, G_{op}, for the input phase reference θ_{op} is

$$\begin{aligned} G_{\mathrm{op}}(s) = \frac{\theta_{\mathrm{out}}(\theta_{\mathrm{op}}(s))}{\theta_{\mathrm{op}}(s)} &= \frac{2G_{\mathrm{C}}G_{\text{ch-2}}G_{\mathrm{U}}(s)}{1+2G_{\mathrm{C}}G_{\text{ch-c}}G_{\text{ch-2}}\dfrac{G_{\mathrm{U}}(s)}{2}} \\ &= \frac{2G_{\mathrm{C}}G_{\text{ch-2}}G_{\mathrm{U}}(s)}{1+G_{\mathrm{C}}G_{\text{ch-c}}G_{\text{ch-2}}G_{\mathrm{U}}(s)} \end{aligned} \tag{4.59}$$

And the complete phase transfer function, $G_{\theta}(s)$, for the modulating phase θ is

$$G_{\theta}(s) = \frac{\theta_{\mathrm{out}}(\theta(s))}{\theta(s)} = \frac{G_{\text{ch-1}}G_{\mathrm{U}}(s) - G_{\text{ch-2}}G_{\mathrm{C}}(s)}{1+G_{\mathrm{C}}G_{\text{ch-2}}G_{\text{ch-c}}G_{\mathrm{U}}(s)} \tag{4.60}$$

These equations have been found using the characteristic denominator of the complete loop, which is

$$D(s) = 1 + G_{\mathrm{C}}G_{\text{ch-c}}G_{\text{ch-2}}G_{\mathrm{U}}(s) \tag{4.61}$$

The objective in the design of complete loop is maintain the output phase equal to the input phase θ_{op} and independent of the modulating phase θ.

The transfer function $G_{\mathrm{op}}(s)$ will have an unitary response if the equations of the sideband generators G_{L} and G_{U} have both unitary responses. The transfer function of the complete loop has a low-pass response with a bandwidth given by the minimum bandwidth between the bandwidths of G_{L} and G_{U}. The transfer function for $G_{\theta}(s)$ does not present a low-pass response, and its shape will be determined by G_{L} and G_{U}. Figure 4.16 sketches this response for idealized low-pass transfer functions of G_{L} and G_{U}. In

this case the responses are one within the bandwidth and zero outside of the bandwidth. Under these conditions, and assuming that the channel has an unitary response, then the response $G_\theta(s)$ will be one for a segment of frequencies if the bandwidth of G_L is lower than the bandwidth of G_U. Thus, this response will be zero for all frequencies if the bandwidth of G_L is greater than the bandwidth of G_U, whereupon the effects of the modulating phase θ are canceled as desired.

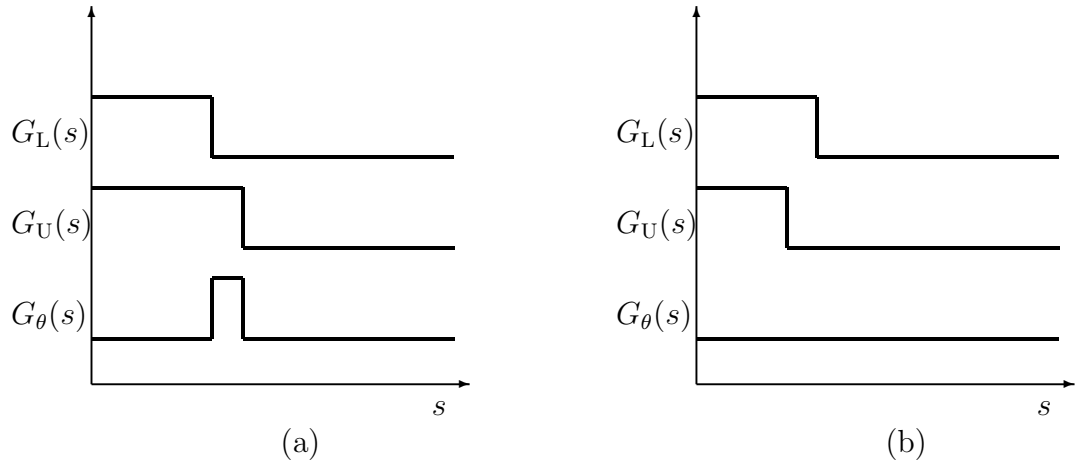

Figure 4.16: Idealized transfer function for the input phase θ to the output phase of the complete loop. (a). The bandwidth of G_L is lower than the bandwidth of G_U. (b). The bandwidth of G_L is greater than the bandwidth of G_U.

The idealized model helps to understand the behavior of the complete loop, however the actual system should be modeled with the non-ideal transfer functions for the G_L and G_U blocks.

The first candidate for the PLL implementation of the sideband generators is the second-order Type-2 PLL. For various reasons Type-2 this is the most popular PLL configuration [8, 39, 40]. The type in a PLL configuration refers to number of integrators within the loop. Type-2 PLLs contain two integrators one in the loop filter and the other in the VCO. The most important advantage of this configuration is that the steady state phase error is zero with relatively small loop gains. This is a crucial feature for a remote phase synchronization application. In addition, second-order Type-2 PLLs are stable for all values of loop gain [8, 39, 40].

The system transfer function for a second-order Type-2 PLL is

$$G(s) = \frac{2\zeta\omega_n s + \omega_n^2}{s^2 + 2\zeta\omega_n s + \omega_n^2}. \tag{4.62}$$

where ω_n is the natural frequency response of the loop and ζ is the damping factor. For conventional PLLs, values of ζ typically lie between 0.5 and 2. The chosen value for ζ determines the loop transient response.

In the following, the transfer functions G_{L} and G_{U} are modeled with a second-order Type-2 transfer function, with a damping factor of $\zeta = 1$.

The transfer functions for the complete loop are analyzed with the frequency variable normalized to the natural frequency w_n. Thus, $G_{\mathrm{L}}(s)$ is

$$G_{\mathrm{L}}(s) = \frac{2\omega_n s + \omega_n^2}{s^2 + 2\omega_n s + \omega_n^2} \tag{4.63}$$

The transfer function $G_{\mathrm{U}}(s)$ has the same expression with another natural frequency ω_{u}, and can be written as

$$G_{\mathrm{U}}(s) = \frac{\omega_{\mathrm{u}} s + \omega_{\mathrm{u}}^2}{s^2 + 2\omega_{\mathrm{u}} s + \omega_{\mathrm{u}}^2} \tag{4.64}$$

The magnitude responses of $G_\theta(s)$, and $G_{\mathrm{op}}(s)$ are plotted in Figure 4.17. The channel transfer functions $G_{\text{ch-1}}(s)$, $G_{\text{ch-2}}(s)$ and $G_{\text{ch-c}}(s)$ are modeled with a constant delay function.

This function, for a time delay τ_d, becomes $e^{-s\cdot\tau_d}$ in the Laplace domain. The τ_d value used for the subsequent plotting is $\omega_n/5$.

The $G_\theta(s)$ and $G_{\mathrm{op}}(s)$ frequency responses are evaluated for two different values of ω_{u}. In the first case this value is twice the natural frequency ω_n and in the second case this value is the half of ω_n.

Figure 4.17 shows how the undesired effects of $G_\theta(s)$ over the output are increased when the bandwidth of $G_{\mathrm{U}}(s)$ is greater than the bandwidth of $G_{\mathrm{L}}(s)$. In particular, the maximum gain of $G_\theta(s)$ is 5.6 dB when the natural frequency of $G_{\mathrm{U}}(s)$ is twice ω_n. Whereas in the second case this gain is reduced to 0.8 dB.

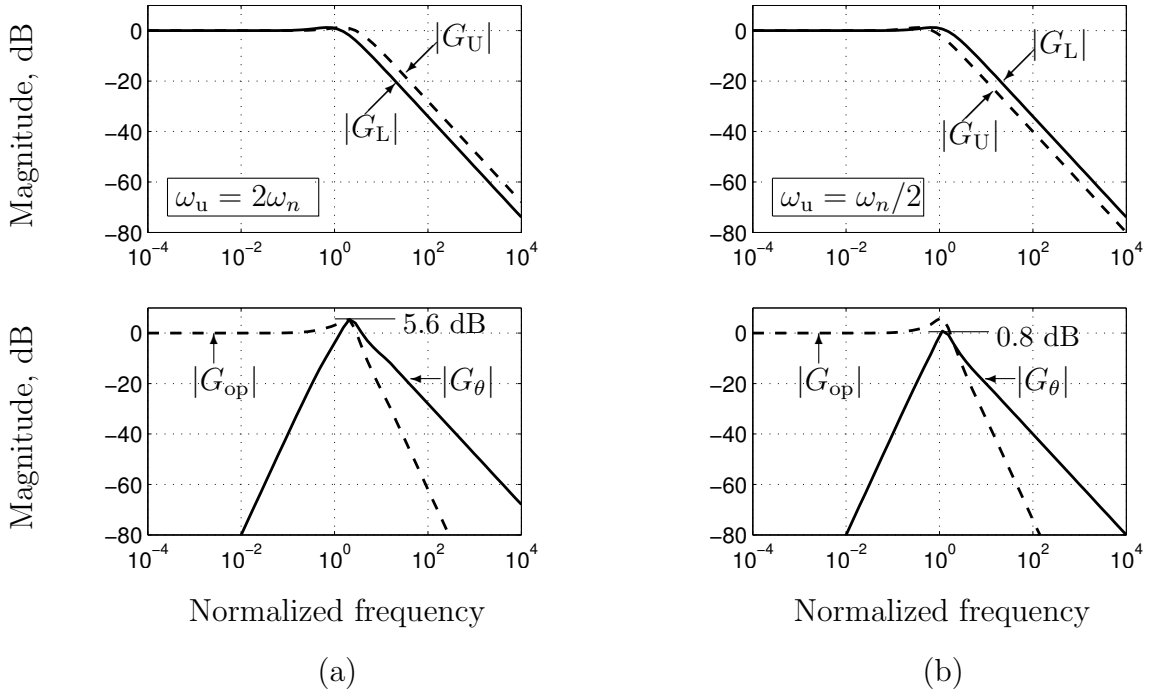

Figure 4.17: Magnitude response of the transfer function of the complete synchronization loop, $|G_{\mathrm{op}}(j\omega)|$ and $|G_{\theta}(j\omega)|$. The frequency is normalized to ω_n. (a). The normalized natural frequency of G_{U} is 2. (b).The normalized natural frequency of G_{U} is 0.5.

The $G_{\mathrm{op}}(s)$ and $G_{\theta}(s)$ responses are also evaluated for ω_{u} values of 1/4 and 1/8 times the natural frequency ω_n, and are plotted in Figure 4.18. Here can be seen how the maximum gain of $G_{\theta}(s)$ is reduced when the bandwidth of $G_{\mathrm{U}}(s)$ is reduced.

Another important analysis that must be done for the transfer functions $G_{\mathrm{op}}(s)$ and $G_{\theta}(s)$ is to quantify the effects of increasing the time delay τ_d associated to the channel. Figure 4.19 plots the responses of $G_{\mathrm{op}}(s)$ and $G_{\theta}(s)$ for various time delay values, specifically 1, 2, 4, and 8 times the natural time response $1/\omega_n$. All plots in Figure 4.19 are analyzed with $\omega_{\mathrm{u}} = \omega_n/2$. From there it can be said that the loop transfer function begins to degrade when the delay is equal or greater than $1/\omega_n$. In these cases the functions $G_{\mathrm{op}}(s)$ and $G_{\theta}(s)$ have an overshoot response, surpassing the zero gain limit, wherewith the effects of the modulating phase θ are increased.

An important parameter of the transfer function $G_{\theta}(s)$ is its steady state response for a given parametric input on $\theta(s)$. For a phase step input, with an unitary amplitude

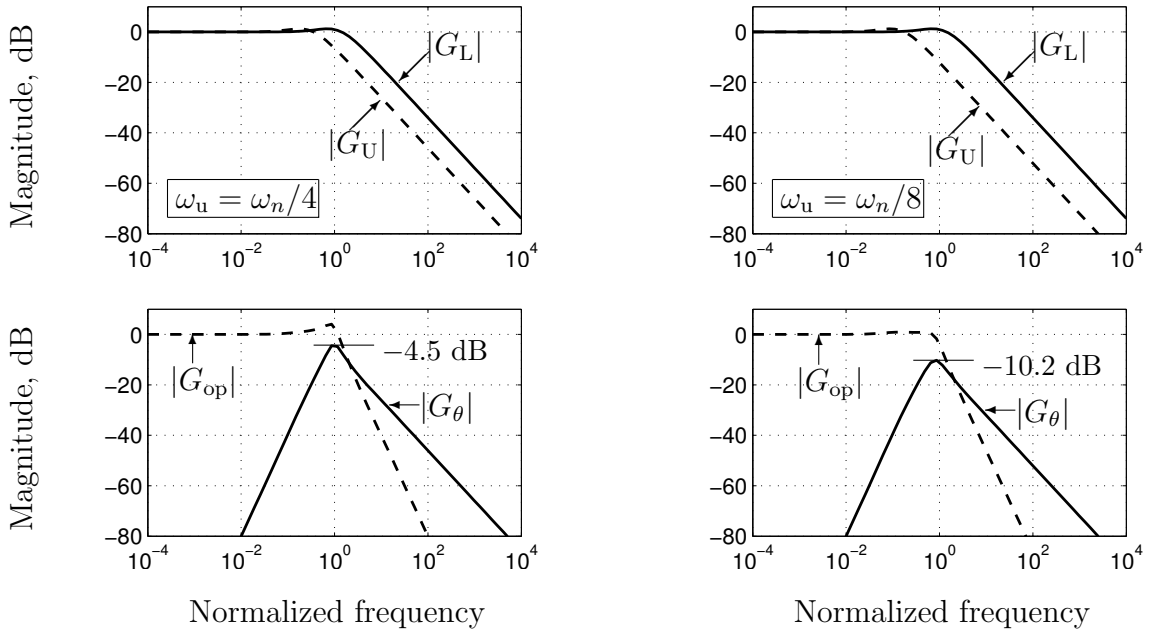

Figure 4.18: Magnitude response of the transfer function of the complete synchronization loop, $|G_{\mathrm{op}}(j\omega)|$ and $|G_\theta(j\omega)|$. The frequency is normalized to ω_n. (a).The normalized natural frequency of G_{U} is 1/4. (b).The normalized natural frequency of G_{U} is 1/8.

(with Laplace transform $1/s$) the steady state response is found to be

$$\lim_{t\to\infty} \theta_{\mathrm{out}}(\theta(t)) = \lim_{s\to 0} s \cdot \left(\frac{1}{s} \cdot G_\theta(s)\right) = \lim_{s\to 0} G_\theta(s) \tag{4.65}$$

Then using the Equation 4.60, and replacing the expressions G_{C}, G_{U}, $G_{\text{ch-1}}$ and $G_{\text{ch-2}}$, it is obtained directly that the steady state phase output is zero for a step input phase.

Similarly, the steady state output to a phase ramp input ($\theta(s) = 1/s^2$) will be equal to

$$\lim_{t\to\infty} \theta_{\mathrm{out}}(\theta(t)) = \lim_{s\to 0} s \cdot \left(\frac{1}{s^2} \cdot G_\theta(s)\right) = \lim_{s\to 0} \left(\frac{G_\theta(s)}{s}\right) \tag{4.66}$$

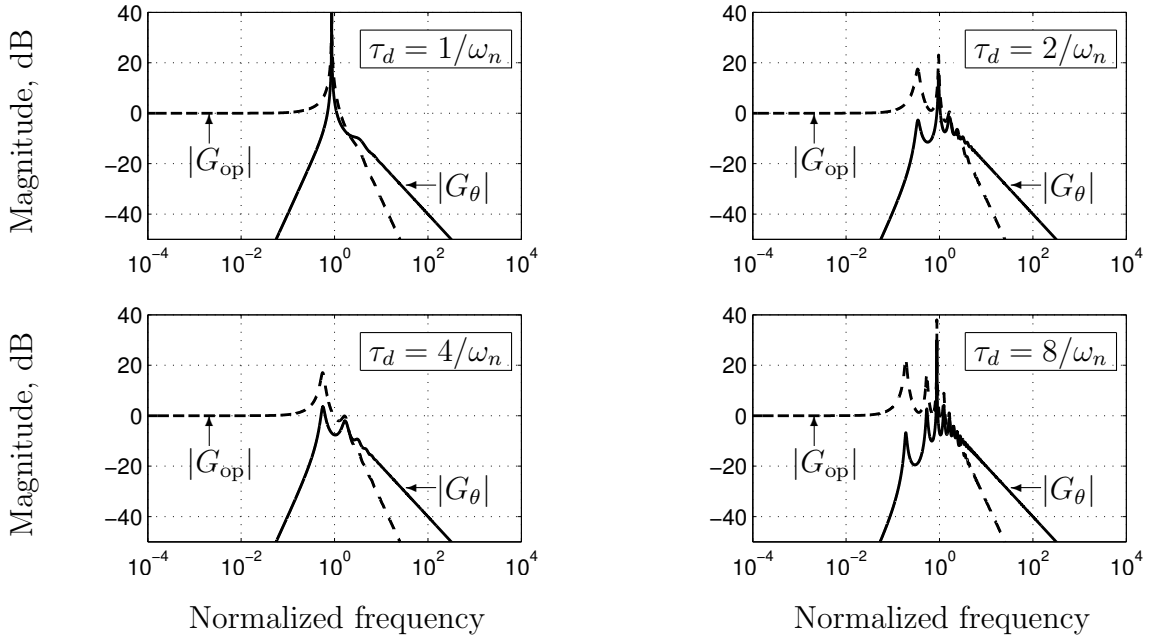

Figure 4.19: Magnitude response of the transfer functions $|G_{\text{op}}(j\omega)|$ and $|G_\theta(j\omega)|$ of the complete synchronization loop for different channel delays τ_d. The frequency is normalized to ω_n and $\omega_{\text{u}} = \omega_n/2$ for all plots

Under the assumption that $G_{\text{ch-1}} = G_{\text{ch-2}}$, the Equation 4.66 can be rewritten as

$$\begin{aligned}
\lim_{t\to\infty} \theta_{\text{out}}(\theta(t)) &= \lim_{s\to 0} \frac{G_{\text{U}} G_{\text{ch-1}} (1 - G_{\text{C}})}{sD(s)} = \lim_{s\to 0} \frac{1 - \dfrac{G_{\text{L}}}{2 - G_{\text{L}}}}{2s} \\
&= \lim_{s\to 0} \frac{1 - G_{\text{L}}}{s(2 - G_{\text{L}})} = \lim_{s\to 0} \frac{(s^2 + 2\omega_n s + \omega_n^2) - (2\omega_n s + \omega_n^2)}{s(2 - G_{\text{L}})(s^2 + 2\omega_n + \omega_n^2)} \qquad (4.67) \\
&= \lim_{s\to 0} \frac{s^2}{s(2 - G_{\text{L}})(s^2 + 2\omega_n s + \omega_n^2)} = 0
\end{aligned}$$

Thus the phase error generated by a ramp in the ancillary modulating phase θ will be negligible in steady state. Figure 4.20 illustrates the time response in θ_{out} to various parametric inputs in $\theta(s)$.

It would be also interesting to evaluate the response to a parabolic phase input (equiv-

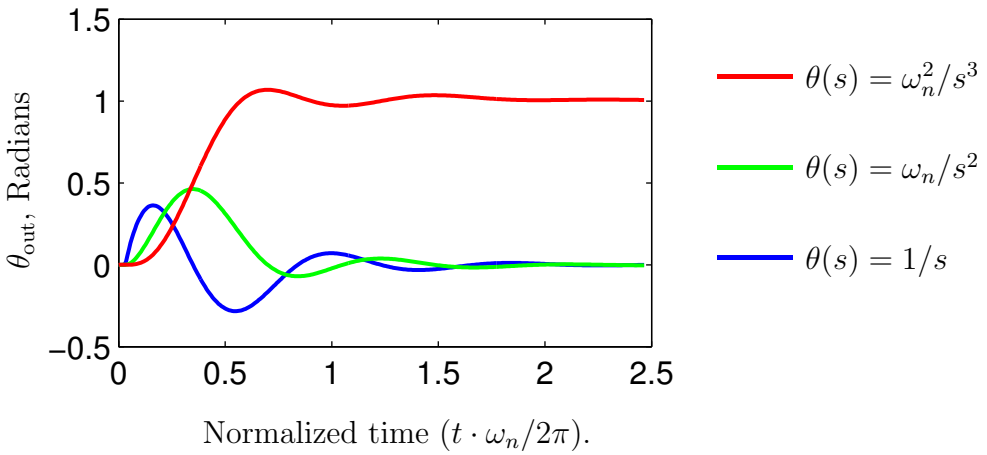

Figure 4.20: Time response of the output phase in complete loop (G_θ) to different parametric θ inputs. Step with 1 Radian amplitude ($1/s$). Ramp with ω_n Radians per second (ω_n/s^2). Parabolic input with ω_n^2 Radians per square second, (ω_n^2/s^3). For all plots $\omega_{\text{u}} = 1/2\omega_n$ and $\tau_d = 1/5\omega_n$.

alent to FM). In this case the phase error in the output will not be neglected in steady state and will be proportional to $1/\omega_n^2$. This steady state input can be eliminated if the the second order PLL in the Central Unit is replaced with a higher order loop. Although, this consideration in not in the scope of the current design, it can be considered in future applications. The modulation of the phase θ with a parabolic shape or other shapes can add new features to the conventional synchronization loop. For example, some clock-distribution systems use spread spectrum techniques in order to reduce EMI effects [50, 51].

Phase transfer function of the complete loop for the channel phase offset (ϕ)

The system response to the channel phase offset is required to analyze the behavior of the synchronization loop for the variations of the channel length.

For this purpose, the channel is characterized with the same model that was used in the Single Carrier CW loop in Section 4.4.

Figure 4.21 show a system diagram whose inputs are the phase delay introduced by the channel at the frequencies f_1, f_2 and f_{c}. This Figure shows three inputs nodes at the channel ends for each transmitted frequency. Each input has two terms, the first

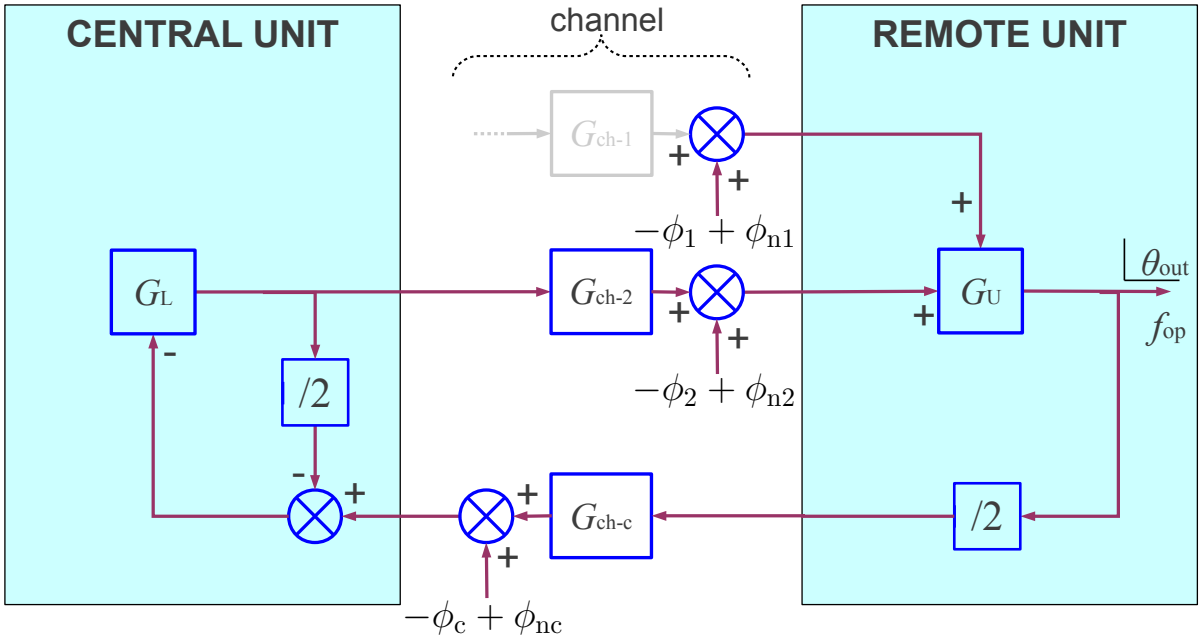

Figure 4.21: Block diagram of the Single Carrier CW Remote Phase Synchronization Scheme. The inputs for this block diagram are: the input phase reference θ_{in}, the phase noise and phase delay added in two points of the channel $-\phi + \phi_{n1}, -\phi + \phi_{n2}$, and the phase noise added by the VCO, $\phi_{n\text{-}vco}$.

term is the deterministic phase offset introduced by channel delay and the second term is the random channel phase noise. For instance, in the first node the deterministic phase input is $-\phi_1$ and the phase noise input is ϕ_{n1}. The three phase noise inputs, ϕ_{n1}, ϕ_{n2}, and ϕ_{nc} are uncorrelated, whereas the phase offsets ϕ_1, ϕ_2, and ϕ_c depend linearly on the electrical length of the channel (this linearity is perfect if the channel is completely non-dispersive).

The transfer functions for the first two nodes are

$$G_{\phi 1}(s) \;=\; G_{\phi 2}(s) \;=\; \frac{G_U(s)}{D(s)} = \frac{G_U(s)}{1 + \dfrac{G_L}{2 - G_L} G_{ch\text{-}c} G_{ch\text{-}2} G_U(s)} \tag{4.68}$$

And the transfer function for the node of the received feedback signal in the Central Unit

(frequency f_c) is

$$G_{\phi c}(s) = \frac{\frac{2G_L}{2-G_L}G_{\text{ch-2}}G_U(s)}{D(s)} = \frac{\frac{-2G_L}{2-G_L}G_{\text{ch-2}}G_U(s)}{1+\frac{G_L}{2-G_L}G_{\text{ch-c}}G_{\text{ch-2}}G_U(s)} \tag{4.69}$$

Equations 4.68 and 4.69 are required to quantify the impact of the phase noise generated by the attenuation and the thermal noise present in the channel. However it is also important to determine the transfer function for a deterministic phase offset.

Now the phase input ϕ is used, with $\phi = 2\pi\tau_d f_c$. Thereby the phase inputs are

$$\begin{aligned} \phi_1 &= \phi\left(1-\frac{f_c-f_1}{f_c}\right) \\ \phi_2 &= \phi\left(1+\frac{f_2-f_c}{f_c}\right) \\ \phi_c &= \phi \end{aligned} \tag{4.70}$$

Wherewith, the output phase as a function of ϕ is

$$\begin{aligned} \theta_{\text{out}}(\phi(s)) &= -\phi_1 G_{\phi 1}(s) - \phi_2 G_{\phi 2}(s) - \phi_c G_{\phi c}(s) \\ &= -\phi\left(1-\frac{f_c-f_1}{f_c}\right)G_{\phi 1}(s) - \phi\left(1-\frac{f_2-f_c}{f_c}\right)G_{\phi 1}(s) - \phi G_{\phi c}(s) \\ &= \phi\cdot(-2G_{\phi 1}(s) - G_{\phi c}(s)) \end{aligned} \tag{4.71}$$

And the transfer function $G_\phi(s)$ for the input $\phi(s)$ is

$$G_\phi(s) = \frac{\theta_{\text{out}}(\phi(s))}{\phi(s)} = -2G_{\phi 1}(s) - G_{\phi c}(s) = \frac{-2G_U(s)\left(1-G_C G_{\text{ch-2}}(s)\right)}{1+G_C G_{\text{ch-c}} G_{\text{ch-2}} G_U(s)} \tag{4.72}$$

Figure 4.22 shows the frequency response of the transfer functions $G_{\phi c}(s)$, $G_{\phi 1}(s)$ (equal to $G_{\phi 2}(s)$), and $G_\phi(s)$, for a loop working with a time delay τ_d equal to one fifth of the characteristic natural time response $1/\omega_n$, and with ω_u equal to one half of ω_n. The response of $G_\phi(s)$ has a passband behavior with a peak response close to the natural frequency ω_n. This peak is reduced (as happens with the peak response of G_θ) when the bandwidth of G_U is reduced in comparison to the bandwidth of G_U.

The transfer function $G_\phi(s)$ has the same form that the channel offset transfer function

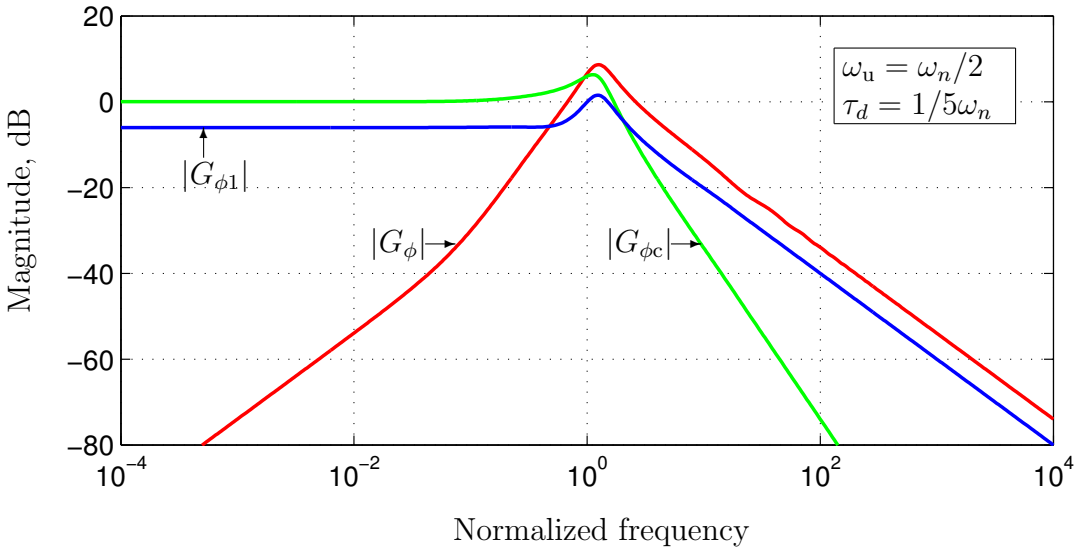

Figure 4.22: Frequency response of the transfer functions for the channel phase variations ϕ. For this set of plots $\omega_u = \omega_n/2$ and $\omega_u = 1/5\omega_n$.

of the single carrier synchronization of Section 4.4 (Equation 4.21). Similarly, the steady state phase output is reduced to zero for a phase step input, and τ_d for a unitary phase ramp input.

Complete loop transfer functions for the VCOs phase noises

The impact of the VCO phase noises on the output phase is obtained by means of the characteristic denominator of the complete loop. Figure 4.23 shows the two inputs nodes to the phase noise generated in the two VCOs. The phase noise generated in the Central Unit in the LSBG is labeled as $\phi_{\text{n-vcoL}}$, and the phase noise generated in the Remote Unit in the USBG is labeled as $\phi_{\text{n-vcoU}}$.

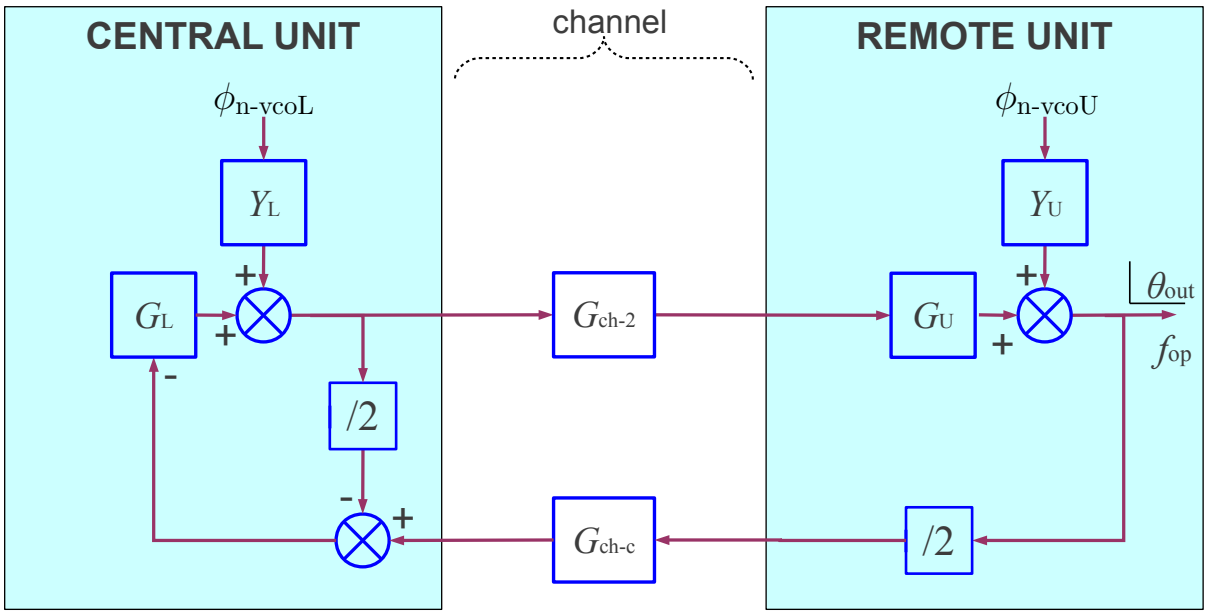

Figure 4.23: Block diagram of the Phase Synchronization Loop adapted to the VCO phase noise inputs. The inputs signals are: $\phi_{\text{n-vcoL}}$ which is the phase noise generated in the VCO of the LSBG, and $\phi_{\text{n-vcoU}}$ which is the phase noise generated in the VCO of the USBG.

The output/input relations for the input VCOs noise to the noise seen at the output of the sideband generators are labeled with Y_{L} and Y_{U}. These functions are equal to

$$Y_{\text{L}} = \frac{1}{1 + G_{\text{o}}(s)} \tag{4.73}$$

and

$$Y_{\text{U}} = \frac{1}{1 + G'_{\text{o}}(s)} \tag{4.74}$$

Where $G_{\text{o}}(s)$ an $G'_{\text{o}}(s)$ are the PLL open loop gains of the LSBG and USBG respectively, as defined in Section 4.5.3

The complete loop transfer functions are

$$G_{\text{n-vcoL}}(s) = \frac{\theta_{\text{out}}(\phi_{\text{n-vcoL}}(s))}{\phi_{\text{n-vcoL}}(s)} = \frac{Y_{\text{L}}(s)\dfrac{2}{2 - G_{\text{L}}(s)} G_{\text{ch-2}} G_{\text{U}}(s)}{D(s)} \tag{4.75}$$

And

$$G_{\text{n-vcoU}}(s) = \frac{\theta_{\text{out}}(\phi_{\text{n-vcoU}}(s))}{\phi_{\text{n-vcoU}}(s)} = \frac{Y_{\text{U}}(s)}{D(s)} \tag{4.76}$$

The functions $Y_{\text{L}}(s)$ and $Y_{\text{U}}(s)$ have a high-pass frequency response. Then, consequently $G_{\text{n-vcoU}}$ will have a high-pass response given by the factor $Y_{\text{U}}(s)$. Whereas, the function $G_{\text{n-vcoL}}$(s) will have a passband frequency response with a peak gain near to the loop natural frequency response. Thus, the impact of the high frequency VCO phase noise in the central unit is reduced in the complete loop. The frequency response of these transfer function is plotted in Figure 4.24.

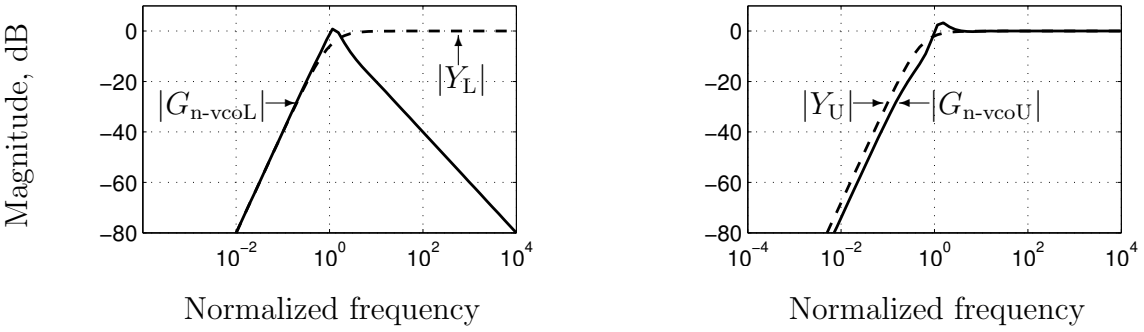

Figure 4.24: Magnitude response of the transfer functions for the phase noise generated in the VCOs. $|Y_{\text{L}}(j\omega)|$, $|G_{\text{n-vcoL}}(j\omega)|$, $|Y_{\text{U}}(j\omega)|$, and $|G_{\text{n-vcoU}}(j\omega)|$. The frequency is normalized to ω_n. For all plots $\omega_{\text{u}} = 1/2\omega_n$ and $\tau_d = 1/5\omega_n$.
.

4.5.5 Dynamic Stability Analysis for the Dual Frequency Phase Synchronization Scheme

The dynamic stability is determined, as explained in Section 4.4.1, using the characteristic denominator of the closed loop transfer function, $D(s)$.

The poles of the complete system are the roots of the characteristic equation

$$D(s) = 1 + G_{\text{C}}G_{\text{U}}G_{\text{ch-c}}G_{\text{ch-2}}(s) = 0 \tag{4.77}$$

From the Bode stability analysis, the system will be stable if the phase lag of the complete

system open loop gain

$$G_{\mathrm{C}}G_{\mathrm{U}}G_{\text{ch-c}}G_{\text{ch-2}}(s) \tag{4.78}$$

is less than 180° at the gain crossover frequency (0 dB). This criterion is valid if all the functions G_{L}, $G_{\text{ch-c}}$, $G_{\text{ch-2}}$, and G_{U} are stable.

These conditions are easily fulfilled because the channel transfer functions are stable, and have a unitary magnitude response for all frequencies. Both channel transfer functions can be modeled with the same delay τ_d, if the dispersive effects of the channel are not taken into account. Thus the channel transfer functions are

$$G_{\text{ch-c}} = G_{\text{ch-2}} = e^{-s\tau_d} \tag{4.79}$$

Moreover, G_{U}, which is the transfer function of a second-order Type-2 PLL, is unconditionally stable for every open loop gain configuration.

Finally, G_{C} will be stable if G_{L} is stable, and G_{L} is also a second-order Type-2 PLL, which will always be stable. The equation of G_{C} resembles also another second-order Type-2 PLL transfer function, whose natural frequency, $\omega_{\mathrm{c}} = (\sqrt{2}/2) \cdot \omega_n$, where ω_n is the natural frequency of G_{L}. While the damping factor of G_{C} is $\sqrt{2}/2$.

Then, the stability of the complete system can be determined with the gain crossover frequency of $G_{\mathrm{C}}G_{\mathrm{U}}(s)$ because the delays have no influence on the magnitude gain of the open loop transfer function of the complete system.

The 0 dB crossover frequency of every second-order Type-2 PLL transfer function is equal to $\sqrt{2}$ times its natural frequency and is independent of its damping factor. Bode plots for $G_{\mathrm{C}}(j\omega)$, $G_{\mathrm{U}}(j\omega)$ and $G_{\mathrm{C}}G_{\mathrm{U}}(j\omega)$ are plotted in Figure 4.25 ($s = j\omega$). Here it can be seen the 0 dB crossover frequencies for G_{U} and G_{C} which are $\sqrt{2}\omega_{\mathrm{u}} = (\sqrt{2}/2) \cdot \omega_n$ and $\sqrt{2}\omega_{\mathrm{c}} = \omega_n$ respectively, given that $\omega_{\mathrm{c}} = (\sqrt{2}/2) \cdot \omega_n$ and $\omega_{\mathrm{u}} = \omega_n/2$. The 0 dB crossover frequency for $G_{\mathrm{C}}G_{\mathrm{U}}$ is found to be

$$\omega_{\text{gxo}} = \sqrt{\omega_{\mathrm{u}}^2 + \omega_{\mathrm{c}}^2} = \sqrt{\frac{3}{4}}\omega_n \tag{4.80}$$

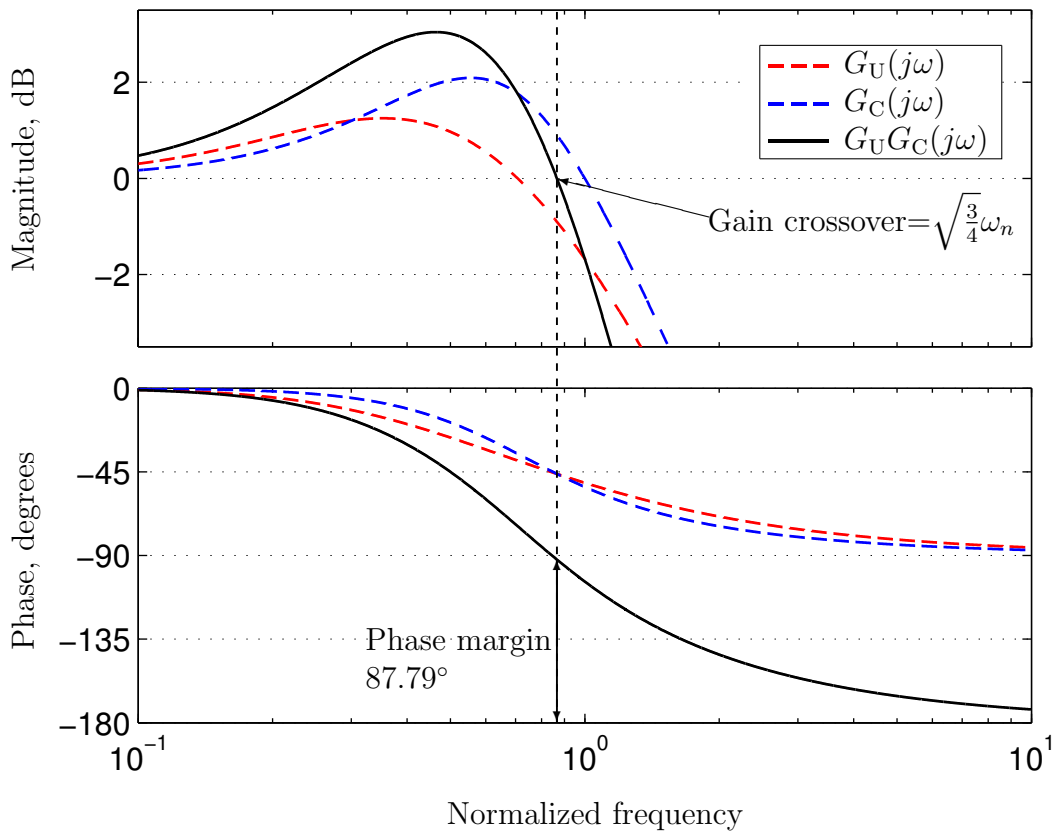

Figure 4.25: Bode plots for $G_C(j\omega)$, $G_U(j\omega)$, and $G_CG_U(j\omega)$ for the stability analysis of the stability of the complete phase synchronization loop. The frequency is normalized to ω_n. ($\omega_u = \omega_n/2$).

The phase lag of G_C and G_U at the 0 dB gain crossover frequency is found to be -46.1 degrees for both transfer functions. Thus the total phase lag of G_CG_U is equal to -92.2 degrees. Wherewith, the phase margin left for the 2-way channel delay, for a stable system is 87.79 degrees.

The 2-way phase delay generated by the function $G_{\text{ch-c}}G_{\text{ch-2}}$ is, in radians, a linear function of frequency given by $2\omega\tau_d$. Thus the maximum tolerable delay, $\tau_{\text{d-max}}$ in a stable system is determined by

$$\begin{aligned} 2\omega_{\text{gxo}}\tau_{\text{d-max}} &= 87.79 \cdot \pi/180 \\ \tau_{\text{d-max}} &= 3.53/\omega_n \end{aligned} \tag{4.81}$$

The only tunable value used to obtain this result is the ratio of the natural frequencies of ω_n and ω_u than in this case is 2. In fact if this ratio is increased then the crossover

frequency is decreased and as a consequence the maximum tolerable delay is increased. For a practical example, if the value of ω_n is $2\pi \cdot 200$ KHz, which is typical value in a conventional PLL, then the maximum allowable 1-way time delay will be 2.8 microseconds, which is equivalent to a maximum distance of 0.84 km for free space propagation.

4.5.6 Signal Quality Analysis of the Complete Loop

One important characteristic of the proposed Phase Synchronization Scheme the ability of to cope with the additive noise introduced in the transmission channel and other nodes among the loop.

The impact of the additive noise is quantified by the transfer functions for the input phases $\phi_{\mathrm{n1}}, \phi_{\mathrm{n2}}$ and ϕ_{nc}, which are respectively $G_{\phi 1}, G_{\phi 2}$, and $G_{\phi \mathrm{c}}$, as explained previously.

The variance of the phase output of the complete loop θ_{out} associated to the ϕ_{n1} input is

$$\begin{aligned}\sigma^2_{\theta \mathrm{out}}(\phi_{\mathrm{n1}}) =& \int_{-\infty}^{\infty} S_{\phi \mathrm{n1}}(f) \ |G_{\phi 1}(f)|^2 \ df \\ =& 2\int_{0}^{\infty} S_{\phi \mathrm{n1}}(f) \ |G_{\phi 1}(f)|^2 \ df \\ =& \frac{N_0 L^2}{P_{\mathrm{T1}}} \int_{0}^{\infty} |G_{\phi 1}(f)|^2 \ df\end{aligned} \tag{4.82}$$

where $S_{\phi \mathrm{n1}}(f) = N_0 L^2 / 2P_{\mathrm{T1}}$ is the power spectral density of the input phase ϕ_{n1}, P_{T1} is the transmitted power, and the symmetry of the spectrum was used. This procedure is also valid for the inputs ϕ_{n2}, and ϕ_{nc}. The integrals

$$\int_{0}^{\infty} |G_{\phi 1}(f)|^2 \ df, \quad \int_{0}^{\infty} |G_{\phi 2}(f)|^2 \ df, \quad \text{and} \quad \int_{0}^{\infty} |G_{\phi \mathrm{c}}(f)|^2 \ df \tag{4.83}$$

define the noise bandwidth for each of the noise inputs. The magnitude response within the loop bandwidth are approximately 0.5. for $G_{\phi 1}$, and $G_{\phi 2}$ and one for $G_{\phi \mathrm{c}}$, as seen in Figure 4.22. Then, for a given loop bandwidth BW, the noise bandwidth is simplified as 0.25BW for $|G_{\phi 1}(f)|$ and $|G_{\phi 2}(f)|$ and 1BW for $|G_{\phi \mathrm{c}}(f)|$.

The total output phase variance for the channel noise inputs of the complete loop $\sigma^2_{\theta\text{out}}(\phi_{\text{n1}}, \phi_{\text{n2}}, \phi_{\text{nc}})$ is equal to the addition of all variances of the outputs associated to each input, given that all inputs are uncorrelated. Thus

$$\sigma^2_{\theta\text{out}}(\phi_{\text{n1}}, \phi_{\text{n2}}, \phi_{\text{nc}}) \;=\; \sigma^2_{\theta\text{out}}(\phi_{\text{n1}}) + \sigma^2_{\theta\text{out}}(\phi_{\text{n2}}) + \sigma^2_{\theta\text{out}}(\phi_{\text{nc}}). \tag{4.84}$$

If it is assumed that the channel attenuation L for at the frequency f_{c} is equal for the three tones (they have similar frequencies) then the total output phase variance is

$$\sigma^2_{\theta\text{out}}(\phi_{\text{n1}}, \phi_{\text{n2}}, \phi_{\text{nc}}) = \frac{N_0 L^2}{P_{\text{T1}}} \cdot 0.25\text{BW} + \frac{N_0 L^2}{P_{\text{T2}}} \cdot 0.25\text{BW} + \frac{N_0 L^2}{P_{\text{Tc}}} \cdot \text{BW} \tag{4.85}$$

For a given total transmitted power, $P_{\text{TT}} = P_{\text{T1}} + P_{\text{T2}} + P_{\text{Tc}}$, the values that minimizes the total output phase variance are $P_{\text{T1}} = P_{\text{T2}} = 0.25P_{\text{TT}}$, and $P_{\text{Tc}} = 0.5P_{\text{TT}}$. Wherewith the output variance becomes

$$\sigma^2_{\theta\text{out}}(\phi_{\text{n1}}, \phi_{\text{n2}}, \phi_{\text{nc}}) = \frac{4N_0 L^2}{P_{\text{TT}}}\text{BW} \tag{4.86}$$

Then this result is compared to the result obtained by the Single Carrier Synchronization Scheme studied in Section 4.4.

The Dual Frequency scheme is compared to a Single Frequency scheme with the same transmitted frequency f_{c}, the same total transmitted power P_{TT}, and the same signal attenuation, but with a frequency doubler at the output of the Single Carrier Scheme. In this case the total channel phase noise variance of the Single Carrier Scheme, which is from Equation 4.31 equal to $(N_0 L^2/P_{\text{TT}})\text{BW}$ is multiplied by four due to frequency doubler at the output. And consequently a phase variance equal to the variance of the Dual Frequency scheme.

One advantage of the proposed scheme is that the peak power for the frequencies f_1 and f_2 is decreased for the same total transmitted power P_{TT}. It is advantageous from a engineering point of view. In particular if it is considered the reduction of the the required power saturation levels for the active devices in the paths for the tones f_1 and f_2.

4.6 Conclusions

In this Chapter a scheme for Carrier Phase Synchronization has been proposed and modeled.

This scheme reduces the overall bandwidth required in the channel and in the components within the loop because the transmission of an low frequency IF signal is not required, hence the implementation is simplified.

The overall bandwidth used is reduced, which causes a reduction of the impact of the dispersive effects of the transmission medium. Also, the frequency reduction in the feedback tone reduces the total attenuation. The main conclusion from this study is that the system bandwidth of the proposed scheme can be arbitrarily small without any loss of accuracy or resolution whereas the only limitation is the ability to filter and separate different tones.

The proposed synchronization loop has the same advantages compared with the Phase Synchronization Loop explained in Section 3.1.1 from [6, 7, 61]. In these schemes the frequencies of the tones transmitted over the channel are very similar to the oscillator frequency that is synchronized, wherewith the performance is similar to the Single-Carrier Synchronization Scheme.

The performance of the proposed loop was analyzed, thus the effects of the additive channel phase noise were quantified. In addition the maximum allowable channel delay for system stability was obtained.

From this theoretical design a practical scheme has been devised. This scheme has been prototyped and tested in order to validate the proposed scheme. The prototype implementation process is documented in the following Chapter.

Chapter 5

Prototype implementation of the Dual Frequency CW Phase Synchronization Loop

This chapter describes the Carrier Phase Synchronization System completely designed and implemented in the frame of this Ph.D. Thesis. The sections of this chapter provide an overall explanation of the constitutive subsystems. In order to give a global understanding a summary will be presented for each subsystem.

In addition this chapter explains the prototyping process that was carried on to validate the theory of the designed system.

Introduction

The first practical application that motivated the design of the proposed scheme was a high precision interferometric distance measurement system, which is the starting point for the implementation of a ground based interferometric radio positioning system. The distance and position information will be required by the UAV based bistatic receiver, SABRINA-UAV.

Notwithstanding, the theory of the proposed synchronization scheme can be used in other applications. For example, the next application will be, among others in other engineering fields, a wireless implementation of the synchronization loop used to synchronize directly the SABRINA-UAV with a ground based phase reference.

The interferometric radio position system will be based on a set of phase-synchronized ground based stations that transmit reference signals to the Bistatic Receiver in order

to determine its position. For convenience, SABRINA-UAV will receive these signals through the RF front-end which is also used to receive the Bistatic radar signals. Therefore, the frequency of the bistatic radar system determined the operation frequency of the phase synchronization link.

The operation frequency (f_{op}) of the synchronization loop must be implemented with the half of the final application frequency. The reason of this requirement is the 180° phase ambiguity that is inherent to the phase synchronization scheme.

The ambiguity of the synchronization scheme can be canceled if its output frequency is multiplied by two. That can be done with a conventional frequency doubler or using the ambiguous operation frequency as a local oscillator input of an sub-harmonic mixer. Another possible solution is to generate the carrier with the desired frequency directly in the VCO of the Remote Unit, and divide by two within the loop. The SABRINA receiver works with C-band frequencies. Some examples of the required central frequencies of the RF signals are:

- 5.300GHz: Central frequency in the ERS-2 orbital SAR system.
- 5.331GHz: Central frequency in the ENVISAT-ASAR orbital SAR system.

For this reason, the operation frequency of the synchronization link, f_{op}, will be one half of the previous frequencies. Thus, for these two examples, f_{op} will be tuned to 2650 MHz and 2665.5 MHz, for ERS-2 and ENVISAT respectively.

On the other hand, the ground based set of stations must be interconnected and synchronized with RF-cables. Therefore the first synchronization loop prototype will use a cable as the transmission channel.

Another design parameter that must be determined is the set of frequencies (f_1 and f_2) that will be used for a given f_{op} frequency. The dispersive characteristics of the selected channel will determine the allowable separation between the frequencies f_1 and f_2.

The channel attenuation and the propagation velocity have also been studied before the selection of the cable used in the implementation of the first prototype.

The following Section of this chapter will explain the transmission media selection, and then the subsequent section will explain the hardware implementation of two constitutive

blocks of the synchronization link: the Central Unit and the Remote Unit.

Each of these units is divided in two subsystems, a phase controller which is based on a single sideband generator and a second subsystem which is used as an interface between the phase controller and the transmission channel. This second subsystem contains, among other elements, a frequency diplexer.

5.1 Transmission media selection, characterization and measurements

As a first step to implement the synchronization loop prototype it was required to select an appropriate transmission media. For the practical implementation costs and availability were also taken into consideration.

One alternative for the implementation of the phase synchronization system is a coaxial cable, in particular the RG-223/U. This cable has 50 ohms impedance, a silver-coated copper conductor with polyethylene insulation and a double silver-coated copper shielding.

This cable was chosen as a first option, by being a good trade-off between price and attenuation performance. This cable can be easily found and is used frequently in laboratory applications. In order to perform the measurements, a 100 m reel was acquired, and terminated with SMA connectors.

The cable segment was measured and characterized in laboratory. The obtained measurements were used to predict the performance of the cable working in open loop and working with the closed loop phase synchronization system. In addition, the frequency allocation of the tones in the system was be based on these measurements.

The parameters measured in the coaxial cable were the phase offset and the attenuation as functions of frequency and temperature.

The attenuation and phase offset were obtained from the S-parameters performed for a set of temperatures, using a Vectorial Network Analyzer (VNA). The network analyzer used was an ZVA-8, manufactured by Rohde-Schwarz.

The 100 m cable reel was introduced inside a climate chamber in order to control its

temperature. The climate chamber was programmed to sweep from temperatures of -15 degrees Celsius to 70 degrees Celsius, in steps of 5 degrees.

The experiment setup is shown in Figure 5.1. This Figure also shows the network analyzer and the extreme of the cables attached to the wall of the climate chamber. The cable was unmovilized using plastic tape in order to keep the cable as rigid as possible in order to avoid changes from each measurement to another.

Figure 5.1: Coaxial cable measurement setup. The cable ends are attached to the wall of the climate chamber.

The attenuation and phase behavior was obtained from transmission measurements (S21 parameters) for the coaxial cable. The transmitted power in the Port-1 was 15 dBm, the frequency step was 100 KHz, and each frequency measurement point was averaged over 1000 samples.

Figure 5.2 shows the attenuation in dB obtained from the magnitude of the S21 measurements. Here the attenuation is shown as a function of frequency, for three different temperatures, $-15\,^{\circ}\mathrm{C}$, $25\,^{\circ}\mathrm{C}$ and $70\,^{\circ}\mathrm{C}$. Here it can be seen how the attenuation increases with temperature, with a value of 87 dB at a frequency of 3 GHz and a temperature of 70 degrees Celsius.

The absolute (unwrapped) phase offset of the coaxial cable was obtained for each temperature. Subsequently, each measurement is compared to the reference phase offset which is the measurement made at 25 °C.

Figure 5.3 shows these phase-offset differences. This graph shows how the differences in phase increases linearly with the frequency.

The phase span from the measurement at −15 °C to the measurement at 70 °C at the frequency 3 GHz is approximately 2700 degrees, or equivalently a phase change of 7.5 complete cycles.

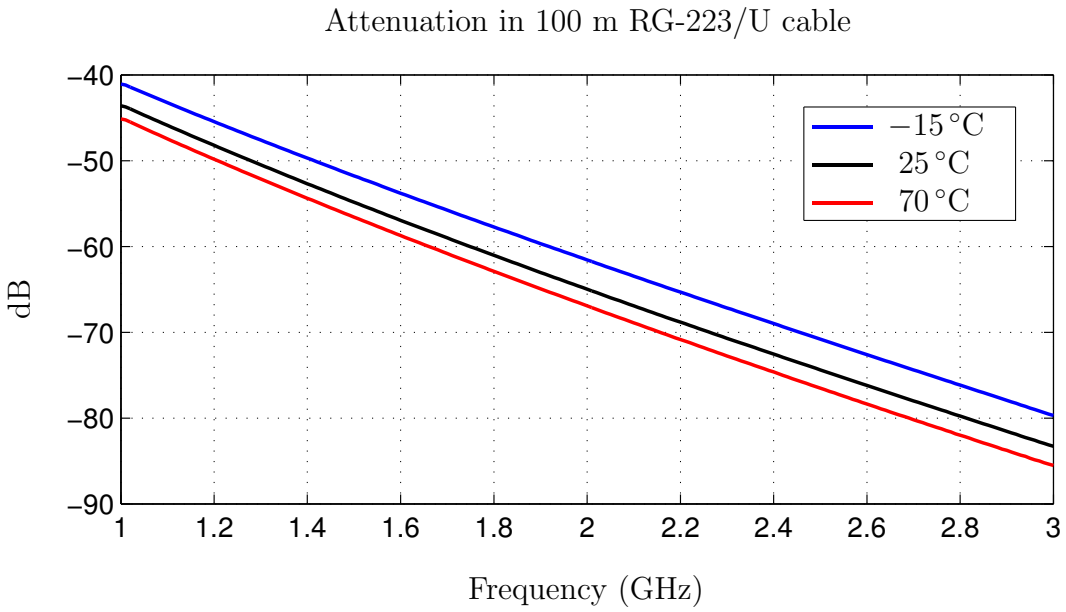

Figure 5.2: Attenuation in a RG-223/U 100 m cable with different temperatures.

In an ideal transmission media the phase offset is a perfectly linear function of the frequency, wherewith the phase difference between two consecutive frequency points must be a constant. Thus the actual phase difference between two adjacent points can be used to quantify the dispersive effects of an non-ideal channel. Figure 5.4 shows the differential phase change between consecutive samples at 70 °C. Here it can be seen that the differential phase has a span of approximately 0.006 degrees in the frequency range from 1 GHz to 3 GHz. The cumulative summation of the differential phase offsets will

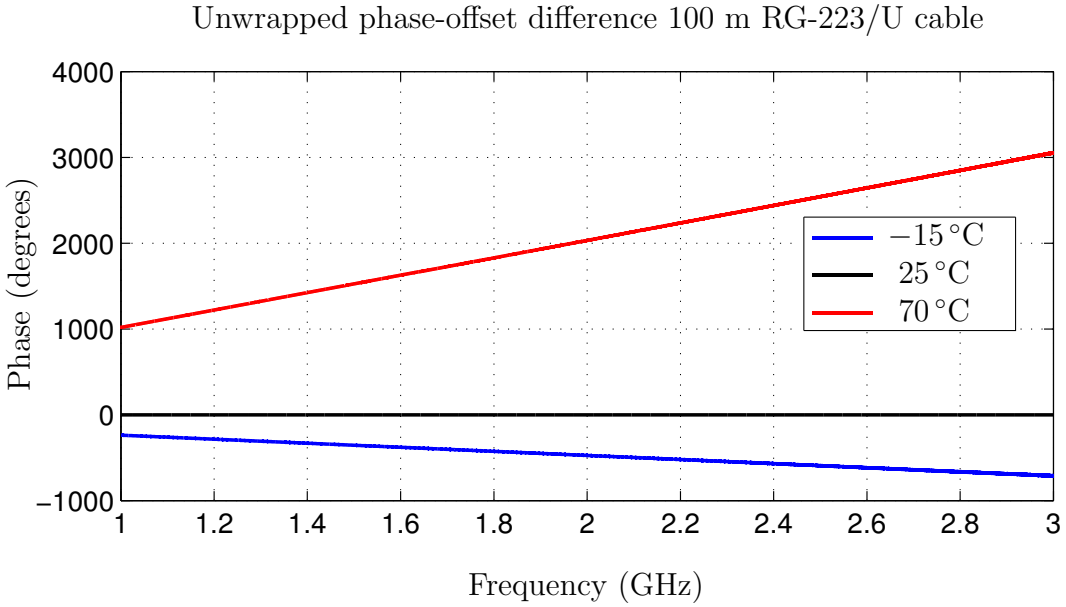

Figure 5.3: Unwrapped phase offset deviation as a function of frequency from the base unwrapped phase offset at temperature 25 °C in 100 m RG-223/U cable. Each plot is obtained from the subtraction of the unwrapped phase at 25 °C to the measured unwrapped phase.

generate a total phase change of approximately 60 degrees.

The plots for the differential phase measured at other temperatures are similar to Figure 5.4, however the measurements at 70 °C are shown because its dispersive effects are more noticeable.

The phase measurements were used to quantify the impact of the the channel dispersive effects over the proposed synchronization loop. From the previous Chapter, the impact of the phase offset for the three different tones over the output phase θ_{out} can be computed with each phase offset transfer function, and is equal to

$$\theta_{\text{out}}(\phi_1, \phi_2, \phi_{\text{c}})(s) = -\phi_1 G_{\phi 1}(s) - \phi_2 G_{\phi 2}(s) - \phi_{\text{c}} G_{\phi \text{c}}(s). \tag{5.1}$$

The steady state magnitude responses of $G_{\phi 1}(s)$ and $G_{\phi 2}(s)$ are one, and the steady state magnitude response of $G_{\phi \text{c}}(s)$ is -2. Wherewith the steady state phase error for a dispersive channel is equal to $-\phi_1 - \phi_2 + 2\phi_{\text{c}}$. This phase error can be computed using the phase measurements of the coaxial cable. In this case the central frequency, which is

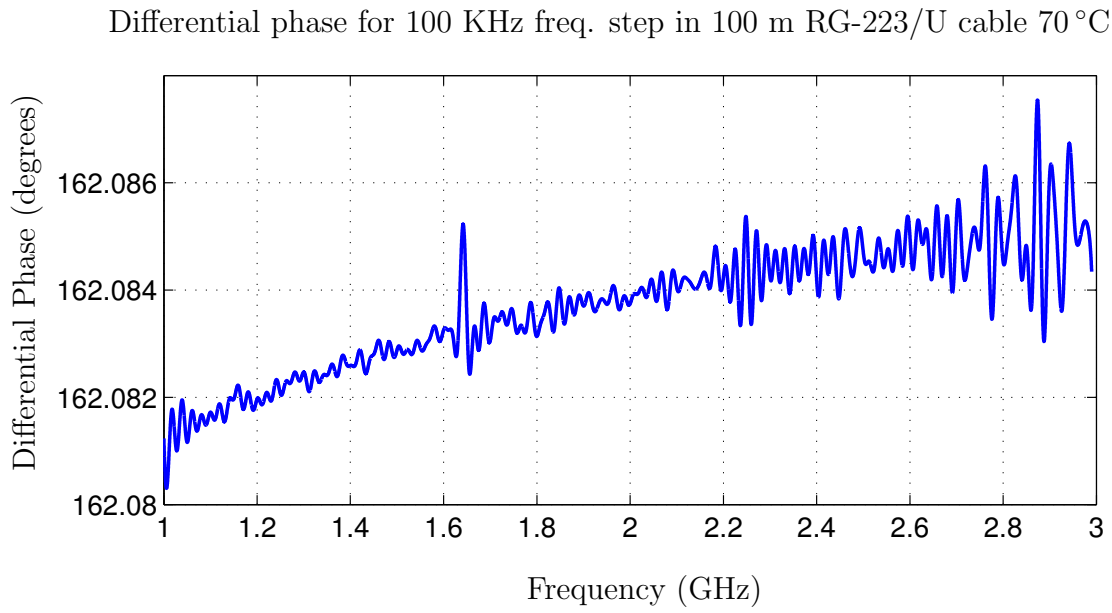

Figure 5.4: Differential phase for a 100 KHz step at 70 °C in 100 m RG-223/U cable. This differential phase should be a constant in a non-dispersive cable.

one half of $f_{\text{op}} = 2.65$ GHz, is previously known. So the phase error can be computed as a function of the separation of the tones f_1 and f_2 from f_{c}.

Figure 5.5 shows the predicted phase error of the compensated system generated by the phase offset non-linearities and as a function of the separation of f_1 (or equivalently f_2) from f_{c}.

Figure 5.5 has three plots for three different temperatures. This shows how the temperature variations in the coaxial cable will affect the phase offset of the complete compensated system.

The final frequency planning of the complete system was made from the considerations obtained from Figure 5.5. If the separation between frequencies is increased then the filtering will be easier in the frequency diplexers in the Central and Remote Units. Whereas, the increasing of this bandwidth will introduce phase errors to the compensated system due to the channel dispersive effects.

Figure 5.5 shows how the dispersive effects begin to be notorious for frequency separations near to 60 MHz. Therefore the highest bandwidth without noticeable dispersive effects is around 55 MHz. This value was chosen for the frequency separation prototyping

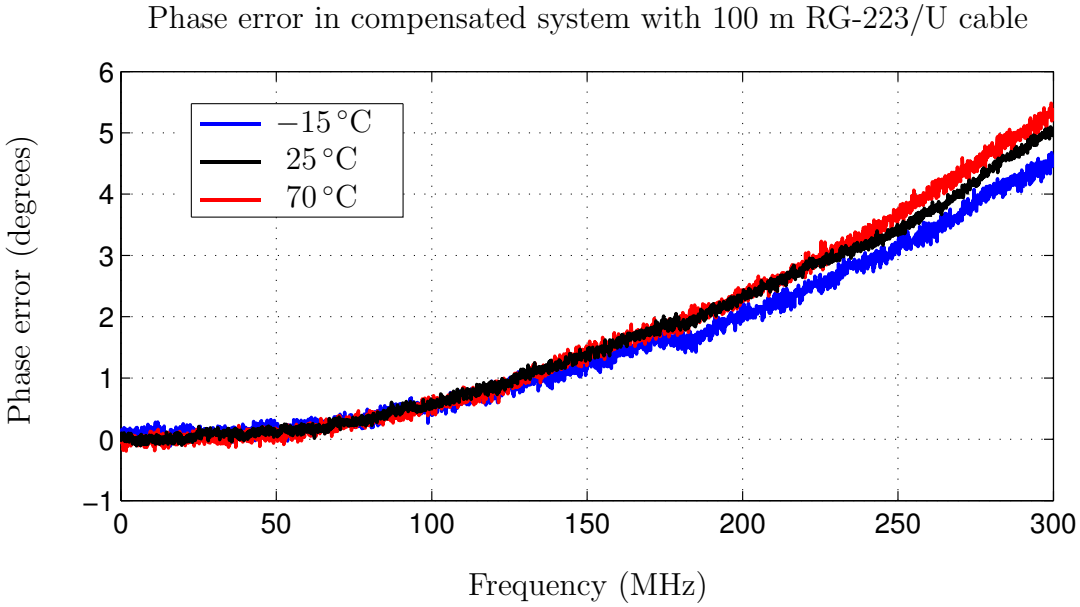

Figure 5.5: Steady state phase error on compensated system as a function of the separation of the f_1 and f_2 from the central frequency $f_c = 1.325$ GHz. (100 m RG-223/U cable). The phase error is equal to $-\phi_1 - \phi_2 + 2\phi_c$.

of the synchronization system.

The final frequency planing, with a separation between frequencies of 55 MHz is shown in Table 5.1. The carrier frequency has two possible values for two possible applications of the synchronization loop.

Application	**Carrier**	f_{op}	f_c	f_1	f_2
ERS-2	**5.300**	**2.6500**	**1.32500**	**1.27000**	**1.38000**
ENVISAT	**5.331**	**2.6655**	**1.33275**	**1.27775**	**1.38775**

Table 5.1: Final frequency planning (GHz).

Central Unit and Remote Unit implementation overview

The complete Phase Synchronization System was prototyped in the laboratory. The Central and Remote Units were implemented using Printed Circuit Board (PCB) integration and commercial components.

The implementation of the Central Unit was divided in two main subsystems:

- Central Unit Phase Controller.
- CUFDSC.

Similarly the Remote Unit was divided in:

- RUFDDC.
- Remote Unit Phase Controller.

Each of these four subsystems were implemented in a single PCB.

An important characteristic of the system prototype is the PLL bandwidth. In fact, this PLL bandwidth was selected in function of other parameters of the actual components. The first parameter to be considered for the bandwidth selection is the channel delay which affects the loop stability.

This prototype was designed to have a channel distance lower than 100 m, which represents approximately a delay lower than 0.5 microseconds. Therefore, the inverse of the loop bandwidth, or equivalent the loop time response must be higher than the channel delay for a good loop performance. In Chapter 4 it was shown that the effects of the channel delay begin to decrease for loop time responses near to five times the channel delay. Thereby, for a channel with 100 m distance the PLL bandwidth must be narrower than 400 KHz.

In addition to the considerations of the channel delay, the PLL bandwidth must be selected in order to minimize the output phase noise. This phase noise is determined by the phase noise introduced by the reference oscillator and the VCOs selected to be used in the system.

For practical reasons, the synchronization system was designed to work with the reference oscillator used in the implementation of SABRINA. The reference oscillator is an ultra low phase noise Oven Controlled Crystal Oscillator (OCXO) which generates a 10 MHz sinusoidal signal. This device is manufactured by Raltron Technologies and has the model reference OX6749. Some values of the phase noise power density of the OX6749 are shown in Table 5.2. The phase noise spectrum of the operation frequency (f_{op}) will be (in the worst case) a scaled version of the phase noise spectrum of this crystal reference.

Offset (Hz)	10	100	1K	10K	100K
Phase Noise(dBc/Hz)	-130	-152	-160	-165	-166

Table 5.2: Phase Noise Spectrum of the 10 MHz Reference Crystal Oscillator OX6749

In this order, the next critical component in terms of addition of phase noise is the VCO in the Remote Unit. This component was selected from the available commercial devices with the following criteria: The interception of the VCO phase noise spectrum and the phase noise spectrum of the operation frequency f_{op} must be at a frequency lower than 400 KHz. In typical PLL configurations the output phase noise is dominated in high frequencies by the VCO noise.

Therefore, the loop bandwidth can be made as narrow as allowed by the VCO phase noise spectrum. There was found a device that fulfilled these conditions manufactured by the company Z-Communications Inc., the VCO CRO2665D. Thus was determined the loop bandwidth for the complete synchronization system. From the product specifications the interception between the phase noise spectrum of the VCO and the scaled crystal oscillator reference is in 215 KHz at a phase noise spectrum density of -138 dBc/Hz.

The loop bandwidth of the Central Unit PLL is one half of the Remote Unit PLL bandwidth (from Section 4.5.2), wherewith the requirements for this VCO are more relaxed, in particular for the phase noise spectrum at high frequencies. The chosen VCO for the LSBG in the Central Unit was the CLV1385E manufactured also by Z-Communication Inc.

In the Central Unit, the Phase Controller contains a LSBG, two frequency mixers used to generate the negative input to the LSBG, and a microwave switch used to coordinate the phase acquisition.

The CUFDSC contains, in addition to the frequency diplexer, amplifiers and frequency dividers for the tones f_1 and f_2.

This distribution is different to the distribution shown in Section 4.5.2, where the frequency dividers appear in the Phase Controller block. Figure 5.6 shows the block diagram of the Central Unit for the hardware implementation. This new distribution was chosen in order to maintain the high frequency paths as short as possible.

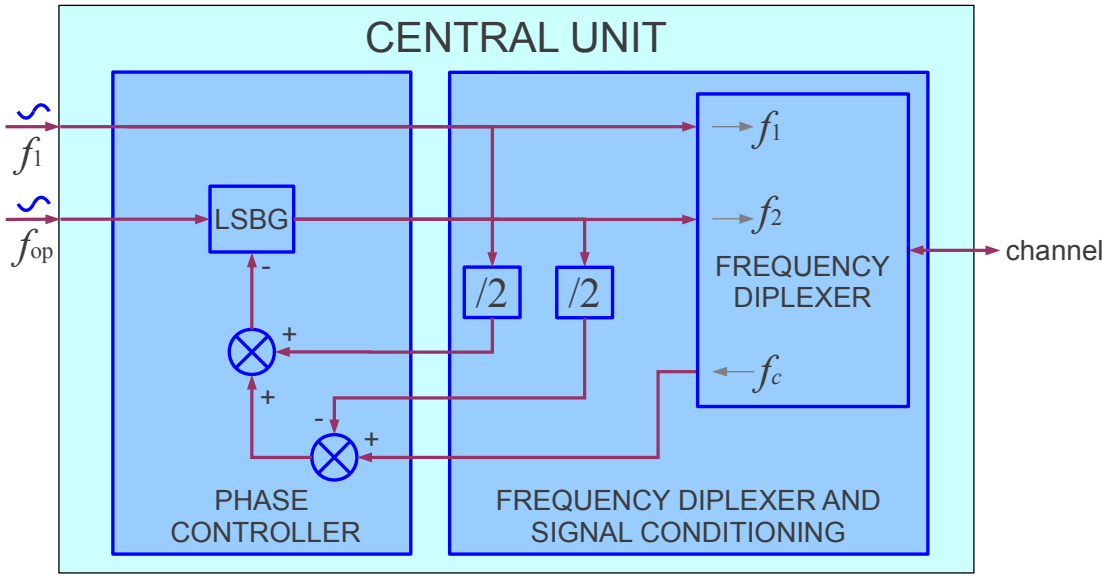

Figure 5.6: Central Unit Simplified Implementation Scheme.

In the Remote Unit, the frequency Diplexer is implemented in the same PCB with the frequency mixers used to downconvert the f_1 and f_2 tones. On the other hand, the Remote Unit Phase Controller is constructed in a single PCB, and is integrated in the same aluminum box with a RF Front-End used as a transmitter in the final application. Figure 5.7 shows a block diagram of the Remote Unit for the hardware implementation.

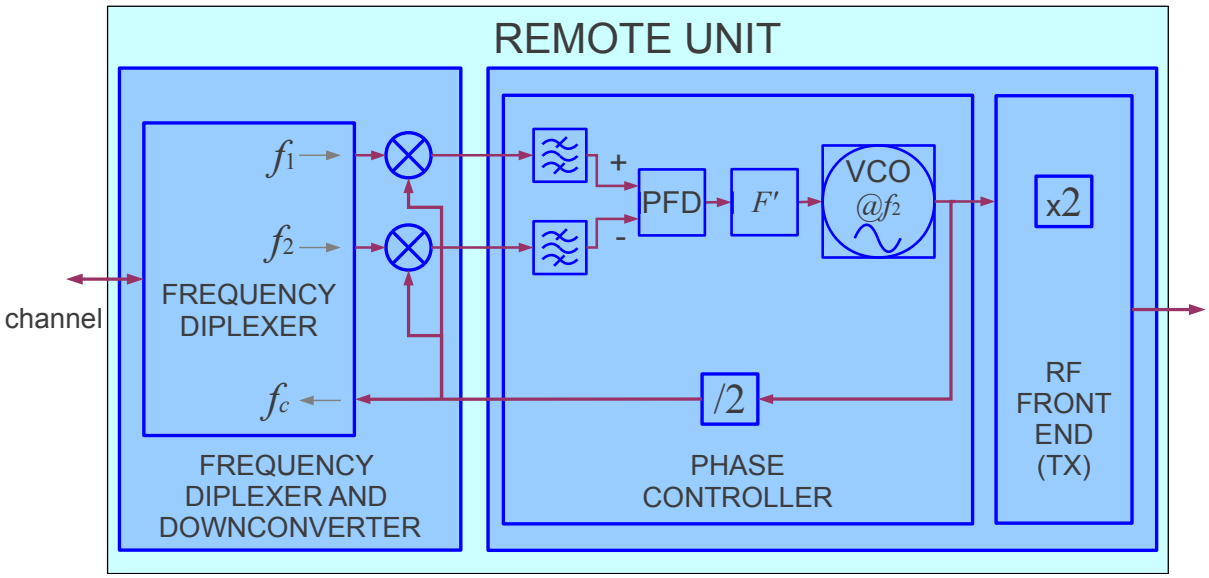

Figure 5.7: Remote Unit Simplified Implementation Scheme.

The prototyping and construction of these four subsystems are explained in the fol-

lowing subsections.

5.2 Central Unit implementation

5.2.1 Central Unit Phase Controller

A simplified schematic of the Central Unit Phase Controller is shown in Figure 5.8. The LSBG block and the frequency shifting circuit are implemented in this schematic. The most remarkable components used in the Phase Controller are a PFD, an active loop filter, a VCO, a microwave switch, three frequency mixers and four filters.

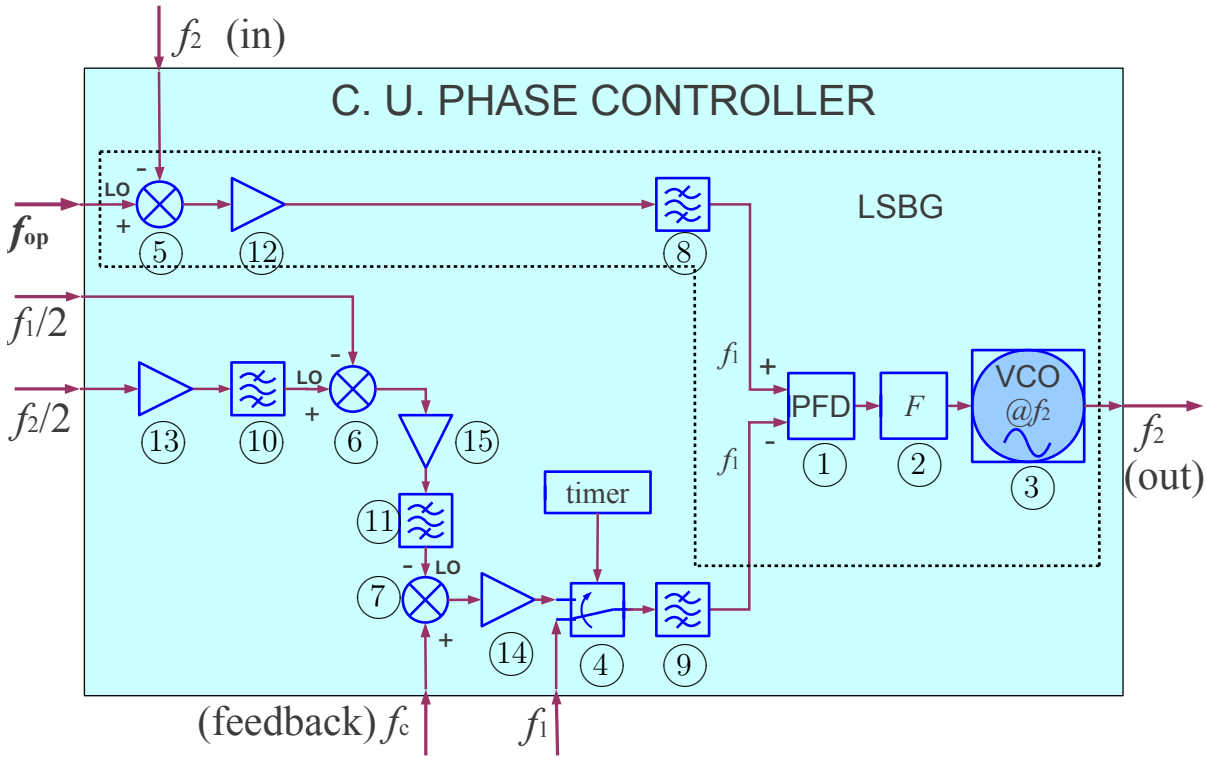

Figure 5.8: Schematic diagram of the Central Unit Phase Controller. This block has six inputs, each one for a single frequency tone and one output with the frequency f_2. The f_2 tone is also one of the six inputs.

In Figure 5.8 the dotted line remarks the equivalent circuitry for the LSBG which is a frequency offset PLL. Here, a tone whose frequency is the difference between the f_{op} and f_2 is introduced to the positive input of the PFD through a SAW filter and an amplifier.

The phase and frequency in the Central Unit and Remote Unit phase controllers is

self-acquired, or in others words, no external circuitry is used to aid the phase-frequency acquisition process. This is possible because the loop works with a Phase and Frequency Detector (PFD), also known as a "digital" phase detector. When the loop is not locked the PFD, which is a digital device, generates two pulsed outputs, UP and DN (Up and Down), with a pulse duration that depends on the frequency difference between the two input signals. Figure 5.9 shows a simplified schematic of the PFD.

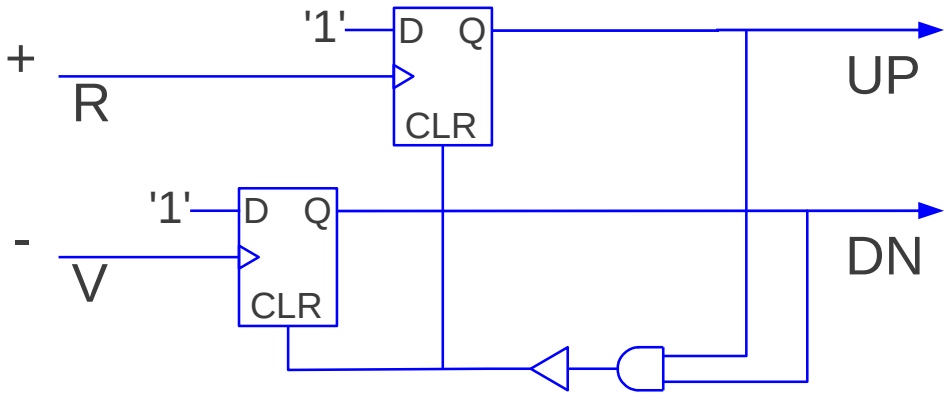

Figure 5.9: Phase and Frequency Detector (PFD).

The overall PFD duty cycle, which is the difference between UP and DN [40], is given by

$$\text{duty} = \begin{cases} 1 - \dfrac{0.5\omega_V}{\omega_R} & \text{if } \omega_R > \omega_V \\ \dfrac{0.5\omega_R}{\omega_V} - 1 & \text{if } \omega_V > \omega_R \end{cases} \tag{5.2}$$

where ω_R is the frequency of the positive input of the PFD (which is associated to the reference input in PLL nomenclature) and ω_V is the frequency of the negative input of the PFD (associated to the VCO). Thus, when the reference input frequency is much higher than the controlled frequency ($\omega_R >> \omega_V$) the U output will be active steadily and the duty cycle will be 1. On the contrary, when $\omega_V >> \omega_R$ the D output will be active steadily and the duty cycle will be -1.

Therefore, the frequency acquisition can be approximated to an exponential process with a time constant proportional to the loop time response $1/\omega_n$ and an initial offset

given by the frequency difference between the two inputs signals [40]. In actual conditions the loop performs quite better than the exponential approximation, because in actual operation the loop goes into a phase-lock state when both input frequencies arrive to a similar value.

This characteristic justifies the use of the PFD in comparison to a conventional multiplicative phase detector, which has a frequency-pull-in time of $(\omega_{\mathrm{R}} - \omega_{\mathrm{V}})^2/2\omega_n^3$ (tenths of seconds for frequency offsets of hundreds of MHz), and strict limits in the initial frequency offset for the frequency pull in.

The phase detector is implemented using a SMD device, the HMC439QS16G manufactured by Hittite, which is able to handle input signals up to 1.3 GHz, with a phase detection constant K_d of 2V/cycle.

In ideal conditions, with the use a PFD the loop will acquire the input frequency for any frequency offset. However, in this implementation the maximum frequency offset is determined by the microwave filters used prior to the PFD inputs (components No. 8 and 9 in schematic of Figure 5.8). This condition depends on the output voltage range of the operational amplifier used to implement the active loop filter.

The minimum output voltage of the filter must generate a VCO frequency which translated to the PFD input frequency remains within the passband of the microwave input filters. These filters were implemented with a Surface Acoustic Wave (SAW) filter manufactured by Golledge Electronics Ltd. The model is the TA0862A, which has a center frequency of 1.268 GHz, a 20.4 MHz bandwidth, 1.7 dB insertion loss, and an attenuation of $\sim$ 60dB for the out of band frequencies.

The active loop filter is implemented with a voltage feedback operational amplifier, and the transfer function was adjusted to obtain a natural frequency response of $\omega_{nl} = 2 \cdot 2\pi \cdot 215$ KHz $= 2\pi \cdot 430$ KHz (double of the Remote Unit bandwidth). The transfer function of the proportional-integral loop filter (used to obtain an overall second order response) is

$$F(s) = \frac{\tau_2 s + 1}{\tau_1 s} \tag{5.3}$$

The values of τ_1 and τ_2 are found in function of the PFD and VCO (CLV1385E) constants. These constants are $K_d = 2$ V and $K_v = 21$ MHz/V respectively, wherewith

τ_1 and τ_2 are

$$\begin{aligned} \tau_1 &= K_d K_v / \omega_{nl}^2 = 5.75\ \mu\text{sec} \\ \tau_2 &= 2/\omega_{nl} = 0.740\ \mu\text{sec} \end{aligned} \tag{5.4}$$

The loop filter is constructed in a differential amplifier configuration, from the two outputs of the PFD, U and D. An schematic of the implementation of the loop filter is shown in Figure 5.10. The values of the components R_1, R_2 and C, are adjusted to generate the filter constants τ_1 and τ_2 and fulfill the conditions

$$\begin{aligned} \tau_1 &= R_1 C, \\ \tau_2 &= R_2 C, \end{aligned} \tag{5.5}$$

Wherewith, the implemented values are $R_1 = 200\Omega$, $R_2 = 25.73\Omega$, and C = 28.76nF.

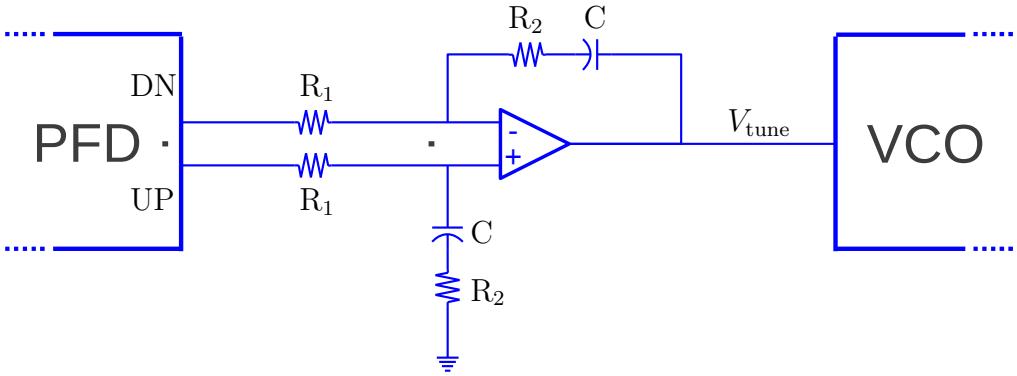

Figure 5.10: Loop Filter for the second-order type 2 PLL

Phase acquisition in PLLs is a difficult and slow process, and even more when the loop is composed of multiple sub-loops each one with a VCO. For this reason, sequencing of the phase acquisition of the multiple sub-loops is commonly used to implement these kind of systems.

Now, in order to close the complete loop, a microwave switch controls the negative input of the PFD. This switch (component No. 4 in schematic of Figure 5.8) is used to ensure the phase acquisition of the complete synchronization system. The microwave switch is controlled by a analog timer which is implemented with a RC circuit and a logic

gate.

Immediately after power-on the switch connects the external f_1 tone to the PFD. Next, after the transient response time of the RC circuit, the logic gate commutes the switch to the f_1 signal generated from the feedback tone and in this moment the complete synchronization loop is closed.

The RC timer circuit was defined to have a characteristic transient response RC of 10 milliseconds. This time is enough for the LSBG to acquire the frequency and phase using the f_1 external reference (with a pull-in time in the order of $1/\omega_{nl} = 1/430\text{KHz} \sim 2\mu\text{sec}$).

The phase of the regenerated f_1 tone is obtained from the phase of the f_c tone that comes from the Remote Unit, and the phase of the reference inputs tones $f_1/2$ and $f_2/2$ which are provided by the CUFDSC.

It is worth noting that for the practical implementation the most convenient configuration was the one shown in Figure 5.8. In that configuration, the tones with frequencies $f_1/2$ and $f_2/2$ are combined first. These tones are locally generated and consequently have a parameterized and constant amplitude. Therefore, a tone with the difference of these frequencies is generated. This tone has a frequency f_m and is cleaned with a low pass filter (component No. 11 in schematic of Figure 5.8). Doing so, the harmonics of the frequency $f_1/2$ (in particular the first harmonic is f_1, which is not discriminated in the next stage by the SAW filter) are canceled.

The input feedback tone f_c is translated in frequency using the f_m tone. This input tone has a variable magnitude, given by the channel attenuation, and can eventually have a considerable small value. This signal is introduced in the last stage, avoiding unnecessary conversions in order to maintain its signal quality.

Table 5.3 summarizes the list of components used to implement the Central Unit Phase Controller. The components numbered in Figure 5.8 are listed in this Table. Here is also shown the power range in the inputs for each component for it correct operation. This range is given by the power range specifications for each component in combination with the power budget of the complete loop.

N°	MAN	MODEL	DESCRIPTION	Gain (dB)	Input Power Range (dBm)	Notes	Price USD
1	Hittite	HMC439 QS16G	Phase Frequency Detector (PFD). Upto 1.3GHz	NA	-10 to 10	10mA/2π	31
2	Linear Tech.	LT1722-SO8	Low Noise Precision Op-Amp for the Loop Filter		NA	200MHz BW	1.8
3	ZCOMM	CLV1385E-LF	VCO 1370 to 1400 MHz	NA	NA	K_v = 21MHz/V	29
4	Hittite	HMC435 MS8G	High Isolation Microwave Switch. Upto 4GHz	0.8	-7.5 to 12.5	50dB Isolation	2
5	Mini-Circuits	MCA1-42+	Freq. Mixer. 1 to 4.2 GHz	-6	-15.3 to 4.7	Level 7	6.9
6	Mini-Circuits	JMS-11X+	Freq. Mixer. 5 to 1900 MHz	-8	-1.3 to 13.7 (2)	Level 7	11.8
7	Mini-Circuits	JMS-11X+	Freq. Mixer. 5 to 1900 MHz	-8	-12.5 to 7.5	Level 7	11.8
8,9	Golledge	TA0862A	SAW Filter 1.268 GHz	-1.7	-8.3 to 11.7	20.4MHz BW	3.5
10	Taiyo Yuden	FI212L069002-T	FILTER LOW PASS 690MHz	-0.9	3.9 to 18.9 (1)	300MHZ BW	0.2
11	Mini-Circuits	RLP-70+	FILTER LOW PASS 70MHz	-0.7	3.7 to 18.7 (2)		8
12	Hittite	HMC374	PHEMT LNA 0.3 to 3 GHZ	13	-21.3 to -1.3	1.5dB NF	3
13	Hittite	HMC374	PHEMT LNA 0.3 to 3 GHZ	13	-9.1 to 5.9 (1)	1.5dB NF	3
14	Hittite	HMC374	PHEMT LNA 0.3 to 3 GHZ	13	-21.3 to -1.3	1.5dB NF	3
15	Analog Devices	ADL5530	IC GAIN BLOCK IF 1GHz	16	-9.3 to 5.7 (2)	3dB NF	1.4

Table 5.3: Central Unit Phase Controller Component list. (1) Input power range to maintain the L.O. level in mixer component **N**°6. (2) Input power range to maintain the L.O. level in mixer component **N**°7. The other power input specifications are refereed to the PFD.

The complete power budget is mainly determined by the input power range of the PDF that is from -10 dBm to +10 dBm. From this power requirement the gains and

losses of the components were chosen, providing also the required local oscillator signals for the mixers within the loop.

The Central Unit Phase Controller Board was built in a 0.5 mm ROGERS 4003C substrate, with dimensions of 97x63.5 mm. This material has an effective dielectric constant of 3.55, and a 0.0021 dissipation factor ($\tan\delta$), using a copper thickness of 18 micrometers. Figures 5.11 and Figures 5.12 are pictures of the Central Unit Phase Controller. The implementation was done following the recommendations from Hittite,

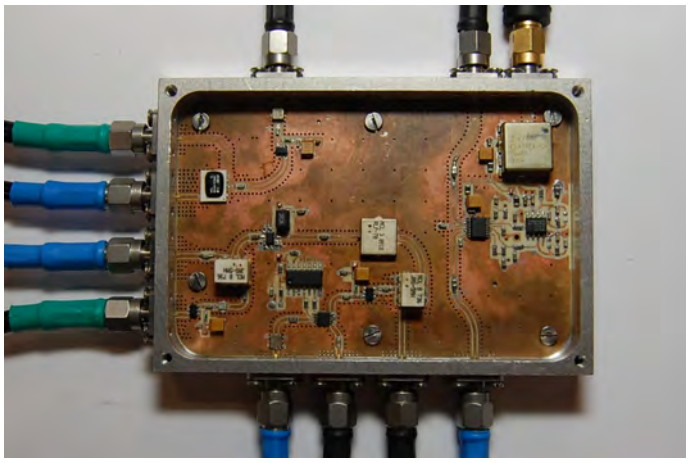

Figure 5.11: Picture of the Central Unit Phase Controller board.

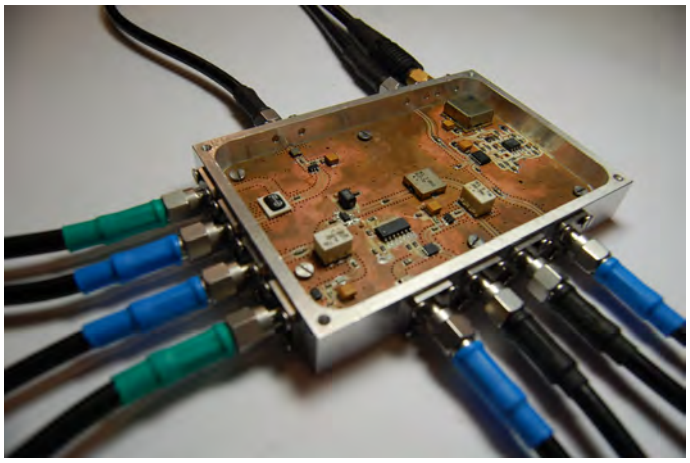

Figure 5.12: Picture in perspective of the Central Unit Phase Controller board.

given in Application Note [17]. The signals used to interconnect the components travel through coplanar 50 ohms wave guides with ground plane, as suggested in [17], and with a 11 mils coplanar gap. The line width was computed using the ADS package (Advanced

Design Software) from Agilent, Inc, obtaining a 34.3 mils line when working at the center frequency f_c (1.325 GHz).

By means of that simulation it was found that an electrical path of 90 degrees was equivalent to 1410.6 mil (3.58 cm) showing an attenuation of 0.066 dB. This attenuation is higher than the attenuation achieved by a conventional Microstrip line at that frequency, which in 90 degrees has a 0.047 dB attenuation in 1340.35 mils (3.40 cm). However, the coplanar-ground wave guides are preferred despite of its higher attenuation because they produce lower radiations, and as a consequence lower inter-signal interferences. All the microwave signals were routed in the upper layer of the board.

5.2.2 Central Unit Frequency Diplexer and Signal Conditioning (CUFDSC)

The CUFDSC is the interface between the channel and the Central Unit Phase Controller. Figure 5.13 shows a simplified schematic of the CUFDSC board.

The CUFDSC receives the tone of frequency f_c from the channel port. This port is connected to a microwave circulator (component No. 1 in the schematic of Figure 5.13), which sends the received f_c tone to the Phase Controller trough a microwave SAW filter centered at the f_c frequency.

In addition to the channel port, the CUFDSC has two main inputs, one for the f_1 tone and other for the f_2. The f_2 tone is received from the Phase Controller and the f_1 tone is received from an external frequency source.

The tones f_1 and f_2 are amplified and connected to directional couplers. Subsequently the outputs of the couplers are connected into a power combiner (component No. 3). These two output tones are also given to the Phase Controller, and as a consequence, the phase variations introduced by the amplifiers are followed by the Phase Controller.

Table 5.4 shows the component list used to implement the Central Unit Frequency Diplexer and Signal Conditioning board.

The components that required special attention in the CUFDSC implementation are listed as follows.

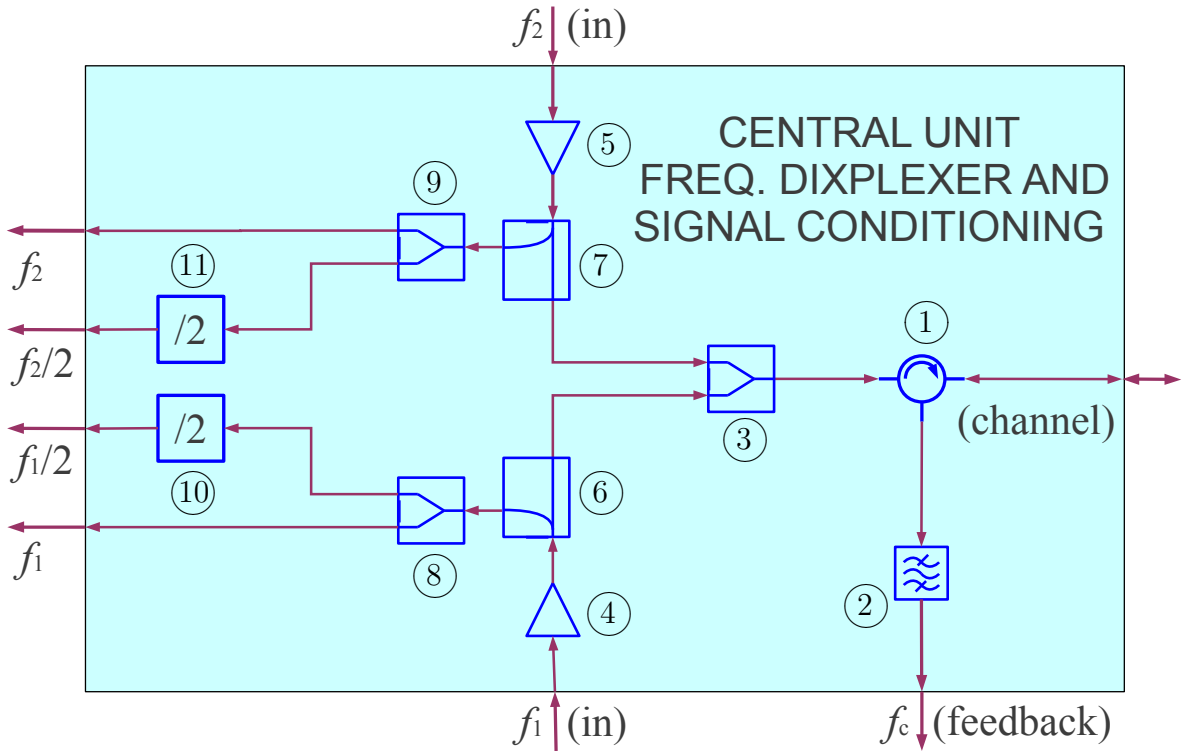

Figure 5.13: Schematic diagram of the Central Unit Frequency Diplexer and Signal Conditioning (CUFDSC). This block has two inputs, f_1 and f_2. f_1 is taken from an external source and f_2 is generated by the Phase Controller.

Custom directional coupler

After amplification a directional coupler (components No. 6 and 7) are used to split the signals f_1 and f_2 in two branches, one that is joined into the channel and another that is given back to the Phase Controller. The directional coupler must be as directive as possible in order to reduce interferences between the tones at frequencies f_1 and f_2.

The most important source of interference between f_1 and f_2 is generated in the power combiner. This device allows interferences between the lines of f_1 and f_2, because it does not have a perfect isolation between its inputs. However, the effects of this interference over the output ports (on the right side of the schematic) can be reduced as a function of the directivity of the directional couplers (components No. 8 and 9).

The directional coupler is crucial for the Central Unit Diplexer implementation. It is not easy to find commercial components with the desired characteristics. These characteristics are summarized as follows:

N°	MAN	MODEL	DESCRIPTION	Gain (dB)	Input Power Range (dBm)	Notes	Price USD
1	Wenteq Corp.	F1568-01333-10	Microwave Circulator 1.26-1.4GHz	-0.5	-7.4 to 11.6 (1)	20dB r. isolattion	58
2	Golledge	TA0566A	SAW Filter 1.330 GHz	-4.6	-7.9 to 12.1 (1)	8MHz BW	6.2
3	Custom	Custom	Custom Willinson Power Combiner 1.325GHz	-3.4	NA		0
4,5	Hittite	HMC374	PHEMT LNA 0.3 to 3 GHZ	13	-5.2 to 7 (2)	1.5dB NF	3
6,7	Custom	Custom	Custom Meandered Directional Coupler 1.325GHz	-0.6	NA	28 dB isolation	0
8,9	Mini-Circuits	BP2G1+	Splitter Combiner 1.2 to 2 GHz	-3.5	NA		0.8
10,11	Hittite	HMC361 S8G	GaAs Divide by 2. 0 to 10 GHz	NA	-15 to 10	Square output	6.9

Table 5.4: CUFDSC Component list. (1) Power range of the channel input. (2) Input power range for the f_1 and f_2 tones.

- Reverse isolation: required in order to minimize the reverse interferences into the coupled output port. An isolation above 20 dB is considered acceptable.

- Coupling: It is required a coupling between the input port and the coupled output port in the order of 15 dB.

- Bandwidth: The phase response for the coupled and direct outputs must be as linear as possible for the range of frequencies f_1 and f_2, and centered at frequency f_c. The dispersive effects at the frequencies f_1 and f_2 will introduce a change in the phase offset of the complete synchronization loop.

- Size: It was convenient to reduce the size of the couplers. For practical reasons, the complete CUFDSC board was designed to have the same size of the Phase Controller. These two devices are stacked together in order to conform a rigid and stable structure.

These requirements were met with a custom meandered directional coupler. As a consequence of the implementation of the coupler with a meandered shape the maximum dimension of the layout is reduced. For this configuration the $\lambda/4$ coupling section is meandered in three subsections.

The coupler was devised from the design proposed in the reference [106], for a central frequency of 1.325 GHz and a bandwidth of 150 MHz. The coupler was implemented with a Microstrip construction in a dielectric material of 0.8 mm ROGERS 4350B substrate. This material has an effective dielectric constant of 3.66, a 0.0031 dissipation factor ($\tan\delta$), and a copper thickness of 35 micrometers. The coupler was designed to be implemented within the complete CUFDSC PCB layout.

The device was drawn and simulated with the ADS software. Figure 5.14 shows the layout of the designed coupler. A stand alone instance of the coupler layout was

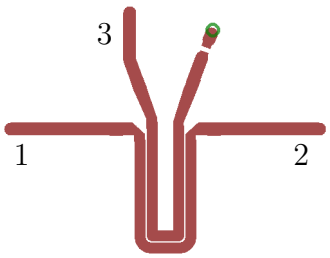

Figure 5.14: Meandered coupler layout. Port 1 is the input, port 2 is the direct output and the port 3 is the coupled output. The green circle is the connection to ground plane of the 50Ω termination.

constructed and tested. The results for the stand alone coupler are shown in Figure 5.15. The measurements where obtained from a Vectorial Network Analyzer (VNA).

As seen in Figure 5.15, at the center frequency, the S21 parameter is -0.6 dB, the S31 parameter is -11.8 dB and the S32 parameter is -28.7 dB, wherewith the requirements are fulfilled.

Custom Wilkinson power combiner

A custom power combiner was designed to be included inside the CUFDSC board. The function of this component (component No. 3) is to combine the f_1 and f_2 tones from direct outputs of the directional couplers. The combiner was tuned for the same substrate

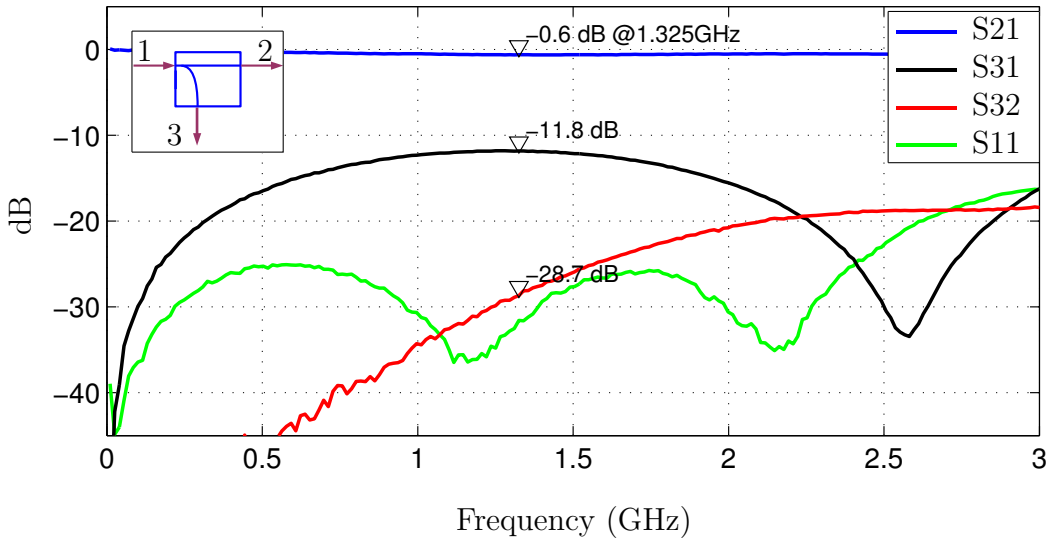

Figure 5.15: Measured S-parameters of the stand-alone meandered coupler. The design was coupled for a center frequency of 1.325 GHz.

in which the directional couplers were implemented. The combiner is centered at the f_c frequency with a bandwidth of 150 MHz. For this particular design, the most important goal is the isolation between the two input ports.

For testing purposes, a stand-alone combiner was constructed, obtaining isolations of -35 dB and -45 dB at f_1 and f_2 frequencies respectively.

The joint output of the power combiner is connected into a microwave circulator (component No. 1), which is the interface between the power combiner and the transmission channel.

Frequency dividers

Finally, another component that is worth to note is the frequency divider (components No. 10, 11). Two dividers were implemented in the CUFDSC using a commercial high frequency digital (counter) frequency halver manufactured by Hittite.

Figures 5.16 and 5.17 show pictures of the CUFDSC board. In these pictures all the

components are already soldered to the board.

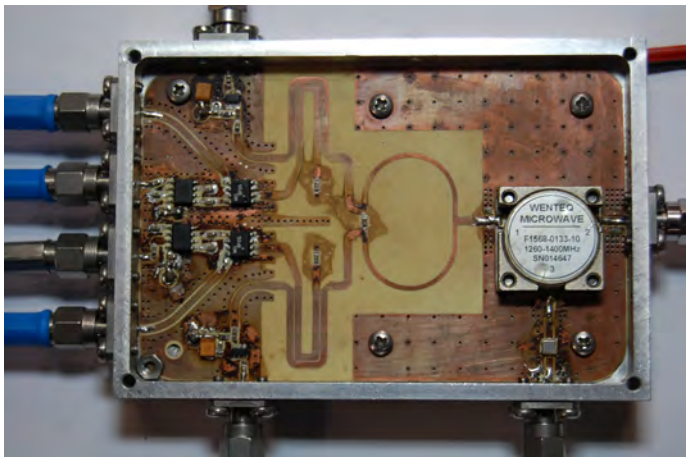

Figure 5.16: Picture of the CUFDSC board.

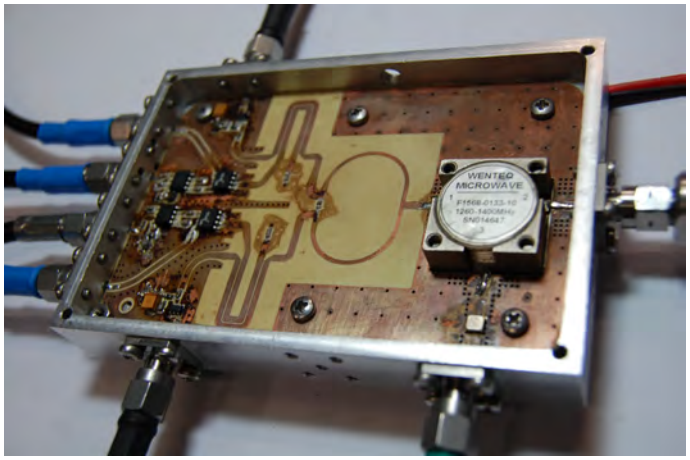

Figure 5.17: Picture in perspective of the CUFDSC board.

A set of tests were performed over the complete CUFDSC board. In addition to the required gain for each input into the channel, it was also important to make a checkout for the required isolation between the input and output ports. Thus, it was required to measure the interference of the input tone of frequency f_1 into the output ports of frequency f_2 and $f_2/2$. Equivalently the interference of the input tone of frequency f_2 into the output ports of frequency f_1 and $f_1/2$.

The capability of reducing these interferences will determine the precision of the complete phase synchronization system. It was measured that the interferences over the f_2 output port from the tone f_1 is -53 dB, and that the interferences over the f_1 port from the tone f_2 is -64 dB.

The CUFDSC was stacked with the Phase Controller in a rigid structure. Figures 5.18 and 5.19 show pictures of the complete Central Unit. Figure 5.19 shows how both aluminum cases, the Phase Controller box and the CUFDSC box, are screwed together.

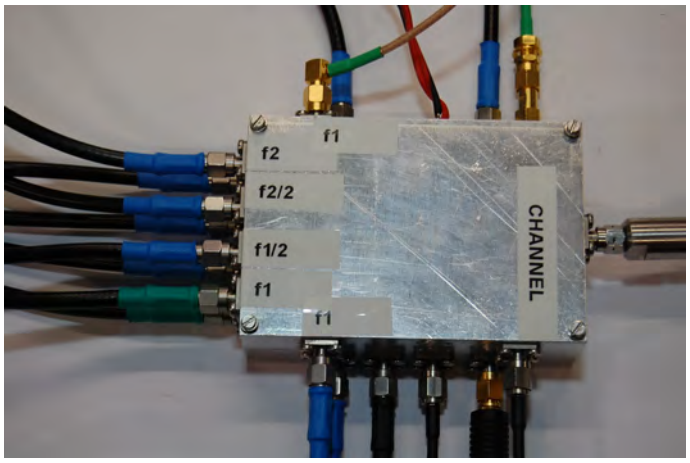

Figure 5.18: Picture of the complete Central Unit

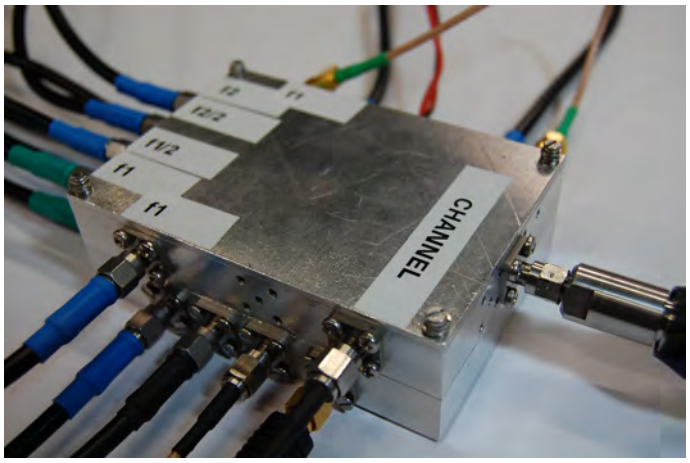

Figure 5.19: Picture in perspective of the complete Central Unit

5.3 Remote Unit implementation

5.3.1 Remote Unit Frequency Diplexer and Down-Converter (RUFDDC)

Within the Remote Unit, the RUFDDC is the interface between the channel and the Remote Unit Phase Controller. This device separates the input tones by means of frequency

filtering. Figure 5.20 shows a simplified schematic of this subsystem.

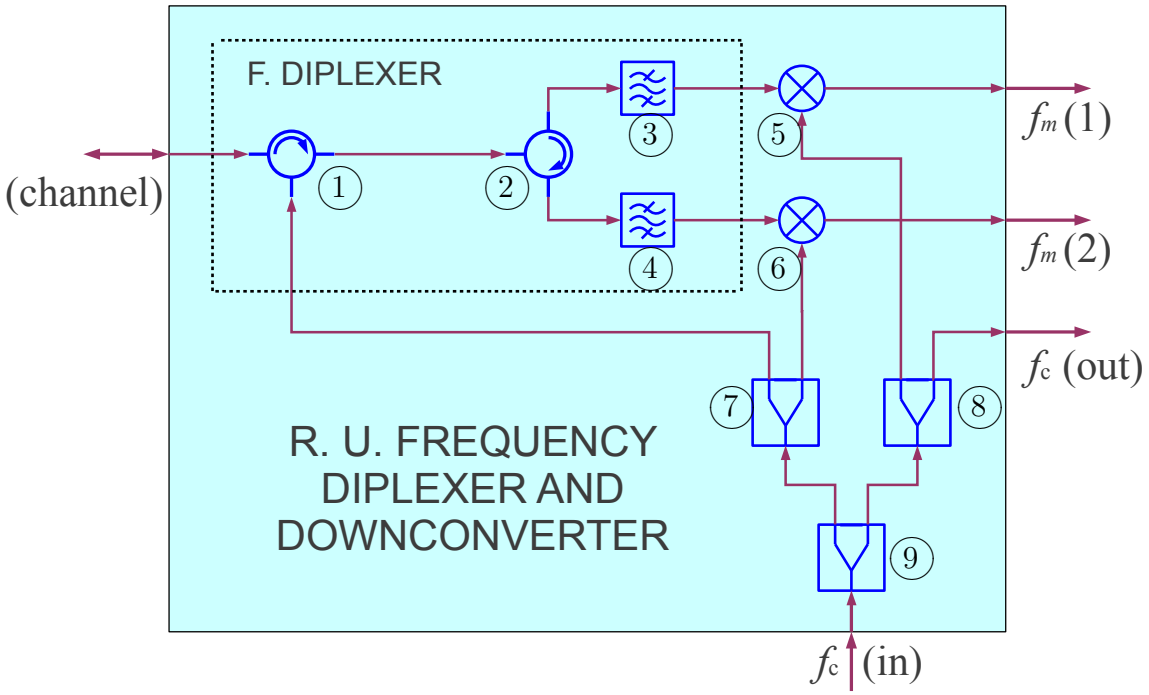

Figure 5.20: Schematic diagram of the RUFDDC.

N°	MAN	MODEL	DESCRIPTION	Gain (dB)	Input Power Range (dBm)	Notes	Price USD
1,2	Wenteq Corp.	F1568-01333-10	Microwave Circulator 1.26-1.4 GHz	-0.5	-12.1 to 7.9 (1)	20 dB r. isolattion	58
3	Golledge	TA0862A	SAW Filter 1.268 GHz	-1.7		20.4 MHz BW	3.5
4	Golledge	TA0921A	SAW Filter 1.370 GHz	-4.2		40 MHz BW	6.5
5,6	Mini-Circuits	JMS-11X+	Freq. Mixer. 5 to 1900 MHz	-8	-17.3 to 2.7 (1)	Level 7	11.8
7,8,9	Mini-Circuits	BP2G1+	Splitter Combiner 1.2 to 2 GHz	-3.5			0.8

Table 5.5: RUFDDC component list. (1) Input power range for the input tone f_2, with power loss of the Frequency Diplexer of 5.2 dB. For the input tone f_1 this range is 3 dB lower (5.2 minus 2.2 dB)

Here the most important components are two microwave circulators and two SAW filters. This SAW filters (components No. 3 and 4 in schematic of Figure 5.20) are centered, one at the f_1 frequency and the other at f_2 frequency.

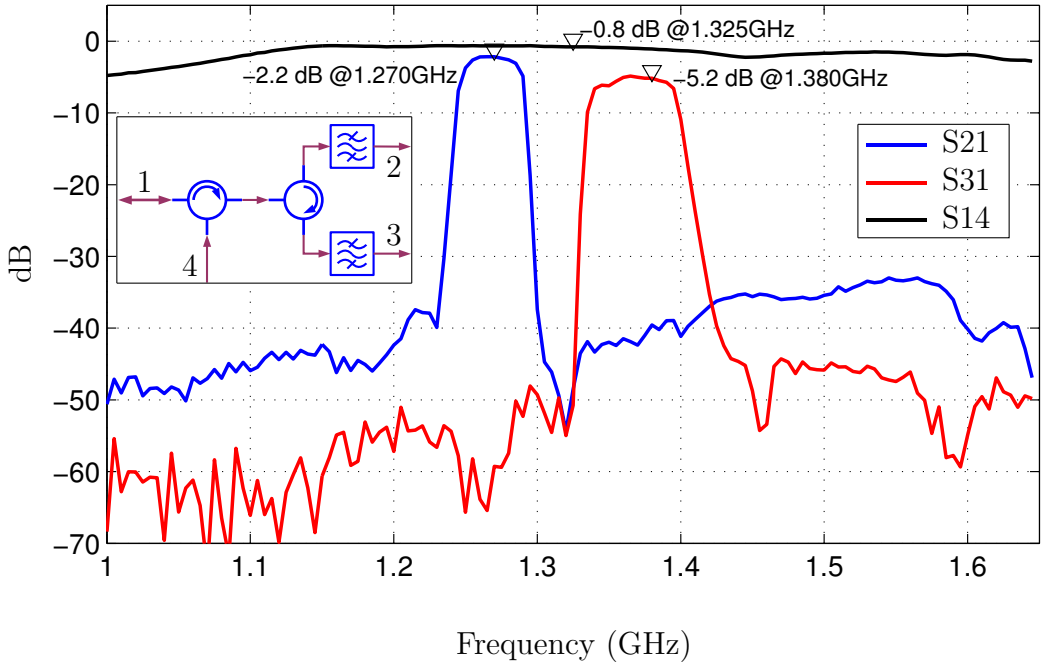

Figure 5.21: S-parameters of a stand-alone Diplexer constructed for testing purposes.

The filtered tones are down-converted with the f_c tone as local oscillator. The down-converted tones, (both with a frequency of f_m) are the outputs which are connected to the Phase Controller board. The f_c tone is received from the Phase Controller board, and is injected into the channel through the first circulator. The allowed range of power in the f_m tones (in Table 5.5) is determined by the allowed input power of the Phase Controller board. This power range is from -25.3 to -5.3 dBm.

Before the complete implementation of the complete RUFDDC an stand-alone frequency diplexer was constructed and tested. This test was done in order to verify the behavior of the SAW filters, with special emphasis in the out-of-band frequencies. The S-parameters of the stand-alone diplexer are shown in Figure 5.21.

Figure 5.21 shows that for a received f_1 tone the losses are 2.2 dB. While the loss given by the specifications of the first (f_1) SAW filter is 1.7 dB.

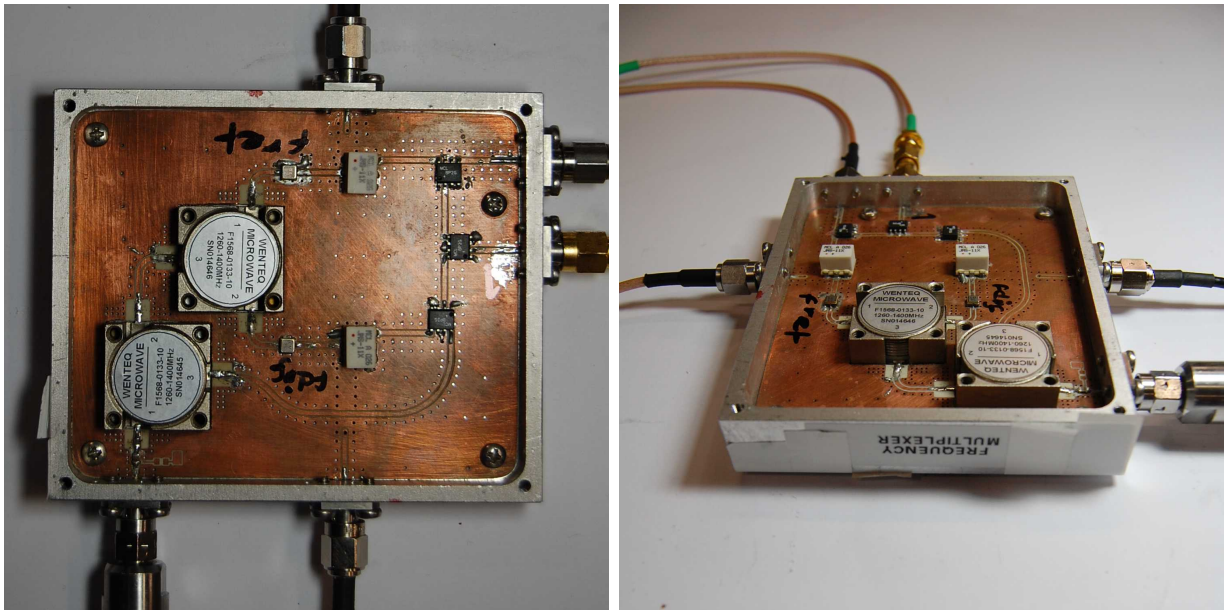

Figure 5.22: Pictures of the RUFDDC board.

The tone f_2 is reflected by the first filter and then goes into the second filter. As can be deducted from the marker of the parameter S31, most of the input power of the f_2 tone is reflected in the first filter without any noticeable loss. The S31 parameter at the f_2 tone is -5.2 dB, while the loss given by the specifications of the second SAW filter is 4.2 dB.

The complete RUFDDC subsystem was implemented in a single PCB, with dimensions of 86 x 72 mm in a 0.5 mm ROGERS 4003C substrate. Figure 5.22 show two pictures of the RUFDDC board.

5.3.2 Remote Unit Phase Controller

The Remote Unit Phase Controller was implemented in hardware following the same guidelines of the Central Unit Phase Controller. A simplified schematic of the Central Unit Phase Controller is shown in Figure 5.23. The optimal value for the PLL bandwidth ω_{nu} of this Phase Controller is 215 kHz. This value was determined previously, as explained at the beginning of Section 5.1.

The transfer function of the proportional-integral loop filter (used to obtain an overall

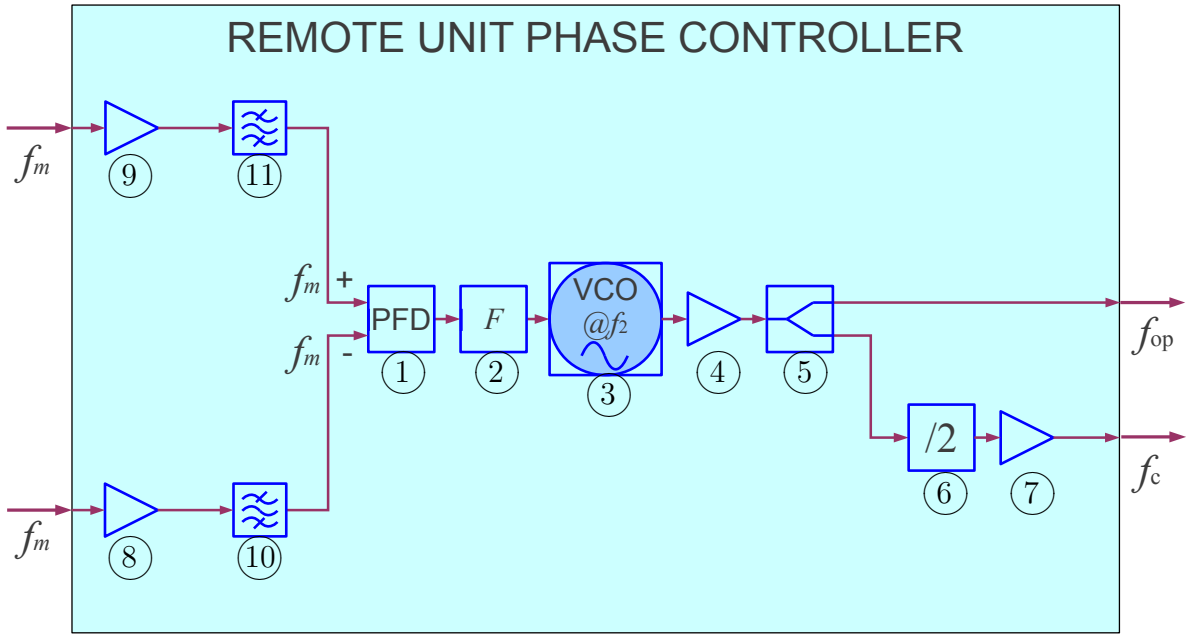

Figure 5.23: Schematic diagram of the Remote Unit Phase Controller.

second order response) is

$$F'(s) = \frac{\tau_2' s + 1}{\tau_1' s} \tag{5.6}$$

The values of τ_1' and τ_2' are found as a function of the PFD and VCO (CRO2665D) constants. These constants are $K_d = 2\text{V/cycle}$ and $K_v = 30\text{MHz/V}$ respectively, wherewith τ_1' and τ_2' are

$$\begin{aligned} \tau_1' &= K_d K_v / \omega_{nu}^2 = 3.28\ \mu\text{sec} \\ \tau_2' &= 2/\omega_{nu} = 1.48\ \mu\text{sec} \end{aligned} \tag{5.7}$$

The values of the components R_1, R_2 and C, are chosen to generate the filter constants, τ_1 and τ_2, under the conditions:

$$\begin{aligned} \tau_1 &= R_1 C, \\ \tau_2 &= R_2 C, \end{aligned} \tag{5.8}$$

Wherewith, the implemented values are $R_1 = 200\ \Omega$, $R_2 = 9.0\ \Omega$, and $C = 164.39$ nF.

The VCO output is amplified and introduced into a power splitter. One output of the splitter is introduced into a frequency divider in order to generate the f_c tone. The other splitter output is taken into an output port. This output will be the local oscillator signal of the RF Front-end which is within Remote Unit. In fact, the RF Front-end is and independent PCB which is assembled in the same aluminum case with the Phase Controller.

Table 5.6 shows the list of components used to implement the Remote Unit Phase Controller.

N°	**MAN**	**MODEL**	**DESCRIPTION**	Gain (dB)	Input Power Range (dBm)	Notes	Price USD
1	Hittite	HMC439 QS16G	Phase Frequency Detector (PFD). Up to 1.3 GHz	NA	-10 to 10	10mA/2π	31
2	Linear Tech.	LT1722-SO8	Low Noise Precision Op-Amp for the Loop Filter			200MHz BW	1.8
3	ZCOMM	CRO2665D-LF	VCO 2640 to 2710 MHz	NA		K_v = 30 MHz/V	29
4,7	Hittite	HMC374	PHEMT LNA 0.3 to 3 GHz	13		1.5 dB NF	3
5	Custom	Custom	Custom resistive power divider	6.3			
6	Hittite	HMC361 S8G	GaAs Divide by 2. 0 to 10 GHz	NA	-15 to 10	Square output	6.9
8,9	Analog Devices	ADL5530	IC GAIN BLOCK IF 1 GHz	16	-25.3 to -5.3 (1)	3dB NF	1.4
10,11	Mini-Circuits	RLP-70+	FILTER LOW PASS 70 MHz	-0.7	-9.3 to 10.7 (1)		8

Table 5.6: Remote Unit Phase Controller Component list. (1) Input power range to maintain the input power range of the PFD.

5.3.3 Remote Unit RF Front-End

The RF Front-end is used for the final application of the complete Phase Synchronization System. The f_{op} carrier is multiplied by two and is used as the local oscillator of an IQ

frequency mixer. The input IQ signals must be provided from an external source. The output of the RF Front-end is then ready to be transmitted using an external antenna.

An schematic of the RF Front-end is shown in Figure 5.24 and the component list is shown in Table 5.7.

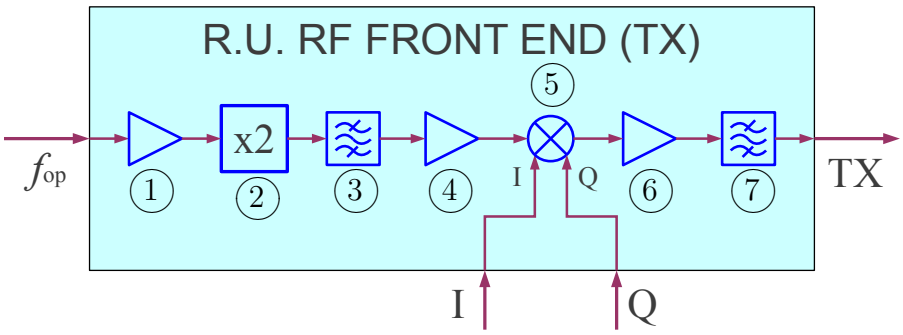

Figure 5.24: Schematic diagram of the Remote Unit RF Front-end.

N°	MAN	MODEL	DESCRIPTION	Gain (dB)	Input Power Range (dBm)	Notes	Price USD
1	Hittite	HMC374	PHEMT LNA 0.3 to 3 GHZ	13	-2.5 to 7.5 (1)	1.5 dB NF	3
2	Hittite	HMC189 AMS8	Passive SMT Freq. Doubler, 2-4 GHz in.	-13	-10.5 to 20.5 (1)		4.1
3	Johanson Tech.	5515BP 15C725E	FILTER BANDPASS 5.5 GHz	-2.5	-2.5 to 7.5 (1)	725 MHz BW	0.9
4	Hittite	HMC604 LP3E	Low Noise Amplifier 4.8-6.0 GHz	15	-5 to 5 (1)	1.5 dB NF	8.2
5	Hittite	HMC525 LC4	GaAs MMIC I/Q Mixer 4-8.5 GHz	-8	3 (2)	Level 13	23
6	Hittite	HMC604 LP3E	Low Noise Amplifier 4.8-6.0 GHz	15		1.5 dB NF	8.2
7	Johanson Tech.	5515BP 15C725E	FILTER BANDPASS 5.5 GHz	-2.5		725 MHz BW	0.9

Table 5.7: Remote Unit RF Front-end Component list (1) Input power range to maintain the L.O. level in mixer component **N**°5 which can be from 10 to 20 dBm. (2) Maximum power in the I/Q mixer inputs.

The RF output of the IQ mixer is amplified 15 dB and is filtered at C-band with a 700 MHz bandwidth (component No. 7).

Finally, Figure 5.25 shows three pictures of the complete Remote Unit.

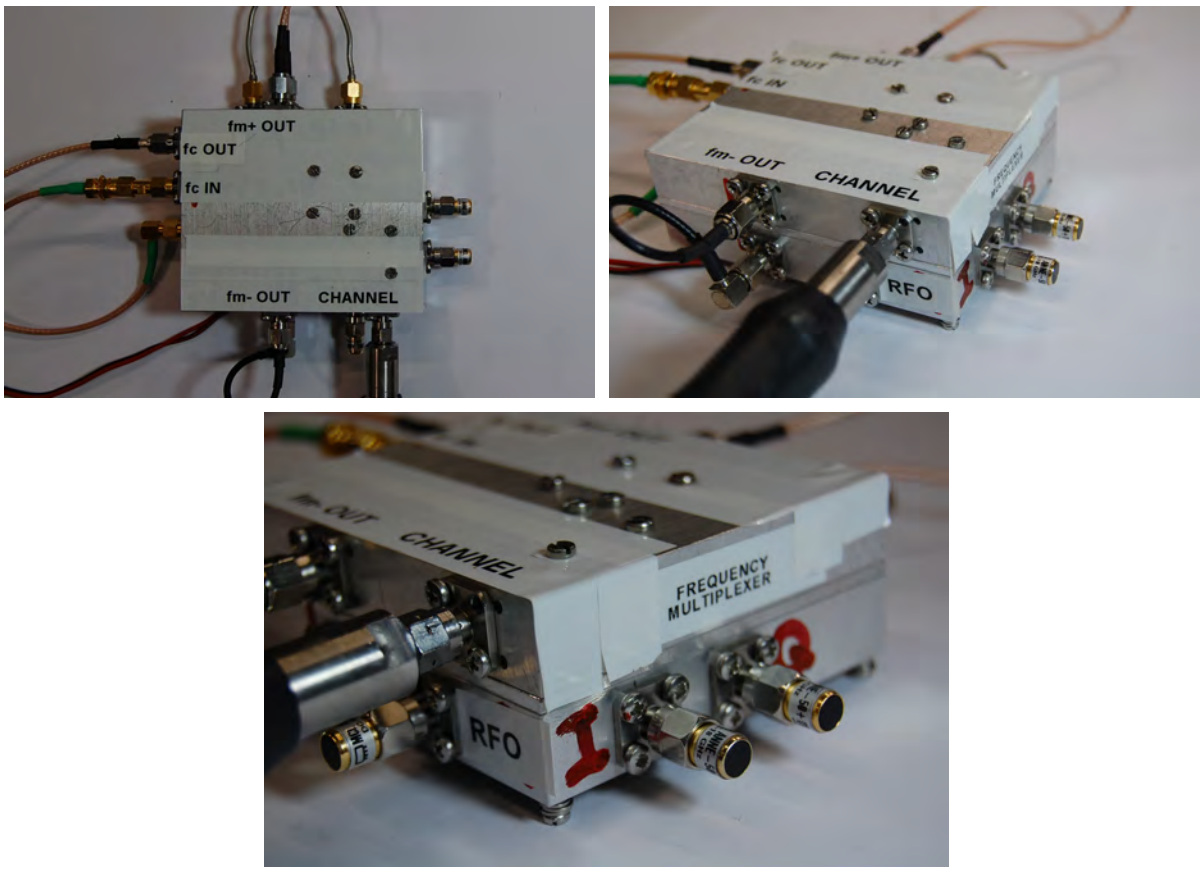

Figure 5.25: Pictures of the complete Remote Unit. Here can be seen how the Phase Controller and the RUFDDC subsystems are assembled together.

5.4 Conclusions

This chapter has described the implementation of the Phase Synchronization prototype and their constitutive subsystems. The prototype was divided in two main blocks, the Central Unit and the Remote Unit. Each one of these units was divided in a Phase Controller and a block which contains a frequency diplexer among other complementary components.

Additionally, the Remote Unit contains an RF Front-End which is used for the trans-

mission and modulation of the synchronized carrier. Thus, the proposed system was adjusted and tuned for a particular application.

The Central Unit and Remote Unit subsystems were implemented successfully, which was proven after individual testing of the different subsystems. Subsequently, the complete Phase Synchronization System was mounted and characterized. The results of these tests and the complete characterization of the system are shown in next chapter.

Chapter 6

Characterization of the Phase Synchronization System Prototype

The complete Phase Synchronization Loop prototype has been designed and constructed as it was described in previous chapters. Then this chapter is devoted to expose the performance tests that have been carried on over the prototype.

The first section of this chapter exposes the phase noise characterization of the output of the Phase Synchronization Loop. This characterization is performed by means of phase noise spectrum measurements. The second section is devoted to the characterization of the phase offset stability of the complete synchronization loop. This characterization is performed by means of absolute phase offset measurements.

6.1 Phase noise measurements for the complete Phase Synchronization Loop

The objective of these set of measurements has been to obtain the phase noise spectrum of the output of the complete Phase Synchronization Loop prototype. This phase noise spectrum can be obtained from the frequency spectrum if the carrier power is known. The frequency spectrum of the complete prototype output has been measured using a Frequency Spectrum Analyzer (FSP).

Prior to the phase noise experiments, some preliminary tests were performed over the prototype. The Central Unit and the Remote Unit were connected to independent power supplies, with a level of 5.9 V. The current consumption of the Central Unit was 0.78 A

and the consumption of the Remote Unit was 0.72 A. Thereby, the power consumption of the complete prototype was lower than 9 Watts.

Under these conditions the phase acquisition of the complete loop was verified, and it has been seen that the the loop locked to the input reference whenever the Central Unit was powered on after the Remote Unit.

Another preliminary experiment was performed in order to verify the three tones which travel in the channel (between the Central Unit and the Remote Unit). Figure 6.1 shows the setup for this experiment. There can be seen the tones f_1, f_2 and f_c in the screen of the FSP. These signals are taken from the channel using a resistive power splitter in series with an additional 5 dB attenuator for a total channel attenuation of 11 dB.

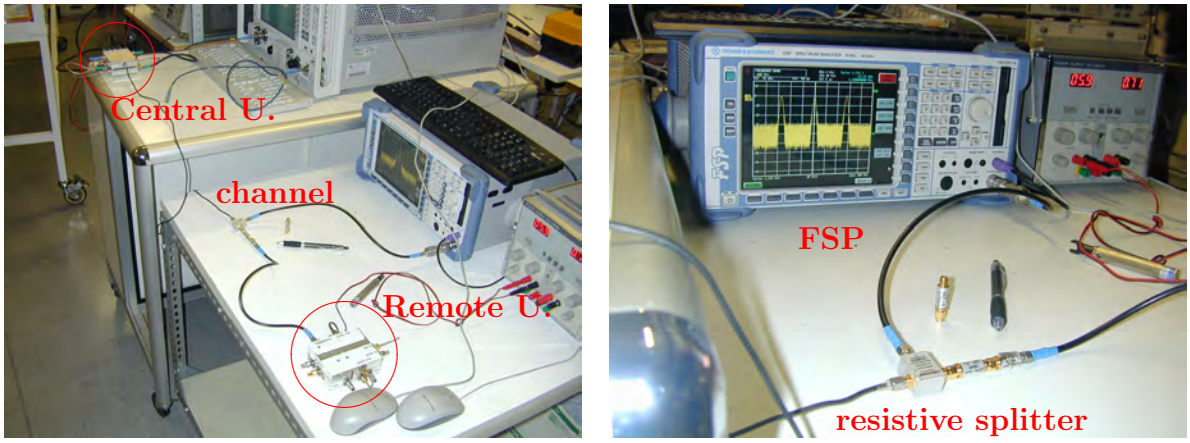

Figure 6.1: Phase synchronization loop measurement settings. Here the frequency spectrum of the signals on the channel are connected to the FSP using a resistive power splitter. Three peaks at the f_1, f_2 and f_c frequencies are observed in the screen of the FSP

The setup for the phase noise experiment is shown in Figure 6.2. In this setup the Central Unit and the Remote Unit are interconnected using a variable attenuator instead of the long coaxial cable. The carrier f_{op} and f_1 are taken from two external signal synthesizers.

The f_{op} (2.65 GHz) frequency, which regenerated in the Remote Unit, is connected into the FSP. The model of the analyzer is FSP40, manufactured by Rohde and Schwarz. The experiment setup for the phase noise measurements (and also for the phase offset measurements) is shown in Figures 6.3, 6.4.

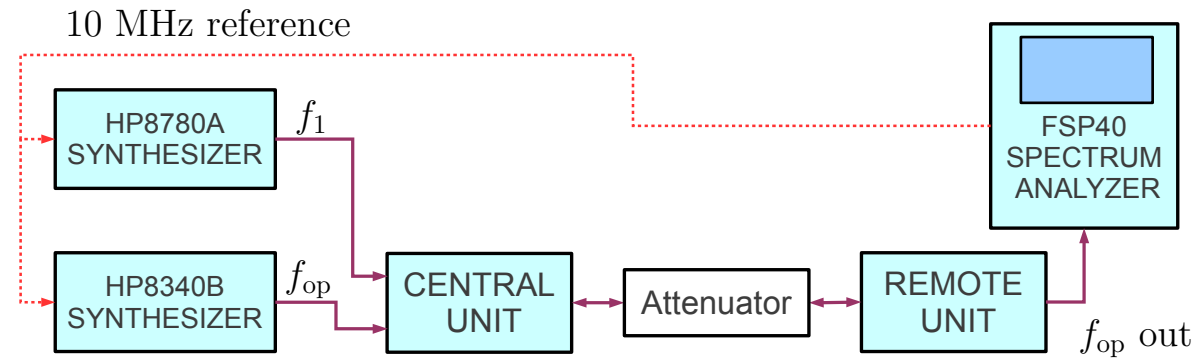

Figure 6.2: Measurement setup for the loop output phase noise.

Figures 6.3 and 6.4 show a mechanical variable phase shifter. This device has been used for the phase offset measurements explained in the next section.

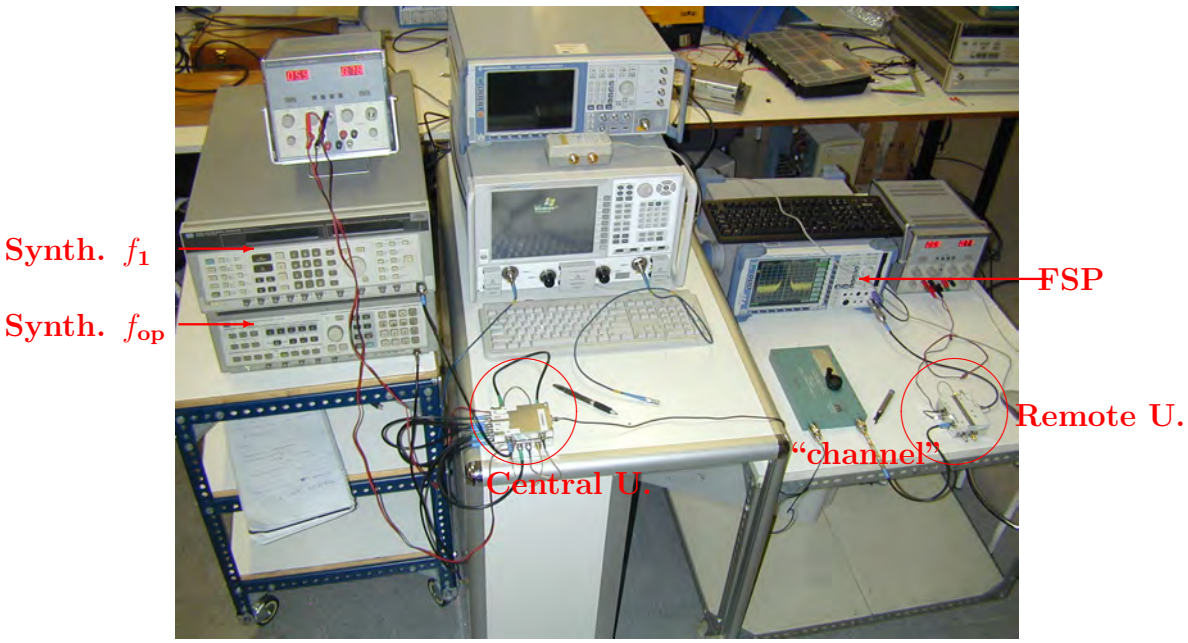

Figure 6.3: Picture of the setup for the phase noise measurements.

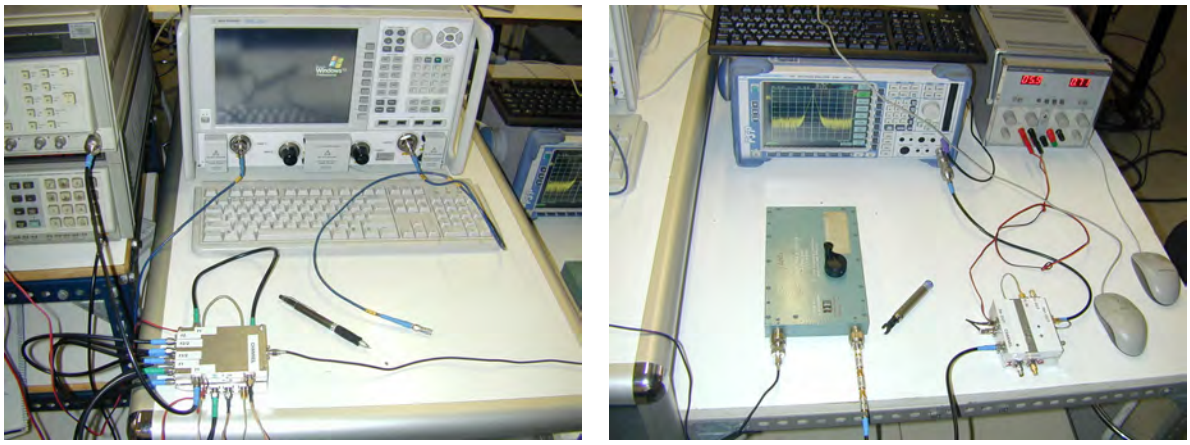

Figure 6.4: Photographies of the setup for the phase noise measurements. The left picture shows the Central Unit and the VNA. The right picture shows the variable phase shifter (the blue device), the Remote Unit, and the Frequency Spectrum Analyzer (FSP)

For the experiments, the synthesizers were synchronized to a common low frequency reference which was obtained from the FSP. Therefore, the frequency spectra of the f_{op} and f_1 tones have a similar shape. On the other hand, the synthesizer which is chosen to generate the f_{op} tone has a lower background noise floor.

The power of the f_{op} tone was adjusted to 7 dBm, and the power of the f_1 tone was adjusted to 0 dBm. The spectrum of these tones were measured in the FSP. Their values will be compared with the spectrum of the loop output.

Spectrum measurement were done for three different attenuation values of 8, 11 and 14 dB. The phase noise for different spans and resolutions are shown if the following.

The frequency spectrum of the regenerated output f_{op} is shown in Figure 6.5. The peak power for the f_{op} tone is 5.65 dBm. This output power remained constant for the three different attenuations. Figure 6.6 shows the single-sided phase noise spectrum with a span of 1.2 kHz. The phase noise spectrum for the three attenuations is very close to the input f_{op} carrier. These measurements were taken with the minimum resolution bandwidth allowed by the spectrum analyzer, which is 10 Hz.

The spectrum of the f_1 reference is plotted with a dashed gray line, and is lower than the phase noise of f_{op} carrier for these low frequencies.

Figure 6.7 shows the single side band phase noise in a span of 20 kHz. In the same way as in Figure 6.6 the phase noise spectrum for the three attenuations is very close to

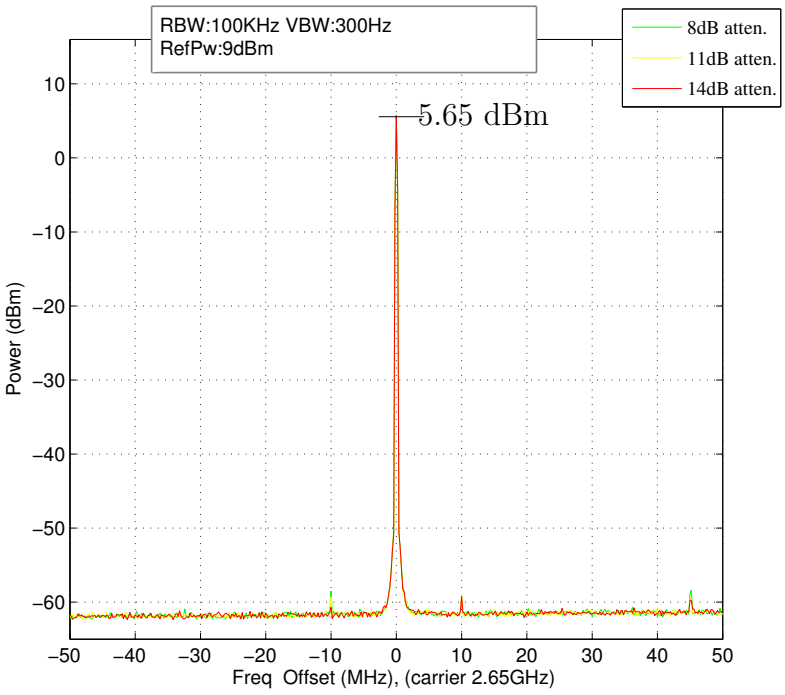

Figure 6.5: Double sided power frequency spectrum of the loop output. 100 MHz span centered at the f_{op} carrier.

the f_{op} input carrier. These measurements were taken with a resolution bandwidth of 30 Hz.

Figure 6.8 shows the single side band phase noise in a span of 2 MHz. These measurements were taken with a resolution bandwidth of 1 kHz. For this frequency range there is no noticeable difference between the phase noise plots for the three attenuations. In this graph the phase noise plots of the system output begin to be greater than the phase noise of the input carrier f_{op}. However, this difference decreases with the frequency. The maximum difference is close to the loop corner frequency and has a value of approximately 5 dB, this difference at 2 MHz offset decreases to 1 dB approximately.

Figure 6.8 also shows how the phase noise of the f_{c} tone crosses the phase noise of the carrier f_1 at a point near to 700 kHz. In this point the greater background noise of the f_1 tone becomes noticeable. This difference continues increasing for higher frequencies. However, it is worth noticing that this behavior does not affect the phase noise spectrum of the loop output.

The lack of correlation between the f_1 tone and the system output is even more

noticeable in Figure 6.9. This Figure shows a double sided phase noise spectrum with a total span of 200 MHz, and a instrument reference power level of -50 dBm.

The phase noise spectrum seen in Figure 6.9 show harmonics of the 10 MHz frequency and other spurs peaks. Notwithstanding, the maximum peak value is at -114 dBc/Hz, observed at a frequency offset of 55 MHz from the carrier, and the next peak in value has -121 dBc/Hz observed at a frequency offset of 10 MHz.

The frequency offset of 55 MHz is equal to the f_m frequency $(f_2 - f_1)$. The frequency offset of the second highest peak appears at the crystal reference frequency of 10 MHz. These spurs are not visible in the phase noise spectrum of f_{op} and f_1.

One characteristic that can be observed in Figure 6.9 is that for high frequencies the phase noise spectrum of the loop output is better than the phase noise of the input reference if the spurs are discarded.

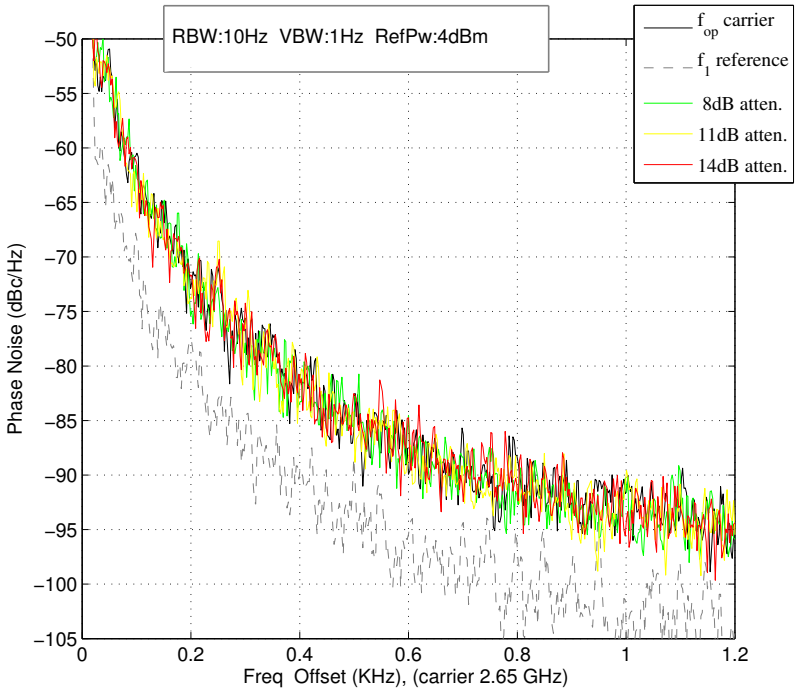

Figure 6.6: System f_{op} output Phase Noise Spectrum. Span=1.2 kHz

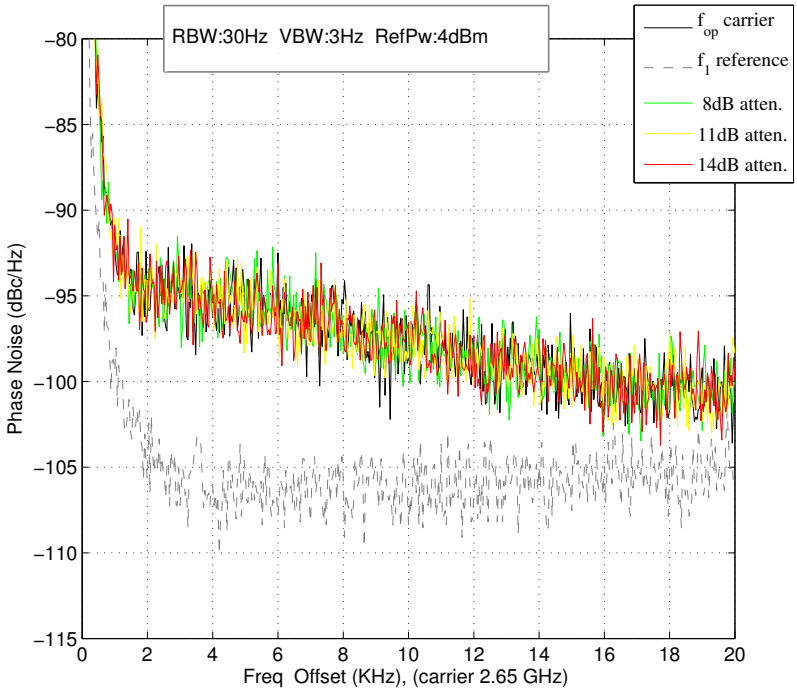

Figure 6.7: System f_{op} output Phase Noise Spectrum. Span=20 kHz

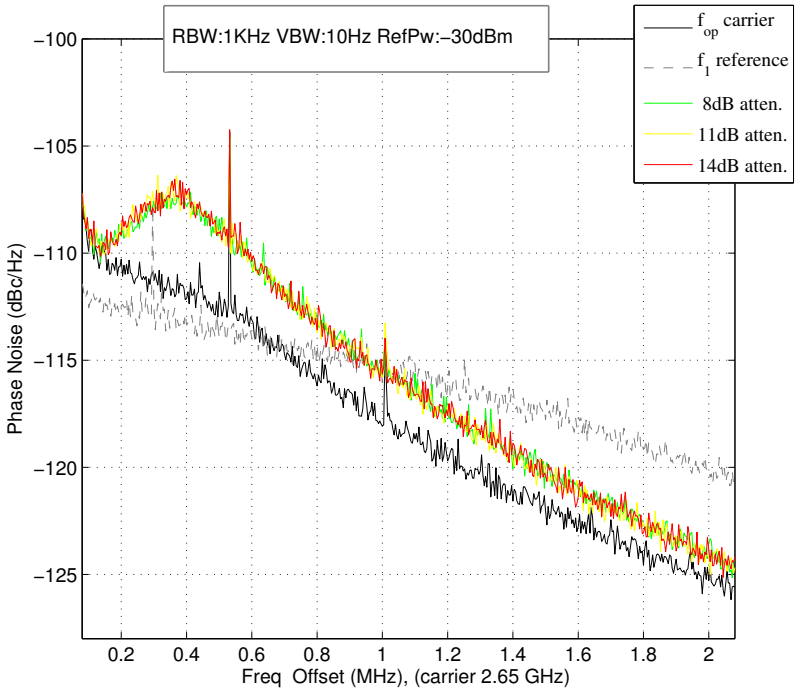

Figure 6.8: System f_{op} output Phase Noise Spectrum. Span=2 MHz

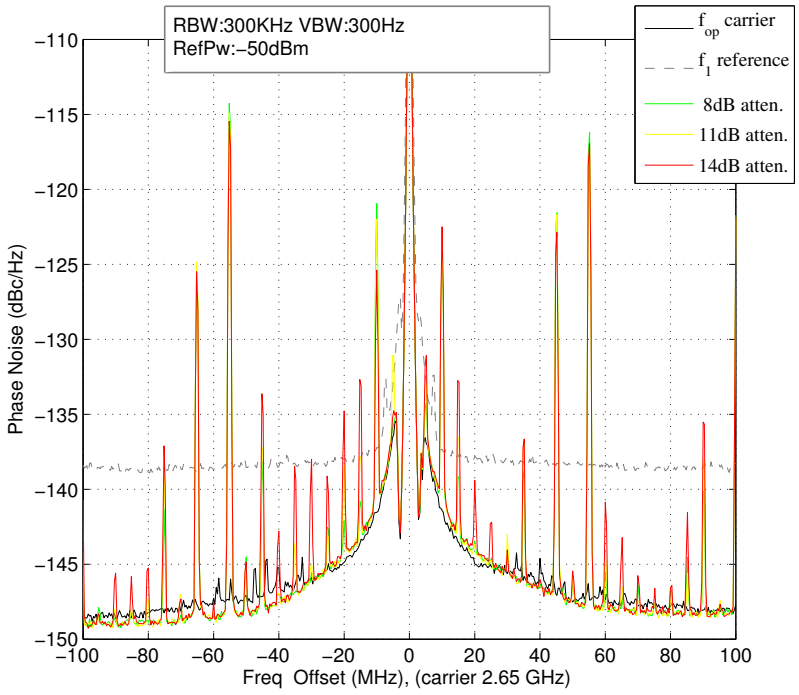

Figure 6.9: System f_{op} output Phase Noise Spectrum. Span=200 MHz Double sided and centered at the carrier.

6.2 Phase offset measurements for the complete Phase Synchronization Loop

The absolute phase offset of the complete Phase Synchronization System was characterized by means of a set of laboratory measurements.

The phase offset was measured from the transmission line parameters (S-parameters) using the VNA. The device used was the model N5245A manufactured by Agilent Technologies. The phase measurement was obtained from the angle of the parameters S21, working in a CW single frequency and time sweep configuration.

The CW frequency of the output port of the VNA was adjusted to 2.65 GHz and its output power was adjusted to 9 dBm. This stimulus was connected to the f_{op} input port in the Central Unit. The port No. 1 of the VNA was the transmitter port (stimulus) and the port No. 2 was the receiver port. The VNA was calibrated for this configuration. A diagram for the setup of the phase offset spectrum measurements is shown in Figure 6.3.

The f_1 input was generated externally with a frequency synthesizer, in the same way as

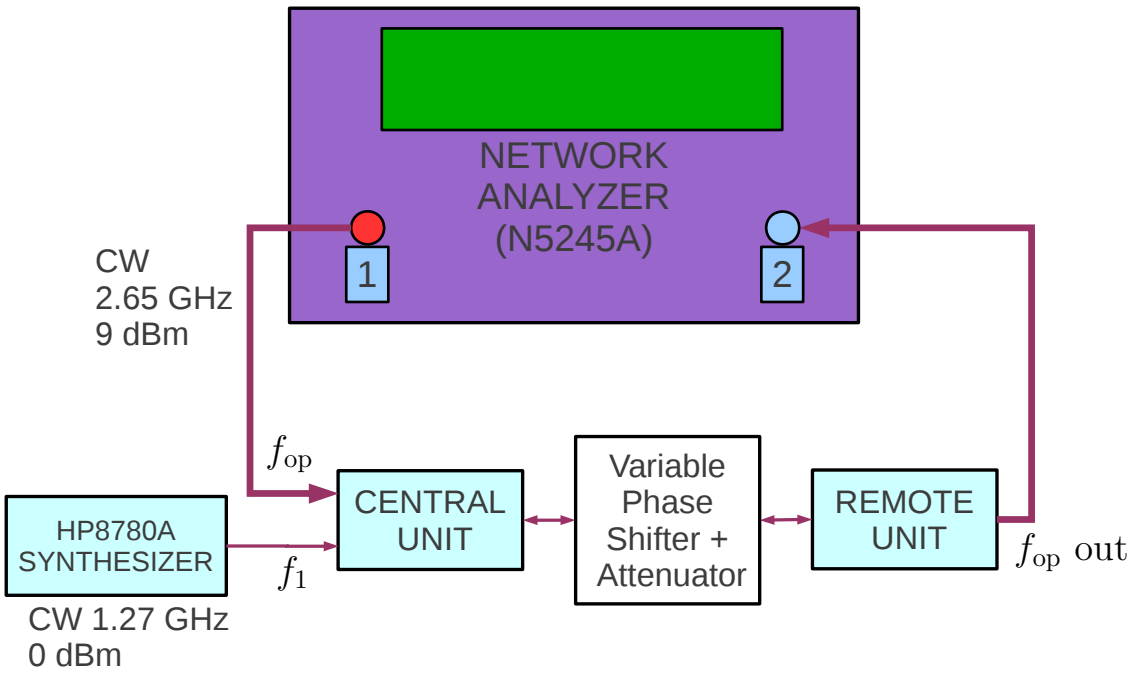

Figure 6.10: Setup for the complete loop phase offset measurements. The phase offset is obtained from the angle of the S21 measurements.

was done in the frequency spectrum measurements explained in Section 6.1. (CW 1.27 GHz with 0 dBm). In addition, the Central Unit and the Remote Unit were connected using a set of attenuators in series with a variable phase shifter.

The S21 parameters were acquired for time sweeps of 300 seconds in 401 samples. Wherewith each measurement is averaged for approximately 0.75 seconds. There were taken measurements for attenuation values of 11 and 14 dB, in two different realizations performed in two subsequent days. (November 22 and November 23 2011. For each different measurement the VNA was re-calibrated).

These phase offset measurements are shown in Figure 6.11. These four plots remained within a range of 0.5 degrees.

A longer measurement, with a duration of 20 minutes was also taken, for the two values of channel attenuation. This measurement of 1200 seconds was acquired in 401 samples for an integration time of approximately 3 seconds per each sample. Figure 6.12 shows these Phase Offset measurements.

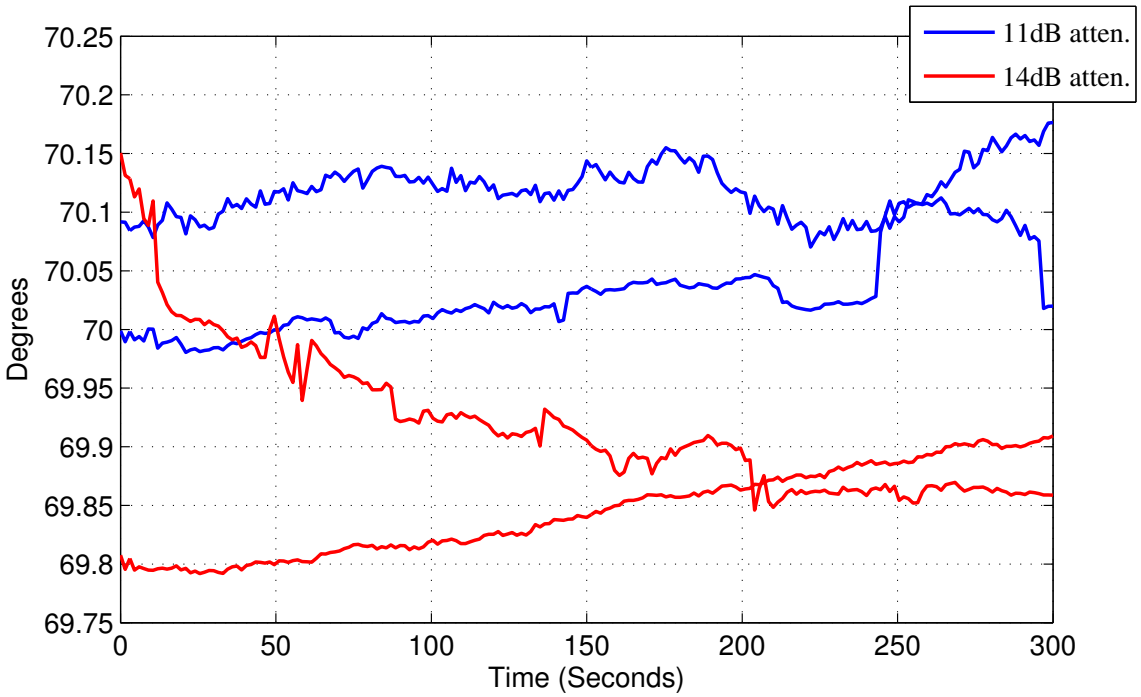

Figure 6.11: Phase Offset of the complete Phase Synchronization System in a 300 seconds time duration, for 2 different realizations of two attenuation values (11 and 14 dB).

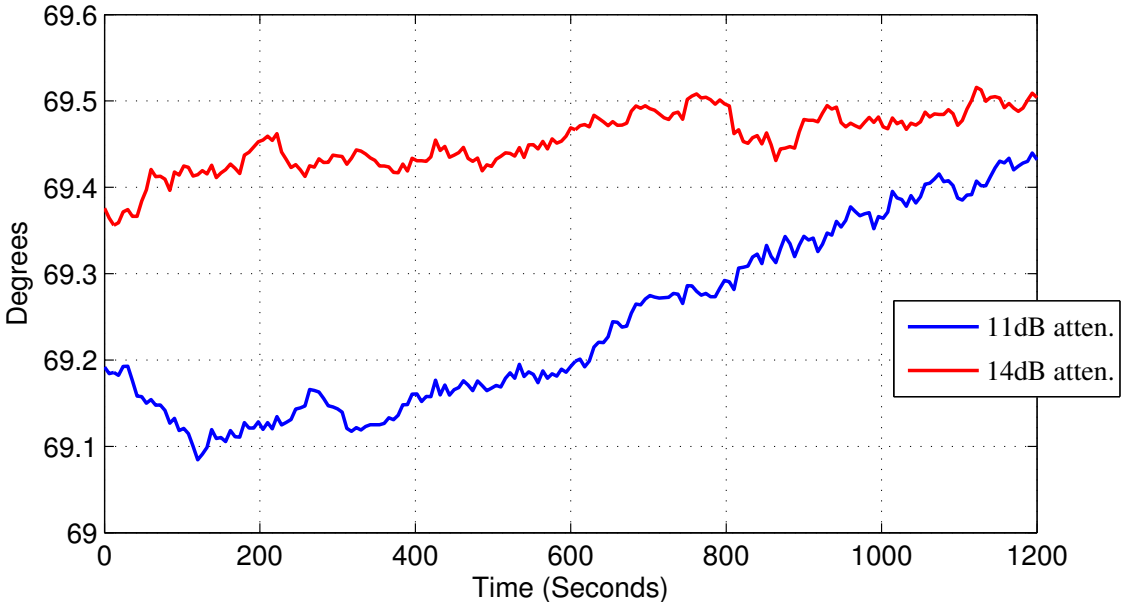

Figure 6.12: Phase Offset of the complete Phase Synchronization System in a 1200 seconds time sweep, for 2 different attenuation values of 11 and 14 dB.

Phase offset measurement with a mechanical variable phase shifter

The absolute phase offset measurement was performed using a mechanical phase shifter (Model 3752 from Narda Microwave Corp.) to interconnect the Central Unit and the Remote Unit in addition to the 11 dB attenuator. The phase shifter has a span of more than one cycle at 2.65 GHz. Then, the phase response of the complete system is measured moving manually the handle of the shifter from one end to the other with a rate near to 32 degrees per second. As it can be seen in Figure 6.13, the phase stability remained within a range of 2 degrees peak-to-peak.

To be more precise, the phase shifter behaves as a constant time delay for all frequencies in its operation bandwidth, which is from 1 GHz to 5 GHz. The difference between the minimum and maximum delays is 0.5083 nanoseconds, which is equivalent to a phase offset of 484.95 degrees at 2.65 GHz. For the 300 second measurement shown in Figure 6.13 the phase shifter moved approximately 10 complete spans of 484.95 degrees.

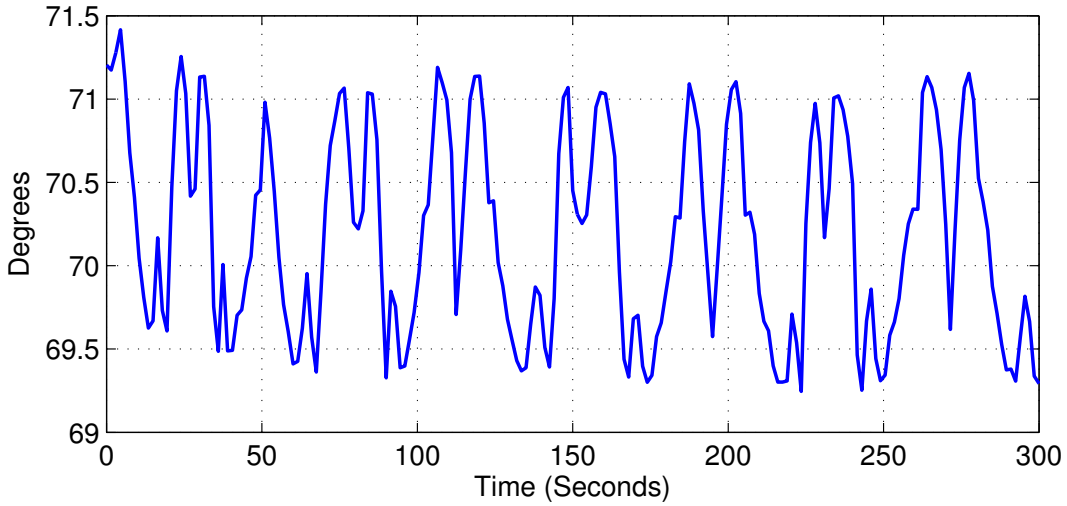

Figure 6.13: Phase Offset of the complete Phase Synchronization System in a 300 seconds duration, with a manual handling of the mechanical phase shifter. With a phase span of 484.95 degrees at 2.65 GHz. During the acquisition the shifter is moved from one extreme to the other 20 times.

Phase offset measurements sweeping the value of the f_1 frequency

In an ideal phase synchronization system the variations in phase and frequency of the tone f_1 will not affect the absolute phase offset between the Central Unit and the Remote

Unit. However, the phase response of the elements within the phase loop vary in function of the frequencies f_1 and f_2. This function does not follow always a perfect linear relation.

In addition, there is a phase transfer function between the input phase, θ of the tone f_1 and the system phase output. (Explained in Chapter 4). The steady state response of this function (for an step input) is zero. Although, their transitory effects can not be obviated.

A first measurement of phase offset with a f_1 modulation was performed with a frequency sweep of 8 MHz for 200 seconds. The initial value of f_1 was 1.27 GHz and the final value was 1.278 GHz.

The acquisition was performed exactly as the the first phase offset experiment, a total duration of 300 seconds in 401 samples. The absolute phase offset obtained from this experiment is shown in Figure 6.14

As it can be seen in Figure 6.14 the variation of the output phase were approximately 35 degrees for the complete frequency sweep of 8 MHz.

Next, another frequency sweep profile was proved, with a sweep time of 5 seconds and sweep bandwidth of 100 kHz. The results are shown in Figure 6.15 The experiment was repeated with the same sweep bandwidth of 100 kHz and with a sweep time of 40 milliseconds. The results are shown in Figure 6.16

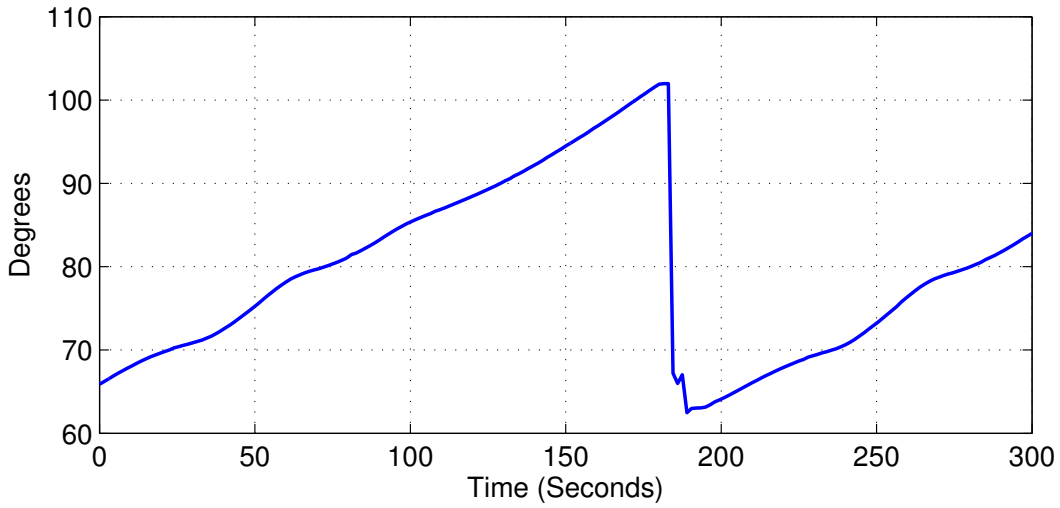

Figure 6.14: Phase Offset of the complete Phase Synchronization System with a f_1 frequency sweep of 8 MHz in 200 seconds. The acquisition length was 300 seconds.

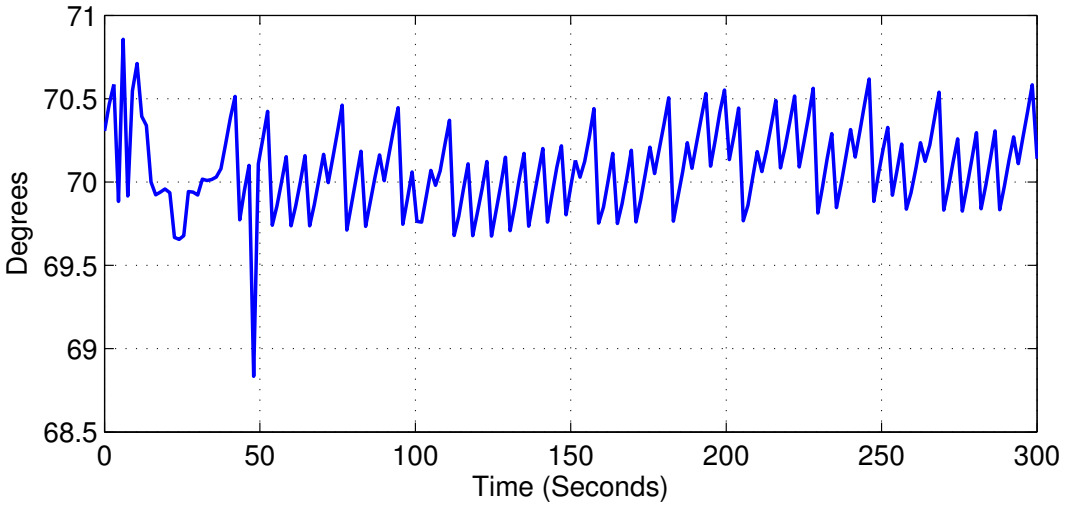

Figure 6.15: Phase Offset of the complete Phase Synchronization System with a f_1 frequency sweep of 100 kHz in 5 seconds. The acquisition length was 300 seconds.

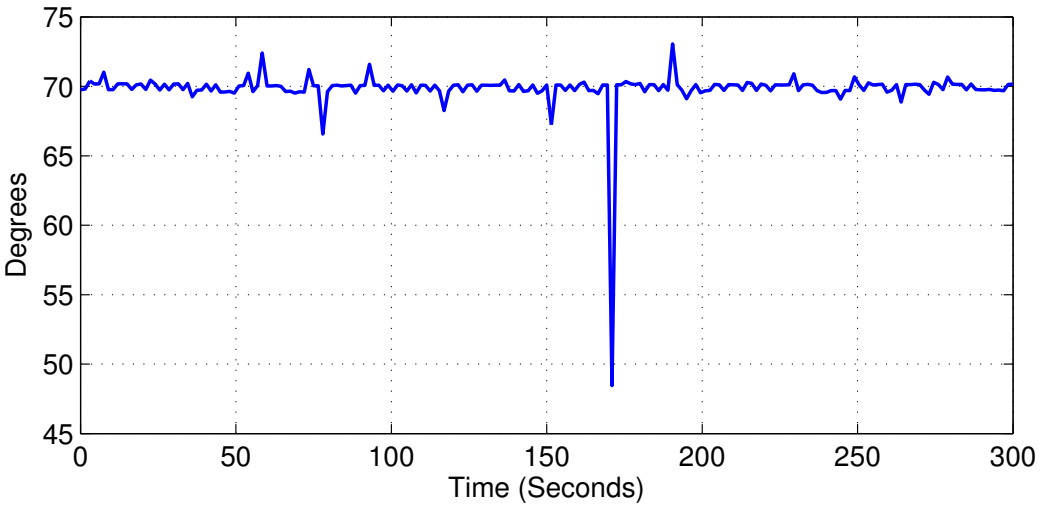

Figure 6.16: Phase Offset of the complete Phase Synchronization System with a f_1 frequency sweep of 100 kHz in 40 milliseconds. The acquisition length was 300 seconds.

Chapter 7

1-D Distance measurement experiments using the Phase Synchronization System

The first application in which the Phase Synchronization System was used has been the measurement of distance variations with high precision. The measurement scheme consists of an unidirectional wireless link (at C-band) between two stations. The measured distance distance ("d") is the separation between the two antennas of the wireless radio link. The distance variation can be obtained from the phase of the down-converted signal using the phase synchronization loop.

Figure 7.1 shows the scheme of the distance measurement system using the phase synchronization link. The local oscillator input of the IQ down-converter in Figure 7.1 is divided by two in frequency and is given to the f_{op} input of the phase synchronization loop in the Central Unit.

The RF Front-end in the Remote Unit contains a frequency doubler which is used to regenerate the carrier of frequency $2f_{\text{op}}$. This carrier is modulated by a complex IQ signal which is generated externally using a two-branch Direct Digital Synthesizer (DDS).

The subsystems of Figure 7.1 explained as follows:

Frequency divider

A stand-alone frequency divider was constructed. The divider was built using the same Hittite chip that was used in the construction of the Central and Remote Units.

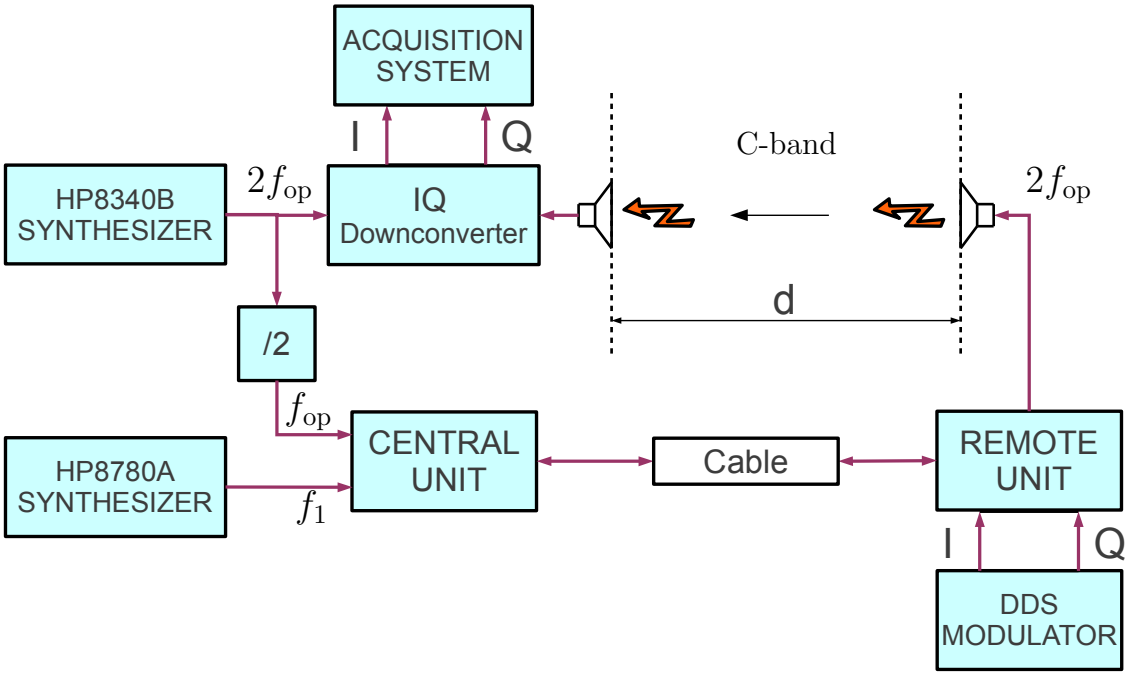

Figure 7.1: 1-D Distance measurement experiment setup.

IQ Downconverter

A stand-alone IQ frequency mixer was constructed. The divider was built using the same Hittite chip that was used in the construction of the RF Front-end of the Remote Unit. The model HMC525 is a level 13 mixer (requires 13 dBm for the local oscillator input) with a conversion loss of 8 dB.

DDS Modulator

An IQ synthesized modulator was constructed. The modulator has two DDS controlled by a Programmable Logic Device (PLD). The DDS used has a resolution of 14 bits in the output DAC (Digital to Analog Converter) and a phase counting resolution of 32 bits, working at a maximum rate of 400 MSPS. This component is the AD9954 manufactured by Analog Devices. The PLD is the FPGA (Field Programmable Gate Array) Spartan 3AN-50 manufactured by Xilinx. Inc.

Each of the complex signals (I or Q) are generated with a separated DDS. The clock input for the DAC of each DDS is obtained from the carrier signal regenerated in the Remote Unit. The f_c carrier ($f_{op}/2$) of the Remote Unit is connected to the DDS

modulator board. Here this signal is divided by 4 in frequency using two frequency halvers in series. Thus a clock signal with 331.25 MHz frequency is generated (1.325/4 GHz).

The layout lines used to provide the DDS clock inputs are designed to have the same electrical lengths. That was done in order to maintain the same phase reference in both DDSs. Moreover, the two DDSs chips implement an additional clock synchronization function between them. With this function the clock reference of each DDS is shared with two synchronization ports, one input port and one output port.

Similarly, both line layouts of the DDSs outputs have exactly the same electrical lengths. Finally, each DDS output path includes an amplifier and a low-pass filter with a 70 MHz bandwidth. Thus, both ports (I and Q) provide approximately 3.5 dBm of output power.

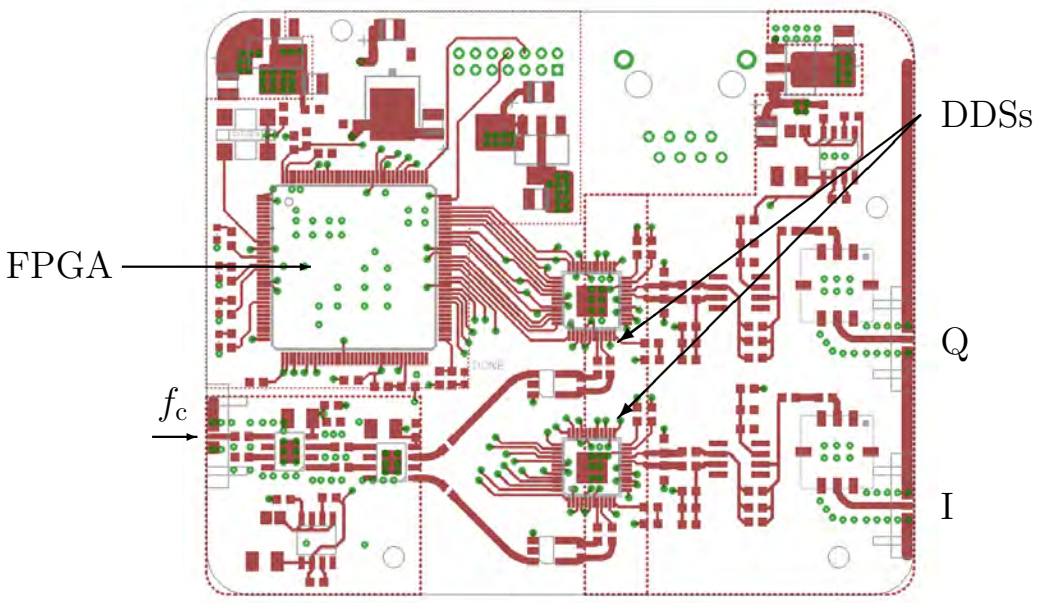

Figure 7.2: DDS Modulator PCB layout (top layer). The board has 4 layers constructed in FR4 substrate.

Figure 7.2 shows the PCB layout of the DDS Modulator board. This board has 86 x 72 mm, the same size of the Remote Unit.

Front-end antennas

The antennas used to transmit the modulated output and receive it prior to the IQ down-converter were designed and constructed. The designed antenna was a four-element patch array working at a central frequency of 5.3 GHz. Figure 7.3 shows the layout of the four-element array antenna.

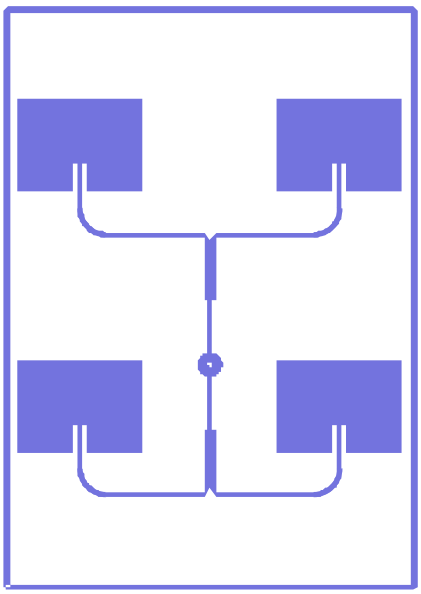

Figure 7.3: Four-element patch array PCB layout.

Each patch has a length computed to obtain a $\lambda/2$ electrical length. The input impedance of the combination of the patch and the input line is adjusted to have 100 Ω.

The first two lines are combined to obtain 50 Ω impedance. This impedance is converted again to 100 Ω with a $\lambda/2$ transformer line with an impedance of $50/\sqrt{2}$ Ω. At the end, the two 100 Ω lines are combined to obtain a total input impedance of 50 Ω.

Finally, the separation between the patches were adjusted manually in order to obtain a main 3dB-gain lobe with of approximately 60 degrees. That was done using the ADS software, with a trial and error test for different separation values. The substrate for the design was ROGERS 4003C (dielectric constant of 3.66) with 1.5 mm thickness.

After construction, the antenna was tested and measured and the S11 parameter had a minimum of -19 dB at the 5.296 GHz frequency, and a 3 dB bandwidth of 40 MHz.

Acquisition System

The acquisition system used to store the down-converted signal is the same used by SABRINA, the PXI system NI5124 manufactured by National Instruments. This acquisition board works on a PXI (PCI eXtensions for Instrumentation) computer platform, has two input channels and works with a maximum sample rate of 200 MSPS and 12-Bit resolution depth.

7.1 Distance variation measurement experiment

The variation of the distance between the two antennas is measured from the down-converted signal stored in the acquisition system. The phase of the received signal depends on the electrical path between the transmitter antenna and the receiver antenna. Therefore, the variations of the distance "d" can be estimated from the down-converted phase. Figures 7.4 and 7.5 show pictures of the complete measurement setup. The experiment was carried out in an anechoic chamber, as it can be seen in Figures 7.4 and 7.5. However another experiment was performed previously in an indoor laboratory environment. For the experiment, the Remote Unit was mounted on a micrometer screw gauge in order to make small and controlled variations over the distance "d".

In the first experiment a continuous frequency sweep was programed in the DDS modulator. The sweep time was adjusted to 1 millisecond arbitrarily, and the bandwidth to 16 MHz.

The ideal frequency ramp would be 16 MHz divided by 1 millisecond, however, the actual ramp value is determined by the resolution of the frequency and phase counters in the DDS. The frequency counter resolution is in this case 32 bits, wherewith the actual final frequency bandwidth becomes 15.999540 MHz instead of 16 MHz (If the floor value of the frequency counter step is chosen).

The I and Q branches of the modulated signals are generated and connected to the I and Q inputs of the RF Front-end of the Remote Unit. The antenna is also connected directly to the RF Front-end of the Remote Unit. On the other end, the other antenna is connected to the IQ Downconverter.

The total distance between the antennas in the experiment done in the anechoic chamber was 7.6 meters, and in the laboratory 12.4 meters.

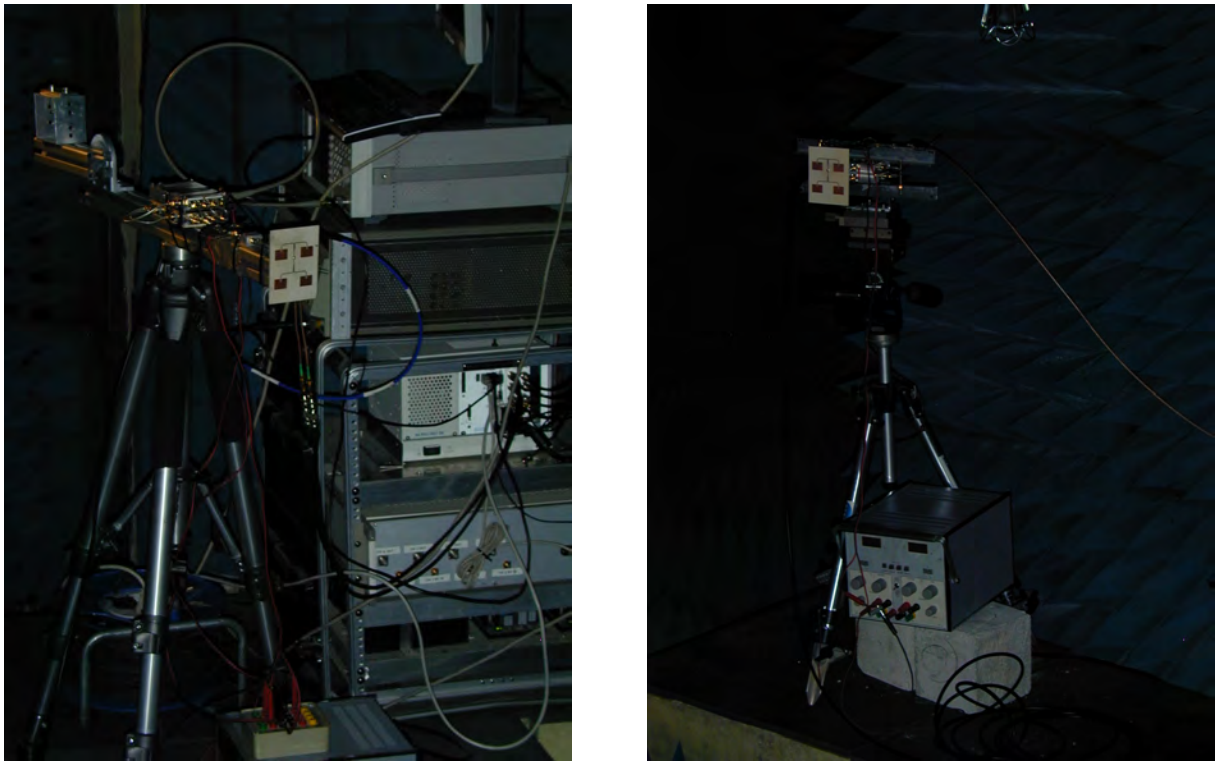

Figure 7.4: Pictures of the setup for the distance measurement experiment. Left: Central Unit, the IQ Downconverter, synthesizers, and acquisition system. Right: Remote Unit and DDS Modulator.

A set of measurements were taken with the acquisition system, at a sampling rate of 40 MSPS for a duration of 2^{25} samples, which is equivalent to 0.838 seconds.

After acquisition the samples are processed and compressed using a previously recorded version of the direct signal generated by DDS Modulator. Then, the phases were obtained from the compressed complex signal.

Two different measurement patterns were done in the experiment. The first pattern consists of a set of 20 measurements with consecutive increments of 0.5 millimeters with the micrometer screw gauge, whereas the second pattern is a set of 20 measurements with an arbitrary displacements multiple of 0.5 millimeters.

In the following, the experimental results are shown and compared with the expected theoretical values for the error in the distance measurement.

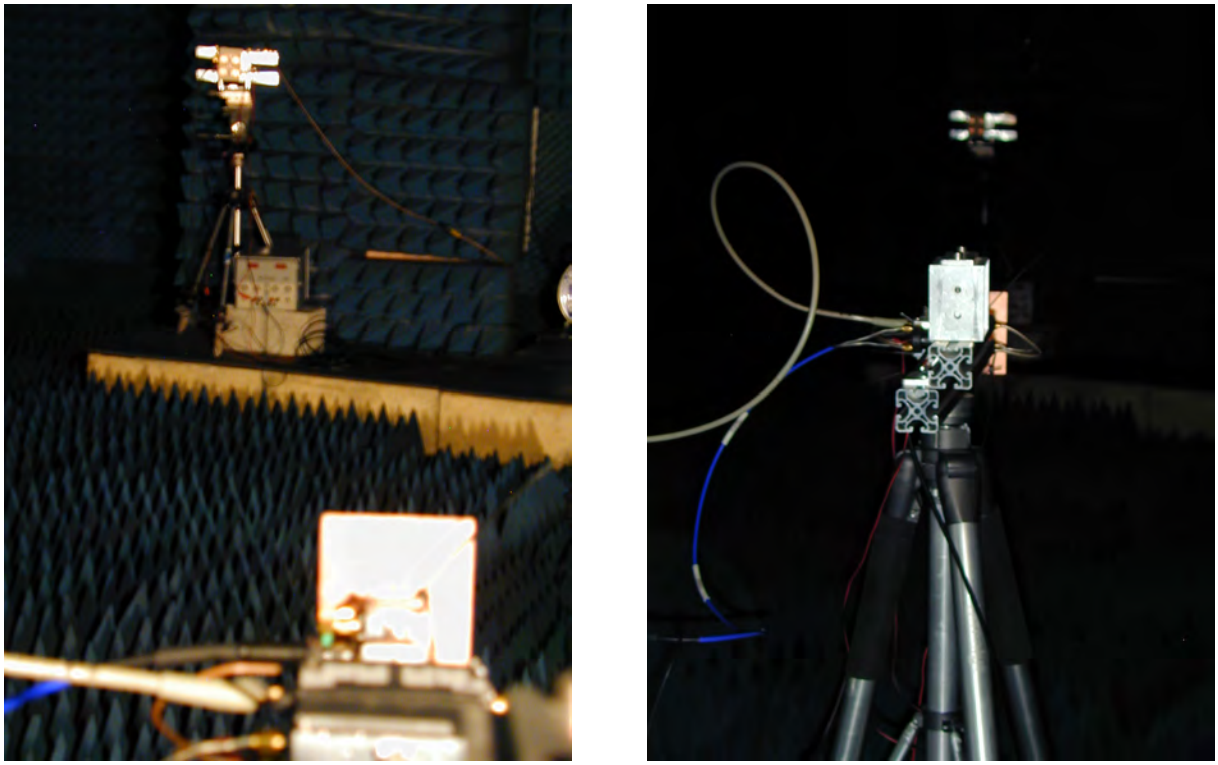

Figure 7.5: Pictures of the setup for the distance measurement experiment. Both antennas are in front of each other.

Distance variation measurement in an indoor hostile environment

The first distance measurement experiment was done in an indoor environment, in the laboratory. The separation between the transmitter and the receiver was adjusted to 12.4 meters.

For each distance measurement an acquisition with 2^{25} samples was performed. Further, the data were processed in lengths of 2^{21} samples.

The pulse duration, which is 1 millisecond, is equivalent to 40000 samples at a rate of 40 MSPS. Thus, in 2^{21} samples 52 complete pulses can be recorded and processed.

The compression of the recorded segment is done by means of the FFT algorithm using Matlab software. After compression, the power peak is found for every segment of 40000 samples. The waveform of the of the compressed signal was checked, and it was found that the maximum was repeated with a periodicity of 40000 samples. Then 52 phase samples are obtained for each measurement.

The phases in 52 points are obtained for the 20 measurements. These phases are

shown in Figure 7.6. Here it can be seen how the phase of the compressed peak varies when the distance between the transmitter and the receiver is changed.

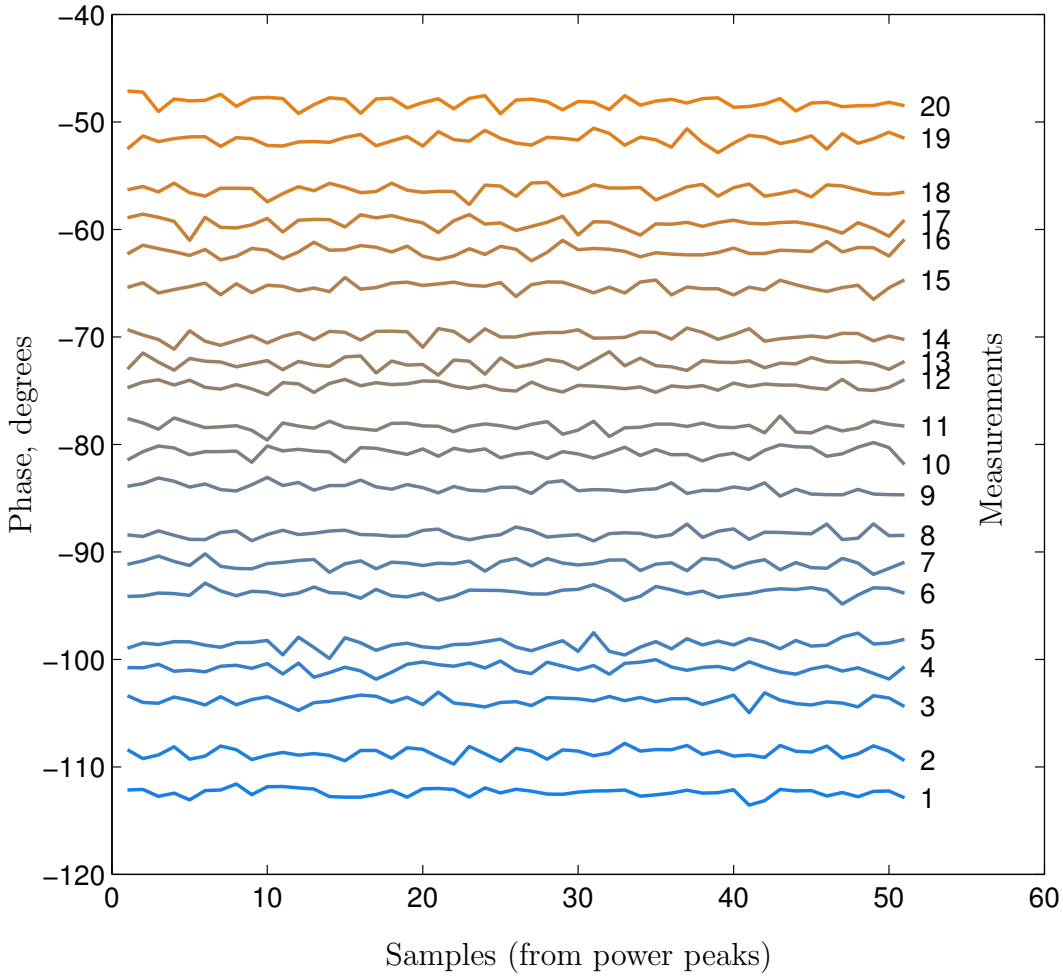

Figure 7.6: Phase of the peaks of the compressed signal for 20 consecutive measurements. Each one with a constant increment of 0.5 mm. This set of measurements was taken in an indoor environment.

The average of the phases obtained from the 52 peaks is obtained and plotted in Figure 7.7. In this plot it can be seen a little difference between the obtained phase and the theoretical phase. This theoretical phase offset is obtained for the propagation in vacuum of the 5.3 GHz carrier.

In principle this error can be attributed to the multi-path effect which is present in the indoor environments. With the bandwidth of 16 MHz the radar resolution is around 9.3 meters which is much more than the distance between the obstacles in the

indoor environment. However, a maximum distance error lower than 600 micrometers was obtained. Figure 7.8 shows the distance error for the measurement set. This error value is obtained from the difference between the phase average of each measurement and the theoretical phase offset. For this difference the first measurement was taken as the reference. In consequence the first point in the plot has no meaning and the error appears to be zero.

In addition to the distance error it is also important to check the stability of each measurement. Therefore the standard deviation was computed for each of the 20 measurements, using segments of 2^{21} samples per measurement. The results are shown in Figure 7.9. Here it can be seen how the standard deviation of the measurement set is between 54 and 87 micrometers.

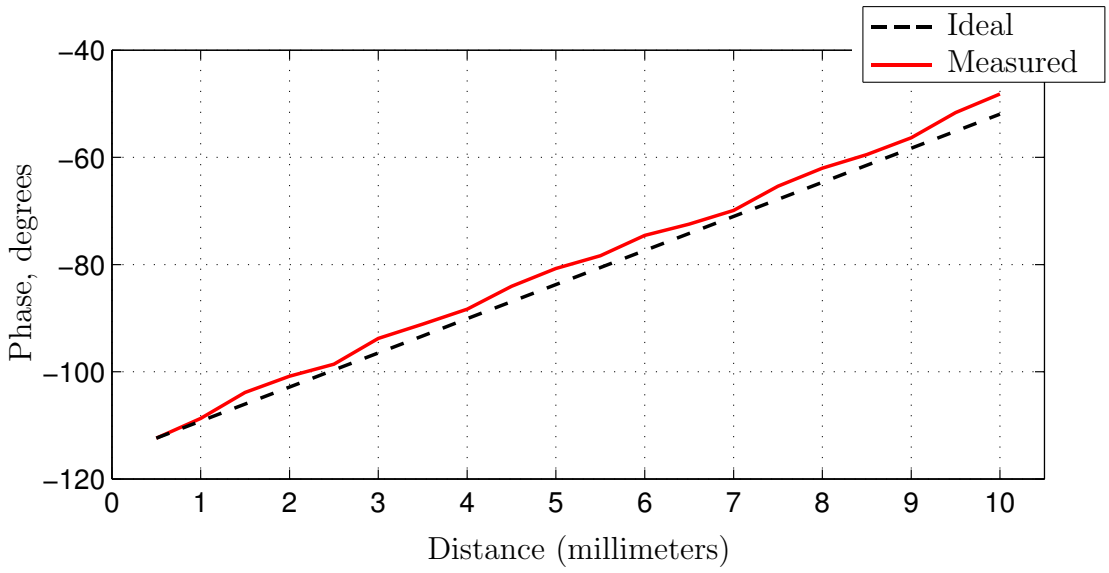

Figure 7.7: Phase average in function of the distances for the measurement set. This phase is compared with the ideal (theoretical) phase offset in function of the distances. The number of samples for the average was 52 (Indoor experiment).

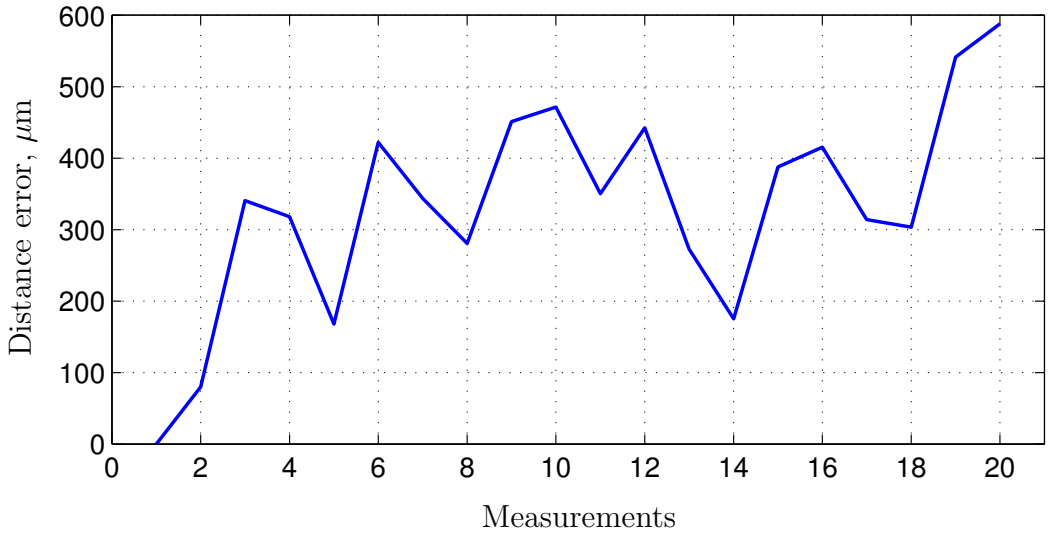

Figure 7.8: Distance error for the measurement set. This value is obtained from the difference between the phase average and the ideal phase. (Indoor experiment).

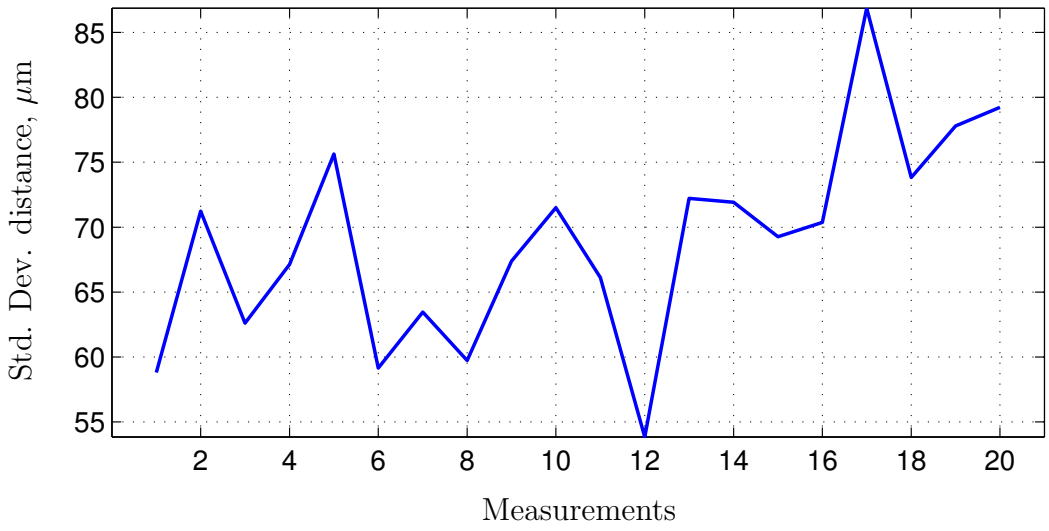

Figure 7.9: Standard deviation in distance for the 52 samples in the measurement set. (Indoor experiment).

Distance variation measurement in an anechoic chamber

The experiment of distance variation measurement was repeated in an anechoic chamber. For space limitations, the distance between the transmitter and receiver was only

of 7.6 meters. Figure 7.10 shows the phases of the 20 measurements obtained in the anechoic chamber. Here it can be seen a phase behavior which is more stable compared to the indoor experiment. The phase averages in function of the known distances in the measurement set is shown in Figure 7.11. This Figure shows that the obtained phases are closer to the theoretical expected values than in the previous experiment. The error in the distance estimation of this experiment is shown in Figure 7.12. In this plot the distance error remains within a window which goes from -150 to 100 micrometers.

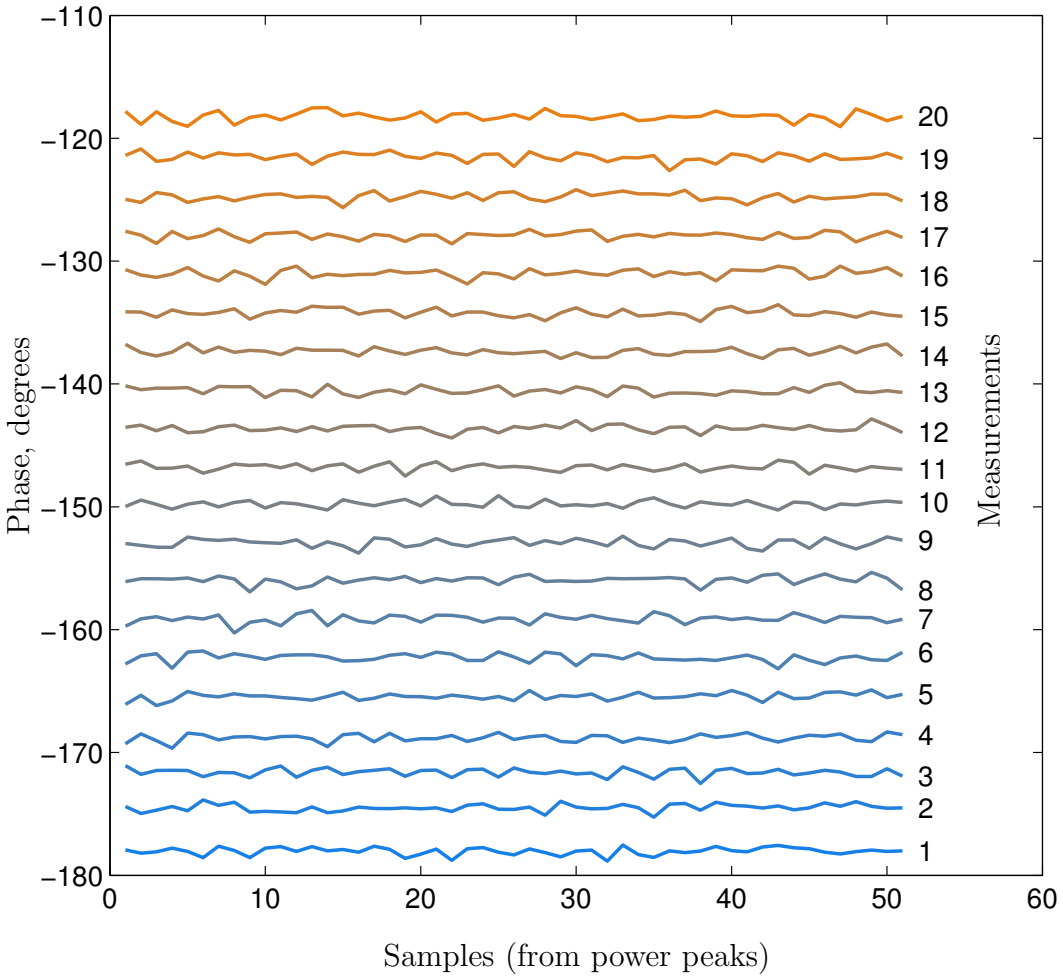

Figure 7.10: Phase of the peaks of the compressed signal for 20 consecutive measurements. Each one with a constant increment of 0.5 mm. This set of measurements was taken in an anechoic chamber.

The standard deviation of each measurement is shown in Figure 7.13. Here it can be seen than these values decreased in comparison to the previous experiment, with values, in this case, that go from 42 to 59 micrometers. The standard deviation values can be interpreted as the quality of the measurements, which is determined by the noise and signal quality of the acquisition. Thereby, in ideal conditions, these values would be expected to be similar to the error of the distance estimation. However, in actual conditions there are other factors that affect the measurement. For example, the position of the antennas was adjusted manually, wherewith, some error in height and horizontal positioning can add bias to the distance estimation.

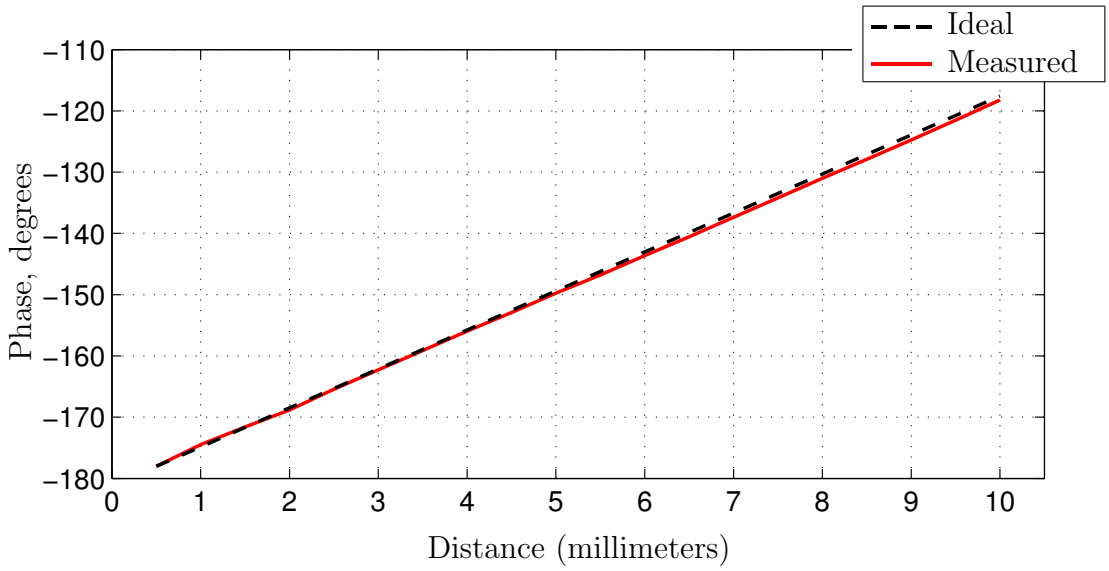

Figure 7.11: Phase average in function of the distances for the measurement set. This phase is compared with the ideal (theoretical) phase offset in function of the distances. The number of samples for the average was 52. (Anechoic chamber experiment).

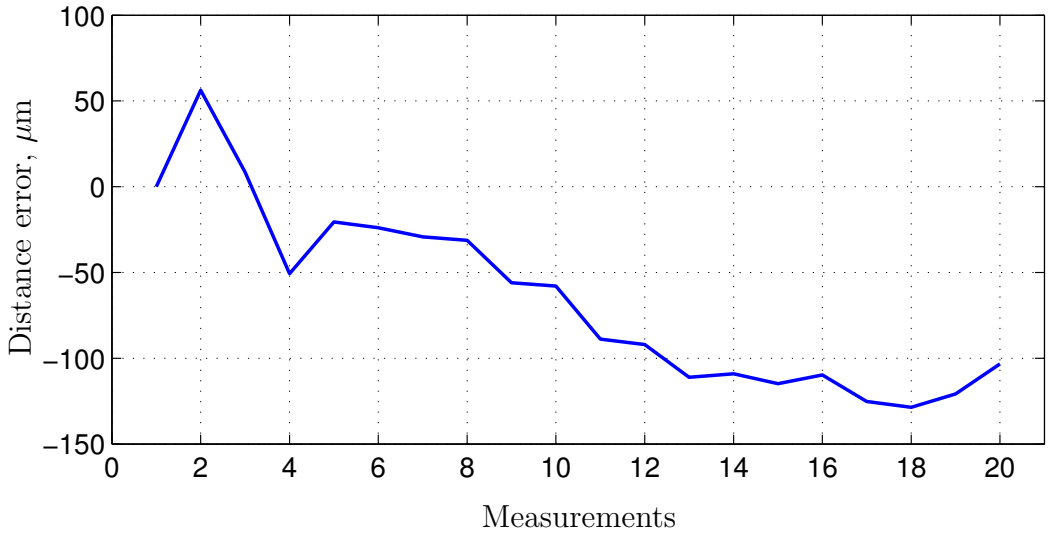

Figure 7.12: Distance error for the measurement set. This value is obtained from the difference between the phase average and the ideal phase.(Anechoic chamber experiment).

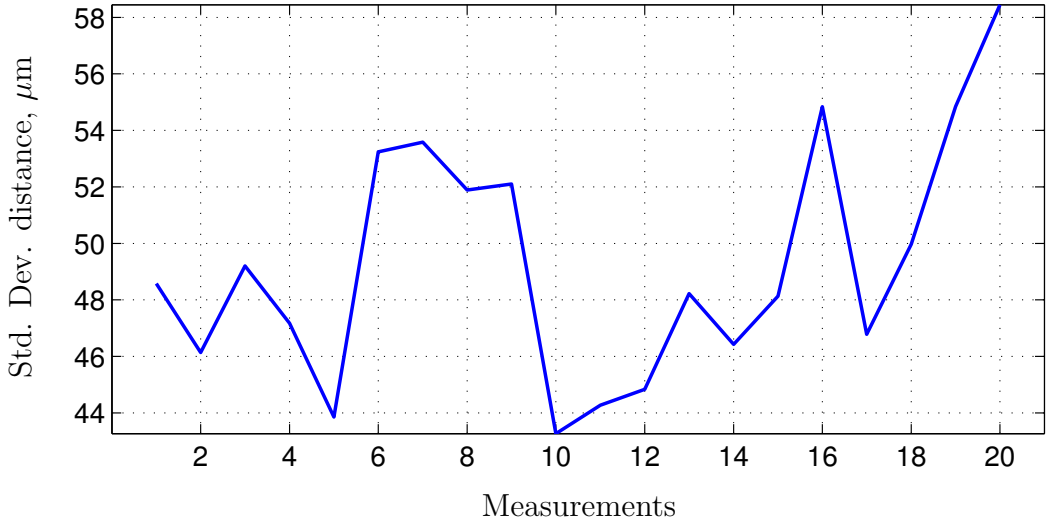

Figure 7.13: Standard deviation in distance for the 52 samples in the measurement set. (Anechoic chamber experiment).

Finally, another experiment was carried out with 20 random and known distances multiples of 0.5 millimeters using the micrometer screw gauge. Thus, 20 random numbers are chosen from an uniform distribution between 1 to 20. This numbers are multiplied by 0.5 millimeters in order to determine the set of displacement values. The obtained

phases of this experiment are shown in Figure 7.14. These phases are shown in a stem plot together with the expected theoretical values.

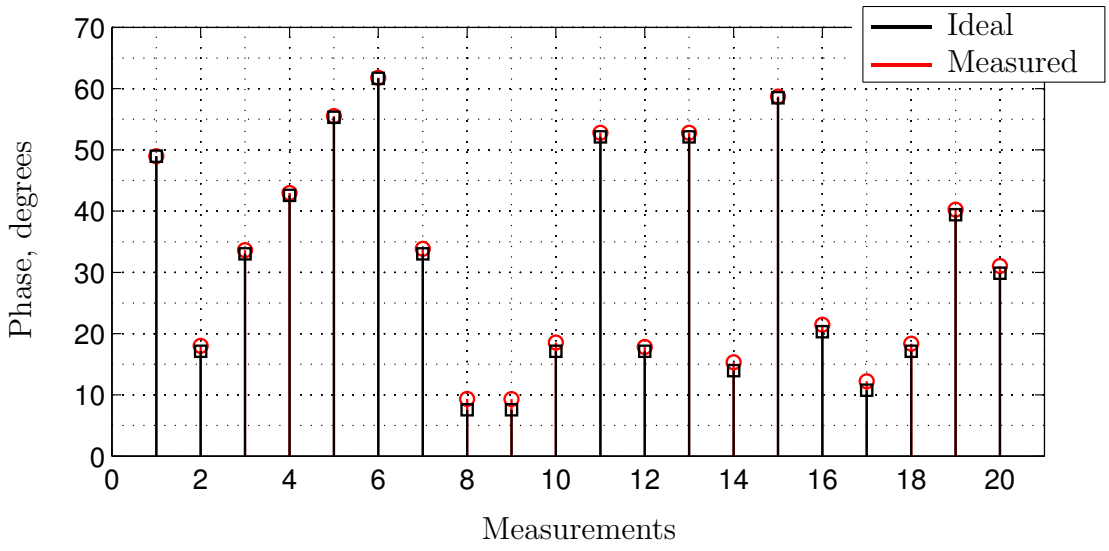

Figure 7.14: Phase average for a set of 20 arbitrary but known distances. This phase is compared with the ideal (theoretical) phase offsets. The number of samples for the average was 52. (Anechoic chamber experiment).

The error on the distance estimations is shown in plot 7.15 and the standard deviation for this measurement set is shown in Figure 7.16. In the last plot it can be seen that the standard deviation is very similar to the standard deviation of the previous experiment (consecutive displacements). However, the distance error is greater and is always positive, with a maximum lower than 300 micrometers.

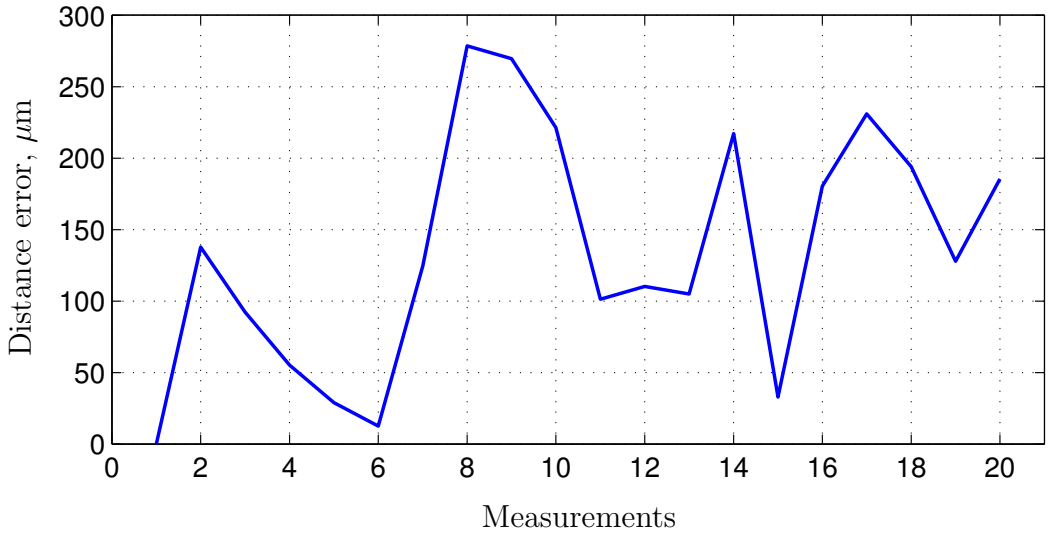

Figure 7.15: Distance error for the measurement set with aleatory distances. This value is obtained from the difference between the phase average and the ideal phase. (Anechoic chamber experiment).

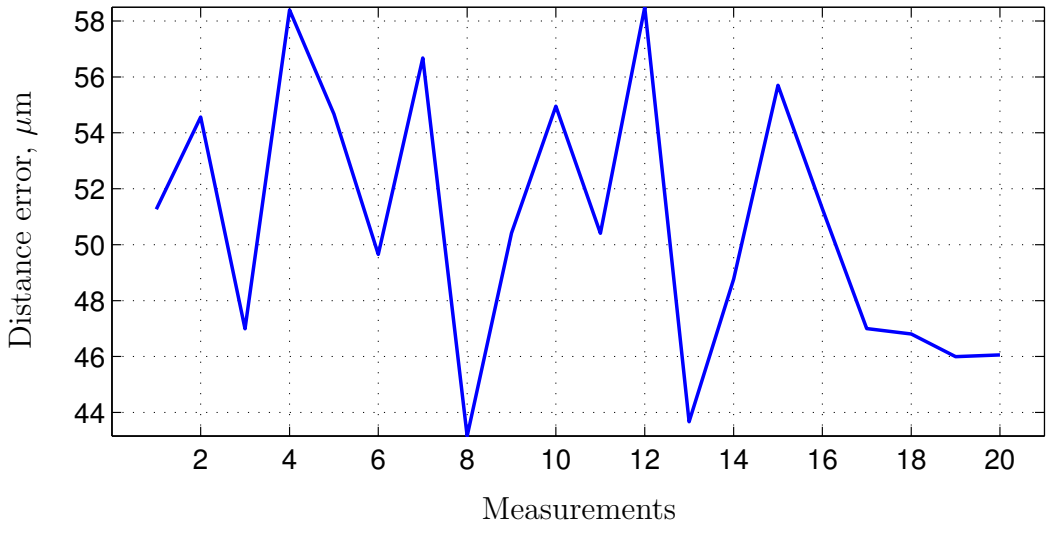

Figure 7.16: Standard deviation in distance for the 52 samples in the measurement set. (Anechoic chamber experiment).

7.1.1 Analysis and comparison between the measurement errors and the theoretically predicted errors

The quality of the measured phase offset depends on many parameters. The most remarkable of these parameters are the quality of the synthesized complex frequency sweep, the noise figure of the transmission and reception subsystems, the quality and resolution of the acquisition system, and finally the most important of them for our study: the quality and **coherence** of the carrier reference signals used to up-convert and down-convert the transmitted waveform.

Thus, it is not only important the quality of the main carrier reference, but also the coherence between the two carriers, one injected to the Central Unit and the other regenerated in the Remote Unit. In other words, it is not only important the phase noise of the main carrier reference but the stability of the Phase Synchronization System.

The received waveform can be expressed in terms of the phases related to the system as follows. First, the synthesized modulating chirp is equal to

$$m(t) = e^{-j\pi Kt^2}\Big|_{-T/2}^{T/2} \tag{7.1}$$

where K is the chirp rate and T is the chirp period. Therefore the received waveform becomes

$$r(t) = e^{-j\pi Kt^2+2\theta_{\text{op}}(t)-\phi_d-2\theta_{\text{out}}(t)} \Big|_{-\frac{T}{2}+t_d}^{\frac{T}{2}+t_d} \tag{7.2}$$

where θ_{op} is the input phase of the synchronization loop, θ_{out} is the output phase of the synchronization loop, ϕ_d is the phase offset induced by the channel propagation between the two antennas and t_d is the propagation delay.

Thus, the propagation phase offset ϕ_d is obtained from the received phase with an error of $\phi_{\text{error}} = 2(\theta_{\text{out}} - \theta_{\text{op}})$. As explained in previous chapters, this phase error is influenced by many factors. Some of these factors are the noise introduced by the VCO used in the synchronization loop, the channel noise, the imperfection of the loop filters,

among others. The standard deviation in the distance measurement is

$$\sigma_d = \left(\frac{\sigma_{\phi\text{error}}}{2\pi}\right) \cdot \lambda.$$

The expected output spectrum of the phase noise contributors within the synchronization loop were computed numerically using the actual values and their corresponding phase transfer functions. The total output phase is given by

$$\theta_{\text{out}} = \theta_{\text{op}} G_{\text{op}} + \theta G_\theta + \phi_{\text{n1}} G_{\text{n1}} + \phi_{\text{n2}} G_{\text{n2}} + \phi_{\text{nc}} G_{\text{nc}} + \phi_{\text{n-vcoL}} G_{\text{vcoL}} + \phi_{\text{n-vcoU}} G_{\text{vcoU}} \quad (7.3)$$

where θ_{op} is the input carrier phase, θ the other modulating phase used in the synchronization loop, ϕ_{n1}, ϕ_{n1}, ϕ_{n2} and ϕ_{nc}, are the additive channel noises of the synchronization loop, and finally $\phi_{\text{n-vcoL}}$ and $\phi_{\text{n-vcoU}}$ are the phase noises of the two VCO used.

The phase error becomes

$$\phi_{\text{error}} = 2\left[\theta_{\text{op}}(G_{\text{op}} - 1) + \theta G_\theta + \phi_{\text{n1}} G_{\text{n1}} + \phi_{\text{n2}} G_{\text{n2}} + \phi_{\text{nc}} G_{\text{nc}} + \phi_{\text{n-vcoL}} G_{\text{vcoL}} + \phi_{\text{n-vcoU}} G_{\text{vcoU}}\right] \quad (7.4)$$

The variance of the phase error is integrated during the chirp period. Thus, the total variance can be computed from each phase noise contributor under the assumption that all of them are uncorrelated.

The integral of the numerical values for 1 KHz bandwidth ($1/T$, with T=1ms) were obtained. The VCO phase noise specifications and a cable attenuation of 11 dB were used for the computations. The total computed standard deviation of the phase was equal to 0.19 degrees.

As can be seen on the Figures from the distance measurement experiment, the standard deviation in distance is between 40 and 60 micrometers, which is equivalent to a standard deviation in the phase between 0.254 and 0.381 degrees.

The increment on the noise of the received phase can be attributed to the signal degradation of the wireless link. This signal degradation is caused by the attenuation and the quantification noise which is present in the DDS modulator and the acquisition system.

Chapter 8

Conclusions

This Ph.D. thesis has investigated carrier phase synchronization techniques. The primary goal of this research has been to devise a phase synchronization scheme between two separated stations that provide the first step towards the implementation of very large baseline microwave coherent arrays.

Within the development of this project a new phase synchronization scheme has been proposed, designed and implemented satisfactorily, hence the objectives of this Ph.D. Thesis have been met. The new scheme characterizes the phase offset of the transmission channel used to synchronize and interconnect two separated units. This characterization is performed by means of the simultaneous transmission a set of tones with similar frequencies.

From the system design it has been found that the resolution of the phase synchronization system does not depend on the bandwidth given by the separation between the frequencies of the transmitted tones. Thus, in the limit, when this bandwidth is zero the system would be equivalent to a phase synchronization loop in which a single frequency is used.

It can be concluded that the bandwidth required to allocate the set of tones is independent of the carrier frequency and can be arbitrarily small, without any loss in the obtained accuracy or resolution. In practice this bandwidth reduction is associated directly to deterioration of the system dynamic response. As far as the filters in the loop become more selective, the overall time response will be longer.

Hence, the limitations are given by the ability to filter and separate different signals. The filters used to separate the received tones will generate a delay on the complete

system and an inability to follow rapid variations of the parameters of the transmission channel. It has been found analytically that the steady state phase error of a single frequency synchronization loop is zero, however, this response is evaluated after infinite time.

On the other hand, the bandwidth reduction decreases the dispersive effects generated by the channel and the transmission and reception subsystems, wherewith the phase errors of the complete loop are drastically reduced. Thus the bandwidth reduction simplifies the system design and implementation, allowing the reuse of components within the system.

As a consequence, the transitory phase error of the phase synchronization loops depends on the transitory response of the complete dynamic system. For the specific case of the proposed synchronization system, the dynamic response is given by the bandwidth of the PLL filters used along the synchronization scheme. The selection of this PLL bandwidth is determined mainly by the stability criterion of the complete loop. While this maximum is a function of the time delay of the transmission channel.

An important source of phase errors is the non-ideal behavior of the analog PLLs. The phase offset between the input and the output of any conventional analog PLL will be zero only if an ideal integrator is within the loop filter. The physical implementation of an ideal integrator requires a loop filter with an amplifier with infinite DC gain. [41]. The practical implementation of a PLL with a non-ideal amplifier will generate a phase error unbounded as the time increases.

A complete prototype of the carrier phase synchronization scheme has been designed and built. Thus, the conceptual proposed scheme has been proven experimentally. The most important goal of the implemented prototype has been to develop a system with a stable phase offsets between the two stations. The performance of the prototype was measured. The results obtained from the measurements were outstanding and consistent with the theoretical predictions in terms of phase noise and phase offset stability. One possible application of the prototype has been evaluated in order to show the excellent behavior of the synchronization loop. Thus, a simple distance measurement experiment has been carried out. The quality of these measurements were consistent with the characterized quality of the phase synchronization loop.

This 1-D distance measurement experiment will be the starting point for a future implementation of a Radio Location System. In this system more than two stations transmit synchronized signals to a mobile receiver in order to determine its position.

The topic of Carrier Phase Synchronization between two or more stations is extensive. Aside from proving that the Carrier Phase Synchronization between two stations is possible, a secondary objective of this thesis is to provide motivation for future research on these systems. Despite the theory of operation of the phase synchronization is well understood, it is required to develop techniques and methodologies for the implementation of these systems.

For future implementations it would be considered a variation over the proposed system in which the phase detection in the Central Unit is performed at a lower frequency. In the proposed scheme the phase detection is performed at a frequency which is similar to the average frequency of the transmitted tones, in contrast to the Remote Unit which the phase detection is implemented at a frequency significantly lower. In a practical implementation the phase detectors have a better phase noise performance when are used at lower frequencies. Moreover, the maximum frequency of operation allowed by the phase detectors imposes a limit for the maximum operation frequency of the complete synchronization scheme. Hence this variation will allow the implementation of the synchronization system at higher carrier frequencies.

Additionally, it will be required to develop techniques to obtain better phase stabilities, investigating on the codification of the signals used to implement the phase synchronization systems. The codification of the phase synchronization scheme would also allow the multiplexing of many synchronization links sharing the same medium. In future researches, attention must be given to obtaining the fundamental limits on phase and frequency tracking and estimation. For these limits it must be included the effect of the oscillator drifts and its statistical properties.

On the other hand, another research line that can be followed is the study of the techniques and methodologies for the implementation of phase synchronization systems. The implementation of the loop using digital PLL techniques can overcome the limitations which are inherent to the analog loops. Thus, for example, the problem unbounded phase

error present in the analog loops can be resolved.

Finally, the phase synchronization of multiple stations has a broad range of new applications. Some of them are the multistatic radars, large baseline synthetic aperture interferometers (VLA), distributed beamforming, MIMO systems, coordinated multi-base and multi-user communication systems.

Chapter 9

List of publications

Journals

1. Carrier Phase Synchronization Scheme for Very Long Baseline Coherent Arrays. J.C. Merlano-Duncan, P. López-Dekker, and J.J. Mallorquí. *Electronic Letters, 2012.* (Submitted)

2. Fixed Receiver Bistatic SAR Along Track Interferometry. P. López-Dekker, S. Duque, J.C. Merlano and J.J. Mallorquí. *Geoscience and Remote Sensing, IEEE Transactions on.* (Accepted in 2010)

Conferences

1. Bistatic SAR along track interferometry with multiple fixed receivers. S. Duque, P. Lopez-Dekker, J.J. Mallorqui, J.C. Merlano. *Geoscience and Remote Sensing Symposium, 2010 IEEE International, IGARSS 2010*

2. Bistatic SAR Tomography: Processing and Experimental Results. S. Duque, P. Lopez-Dekker, J.J. Mallorqui, J.C. Merlano. *Geoscience and Remote Sensing Symposium, 2010 IEEE International, IGARSS 2010.*

3. Bistatic SAR based on Terrasar-X and ground based receivers. A. Broquetas, M. Fortes, M. Siddique, S. Duque, J.C. Merlano, P. Lopez-Dekker, J.J. Mallorquí, A. Aguasca. *Geoscience and Remote Sensing Symposium, 2010 IEEE International, IGARSS 2010.*

4. Fixed Receiver Bistatic SAR Along-Track Interferometry: First Results. P. López-Dekker, S. Duque, J.C. Merlano, and J.J. Mallorqui. *8th European Conference on Synthetic Apeture Radar, Aachen, Germany, June 2010.*

5. SABRINA-X: Bistatic SAR receiver for TerraSAR-X. A. Broquetas, P. Lopez-Dekker, J.J. Mallorqui, A. Aguasca, M. Fortes, J.C. Merlano and S. Duque. *8th European Conference on Synthetic Aperture Radar, Aachen, Germany, June 2010.*

6. Phase Synchronization Scheme for Very Long Baseline Coherent Transmitters. J.C. Merlano, MSc Thesis, Universitat Politécnica de Catalunya, September 2009.

7. Repeat-pass interferometry using a fixed-receiver and ERS-2/ENVISAT as transmitters of opportunity. S. Duque, P. López-Dekker, J.J. Mallorqui, J.C. Merlano. *Geoscience and Remote Sensing Symposium, 2009 IEEE International, IGARSS 2009.*

8. Airborne Bistatic SAR receiver with the capability of use different opportunity transmitters. J.C. Merlano, P. López-Dekker, J.J. Mallorqui, and S. Duque. *Geoscience and Remote Sensing Symposium, 2008 IEEE International, IGARSS 2008.*

9. Back and Forward Bistatic Interferometry, S. Duque, P. López-Dekker, J.J. Mallorquí, and J.C. Merlano. *Geoscience and Remote Sensing Symposium, 2008 IEEE International, IGARSS 2008.*

10. Bistatic SAR Interferometry Using ENVISAT and a Ground Based Receiver: Experimental Results. P. López-Dekker, J.C. Merlano, S. Duque, J.Sanz-Marcos, A. Aguasca, J.J. Mallorquí. *Geoscience and Remote Sensing Symposium, 2007 IEEE International, IGARSS 2007.*

Bibliography

[1] S.M. Alamouti. A simple transmit diversity technique for wireless communications. *Selected Areas in Communications, IEEE Journal on*, 16(8):1451–1458, October 1998.

[2] G. Avitabile, F. Cannone, and A. Vania. Phase shifter based on DDS-driven offset-PLL. *Electronics Letters*, 42(25):1438–1439, 7 2006.

[3] Zarikoff B. *Frequency synchronization techniques for coordinated multibase MIMO wireless communication systems*. PhD thesis, Simon Fraser University, 2008.

[4] A. Babkovsky and N. Seleznyov. Hybrid PLL/DDS frequency synthesizers. In *Microwave and Telecommunication Technology, 2001. CriMiCo 2001. 11th International Conference on*, 2001.

[5] G. Barriac, R. Mudumbai, and U. Madhow. Distributed beamforming for information transfer in sensor networks. *Proc. Info. Process Sensor Net., 3rd Int'l. Wksp., Berkeley, CA*, April 2004.

[6] L. Belostotski, T.L. Landecker, and D. Routledge. Distance measurement with phase-stable CW radio link using the Chinese remainder theorem. *Electronics Letters*, 37(8):521 –522, apr 2001.

[7] Leonid Belostotski, T. L. Landecker, and D. Routledge. A technique for microwave ranging and remote phase synchronization. *IEEE Trans. on Instrumentation and Measurement.*, 51(3):551–559, June 2002.

[8] Roland E. Best. *Phase-Locked Loops. Design, simulation and applications*. McGraw-Hill, New York., 2003.

[9] S.R. Best. Distance-measurement error associated with antenna phase-center displacement in time-reference radio positioning systems. *Antennas and Propagation Magazine, IEEE*, 46(2):13–22, 2004.

[10] H. Braubach and M. Völker. Method for drift compensation with radar measurements with the aid of reference radar signals. U.S. Patent 2005/0 083 225 A1, U.S. Off. Pat. Office, Washington, DC, Apr. 21, 2005.

[11] P.V. Brennan and A.W. Houghton. Phased array beam steering using phase-locked loops. *Electronics Letters*, 26(3):165–166, 1990.

[12] A. Broquetas, M. Fortes, M.A. Siddique, S. Duque, J.C. Merlano, P. Lopez-Dekker, J.J. Mallorqui, and A. Aguasca. Bistatic SAR based on Terrasar-X and ground based receivers. In *Geoscience and Remote Sensing Symposium (IGARSS), 2010 IEEE International*, pages 114 –117, 2010.

[13] A.K. Brown and J.W. Lavrakas. An overview of space-based radionavigation systems. In *Electronics and Aerospace Conference, 1988. 'How will Space and Terrestrial Systems Share the Future?' Conference Proceedings, IEEE EASCON '88., 21st Annual*, pages 161 –171, November 1988.

[14] D.R. Brown and H.V. Poor. Time-slotted round-trip carrier synchronization for distributed beamforming. *Signal Processing, IEEE Transactions on*, 56(11):5630–5643, 2008.

[15] D.R. III Brown, G.B. Prince, and J.A. McNeill. A method for carrier frequency and phase synchronization of two autonomous cooperative transmitters. In *Signal Processing Advances in Wireless Communications, 2005 IEEE 6th Workshop on*, pages 260–264, 2005.

[16] D. Carter. Phase centers of microwave antennas. *Antennas and Propagation, IRE Transactions on*, 4(4):597–600, 1956.

[17] Hittite Microwave Corporation. Layout guidelines for MMIC components. Technical report, Hittite Microwave Corporation, 2007.

[18] J.C. Curlander and R.N. McDonough. *Synthetic aperture radar: systems and signal processing*. Wiley series in remote sensing. John Wiley & Sons, Inc., Hoboken, NJ., 1991.

[19] A. Demir, A. Mehrotra, and J. Roychowdhury. Phase noise in oscillators: a unifying theory and numerical methods for characterization. *Circuits and Systems I: Fundamental Theory and Applications, IEEE Transactions on*, 47(5):655 –674, may 2000.

[20] S. Draganov, J. Weinfield, and Lin Haas. Inverse beamforming for navigating in multipath environments. In *Acoustics, Speech and Signal Processing, 2008. ICASSP 2008. IEEE International Conference on*, 31 2008.

[21] S. Duque, P. Lopez-Dekker, and J.J. Mallorqui. Single-pass bistatic SAR interferometry using fixed-receiver configurations: theory and experimental validation. *Geoscience and Remote Sensing, IEEE Transactions on*, 48(6):2740 –2749, 2010.

[22] S. Duque, P. Lopez-Dekker, J.J. Mallorqui, and C.L. Martinez. A bistatic SAR interferometric simulator for fixed receiver configurations. In *Geoscience and Remote Sensing Symposium, 2007. IGARSS 2007. IEEE International*, pages 2130 –2133, 2007.

[23] S. Duque, P. Lopez-Dekker, J.J. Mallorqui, and J.C. Merlano. Repeat-pass interferometry using a fixed-receiver and ERS-2/ENVISAT as transmitters of opportunity. In *Geoscience and Remote Sensing Symposium,2009 IEEE International,IGARSS 2009*, volume 2, pages II–246 –II–249, 2009.

[24] S. Duque, P. Lopez-Dekker, J.C. Merlano, and J.J. Mallorqui. Bistatic SAR along track interferometry with multiple fixed receivers. In *Geoscience and Remote Sensing Symposium (IGARSS), 2010 IEEE International*, pages 4099 –4102, july 2010.

[25] S. Duque, P. Lopez-Dekker, J.C. Merlano, and J.J. Mallorqui. Bistatic SAR tomography: Processing and experimental results. In *Geoscience and Remote Sensing Symposium (IGARSS), 2010 IEEE International*, pages 154 –157, 2010.

[26] Duque, S. and Lopez-Dekker, P. and Mallorqui, J.J. and Merlano, J.C. Back and forward bistatic interferometry. In *Geoscience and Remote Sensing Symposium, 2008. IGARSS 2008. IEEE International*, volume 3, pages III –601 –III –604, 2008.

[27] R. Calderbank A. Constantinides A. Goldsmith A. Paulraj H. V. Poor" "E. Biglieri. *MIMO Wireless Communications*. Cambridge University Press, Cambridge, MA., 2007.

[28] C.W. Earp. Features of a new Doppler VOR beacon. *Electrical Engineers, Proceedings of the Institution of*, 112(4):698 –702, 1965.

[29] W.F. Egan. Modeling phase noise in frequency dividers. *Ultrasonics, Ferroelectrics and Frequency Control, IEEE Transactions on*, 37(4):307–315, July 1990.

[30] M. Eineder. Ocillator clock drift compensation in bistatic interferometric SAR. In *Geoscience and Remote Sensing Symposium, 2003. IGARSS '03. Proceedings. 2003 IEEE International*, volume 3, pages 1449 – 1451, july 2003.

[31] Warren B. Bruene E.W. Pappenfus and E.O. Schoenike. *Single sideband principles and circuits.* McGraw-Hill, New York., 1964.

[32] Torres F. *Contribution to the study and desing of synthesized microwave oscillators of great spectral purity.* PhD thesis, Politechnical University of Catalonia (UPC), Department of Signal Theory and Communications, (TSC)., 2008.

[33] H. Fiedler, G. Krieger, M. Zink, M. Younis, M. Bachmann, S. Huber, I. Hajnsek, and A. Moreira. The TanDEM-X mission: an overview. In *Radar, 2008 International Conference on*, pages 60 –64, sept. 2008.

[34] J. Figueiras and S. Frattasin. *Mobile positioning and tracking : from conventional to cooperative techniques.* Wiley Series in Microwaves and Optical Engineering. John Wiley & Sons, Inc., Hoboken, NJ., 2010.

[35] P.G. Flikkema. Spread-spectrum techniques for wireless communication. *Signal Processing Magazine, IEEE*, 14(3):26 –36, may 1997.

[36] N. Fourikis. *Advanced array systems, applications and RF technologies*. Signal Processing and its applications. Academic Press, Harcourt Science Technology Company, London UK, 2000.

[37] L. Franks. Carrier and bit synchronization in data communication–a tutorial review. *Communications, IEEE Transactions on*, 28(8):1107 – 1121, aug 1980.

[38] H. Fu and P.Y. Kam. Exact phase noise model for single-tone frequency estimation in noise. *Electronics Letters*, 44(15):937 –938, 17 2008.

[39] Floyd M. Gardner. *Phaselock Techniques*. John Wiley & Sons, Inc., Hoboken, NJ., 2nd edition, 1979.

[40] Floyd M. Gardner. *Phaselock techniques*. John Wiley & Sons, Inc., Hoboken, NJ., 3rd edition, 2005.

[41] F.M. Gardner. Can Analog PLLs Hold Lock? A Paradox Explored . *Circuits and Systems Magazine, IEEE*, 7(3):46 –52, quarter 2007.

[42] Ramakant A. Gayakwad. *Op-Amps and linear integrated circuits*. Prentice Hall. Upper Saddle River, NJ., 4th edition, 2000.

[43] R. Gierlich, J. Huttner, A. Dabek, and M. Huemer. Performance analysis of FMCW synchronization techniques for indoor radiolocation. In *Wireless Technologies, 2007 European Conference on*, pages 24 –27, oct. 2007.

[44] L.C. Godara. Application of antenna arrays to mobile communications. II. Beam-forming and direction-of-arrival considerations. *Proceedings of the IEEE*, 85(8):1195–1245, August 1997.

[45] L.C. Godara. Applications of antenna arrays to mobile communications. I. Performance improvement, feasibility, and system considerations. *Proceedings of the IEEE*, 85(7):1031–1060, July 1997.

[46] Y.G. Gouzhva, A.G. Gevorkyan, and V.V. Korniyenko. Atomic frequency standards for satellite radionavigation systems . In *Frequency Control, 1991., Proceedings of the 45th Annual Symposium on*, pages 591 –593, May 1991.

[47] Jerald G. Graeme. *Application of operational amplifiers. Third-generation techniques*. McGraw-Hill, New York., 1973.

[48] M.S. Gupta. Noise in high speed digital systems. In *Microwave Symposium Digest, 1988., IEEE MTT-S International*, pages 1127–1130 vol.2, May 1988.

[49] Robert C. Hansen. *Phased Array Antennas*. Wiley Series in Microwaves and Optical Engineering. John Wiley & Sons, Inc., Hoboken, NJ., 2nd edition, 2009.

[50] K. Hardin, R.A. Oglesbee, and F. Fisher. Investigation into the interference potential of spread-spectrum clock generation to broadband digital communications. *Electromagnetic Compatibility, IEEE Transactions on*, 45(1):10 – 21, feb 2003.

[51] K.B. Hardin, J.T. Fessler, and D.R. Bush. A study of the interference potential of spread spectrum clock generation techniques. In *Electromagnetic Compatibility, 1995. Symposium Record. 1995 IEEE International Symposium on*, pages 624 –629, aug 1995.

[52] D.M. Harrison, M.J. Howes, and R.D. Pollard. The evaluation of phase noise in low noise oscillators. In *Microwave Symposium Digest, 1987 IEEE MTT-S International*, 9 1987.

[53] S. Horst, S. Phillips, H. Lavasani, F. Ayazi, and J.D. Cressler. SiGe digital frequency dividers with reduced residual phase noise. In *Custom Integrated Circuits Conference, 2009. CICC '09. IEEE*, pages 251–254, 2009.

[54] A.W. Houghton. Phase-locked loop control of antenna arrays. In *Antennas and Propagation, 1993., Eighth International Conference on*, 1993.

[55] A.W. Houghton and P.V. Brennan. Phased array control using phase-locked-loop phase shifters. *Microwaves, Antennas and Propagation, IEE Proceedings H*, 139(1):31 –37, feb 1992.

[56] J. Kim and B. D. Tapley. Simulation of dual one-way ranging measurements. In *J. Spacecr. Rockets,*, volume 40, page 419–425, may. 2003.

[57] J.L. Klein and K. Chang. Optimum dielectric overlay thickness for equal even- and odd-mode phase velocities in coupled microstrip circuits. *Electronics Letters*, 26(5):274–276, 1990.

[58] G. Krieger, A. Moreira, H. Fiedler, I. Hajnsek, M. Werner, M. Younis, and M. Zink. TanDEM-X: a satellite formation for high-resolution SAR interferometry. *Geoscience and Remote Sensing, IEEE Transactions on*, 45(11):3317 –3341, nov. 2007.

[59] G. Krieger and M. Younis. Impact of oscillator noise in bistatic and multistatic SAR. *Geoscience and Remote Sensing Letters, IEEE*, 3(3):424 –428, july 2006.

[60] V.F. Kroupa. Jitter and phase noise in frequency dividers. *Instrumentation and Measurement, IEEE Transactions on*, 50(5):1241–1243, October 2001.

[61] T. L. Landecker and J.F. Vaneldik. A phase-stabilized local-oscillator system for a synthesis radio telescope. *IEEE Trans. on Instrumentation and Measurement.*, 31(3):185–192, September 1982.

[62] W. Lindsey and Chak Chie. Performance Measures for Phase-Locked Loops–A Tutorial. *Communications, IEEE Transactions on*, 30(10):2224–2227, October 1982.

[63] A. Little, R. Hunstead, and G. Calhoun. A constant phase local oscillator system for a cross type radio telescope. *Antennas and Propagation, IEEE Transactions on*, 14(5):645 – 646, sep 1966.

[64] P. Lopez-Dekker, S. Duque, J.C. Merlano, and J.J. Mallorqui. Fixed receiver bistatic SAR along track interferometry. *Geoscience and Remote Sensing, IEEE Transactions on*, 2011.

[65] P. Lopez-Dekker, J.J. Mallorqui, P. Serra-Morales, and J. Sanz-Marcos. Phase and temporal synchronization in bistatic SAR systems using sources of opportunity. In *Geoscience and Remote Sensing Symposium, 2007. IGARSS 2007. IEEE International*, pages 97 –100, 2007.

[66] P. Lopez-Dekker, J.J. Mallorqui, P. Serra-Morales, and J. Sanz-Marcos. Phase synchronization and Doppler centroid estimation in fixed receiver bistatic SAR

systems. *Geoscience and Remote Sensing, IEEE Transactions on*, 46(11):3459 – 3471, 2008.

[67] P. Lopez-Dekker, J.C. Merlano, S. Duque, J. Sanz-Marcos, A. Aguasca, and J.J. Mallorqui. Bistatic SAR interferometry using ENVISAT and a ground based receiver: Experimental results. In *Geoscience and Remote Sensing Symposium, 2007. IGARSS 2007. IEEE International*, pages 107 –110, 2007.

[68] J.L. Macarthur and A.S. Posner. Satellite-to-satellite range-rate measurement. *Geoscience and Remote Sensing, IEEE Transactions on*, GE-23(4):517 –523, july 1985.

[69] M. Maroti, P. Volgyesi, S. Dóra, B. Kusy, A. Nádas, and Á. Lédeczi. Radio Interferometric Geolocation. In *Embedded networked Sensor Systems, International Conference on, San Diego, California, USA*, pages 1–12, 2005.

[70] D. Massonnet and H. Vadon. ERS-1 internal clock drift measured by interferometry. *Geoscience and Remote Sensing, IEEE Transactions on*, 33(2):401 –408, mar 1995.

[71] U. Mengali. Acquisition behavior of generalized tracking systems in the absence of noise. *Communications, IEEE Transactions on*, 21(7):820 – 826, jul 1973.

[72] U. Mengali and A.N. D'Andrea. *Synchronization techniques for digital receivers*. Applications of communications theory. Plenum Press, 1997.

[73] J.C. Merlano-Duncan, P. Lopez-Dekker, J.J. Mallorqui, and S. Duque. Airborne bistatic SAR receiver with the capability of Use different opportunity transmitters. In *Geoscience and Remote Sensing Symposium, 2008. IGARSS 2008. IEEE International*, volume 3, pages III –609 –III –612, 2008.

[74] H. Moheb, A. Sebak, and L. Shafai. Phase centre analysis of array antennas and its significance for microwave landing system. In *Antennas and Propagation, 1991. ICAP 91., Seventh International Conference on (IEE)*, pages 213–216, April 1991.

[75] M. Morelli. Timing and Frequency Synchronization for the Uplink of an OFDMA System. *Communications, IEEE Transactions on*, 52(1):166, jan. 2004.

[76] R. Mudumbai, G. Barriac, and U. Madhow. On the feasibility of distributed beamforming in wireless networks. *Wireless Communications, IEEE Transactions on*, 6(5):1754–1763, May 2007.

[77] R. Mudumbai, D.R. Brown, U. Madhow, and H.V. Poor. Distributed transmit beamforming: challenges and recent progress. *Communications Magazine, IEEE*, 47(2):102–110, 2009.

[78] R. Mudumbai, J. Hespanha, U. Madhow, and G. Barriac. Distributed transmit beamforming using feedback control. *Information Theory, IEEE Transactions on*, 56(1):411–426, 2010.

[79] Boon Loong Ng, J.S. Evans, S.V. Hanly, and D. Aktas. Transmit beamforming with cooperative base stations. In *Information Theory, 2005. ISIT 2005. Proceedings. International Symposium on*, pages 1431 –1435, sept. 2005.

[80] H. Nies, O. Loffeld, and K. Natroshvili. Analysis and focusing of bistatic airborne sar data. *Geoscience and Remote Sensing, IEEE Transactions on*, 45(11):3342 –3349, nov. 2007.

[81] Mi-Kyung Oh, Xiaoli Ma, G.B. Giannakis, and Dong-Jo Park. Cooperative synchronization and channel estimation in wireless sensor networks. In *Signals, Systems and Computers, 2003. Conference Record of the Thirty-Seventh Asilomar Conference on*, volume 1, pages 238 – 242 Vol.1, nov. 2003.

[82] A.S. Palatnick. Wide-aperture digital VOR. *Aerospace and Electronic Systems, IEEE Transactions on*, AES-14(6):853 –865, 1978.

[83] M. Pichler, A. Stelzer, P. Gulden, C. Seisenberger, and M. Vossiek. Phase-error measurement and compensation in PLL frequency synthesizers for FMCW sensors–I: context and application. *Circuits and Systems I: Regular Papers, IEEE Transactions on*, 54(5):1006 –1017, may 2007.

[84] M. Pichler, A. Stelzer, P. Gulden, C. Seisenberger, and M. Vossiek. Phase-error measurement and compensation in PLL frequency synthesizers for FMCW Sensors–II:

theory. *Circuits and Systems I: Regular Papers, IEEE Transactions on*, 54(6):1224 –1235, june 2007.

[85] J.G. Proakis and D.G. Manolakis. *Digital signal processing: principles, algorithms, and applications*. Prentice Hall. Upper Saddle River, NJ, 1996.

[86] F. Rashid-Farrokhi, K.J.R. Liu, and L. Tassiulas. Transmit beamforming and power control for cellular wireless systems. *Selected Areas in Communications, IEEE Journal on*, 16(8):1437 –1450, oct 1998.

[87] G. Rebeiz and Kwang jin Koh. Silicon RFICs for phased arrays. *Microwave Magazine, IEEE*, 10(3):96–103, May 2009.

[88] M. Rodriguez-Cassola, S.V. Baumgartner, G. Krieger, and A. Moreira. Bistatic TerraSAR-X/F-SAR spaceborne – Airborne SAR experiment: description, data processing, and results. *Geoscience and Remote Sensing, IEEE Transactions on*, 48(2):781 –794, feb. 2010.

[89] R.S. Roger, C.H. Costain, J.D. Lacey, T.L. Landecker, and F.K. Bowers. A supersynthesis radio telescope for neutral hydrogen spectroscopy at the dominion radio astrophysical observatory. *Proceedings of the IEEE*, 61(9):1270–1276, 1973.

[90] J. Rutman. Characterization of phase and frequency instabilities in precision frequency sources: Fifteen years of progress. *Proceedings of the IEEE*, 66(9):1048 – 1075, sept. 1978.

[91] J. Rutman and F.L. Walls. Characterization of frequency stability in precision frequency sources. *Proceedings of the IEEE*, 79(7):952 –960, jul 1991.

[92] A.M.E. Safwata, K.A. Zaki, W. Johnson, and C.H. Lee. Novel design for coplanar waveguide to microstrip transition. In *Microwave Symposium Digest, 2001 IEEE MTT-S International*, 2001.

[93] J. Sanz-Marcos, P. Lopez-Dekker, J.J. Mallorqui, A. Aguasca, and P. Prats. SABRINA: A SAR Bistatic Receiver for Interferometric Applications. *Geoscience and Remote Sensing Letters, IEEE*, 4(2):307 –311, 2007.

[94] J. Sanz-Marcos, J.J. Mallorqui, A. Aguasca, and P. Prats. First ENVISAT and ERS-2 parasitic bistatic fixed receiver SAR images processed with the subaperture Range-Doppler algorithm. In *Geoscience and Remote Sensing Symposium, 2006. IGARSS 2006. IEEE International Conference on*, 31 2006.

[95] M.I. Skolnik. *Radar Handbook*. McGraw-Hill, New York., 1970.

[96] G. Swarup and K. Yang. Phase adjustment of large antennas. *Antennas and Propagation, IRE Transactions on*, 9(1):75 –81, january 1961.

[97] Jr. Thompson, M., L. Wood, D. Smith, and W. Grant. Phase stabilization of widely separated oscillators. *Antennas and Propagation, IEEE Transactions on*, 16(6):683 – 688, nov 1968.

[98] Yung-Szu Tu and G.J. Pottie. Coherent cooperative transmission from multiple adjacent antennas to a distant stationary antenna through AWGN channels. In *Vehicular Technology Conference, 2002. VTC Spring 2002. IEEE 55th*, 2002.

[99] P. Ubolkosold, G.F. Tchere, S. Knedlik, and O. Loffeld. Simple carrier frequency offset estimators in frequency flat-fading channels. In *Communications, 2007. ICC '07. IEEE International Conference on*, pages 2671 –2675, june 2007.

[100] F.T. Ulaby, R.K. Moore, and A.K. Fung. *Microwave remote sensing: active and passive, from theory to applications*. Microwave Remote Sensing. Artech House, 1986.

[101] David van der Merwe, Leenta Grobler, and Melvin Ferreira. A study of q-range ambiguity in the radio interferometric positioning system. In *Telecommunications (ICT), 2011 18th International Conference on*, pages 412 –415, may 2011.

[102] B. Vezant, C. Mansuy, Hung Tien Bui, and F.-R. Boyer. Direct digital synthesis-based all-digital phase-locked loop. In *Circuits and Systems and TAISA Conference, 2009. NEWCAS-TAISA '09. Joint IEEE North-East Workshop on*, pages 1 –4, 28 2009-july 1 2009.

[103] I. Walterscheid, J.H.G. Ender, A.R. Brenner, and O. Loffeld. Bistatic sar processing and experiments. *Geoscience and Remote Sensing, IEEE Transactions on*, 44(10):2710 –2717, oct. 2006.

[104] Chen Wang, Wei Han, Qinye Yin, Wenjie Wang, and Jie Chen. A distributed localization system based on phase measurement for wireless sensor networks. In *Networks Security, Wireless Communications and Trusted Computing, 2009. NSWCTC '09. International Conference on*, volume 1, pages 505–508, 2009.

[105] Ping-Ying Wang, J.-H.C. Zhan, Hsiang-Hui Chang, and H.-M.S. Chang. A digital intensive fractional-N PLL and all-digital self-calibration schemes. *Solid-State Circuits, IEEE Journal of*, 44(8):2182–2192, 2009.

[106] Shih-Ming Wang, Chin-Hsiung Chen, and Chi-Yang Chang. A study of meandered microstrip coupler with high directivity. In *Microwave Symposium Digest, 2003 IEEE MTT-S International*, volume 1, pages 63–66 vol.1, 2003.

[107] Wenqin Wang. Approach of adaptive synchronization for bistatic SAR real-time imaging. *Geoscience and Remote Sensing, IEEE Transactions on*, 45(9):2695 –2700, sept. 2007.

[108] M. Weiß. Time and frequency synchronisation aspects for bistatic SAR systems. In *Proc. EUSAR*, pages 395–398, may. 2004.

[109] R.A. White, R.N. Clarke, and R.W. Yell. VOR waveform synthesis and calibration. *Communications, Radar and Signal Processing, IEE Proceedings F*, 128(7):443 – 450, 1981.

[110] Robert A. White and Ralph W. Yell. Precise differential-phase generator. *Instrumentation and Measurement, IEEE Transactions on*, 29(4):373 –375, 1980.

[111] Costa X. Disseny i caracterització d'un capçal de RF compacte en banda C i X per un receptor SAR biestàtic (in Catalan), Barcelona, Spain, 2011.

[112] Xiang-Gen Xia and Genyuan Wang. Phase unwrapping and a robust chinese remainder theorem. *Signal Processing Letters, IEEE*, 14(4):247 –250, april 2007.

[113] M. Younis, R. Metzig, and G. Krieger. Performance prediction of a phase synchronization link for bistatic SAR. *Geoscience and Remote Sensing Letters, IEEE*, 3(3):429 –433, july 2006.

[114] M. Younis, R. Metzig, G. Krieger, and R Klein. Performance prediction and verification for bistatic SAR synchronization link. German Aerospace Center (DLR), Microwaves and Radar Institute. `http://elib.dlr.de/47874/1/Younis_SynchPaper.pdf`, 2006.

[115] B.W. Zarikoff and J.K. Cavers. Coordinated Multi-Cell Systems: Carrier Frequency Offset Estimation and Correction. *Selected Areas in Communications, IEEE Journal on*, 28(9):1490 –1501, december 2010.

[116] Y. Zhao, L. Wang, J.F. Frigon, C. Nerguizian, K. Wu, and R.G. Bosisio. UWB positioning using six-port technology and a learning machine. In *Electrotechnical Conference, MELECON IEEE Mediterranean*, pages 352 –355, May 2006.

Acronyms

ADC Analog to Digital Converter

ADS Advanced Design Software

AM Amplitude Modulation

CUFDSC Central Unit Frequency Diplexer and Signal Conditioning

CW Continuous Wave

DAC Digital to Analog Converter

DC Direct Current

DDS Direct Digital Synthesizer

ENVISAT ESA Environmental Satellite

ERS European Remote Sensing Satellite

ESA European Space Agency

FFT Fast Fourier Transformation

FPGA Field Programmable Gate Array

FSP Frequency Spectrum Analyzer

GPS Global Positioning System

IF Intermediate Frequency

IQ In-phase and Quadrature

LAR Large Adaptive Reflector

LSBG Lower Side Band Generator

MIMO Multiple Input Multiple Output

OCXO Oven Controlled Crystal Oscillator

OPLL Offset Frequency PLL

PCB Printed Circuit Board

PFD Phase and Frequency Detector

PLL Phase Locked Loop

PRF Pulse Repetition Frequency

PXI PCI eXtensions for Instrumentation

RADARSAT Radar Satellite Canadian Space Agency

RC Resistance Capacitor circuit

RF Radio Frequency

RUFDDC Remote Unit Frequency Diplexer and Down-Converter

SABRINA SAR Bistatic Receiver for INterferometric Applications

SAR Synthetic Aperture Radar

SAW Surface Acoustic Wave

SMD Surface Mount Device

SNR Signal to Noise Ratio

TanDEM-X TerraSAR-X add-on for Digital Elevation Measurement

TDD Time Division Duplex

TDMA Time Division Multiple Access

TerraSAR-X X-band German Earth observation Satellite

UAV Unmanned Aerial Vehicle

USBG Upper Side Band Generator

USO Ultra Stable Oscillator

VCO Voltage Controlled Oscillator

VLA Very Large Array

VLBI Very Large Baseline Interferometer

VNA Vectorial Network Analyzer

VOR VHF Omnidirectional Radio range